TEMPERATURE DEPENDENCE OF MAGNETIZATION AND INDUCED MAGNETIC ANISOTROPY OF SOME Fe, Co AND Ni-BASED AMORPHOUS RIBBONS

BY

SHIBENDRA SHEKHER SIKDER
B.Sc.(Hons), M.Sc.(D.U.), M.Phil.(BUET)

A THESIS SUBMITTED TO THE DEPARTMENT OF PHYSICS, BANGLADESH UNIVERSITY OF ENGINEERING & TECHNOLOGY IN PARTIAL FULFILMENT OF THE REQUIREMENT FOR THE DEGREE OF DOCTOR OF PHILOSOPHY

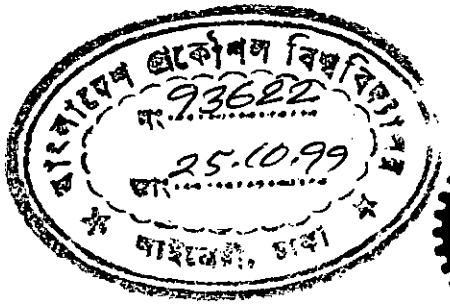

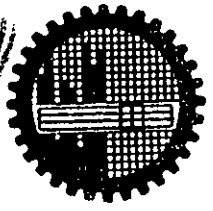

BANGLADESH UNIVERSITY OF ENGINEERING & TECHNOLOGY
DHAKA, BANGLADESH

JULY 1999

BANGLADESH UNIVERSITY OF ENGINEERING AND TECHNOLOGY
DHAKA
DEPARTMENT OF PHYSICS

Certification of thesis work
A Thesis on
Temperature Dependence of Magnetization and Induced Magnetic Anisotropy of Some Fe, Co And Ni-Based Amorphous Ribbons
By
Shibendra Shekher Sikder

has been accepted as satisfactory in partial fulfilment for the degree of Doctor of Philosophy in Physics and certify that the student demonstrated a satisfactory knowledge of the field covered by his thesis in an oral examination held on October 13, 1999.

Board of Examiners

1. **Prof. M. Ali Asgar**
   Department of Physics,
   BUET, Dhaka
   ..... Chairman & Supervisor

2. **Prof. Md. Abu Hashan Bhuiyan**
   Head, Department of Physics
   BUET, Dhaka
   ..... Member

3. **Prof. Gias uddin Ahmad**
   Department of Physics
   BUET, Dhaka
   ..... Member

4. **Prof. Tafazzal Hossain**
   Department of Physics
   BUET, Dhaka
   ..... Member

5. **Prof. Md. Mohar Ali**
   Department of Mats. & Met. Engg.
   BUET, Dhaka
   ..... Member

6. **Prof. Mesbahuddin Ahmed**
   Department of Physics
   Dhaka University, Dhaka
   ..... Member

7. **Prof. S. P. Sen Gupta**
   Head, Material Science Division
   &
   Indian Association for the Cultivation of Science (IACS)
   Jadavpur, Calcutta 70032
   India
   ..... Member (External)

BANGLADESH UNIVERSITY OF ENGINEERING AND TECHNOLOGY
DHAKA
DEPARTMENT OF PHYSICS

Certification of thesis work
A Thesis on
Temperature Dependence of Magnetization and Induced Magnetic Anisotropy of Some Fe, Co And Ni-Based Amorphous Ribbons

By
Shibendra Shekher Sikder

I consider that the thesis can be accepted as satisfactory in partial fulfilment for the degree of Doctor of Philosophy in Physics and certify that the student demonstrated a satisfactory knowledge of the field covered by his thesis.

Prof. Md.Mohar Ali
Department of Mats. & Met. Engg.
BUET, Dhaka

Md. Mohar Ali
Member

CERTIFICATE

This is to certify that this thesis which the candidate has presented for a Ph.D. degree has been done by the candidate himself and does not contain any material extracted from elsewhere or from a work published by any body else. The work of this thesis has not been presented by the candidate for another degree or diploma in any other University. No other person's work has been used without due acknowledgement.

Supervisor

Candidate

Dedicated to the memory of my beloved Mother, Father-in-law, Mother-in-law and my Late Father.

ACKNOWLEDGEMENT

First and foremost I would like to express my thanks to my supervisor Professor M. Ali Asgar for introducing me to the exciting field of amorphous ferromagnetism and guiding me actively through out this work. Without his able guidance and encouragement this work would not have been possible.

I would like to thank Prof. Abu Hashan Bhuiyan, Head of the Department of Physics, Bangladesh University of Engineering and Technology for his valuable advice during the course of my work.

I would like to express my gratitude to Prof. Gias uddin Ahmed, Prof. Tafazzal Hossain and Professor Mominul Huq, Department of Physics, BUET for their inspiration and help in various stages of this work.

I also express my sincere gratitude to Prof. Md. Mohar Ali, Department of Metallurgical Engineering and Material Science, BUET for his valuable suggestions and encouragement.

I would like to thank Prof. Mesbahuddin Ahmad, Department of Physics, Dhaka University for his stimulating suggestions.

My thanks are also due to Prof. Nguyen Chau, National University of Hanoi, Vietnam and Prof. Neguyen Houng Nghi, Vice Director, Chief of the Lab. of Amorphous Magnetic Materials, Hanoi University of Technology, Vietnam for many useful discussions and their assistance in the preparation of the amorphous ribbons. Thanks are also due to Dr. Nguyen Xuan Phuc, Institute of Material Science, National Centre for Science and Technology of Vietnam, Hanoi, Vietnam for allowing me to use his V.S.M. I am grateful to Dr. B. T. Cong and Dr. Le Minh, National University of Hanoi, Vietnam for their encouragement during my stay in Hanoi.

I am thankful to Dr. B. K. Srivastava, Dr. Y. K. Sharma and Dr. A. Krishnamurthy, Associate Professors, Department of Physics, University of Rajasthan, Jaipur, India for their assistance in the Mössbauer Spectroscopy. I am thankful to A. V. Ramesh Babu, research fellow, Department of Physics, University of Rajasthan, Jaipur, India, for helping me in computer works for Mössbauer parameter analysis.

My thanks are also due to Mr. M. A. Mazid, Mr. M. A. Chowdhary, Dr. M. A. Hakim, Mr. M. R. Bari and Mr. Abul Kalam, of the Magnetic Material Division, Bangladesh Atomic Energy Commission, Dhaka, Bangladesh, for their generous help and for allowing me to use their facilities.

I am grateful to Dr. Aktl:er Hossain, P.S.O., House Building Society, Mirpur, Dhaka, who has kindly allowed me to use the DTA apparatus in his laboratory.

I am grateful to Dr. Md. F. Alam Khan for assisting me in the magnetic torque measurements.

My thanks are also due to Dr. Nazma zaman, Dr. Jibbon Podder, Mrs. Dil Afroz Ahmed and all other members of Physics Department, BUET, Dhaka, for their encouragements during the period of my thesis work.

It is my great pleasure to express my cordial thanks to Dr. Farida Begum of BARI and members of the magnetism group Mr. A. J. S. Ahmed Khandaker, Mr. Faruque-Uz-Zaman Chowdhary, Mr. Sk. Md. Yunus and Mr. A. K. M. Zakaria for their friendly cooperation during the course of this thesis work.

My special thanks are due to Dr. Lennart Hasselgren, Director, International Programs in the Physical Science (IPPS), Uppsala University, Sweden, for financial support to visit National University of Hanoi, Hanoi, Vietnam and Rajasthan University, Jaipur, India in connection with the research work.

I wish to extend my heartfelt gratitude to the library staff of BUET for their co-operation. I would also like to thank Mr. Md. Liaquat Ali for helping me in typing the thesis.

I am grateful to the authority of BIT, Khulna for granting me deputation and the authority of BUET for providing me with a scholarship and financial supports for carrying out this research work.

I wish to express my thanks to my wife Nandita for keeping me free from family affairs during my work and also for her sustained inspiration, encouragement and continuous co-operation. Finally my thanks are due to my daughter Priom.

ABSTRACT

Ferromagnetic amorphous ribbons of Fe-Si-B, Ni-Fe-B and Co-Fe-B-Si series have been prepared by rapid quenching technique and the amorphousity of the samples has been confirmed by X-ray diffraction technique. The kinetics of glass formation and crystallization as affected by a slight change in composition is studied by differential thermal analysis (DTA). It is observed that the thermodynamics of the amorphous ribbons in respect of the formation of glassy state and its stability is affected by the complexity of the composition. The magnetic ordering of Fe-based, Ni-based and Co-based amorphous ribbons is studied by measuring A.C. and D.C. magnetization as functions of temperature. D.C. measurements are made by using a vibrating sample magnetometer and A.C. initial permeability is measured, using a furnace in which the heating wire is wound in accordance with the bifiller technique.

Coercivity, remanence, saturation magnetization and maximum permeability have been determined as static magnetic properties for Fe-based, Ni-based and Co-based specimens from the hysteresis loops obtained by Ballistic method. The dynamic characteristic such as the real and imaginary components of the complex permeability in A.C. conditions have been measured as a function of the instantaneous value of a sine wave core current density by means of an adapted LCR bridge method. Initial permeability, frequency dependence of complex permeability and relative quality factor have been measured in the frequency range 0.5KHz to 13MHz for all the different compositions and for annealing effect of initial permeability.

The measurements of saturation specific magnetization of Fe-based, Ni-based and Co-based amorphous ribbons have been measured by V.S.M. We have correlated the behaviour of magnetic moment in amorphous alloys containing 3d transition metals on the basis of rigid band model, assuming that the metalloid atoms contribute some of their S electrons and P electrons to fill the d band of the transition metal. This accounts for the reduction of magnetization of all the amorphous ribbons with increasing metalloid content. The temperature dependence of magnetization, of amorphous system decreases faster with increasing temperature as compared to crystalline materials . According to the mean field approximation, reduced magnetization versus reduced temperature graphs for different Fe-based, Ni-based and Co-based amorphous ribbons leads to fluctuation in the exchange interaction giving rise to a structural disorder.

Induced magnetic anisotropy of amorphous ribbons having Fe-based, Ni-based and Co-based system have been measured for temperature and field dependence using torque magnetometer with proportional integrating differentiating compensation. The results of compositional dependence of initial permeability, coercive force and induced anisotropy are found to be mutually consistent for all the samples. The origin the uniaxial anisotropy in these amorphous materials is assumed to be the stress, induced during the preparation. The temperature dependence of uniaxial anisotropy is caused by stress, relieving and decreases with the increase of temperature. The corresponding curves of $\ln\left[\frac{K_u(0)}{K_u(T)}\right]$ versus $\ln\left[\frac{\sigma_s(0)}{\sigma_s(T)}\right]$ in amorphous ribbons with Fe-based, Ni-based and Co-based system follow straight lines arising from the disorder caused by randomly oriented easy axes. The values of the exponents are different for the different samples.

All amorphous ribbons have been investigated using Mössbauer spectroscopy. The Mössbauer measurements were performed with a conventional constant acceleration spectrometer at room temperature in transmission geometry, using ^{57}Co in a rhodium matrix. The velocity scale of a thin ^{57}Fe sample and the isomer shifts are given relative to the centroid of the spectrum. The isomer shifts of Fe-atoms in all the Fe, Ni and Co-based samples behave as trivalent ions. The spectrum for the as prepared samples consists of six lines which are broadened as compared with the Mössbauer spectrum of a pure ^{57}Fe sample in the form of a thin foil. The curve for the experimental spectrum is obtained by using the best fit of the distribution of hyperfine fields. The consistency between the average magnetization measured by V.S.M. and the magnetic moment of the Fe-atom as estimated from the hyperfine field distribution confirms the collinearity of the magnetic ordering of the sample.

LIST OF THE SYMBOLS USED

TM	Transition metal
TM-M	Transition metal-metalloid
RE-TM	Rear-earth transition metal
DTA	Differential Thermal Analysis
η	Viscosity
V_c	Critical velocity
f	Frequency
τ	Reduced glass transition temperature
T_m	Melting temperature
T_g	Glass transition temperature
T_x	Crystallization temperature
T_x'	Secondary crystallization temperature
T_c	Curie temperature
C_Ψ	Ballistic galvanometer constant
H_c	Coercive force
B	Magnetic induction
B_m	Maximum magnetic induction
B_s	Saturation magnetic induction
B_r	Remanence
μ	Permeability
μ_m	Maximum permeability
μ_i	Initial permeability
μ'	Real part of the complex permeability
μ''	Imaginary part of the complex permeability
L_s	Self-inductance of the sample core
L_0	Inductance of the winding coil without sample
$\tan\delta$	Loss factor
$\mu_i / \tan\delta$	Relative quality factor
V.S.M.	Vibrating Sample Magnetometer
P.I.D.	Proportional Integrating Differentiating
H	Magnetic field
M	Magnetization
$M_s(0)$	Saturation magnetization at 0^0K
$M_s(T)$	Saturation magnetization at T^0K

H_m	Molecular field
C	Curie constant
J	Total angular momentum
g	Lande 'g' factor
λ	Weiss constant
α	Direction constant
K_B	Boltzmann constant
B_J	Brillouin function
σ_s	Saturation specific magnetization
$\sigma_s(0)$	Saturation specific magnetization at 0^0K
$\sigma_s(T)$	Saturation specific magnetization at T^0K
m	Reduced magnetization
E_n	Total anisotropy energy
K_u	Stress induced anisotropy
$K_u(T)$	Stress induced anisotropy at T^0K
$K_u(0)$	Stress induced anisotropy at 0^0K
K_{u_1}	First uniaxial anisotropy constant
K_{u_2}	Second uniaxial anisotropy constant
K_0	Zero order anisotropy constant
MCA	Multi channel analyser
FWFM	Full Width Half Maximum
IS	Isomer shift
E_Q	Quadrupole splitting
H_{hf}	Hyperfine field

CONTENTS

CHAPTER-4 EXPERIMENTAL DETAILS

CHAPTER-5 RESULTS AND DISCUSSION OF Fe-BASED AMORPHOUS RIBBONS

CHAPTER-6 RESULTS AND DISCUSSION OF Ni-BASED AMORPHOUS RIBBONS

CHAPTER-1 INTRODUCTION

1.0. Introduction

Amorphous metallic alloy is a metastable state of matter where the random configurations of the liquid state of the alloy with no long range order is frozen in. This state is created by fast cooling the melt where by the nucleation and growth of crystallites are inhibited. The present great interest in amorphous metals stems from the works of Duwez *et. al.*(1.1) on the preparation and properties of amorphous metallic alloys. Simpson and Brambley (1.2) appear to have been the first to point out that the amorphous alloys are expected to have no magnetocrystalline anisotropy and should have very low coercivity. Amorphous alloys of Fe-Ni-P-B prepared by the melt-spinning technique in the form of ribbons by solidification of the melt on the surface of a rapidly rotating drum exhibit even lower coercivities, of the order of 8A/m. Luborsky *et. al.*(1.3) first demonstrated the reduction of coercivity in these alloys, down to less than 0.8A/m by suitable annealing and showed that the changes in their properties are correlated with the relief of internal strains. At about the same time Egami *et. al.*(1.4) showed that annealing under tensile stress reduced the coercivity of an Fe-Ni-P-B-Si alloy to 0.3A/m.

Amorphous states for pure metals like Fe, Co , Ni etc. are obtained only at extremely low temperatures. The disorder in the amorphous state can be classified into two types: one is the structural disorder which is lack of periodicity in the atomic arrangements and the other is chemical disorder in which the chemical composition looses its periodicity. In metallic glass the macroscopic quantities which are the averages of properties in the atomic scale are perturbed by structural disorder. It is apparent that the chemical and structural disorders interfere with each other and the effects of each kind on the physical properties are difficult to isolate.

The studies of the effects of magnetic annealing on stability and magnetic properties have led to the prediction and preparation of alloy compositions that have greatly improved stability. By suitably annealing these amorphous alloys, ribbons with varying compositions have been demonstrated to have different dynamic losses, permeabilities and magnetizations which make them competitive in quality to existing crystalline magnetic materials. The magnetic and structural stability has been evaluated at higher temperatures and are found to be adequate for most foreseeable applications.

There is no satisfactory theory developed yet to explain the temperature irreversible behaviour of magnetization in amorphous magnetic alloys. Recently, soft magnetic amorphous alloys have been developed, and they are used for the magnetic

cores of switched-mode power supplies, magnetic recording heads and other devices by T.Miyazaki *et. al.*(1.5) and O.Komoto *et. al.*(1.6) Most of the amorphous materials useful for these applications are manufactured from Co-based amorphous ribbons as reported by H.Fujimori *et. al.*(1.7) with nearly zero magnetostriction. On the other hand, Fe-based amorphous ribbons as reported by H.Warliment *et.al.*(1.8) are excellent in their high saturation flux density, but they are inferior in the soft magnetic properties in comparison with Co-based amorphous ribbons. For Fe- and Fe-Ni based amorphous ribbons, the change of magnetostriction is relatively small, but this change is remarkable in the Co-based amorphous ribbons.

Increased attention is being given to the production of wide ribbons and the preparation of amorphous ribbons for particular applications and for understanding the origin of their extrinsic and intrinsic properties. In a qualitative sense, the intrinsic properties are magnetization, Curie temperature, glass transition temperature, induced anisotropy, magnetostriction and hyperfine field and the extrinsic properties are coercive force, remanence to saturation ratio, permeability, relative quality factor and the loss factor as a function of frequency. These are important for practical applications of magnetic materials and for evaluating and understanding the magnetic properties and long-term stability of these amorphous ribbons.

Present research involves the preparation of Fe, Ni and Co-based amorphous ribbons. In Fe-based samples Si and B have been used as glass forming materials, where Fe have been partially replaced by Si keeping the B percentage fixed, the general composition being $Fe_{90-x}Si_xB_{10}$ [x = 6, 8, 10, 12 and 14]. In Ni-based amorphous ribbons Ni have been replaced by Fe, while the percentage of B has been kept fixed, the general composition being $Ni_{80-x}Fe_xB_{20}$ [x = 20, 30, 40 and 50]. In Co-based amorphous ribbons Co have been slightly replaced by Fe, keeping the glass forming materials Si and B fixed, the general composition being $Co_{80-x}Fe_xB_{10}Si_{10}$ [x = 0, 2, 4, 6 and 8]. The melt-spinning technique has been used for the preparation of the ribbons and the amorphousity of the samples has been confirmed by X-ray diffraction technique. The preparation procedure, conditions for forming amorphous material and factors controlling the thickness of the ribbons are discussed in chapter-2, A short account of other methods of preparing amorphous ribbon are also given in these chapter along with a short review of others.

The class of amorphous TM-M alloys with TM = Fe, Co or Ni and M = B, P, C, Al or Si have received much attention in respect of their favourable properties and various commercial applications such as power generator, transformers, magnetic

heads, and magnetic shielding. The study of the magnetic parameters of amorphous ribbons are generally significant for a variety of applications. These applications may be determined either by static or dc properties, or by dynamic or ac properties of the ribbons.

In addition to the magnetic properties, their temperature dependence and the stability and cost of materials must be considered. The properties available in the amorphous ribbons cover a wide range when the alloy composition is changed and heat treated, as has been presented. The properties can also be varied by changing the induced anisotropy. The wide range of dc and ac properties provide characteristics suitable for different types of applications. Generally amorphous ribbons are characterized by a high electrical resistivity, high mechanical strength, good corrosion resistance, absence of crystalline anisotropy, structural defects and grain boundaries. The magnetic properties such as saturation flux density, Curie temperature, magnetostriction and induced anisotropy can be controlled by the alloy composition and a subsequent heat treatment. The Fe-based amorphous ribbon exhibit the highest saturation flux density and the Co-based amorphous ribbons are characterized by low magnetostriction, very high permeabilities and low magnetic losses.

Amorphous ribbons with high B_r/B_S are practically suited to devices such as switch cores, high gain magnetic amplifiers and low frequency inverters or transformers where minimum losses are important. The high electrical resistivity and the small thickness of the melt-quenched ribbons lead to low eddy current losses. The low hysteresis losses, results in very low core losses which is of interest for power electronics at high frequencies. For application in small electronic devices, the amorphous ribbons have somewhat poorer losses and permeabilities than the conventional Fe-Ni-B ribbon but have better performance than the Fe-Co-B-Si and Fe-B-Si ribbons. The design optimization requires lower cost of amorphous ribbons, higher induction compared to the Fe-Ni-B ribbons or lower losses compared to the Fe-Co-B-Si, Fe-Si-B and the Fe-Ni-B ribbons at higher frequencies. Co-based amorphous ribbons are also suitable as soft-magnetic materials for magnetic shielding due to their high permeability. Amorphous ribbon has many refined applications like development of magnetic bubbles for computer memory, amorphous supper conductors etc.

Research in the theoretical understanding and development and application of amorphous ribbon can thus be profitable, specially at its present new phase.

Important thermodynamic parameters of amorphous ribbons like glass transition temperature (T_g) and crystallization temperature (T_x) have been studied by differential thermal analysis (DTA). The DTA technique was first suggested by Le Chatelier [1.9] in 1887 and was applied to the study of clays and ceramics. The study of thermal behaviour of carbonising materials by DTA was first introduced at the 4th Carbon Conference by Nakamura and Altas[1.10]. DTA is the process of estimating the heat capacity of a specimen by measuring the difference in the temperature between a thermo-couple embedded in the sample and a thermocouple in a standard inert material such as aluminium oxide while both are being heated at a uniform rate. The study of T_g and T_x of amorphous ribbons has been made by Naka *et. al.*[1.11] for the series $Fe_{80-x}M_xP_{13}C_7$. Luborsky [1.12] used the series $Fe_{80-x}Ni_xP_{14}B_6$. Calorimetric measurements were made at the heating rates of 5^0C / min. and 40^0C / min. respectively to determine T_g and T_x, the temperature of the beginning of the exothermic peak.

There is no direct relation between the cause of formation and the resultant stability of amorphous ribbons. Cohen and Turnbull[1.13] noted that the composition which is most favourable for glass formation is near the eutectic; the deeper the eutectic the better is the glass forming ability. Using the same principle we looked for the glass transition temperature and crystallization phase transition. Zhu *et al.*[1.14] and J. Bigot *et. al*[1.15] found that the first DTA peaks corresponds to the precipitation of an ordered bcc α-FeSi solid solution embedded in an amorphous phase and the second to the crystallization of Fe-B-Si compounds. DTA trace of iron-boron ribbons with composition $Fe_{82}B_{18}$ and $Fe_{80}B_{20}$ showed two exothermic peaks in temperature VS time curve. The first peak corresponds to T_g and second peak to the T_x by S.S.Sikder *et. al.*[1.16].

The theoretical basis of the stability of the amorphous ribbons has been discussed in chapter-3 and experimental arrangements for DTA is described in chapter-4. The results of DTA for different compositions are presented in respective chapters on Fe-based, Ni-based and Co-based ribbons, i.e in chapter-5, chapter-6 and chapter-7 respectively.

Important magnetic characteristics of the ribbons that have been studied are Curie temperature (T_c), coercive force (H_c), remanence (B_r), initial permeability (μ_i), saturation specific magnetization (σ_s), induced anisotropy (K_u) and hyperfine field (H_{hf}). It is important to study T_c at which thermal excitation of structural relaxations and stress relief take place. The relaxation of local atomic configurations perturb both the magnetic and chemical environment, and as such, the moment distribution changes

as observed by J.W.Cable[1.17] . Consequently, as temperature is raised towards T_c, substantial irreversible changes in moment distribution and reordering of paramagnetic inclusions is expected. Thus, although the samples can preserve the amorphous state, they are structurally different on a local scale as compared to the as-quenched system. Therefore, T_c has to be considered as the spin order-disorder transition temperature of a relaxed system that preserves the amorphous state as explained by E. Figueroa *et. al.*[1.18] and R.Malmhall *et. al.*[1.19]

The optimal, soft magnetic properties of amorphous ribbons can be developed through a variety of thermal treatments. A significant increase of magnetic permeability can usually be induced by thermal treatment at a temperature above the Curie point T_c of the material, as well as by field anneal at $T < T_c$, when the magnetic field is applied along the longitudinal axis of the ribbon.

When the thermal treatment was performed in zero field at $T < T_c$, a degradation of the magnetic properties of the material was observed by R.Valenzuela *et. al.*[1.20] , K.Shiiki *et. al*[1.21] and T.Sasaki *et. al.*[1.22]. This decrease in permeability in binary magnetic alloys has been interpreted by H.Fujimori *et. al.*[1.23] on the basis of a directional ordering of atom pairs in the domains, which leads to an enhanced domain wall pinning. Thermal treatments at temperatures higher than the Curie point result in a significant increase in the permeability value. This effect is explained as follows: The Curie temperature is determined by the volume average of local magnetic interactions and any increase in T_c in a single magnetic ion alloy suggests that change in topological short range order occurs, resulting in changes in Fe-Fe correlations within the first peak of the radial distribution function as observed by K.Doi *et.al.*[1.24] .

The dependence of T_c on the composition and the nature of the metalloids is not very systematic. T_c of Fe-based metallic glasses increase while that of Co-based as well as Ni-based amorphous alloys decrease with the increase of metalloid concentration. Curie temperatures of alloys with boron as glass forming material are higher compered to there alloys with phosphorus as glass forming material. T_c's of $Fe_{80}G_{20}$ glass decreases in the order G = Si, B, C, P, which shows no correlation either with magnetic moment of Fe or with the valence of the metalloid as reported by H.S.Chen *et. al.*[1.25] . Addition of Ni or Co in Fe-based glass with fixed metalloid concentration increases T_c for low concentration but at higher concentration T_c falls sharply.

The Curie temperature of most TM-M glasses increases by annealing at temperature well below the crystalization temperature. The change in T_c depends on the annealing time and temperature and also on the nature of metalloid cogent such variation is caused by the relaxation of micro structural quantities like long-range internal stress. Topological and chemical short-range order is observed by C.L.Chen and R.S.Hasegawa[1.26].

The present work involves the measurements of permeability as a function of temperature and the finding of Curie temperature from the sharp fall of the dM/dt curve. The different experimental technique for determination of T_c has been described in chapter-4. The results for the Fe-based, Ni-based and Co-based samples are discussed in chapter-5, chapter-6 and chapter-7 respectively.

A dc current flowing in a ferromagnetic amorphous ribbon reduces the coercivity and the Barkhausen noise of B-H longitudinal loops which is reported by R. N. G. Dalpadodo *et. al*[1.27] and G. Buttino *et. al*[1.28] . The 'as-quenched' TM-M glasses always have anisotropy due to stress produced during the quenching process. As part of it is averaged out, the coercive fields (H_c) is much reduced in glassy state. By relieving the stress by annealing, H_c can be reduced. This makes amorphous ferromagnet a magnetically soft material.

But at the same time the saturation moment (B_s) and the remanance (B_r) are much reduced. The remanance $B_r \cong 0.45B_s$ and $H_c \cong 0.01$oe have been observed in TM-M glasses by F. E. Lubrosky *et. al*[1.29]. The RE-TM glass except Gd-Tm are magnetically hard material with large coercive fields as reported by J. J. Rhyne *et. al*[1.30]. The value of B_r/B_s is then determined. In the $Fe_{40}Ni_{40}P_{14}B_6$ amorphous alloy B_r/B_s depends on the magnetic field and heat treatment used, for example, Luborsky *et. al*[1.31] reported values of B_r/B_s up to about 0.9.

Our measurements involve the determination of coercive force, remanance, the ratio B_r/B_s and maximum permeability from initial magnetization curves of the samples chosen. The theoretical origin of coercive force is given chapter-3 and the experimental technique is described in chapter-4. The results are discussed in the respective chapter of the different amorphous systems.

The low-field behaviour corresponds to the reversible initial permeability of domain walls which are pinned due to inhomogeneities of the sample as reported by E. Amano *et. al*[1.32] and J. T. S. Irvine[1.33] . The measurement of complex

permeability gives us valuable information about the domain wall movements. Theoretical models have been proposed for describing the motion of 180^0 Bloch walls as described by K. M. Polivanov *et. al*(1.34), R. H. Pry *et. al*(1.35), J. E. L. Bishop(1.36) and G. Ban *et. al*(1.37) . Earlier complex permeability measurements by G. Ban *et. al*(1.38) performed on polycrystalline permalloy and perminvar materials could be fitted as developed by Polivanov *et. al.*(1.34) .The real and imaginary components of the complex permeability in ac condition have been measured as a function of the instantaneous value of a sine wave core current density by means of an adapted ac bridge method as described by G. Buttino *et. al.*(1.39). Actually under ac condition the number of domain walls increases and more deeply pinned walls begin to move as the frequency is increased as explained by S. D. Washko *et. al.*(1.40).

The amorphous ribbon specimens of ring-shaped cores with outside/inside diameter = 34/30 were made from the as-cast ribbons. At room temperature the frequency and field dependence of the complex permeability $\mu = \mu' - i\mu''$ and the core loss of the tape wound core were measured by impedance bridge up to the MHz range and by a core loss measuring equipment for Sine wave induction in the frequency range f= 1-300KHz by G. Lehmann *et. al*(1.41) and M. Schaefer *et. al.*(1.42) .

The magnetic permeability relaxation is of great importance to practical applications. The experiments have shown that the total permeability relaxation consists of ordinary disaccommodetion (DA) and a continuous permeability decay of $Fe_{82}B_{18-x}C_x$ and $Fe_{82}B_{18-x}Si_x$ metallic glasses occurs as reported by Zhang Yan Zhong *et. al.*(1.43), Y. Z. Zhang *et. al.*(1.44-45) and K. Ohta *et. al.*(1.46) .The measurements of permeability with increasing field were used for this purpose by Mizoguch, T. *et. al.*(1.47) the permeability, which gradually decreases with time after demagnetization undergoes a sudden drop with a certain time period which depends on the applied field amplitude and frequency as well as temperature as measured by Jagiclinski *et. al.*(1.48).

Our measurements involve the determination of initial permeability, real part of the complex permeability, imaginary part of the complex permeability, loss factor and relative quality factor and their anneal effects on our samples. Theoretical aspects of initial permeability is described in chapter-3 and the experimental set-up in chapter-4. The results for different amorphous systems are discussed in the respective chapters.

Magnetization is the most common parameter of a magnetic material. A brief discussion of amorphous alloys is reported by Alben *et. al.*(1.49), which follows from the ideas of local chemical bonding. The atomic states of high spin have low electron-

electron coulomb repulsion energies. The behaviour of the amorphous Fe-based ribbon is very different from Co-based ribbons. Apparently a small amount of impurity is necessary to stabilize the strong ferromagnetism in the amorphous FeSi alloy as reported by Felsch[1.50] ,but this is not confirmed by the results of Shimada and Kojima[1.51] . Wright[1.52] has recently reviewed the status of the information available on "pure" amorphous elements. In all cases it appears that the saturation moment is the same or less than its value in the crystalline state, which shows that no effective electron transfer occurs from the magnetic atoms to the matrix.

Becker *et. al.*[1.53] showed that the rigid band model as above is some what more satisfying to the data as obtained by using individual moments varying with composition. This is described by Kouvel[1.54] in his analysis of crystalline alloys. The individual atomic moments of Fe and Ni are then given by

$\mu_{Fe} = 2.20 + 0.80(1\text{-}x)$ and

$\mu_{Ni} = 0.57 + 0.20x$ in Fe_xNi_{1-x}

Becker[1.53] studied the moment and Curie temperature of amorphous ribbons of $(Fe\text{-}Ni)_{80}(P\text{-}B)_{20}$. The room temperature saturation magnetizations are of more practical importance.

The Barkhausen jumps occurring during the magnetization of the amorphous Fe-Ni-B-Si alloys have been studied by the measurements of the derivative of magnetization with respect to time (dM/dt). The peaks in dM/dt VS. applied field (H) are reproducible after averaging over some fifty cycles of magnetization as observed by J. Horvat *et. al.*[1.55]. The derivative of magnetization with time (dM/dt) in respect to M_m can provide a more direct justification of the use of the model for the explanation of the processes of magnetization in soft magnetic materials as suggested by J.. Horvat *et. al.*[1.56].

The temperature dependence of the magnetization was measured with a vibrating sample magnetometer and the spin-wave measurements were carryout using inelastic neutron scattering techniques. The magnetization is found to obey the usual law $M_s(T) = M_s(0)\left[1 - BT^{3/2} - CT^{3/2} - \ldots\ldots\right]$. This dependence has been observed over an unusually wide range of temperature in the present amorphous metal system, as well as in many other amorphous ferromagnets by J. H. Lynn *et. al.*[1.57] and S. C. Yu *et.al.*[1.58] Fe-based ferromagnetic amorphous ribbons are mostly soft magnetic materials. Fe-Cu-Nb-Si-B amorphous ribbon shows excellent soft magnetic properties after annealing at a relatively high temperature, where partial crystallization take place as measured by Lu Bang *et. al.*[1.59] and Y. Yoshizawa *et. al*[1.60].

The experimental temperature dependence of magnetization [M(T)curves] of the $Co_{80-x}B_{20}Si_x$ [$x \cong 2$ to 12] amorphous ribbons is presented. The magnetization changes anomalously at the crystallization temperature. The Curie temperature decreases and crystallization temperature increase with the increasing of Si content as observed by Le Minh et. al(1.61). The magnetization process of $Fe_{80-x}B_x$ ribbons have been measured as a function of field and the saturation magnetization for these ribbons have slightly higher values for higher percentage of iron as reported by S. S. Sikder et. al.(1.16).

The theories of magnetization in amorphous system as distinct from crystalline materials are discussed in chapter-3 and the experimental technique used is described in chapter-4. The results and discussions for the Fe-based, Ni-based and Co-based samples are includes in the respective chapters (i.e chapter-5, chapter-6 and chapter-7).

Although amorphous materials are not likely to have magnetocrystalline anisotropy, it is an experimentally observed fact that there is usually an induced anisotropy technically produced due to the asymmetry of the preparation condition. The kinetics of formation of the field-induced anisotropy has been investigated in the past by Kay-Yuan Ho *et. al.*(1.62), J.D. Livestigated *et. al.*(1.63) and J. De wit *et. al.*(1.64). Some works have been done by G. Herzer *et.al.*(1.65) with composition $Co_{71}Fe_4B_{15}Si_{10}$. However, little quantitative information has so far been gained on the ensuing nature of the magnetization processes and their role on the power losses, whose control is basic to optimum applications of the Co-based amorphous ribbons. The induced anisotropy and its changes with time are taken as a basis for the explanation of magnetic after etfects in amorphous systems by Allia, P. *et.al.*(1.66). The existence of induced anisotropy in various metallic glasses was experimentally shown by Allia, p.*et. al.*(1.67), Miyazaki, T. *et. al.*(1.68) and Ohta, K. *et. al.*(1.69) on the field-annealed samples from direct torque measurements

Kronmuller *et. al.*(1.70) and Bourrous *et. al.*(1.71) have shown that it is possible to obtain important information about the nature of the amorphous state through studies of the induced anisotropy and the magnetic after-effect. Quantitative discussions of the influence of reversible and irreversible relaxation processes on the induced anisotropy and the coercive field have been reported for the amorphous ribbon $Co_{58}Ni_{10}Fe_5Si_{11}B_{16}$ by Kronmuller *et. al.*(1.70). H. Kronmuller(1.72) and A. M. Severino *et. al.*(1.73) obtained spectra of activation energies using a micromagnetic theory of the induced anisotropy for the amorphous ribbon $Co_{70.5}Fe_{4.5}Si_{15}B_{10}$.

Magnetic anisotropic behaviour reflects the existence of short-range order in the amorphous ribbon. It has become commonly known that in an ideal amorphous ribbon the atomic scale anisotropy would be averaged away so that there would be no anisotropy effects visible. Chi and Alben[1.74] have shown from a simple model calculation that when the local random anisotropy is small the coercivity induced is small but high coercivities are abruptly obtained as the local anisotropy increases and dominates the behaviour. Fujimori *et. al.*[1.75] studied the magnetically induced anisotropy in $(Fe_xCo_{1-x})_{78}Si_{10}B_{12}$ amorphous ribbons. Their results for the maximum values of K_u obtained by annealing in a field for 15min. at increasing temperatures are shown by the solid circles. Sherwood *et. al.*[1.76] found for ferromagnetic-antiferromagnetic "exchange anisotropy" in the amorphous alloy $Fe_{37.5}Mn_{37.5}P_{16}B_6Al_3$. This appears to be the first demonstrated example of exchange anisotropy in an amorphous transition metal-metalloid alloy.

Our measurements involves compositional dependence of stress induced anisotropy and temperature dependence of the induced anisotropy up to ferromagnetic transition temperature. Theoretical aspects of induced anisotropy is discussed in chapter-3 and the experimental details are presented in chapter-4. The results of Fe, Ni an Co-based amorphous ribbons are discussed in chapter-5, chapter-6 and chapter-7 respectively.

Mössbauer spectroscopy is a very powerful method to study the hyperfine field in amorphous materials which is affected by the nature and distribution of the neighbouring atoms of the magnetic ions. From the study of the Mössbauer spectrum as affected by the hyperfine field valuable information regarding the distribution and nature of the constituent atoms can be obtained. Mössbauer spectroscopy studies of the annealed amorphous $Fe_{74}B_{26}$ ribbon shows that the width of the magnetic hyperfine field distribution decreases for annealing temperature below 100K as observed by SΦ ren Lideroth[1.77], and leads to a narrowing of the absorption lines and the magnetic hyperfine field distribution as measured by ^{57}Fe. The distribution and dynamics of the magnetic moment in $(Co_{0.93-y}Ni_yFe_{0.07})_{75}Si_{15}B_{10}$ amorphous Pseudobinary alloys have been studied mainly by means of magnetometric and Mössbauer techniques by L. Dobrzynski *et. al.*[1.78].This amorphous alloy is a ribbon with very low magnetostriction and very high magnetic permeability as reported by K.I. Arai *et. al.*[1.79]

Mössbauer measurement for standard magnetic moment establishes only the average moment of metal atoms, due to inequivalency of sites. It is not true that each atom carries the same average moment. In fact, there is a distribution in the magnitude of moments. The distribution width is expected to be largest for 3d-ions and narrowest in rare-earth's as 4f shell are well shielded from its environments. Moment distribution is best demonstrated by Mössbauer by T. E. Sharon *et. al.*(1.80) and by NMR experiments by K. Raj *et. al.*(1.81). Mössbauer spectrum of ferromagnetic $Fe_{75}P_{15}C_{10}$ measured by T. E. Sharon *et. al.*(1.80) are fitted with asymmetrical distribution of hyperfine fields. This means that a considerable portion of Fe-nuclei are in zero hyperfine (h.f.) field by K. Raj *et. al.*(1.81). Information about the distribution of h.f. field from NMR are more direct and are free from fitting procedure which is important for Mössbauer analysis. Assuming the proportionality between h.f. field and magnetic moment, the moment is found to decrease with metalloid concentration in TM-M glass.

At Curie temperature the typical Mössbauer spectra for amorphous ferromagnetic alloys such as $Fe_{75}P_{15}C_{10}$ show two peaks characteristic of quadrupole splitting. Below the Curie temperature the spectra consist of six peaks symmetric with respect to their centre, but very broad compared to corresponding crystalline alloys. The broadening is attributed to the random nature of the structure. Thus amorphous $Fe_{80}B_{20}$ reported by Chien and Hasegawa(1.82) has a narrower distribution of hyperfine fields than $Fe_{75}P_{15}C_{10}$ as reported by Tsuei and Lilenthal(1.83) and in $Fe_{40}Ni_{40}P_{14}B_6$ as reported by Chien and Hasegawa(1.84).

Mössbauer spectoscopy, because of the influence of the local environment on the iron moment, is directly reflected in the hyperfine field distribution studied by Rodmarcq *et. al.*(1.85), Chappert *et. al.*(1.86) and Chien *et. al.*(1.87). The moment variation can be directly derived from the hyperfine field distribution, because the proportionality between hyperfine field and magnetic moment was established from crystalline by Gubbens *et. al.*(1.88)

Our studies involves the finding of how the iron moment is directly reflected in the hyperfine field distribution measurements by Mössbauer spectroscopy, because of the influence of the local environment. We have measured the Isomer shift (IS), Quadrupole splitting (E_Q), Hyperfine field (H_{hf}), Full Width Half Maximum (FWFM) and absorption percentage. The principle of these measurements are given in the chapter-3 and description of experimental set-up and computer analysis are presented in chapter-4. The results and discussion for the different systems are given in their respective chapters.

CHAPTER-2 PREPARATION OF AMORPHOUS RIBBONS BY RAPID QUENCHING METHOD

2.1. Introduction
2.2. The structure of an amorphous alloy
2.3. Conditions for forming amorphous material
2.4. Conditions necessary for preparing amorphous materials
2.5. Preparation technique of amorphous ribbon
2.5.1. The atomic deposition methods
2.5.2. The fast cooling of the melt
2.5.3. Rapid quenching method
2.6. Experimental details of the preparation of amorphous ribbon
2.6.1. Important factors to control the thickness of ribbons
2.7. Factors contributing to glass formation
2.8. Examining the amorphousity

2.0. Preparation of amorphous ribbons by rapid quenching method

2.1. Introduction

Since the discovery of metallic glass by Dewez *et. al.*[2.1] ,in the same year Gobonov[2.2] predicted the possible existence of ferromagnetic ordering in non crystalline solids on the basis of theoretical analysis. The interest in amorphous materials is increasing steadily for technological application and scientific understanding. A real technological interest developed after Pond and Maddin[2.3] reported on the preparation of continuous ribbons of amorphous alloys. The theoretically expected retention of ferromagnetic behaviour in amorphous solids was first demonstrated by Mader and Nowick[2.4] in theirs work on vacuum deposited Co-Au alloys and soon there after by Tsuei and Duwez[2.5] in their works on split-cooled Pd-20at.% Si containing some ferromagnetic element partially substituted for the Pd.

Amorphous states of pure metals like Fe, Co, Ni etc can be obtained only at a very low temperature. Alloys of the these metals with glass forming materials can be obtained in the amorphous state by cooling the melt at a relatively lower rate of million degrees per second which can remain in the metastable state over an extended range of temperature. Two important classes of amorphous magnetic materials are being studied intensively in recent time. They are the transition metal-metalloid (TM-M) glass and the rare-earth transition metal glass (RE-TM) reported by T.Mizoguchi[2.6], R.Alben *et. al.*[2.7], E.M.Gyorgy [2.8]and G.S.Cargill[2.9]. TM-M glasses are stable for composition around 75-80% of TM (Fe, Co, Ni etc or in their combinations) and 25-20% of the metalloid (P, C, Si, B or in their combinations). Typical composition for RE-TM glass is RE_{33}-TM_{67} where RE is one of the heavier rare-earth metals like Gd, Tb, Dy, Y etc and TM is one of the 3d transition metals like Fe, Co or Ni. Recently the metalloids in TM-M glass are replaced by non-magnetic metals like Zr, Hf etc by T.Masumoto *et. al.*[2.10]. The new amorphous and metastable alloys prepared by such techniques were used in the early works to explore the many possibilities opened up by these new rapid quenching techniques.

2.2. The structure of an amorphous alloy

The structures of amorphous alloys have been given by Cargill[2.11-2.12] and also a detail discussion is given by Asgar[2.13]. An amorphous material has no long range order and the co-relations that exist must be of short range order in the sense that

certain values of the interatomic distance r are more common than others. The stability increases with the number of components in an amorphous ribbon. The disorder can be classified into two types following Alben *et. al.*(1977)(2.14)

(1). Structural disorder -- lack of periodicity in atomic arrangement and

(2). Chemical disorder -- lack of periodicity in chemical environment.

The chemical species and relative positions of the nearest neighbours of an atom are thus randomly altered in a chemically disordered solid. The structural arrangement of the atoms in amorphous solids can be given in terms of a radial distribution function. For identical atoms this describes the average number of atoms at distance between r and r+dr from some chosen atom as origin. This is averaged by taking each atom in turn as the origin. The average number of atoms between spheres of radii r and r+dr is then given by $4\pi r^2\rho(r)dr$, where $\rho(r)$ is the atomic density.

The distribution function is sometimes presented in slightly different form

$$F(r) = 4\pi r^2\rho(r) \qquad (2.1)$$

$$\text{as } G(r) = 4\pi r[\ \rho(r) - \rho_0\ ] \qquad (2.2)$$

If we consider the density ρ_0 as constant, then $F(r) = 4\pi\rho_0 r^2$

Since the density is constant so $F(r)$ follows the parabolic distribution.

$$W(r) = \frac{F(r)}{4\pi r^2\rho_0} = \frac{4\pi r^2\rho(r)}{4\pi r^2\rho_0}$$

$$W(r) = \frac{\rho(r)}{\rho_0} \qquad (2.3)$$

when $\rho(r)$ = constant, then $W(r) = 1$

Theoretical curve of the radial distribution function as a function r is shown in Fig-2.1

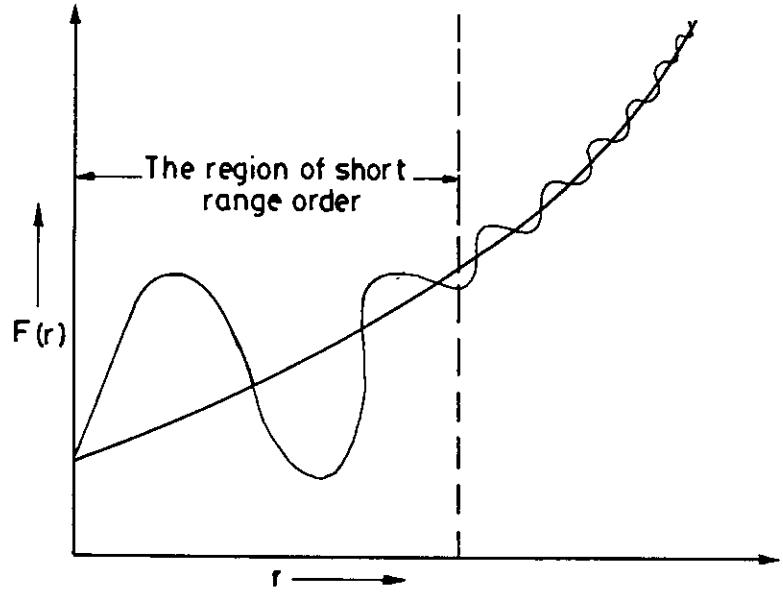

Fig;- 2.1 Short range order as a function of radial distance r

The structure of an amorphous solid can be discussed on many levels. For example, interms of the external size and shape of the solid, interms of cracks, voids, inclusions, composition gradients and other heterogeneeties resolvable by optical microscopy or other technique.

Amorphous solids can be considered as a supercooled liquid. A metallic glass is distinct from a liquid or a solid, because of its deviation from thermodynamic equilibrium while both a melt and its corresponding crystalline phase have minimum free energy, an amorphous materials because of its non equilibrium state is at a higher values of free energy. Free energy as a function of temperature for a crystalline solid, an amorphous solid and a liquid is shown in Fig-2.2.

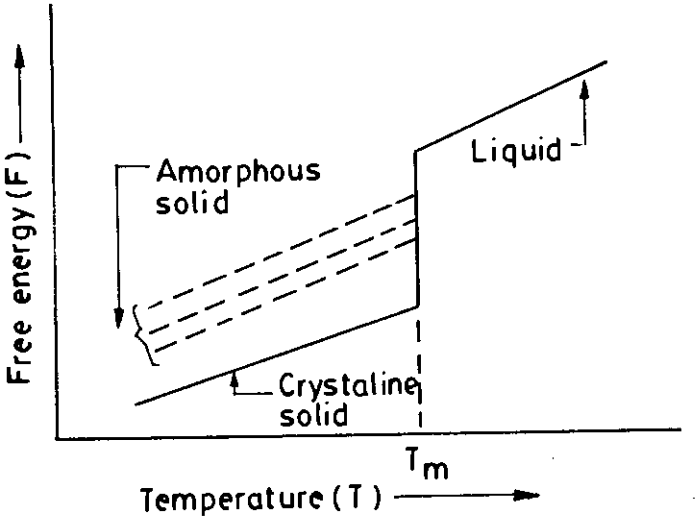

Fig:- 2.2 Free energy versus temperature curve

Fig-2.3 shows the reduced glass transition temperature $\tau = T_g/T_m$ for amorphous solids compered to crystalline solids. It is to be noted that for higher values of τ only glass formation is possible.

When a melt is cooled too rapidly, its viscosity and relaxation time increase to the point where the internal equilibrium can no longer be maintained and the equilibrium configuration become inaccessible.

Two ways of solidification

(1). Crystalization Process and

(2). By increasing Viscosity.

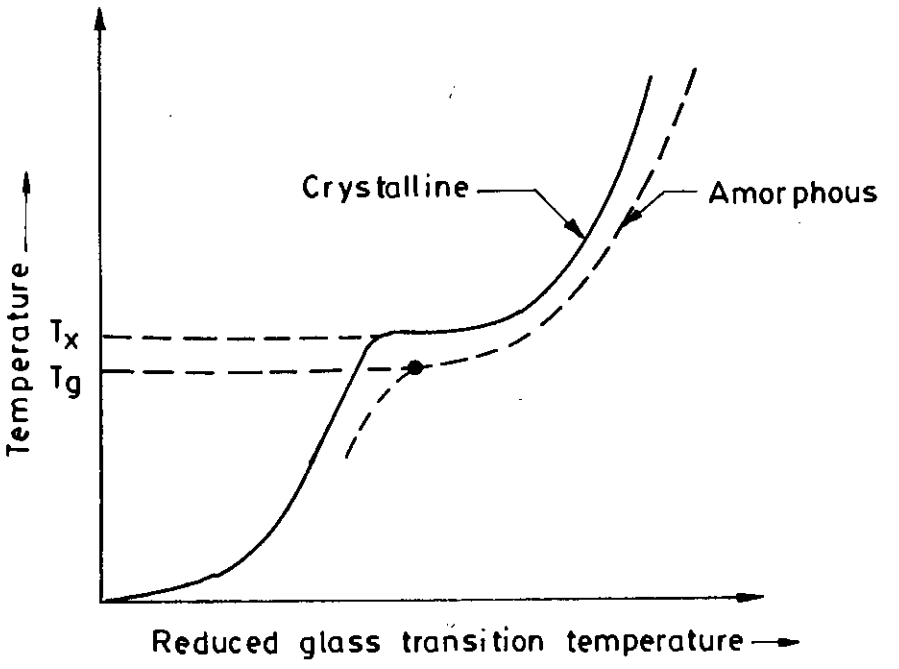

Fig:-2.3. Glass formation as a function of reduced glass transition temperature

Mechanical heardness of the condensed mater is dependent on the viscosity such that although amorphous materials structurally resemble a liquid state, their viscosity become comparable to that of a solid and this determines the stability of amorphous materials. Fig-2.4 represents the variation of viscosity of amorphous materials with temperature.

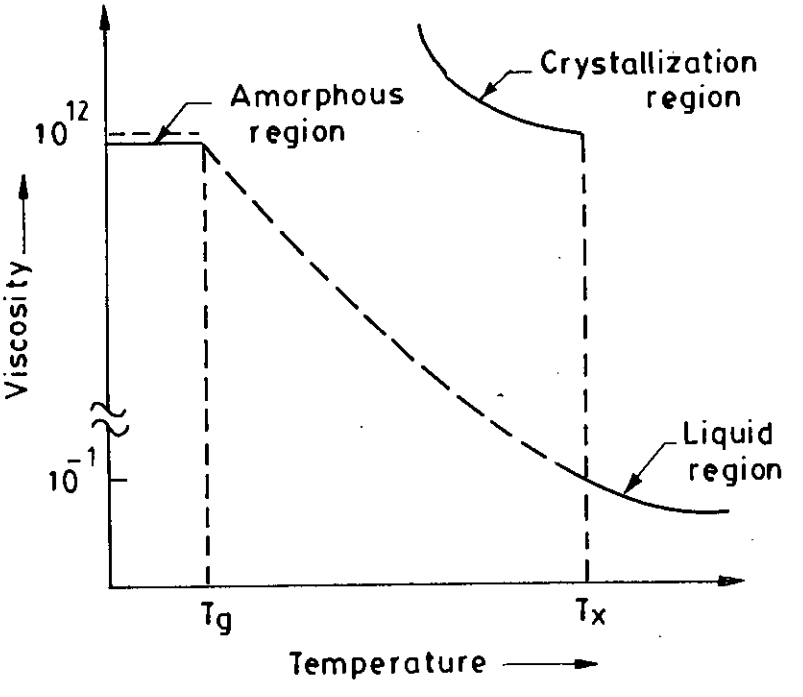

Fig:-2.4 Viscosity versus Temperature curve

2.3. Conditions for forming amorphous material

It is very difficult to get pure metals in the amorphous state. It is necessary to add glass forming materials to pure metals or alloys to get the amorphous state and to bring the cooling rate within a reasonable rate. Usually around 20% of glass forming materials like B, Si, P, C etc which have atomic radii relatively small compare to these of metallic atoms and the glass forming atoms occupy the voids left between the bigger atoms of metals when they are closely packed. It can be showed that when there is random close packing of hard spheres there is about 20% voids created between these atoms. The glass forming materials which have smaller atoms occupy these voids which explain the importance of the glass forming material in the preparation of an amorphous ribbons. The glass forming material also reduces the melting point of the alloys and there by the separation between the glass forming temperature and the crystallization temperature is reduced. In fact T_g / T_m which is called the reduced glass transition temperature is an important parameter determining the glass forming tendency of an alloy.

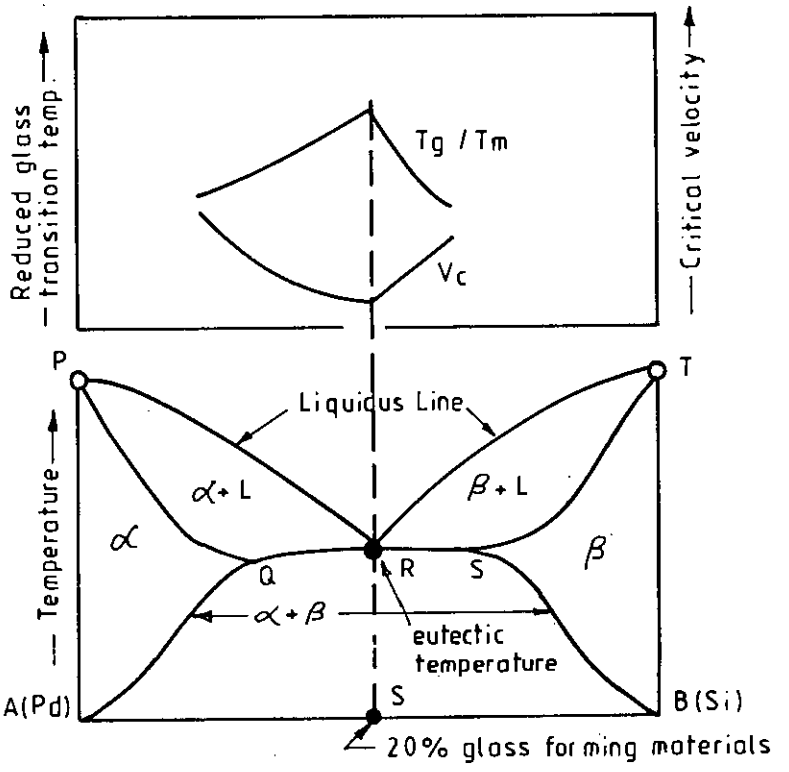

PRT → Liquidus line; PQRST→ Solidus line;

α → Solid solution of B in A; β → Solid solution of A in B

Fig:-2.5 Compositional dependence of melting point

The more complex an alloy is greater is the possibility of forming the amorphous state. This is because the arrangement of the atoms in the crystalline form of complex system takes more time which means a greater relaxation time. The presence of glass forming materials contributes to this complexity and there by increases the relaxation time. The stability of a metallic glass is also increased due to the presence of the glass forming material. Since a metallic glass is in a metastable state the stability with respect to temperature is determine by the local potential barrier produced by the disordered state of the amorphous material. When T_g / T_m is large the cooling rate needed for glass formation may be reduced, this mean that critical velocity of the copper disk can be reduced. The dependence of reduced glass transition temperature and the phase diagram indicating the dependence of melting point on composition of the melt is shown in Fig-2.5.

To increase the stability it is necessary to introduce some atoms of B, Si or P (i,e atoms with smaller radius) in the matrix. From statistics we know that the amorphous material has a porosity of 20% on the average therefore $TM_{80}M_{20}$ (M = B, P, Si, C etc = 20% at atomic) is generally introduced to form a good amorphous material. From Fig-2.6 it is observed that the minimum linear velocity of the drum is around 10m/min for preparation of an amorphous ribbon by melt spinning technique.

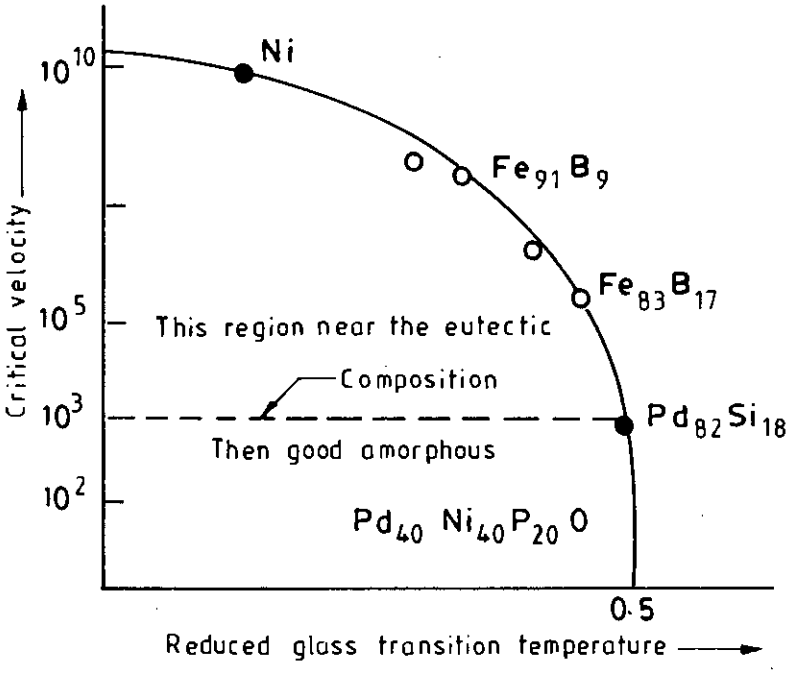

Fig:-2.6 Experimental values of critical velocity versus reduced glass transition temperature

2.4. Conditions necessary for preparing amorphous materials

Interms of viscosity and diffusion co-efficient we can find the condition for formation of glass

[1] For metals atomic bonding is metallic and the viscosity is lower than the diffusion co-efficient and mobility is high.

[2] In the case of amorphous materials viscosity is very high and the mobility and the diffusion co-efficient is low. Atomic bonds tends to be covalent as in the case of silicate (SiO_2).

2.5. Preparation technique of amorphous ribbon

There are various techniques in use to produce a metallic alloy in an amorphous state where the atomic arrangements have no long range periodicity. The different experimental techniques developed to produce amorphous metallic glass can be classified into two groups

[1] The atomic deposition methods. and
[2] The fast cooling of the melt.

2.5.1. The atomic deposition methods

Deposition can be described in terms of whether the added atom is prevented from diffusing more then an atomic distance before it is fixed in position due to cooling and increased viscosity. The atomic deposition methods include condensation of a vapour on a cooled substrate by

[a] Vacuum deposition
[b] Sputter deposition
[c] Electro deposition and
[d] Chemical deposition

2.5.2. The fast cooling of the melt

For producing an amorphous state by any of the liquid quenching devices, the alloy must be cooled through the temperature range from the melting

temperature (T_m) to the glass transition temperature (T_g) very fast allowing no time for crystallization. The factors controlling T_g and crystallization are both structural and kinetic. The structural factors are concerned with atomic arrangement, bonding and atomic size effects. The kinetic factors as discussed by Turnbull[2.15] are the nucleation, crystal growth rate and diffusion rate compered to the cooling rate. The interest in this method stems from the wide variety of alloys that can be made as well as from the potential low cost of preparation. In the pioneering work of Duwez *et al* [2.16] , a number of devices have been reported for obtaining the necessary high quenching rates and for producing continuous filaments. The methods using the principle of fast cooling of melt techniques are

[1] The gun techniques
[2] Single roller rapid quenching techniques
[3] Double roller rapid quenching techniques
[4] Centrifuge and rotary splat quencher techniques
[5] Torsion catapult techniques
[6] Plasmat-jet spray techniques
[7] Filamentary casting techniques
[8] Melt extraction techniques
[9] Free jet spinning techniques and
[10] The melt spinning techniques

Although the different methods used in preparing amorphous metallic ribbons are mentioned here, only the single roller rapid quenching technique which was used to prepare the specimens for the present work will be discussed.

2.5.3. Rapid quenching method

As shown in a schematic diagram in Fig-2.7, the rapid quenching technique apparatus consists mainly of a copper roller, an induction heater and a nozzle. The roller was driven by a variable speed motor via a tooth belt. The angular velocity was 2000 rev./min.. Use of log wheel rotation enable us to very the surface velocity in the range 20 to 30m/s. The diameter of the copper roller was 10cm. The use of copper for the roller material was chosen for its good conductivity and mechanical softness, which allowed cleaning and polishing to be carried out easily. For room temperature work, it showed no contamination of the ribbon from the roller material and the careful preparation of the surface was more important than the material of the roller.

In this process one has to consider that vibration of the roller should be well below the high frequency vibration of the melt puddle to avoid any influence of it on the geometry and uniformity of the ribbon. One has to be careful and see that the ribbon does not remain in contact with the surface of the roller for a whole revolution and be hit, from the back. A bigger diameter is thus preferred for the roller. The induction heater coil is made of hollow copper tubing which is cooled simultaneously by circulating water through its inner hole. The shape and diameter of the induction heater as also its winding is to be adjusted to produce proper temperature gradient. This is to avoid, sudden cooling of the melt in its way out of the crucible and blocking the nozzle. the quartz tubing having outer diameter 20mm which is narrowed down conically to 1mm with a hole for the nozzle 0.1 to 0.2mm.

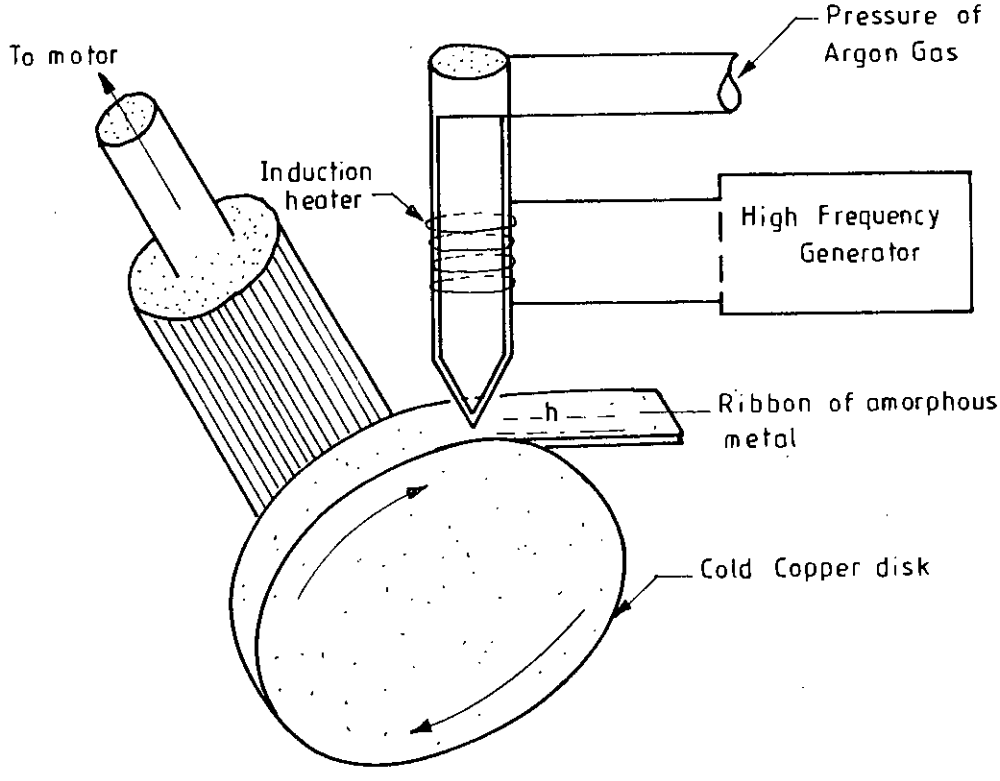

Fig:-2.7 Thin layer of molten alloy intimate contract with the outer surface of metallic rotor is quenched in to amorphous

The nozzle geometry is selected to minimize the contraction in the cross-sectional area of the molten zet as it leaves the nozzle orifice. Quartz tube is suitable for repeated use in several successful runs and should be transparent to make the melting process visible. It should withstand the sudden fast changes in temperature.

2.6. Experimental details of the preparation of amorphous ribbon

The amorphous ribbons are prepared in a furnace in an argon atmosphere (0.2 to 0.3 atms.). The buttons prepared are about 50 grams each. Care is taken to ensure through mixing and homogeneity of the alloy composition, by turning over and remelting each button few times. The mother alloys which are formed in the form of buttons in a furnace by sudden cooling and is then cut into small pieces and is introduced in the quartz tube. The quartz tube is connected from the top by rubber 'O' rings and metal rings to the argon cylinder through a valve and a pressure gauge.

After proper cleaning of the roller surface and adjusting its speed to the desired value, as measured by stroboscope the induction furnace is powered using high frequency generator. When the melting temperature is reached as observed through a protective spectacle, the injection pressure is applied by opening the pressure valve. To avoid the turbulence of the wind, arising from the high speed of the roller in disturbing the melt puddle, cotton pad and metallic shield are usually used just beneath the roller. To avoid oxidation of the ribbon during its formation an inert atmosphere can be created around the roller by a slow stream of helium gas.

The speed of the roller, the volumetric flow rate, the orifice diameter, the substrate orifice distance, the injection angle etc. are adjusted by trial and error to get the best result in respect of the quality and the geometry of the ribbons.

2.6.1. Important factors to control the thickness of ribbons are:

[1] Rotating speed

(a) Angular velocity ω = 2000 rev./min. and

(b) Surface velocity v = 20m/s

[2] Gap between nozzle and rotating copper drum h = 100 to 150μm

[3] Oscillation of the rotating copper drum both static and dynamic have maximum displacement 1.5 to 5μm.

[4] Pressure = 0.2 to 0.3 argon atmosphere

[5] Temperature of metals $T_m \approx 1500^0 C$

The temperature did not exceed $1800^0 C$ otherwise quartz tube would be melt.

[6] Stability was ensured for the drop in the surface of drum.

2.7. Factors contributing to glass formation

There are three interrelated factors that determine glass forming tendency. These are thermodynamic conditions that favour the liquid phase relative to the crystalline phase, the kinetic conditions that inhibit crystallization and the process factors that arise due to experimental conditions.

The thermodynamic factors for glass formation are liquidus temperature T_m at which the alloy melts, the heat of vaporization and the free energy of all the phases that arise or could potentially arise during solidification process. Viscosity of the melt, the glass transition temperature T_g and the homogeneous nucleation rate belongs to kinetic parameters. The glass transition temperature is defined as the temperature at which the supercooled liquid takes on the rigidity of a solid or more specifically at which the viscosity approaches 15 poise.

Processing parameters are the cooling rate, the heterogeneous nucleation rate and the supper cooling temperature interval. The temperature of the glass transition is slightly dependent on the cooling rate. At each cooling rate the glass will freeze in a different state of internal energy is shown in Fig-2.8

At the melting point T_m, the enthalpy H of a crystal includes latent heat of fusion due to long range order. In the case of rapid cooling of the melt the free energy decreases since long range order do not take place, thus leaving the system at a higher energy state. Heat treatment, relaxation and stability are thus important considerations in metallic glass. The glass forming tendency also arises from as size difference between the constituent elements. It appears that appreciable size difference between the components in the glassy alloy is a necessary condition for ready glass formation.

A single parameter that expresses glass forming tendency is the ratio of the glass transition temperature to the melting temperature defined as

$$\tau = \frac{T_g}{T_m} \qquad (2.4)$$

Higher values of τ obviously favour glass formation. For metallic glass to be formed by rapid cooling, τ should be greater than 0.45 by H. S. Chen[3.17]. Based on alloy composition there are two major groups that rapidly form glasses. In one of these groups the metal is form Fe, Co, Ni, Pd or Pt and the metalloid is B, C, Si, Ge or P. these metallic glasses constitute soft amorphous magnetic materials. Our working sample prepared shown by table-1

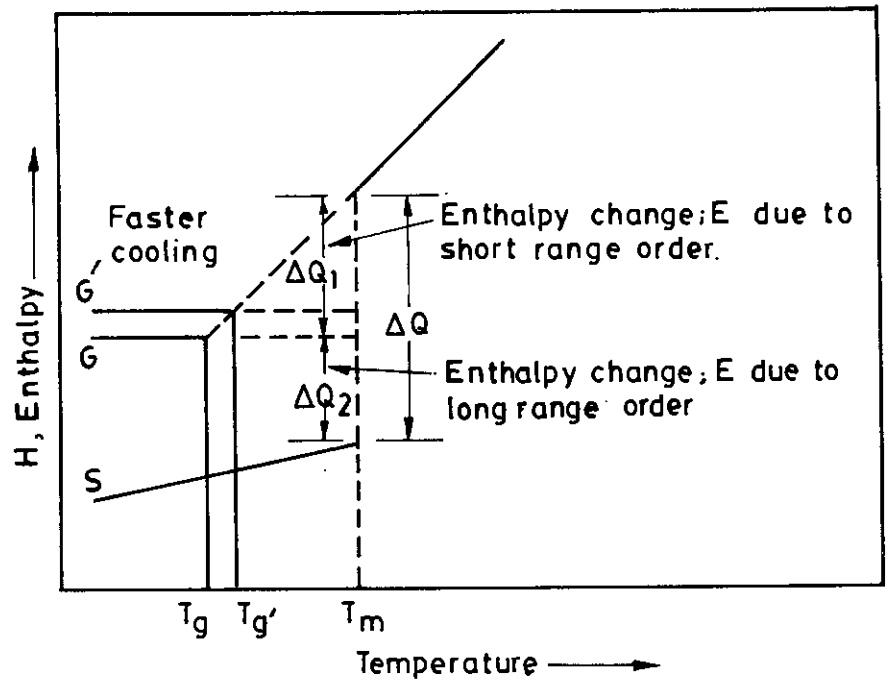

Fig:-2.8 Temperature dependence of enthalpy H. G and G′ correspond to glass transition and S corresponds to the transition to the crystalline state

Table-1

Fe-based ribbons	Thickness	Co-based ribbons	Thickness	Ni-based ribbons	Thickness
$Fe_{76}Si_{14}B_{10}$	24μm	$Co_{72}Fe_8Si_{10}B_{10}$	24μm	$Ni_{60}Fe_{20}B_{20}$	22μm
$Fe_{78}Si_{12}B_{10}$	22μm	$Co_{74}Fe_6Si_{10}B_{10}$	26μm	$Ni_{50}Fe_{30}B_{20}$	20μm
$Fe_{80}Si_{10}B_{10}$	26μm	$Co_{76}Fe_4Si_{10}B_{10}$	26μm	$Ni_{40}Fe_{40}B_{20}$	23μm
$Fe_{82}Si_8B_{10}$	34μm	$Co_{78}Fe_2Si_{10}B_{10}$	28μm	$Ni_{30}Fe_{50}B_{20}$	19μm
$Fe_{84}Si_6B_{10}$	18μm	$Co_{80}Si_{10}B_{10}$	21μm		

2.8. Examining the amorphousity

The amorphousity of all the ribbons have been confirmed by X-ray diffraction using Cu-K_α radiation. All the ribbons were found to be amorphous as shown in Fig-2.9.

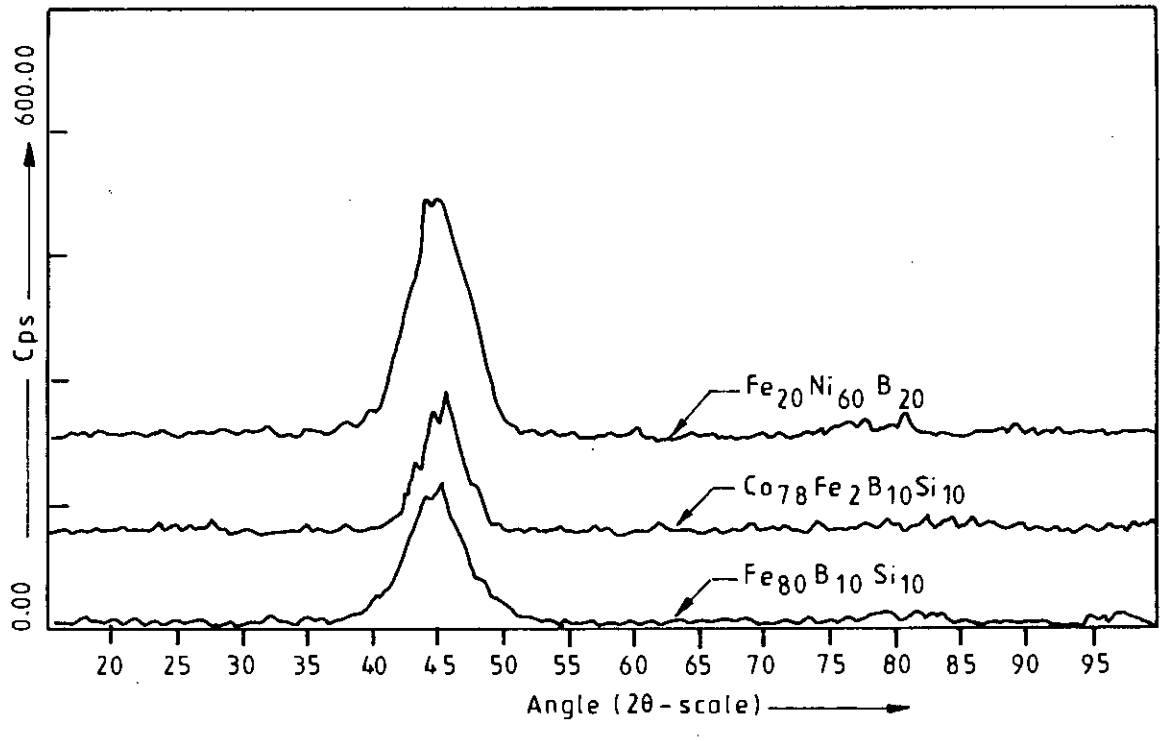

Fig- 2.9. X-ray diffraction from the top surface of some amorphous ribbon

The ribbons showed broad diffraction maximum and no low angle scattering. These ribbons were also ductile and those cases for which low angle scattering appear and the broad diffraction peak are subdued there is some presence of micro crystalline phase. These could be removed if the speed of the roller was increased. The thickness of an amorphous is controlled by the linear speed of the roller, the gap between the nozzle and the rotating drum which was about 1.5 to 5μm, oscillation of the drum, both static and dynamic, pressure and temperature of the melt and the stability of the drop on the surface of the drum. The nature of the broad diffraction peak as observed is shown in fig-2.9 for some of the samples.

CHAPTER-3 THEORETICAL ASPECTS

3.0. Theoretical Aspects

3.1. Stability of Amorphous Alloys

Amorphous alloys represent metastable states and tend to transform into stable crystalline phases. At temperatures below the crystallization temperature, structural relaxation effects take place and are caused by atomic rearrangements. The formation and resultant stability of amorphous alloys are important topics both theoretically and technologically. Which has been treated by turnbull[3.1] and Takayama[3.2] from thermodynamic view point. The ability of an alloy to be quenched into glassy state is generally measured by the magnitude of the quantity.

$$\Delta T_g = T_m - T_g, \qquad (3.1)$$

where T_m and T_g are the melting and glass transition temperatures respectively. In a similar manner the stability of the glass after formation is generally measured by the magnitude of the quantity

$$\Delta T_x = T_x - T_g, \qquad (3.2)$$

where T_x is the temperature for the onset of crystallization. As the temperature decreases from T_m, the rate of crystallization will increase rapidly but then fall as the temperature decrease below T_g. Thus by quenching a molten alloy rapidly enough to a temperature below T_g, a quasi-equilibrium amorphous phase can be obtained. There is no direct relation between the case of formation and the resultant stability of an amorphous alloy. The amorphous alloy composition most favourable for glass formation is near the eutectic; the deeper the eutectic the better is the glass forming ability as noted by Cohen and Turnbull[3.3]. At eutectic point the liquid is particularly stable against crystallization. The crystallization is associated with nucleation and growth processes. Since the formation of an amorphous alloy depends on the absence of long range order, Change of composition is expected to affect T_g and T_x. This is because, the long range ordering of atoms depends on the free energy difference between the crystalline state and the amorphous state. The change of composition affects the growth kinetics in a complicated way which can only the determined experimentally.

The transition to the glassy state and the crystalline state is accompanied by an exothermic heat effect giving rise to a sharp peak in the temperature dependence of the exothermic heat. Therefore, differential thermal analysis (DTA) is a widely used technique to study thermally induced transformations in amorphous alloys and to determine T_g and T_x. The magnitude of T_g and T_x are very different for amorphous materials and depend strongly on composition. The activation energy ranges typically between 2 and 6ev[3.4].

The dependence of T_g on the heating rate S = dT/dt can be used to determine the activation energy of crystallization[3.5]. Considering the fraction x of amorphous material transformed into the crystalline state in time t and at temperature T, one obtains for the first order rate process

$$(\delta x/\delta t)_T = K(1-x). \tag{3.3}$$

For thermally activated process, the rate constant K obeys an Arrhenius type of equations

$$K = K_0 \exp\left(\frac{-\Delta E}{RT}\right), \tag{3.4}$$

where K_0 is a constant and ΔE is the activation energy. Combining eq^n(3.3) and eq^n(3.4) and using $dX = (\delta x/\delta t)_t dt + (\delta x/\delta t)_t dT$ with $(\delta x/\delta t)dt \cong 0$, one obtains

$$\frac{dx}{dt} = K_0(1-x)\exp\left(\frac{-\Delta E}{RT}\right). \tag{3.5}$$

At the peak of the exothermic heat, the change of the reaction rate $\frac{d^2x}{dt^2}$ is equal to zero, yielding, with $T = T_x$,

$$K_0 \exp\left(\frac{-\Delta E}{RT_x}\right) = \left(\frac{\Delta E}{RT_x^2}\right)S. \tag{3.6}$$

ΔT_x for the stability of amorphous alloys as given by eq^n(3.2) and is obtained from DTA. The values of ΔE also appear to correlate well with the number of atomic species in the alloy; the more complex the alloy the greater is ΔE. Similar correlation between thermal stability as measured by ΔT_x and ΔE appears to small.

3.2. Magnetization of the Amorphous Ribbons

The saturation magnetization of material at a temperature of 0°K is one of its basic properties. Measurements are usually expressed as average moment per magnetic atom in units of the Bhor magneton, μ_B, or as specific saturation magnetization for the amorphous alloy, σ_s, in units of Am^2/Kg. The moments of most amorphous alloys are lower than those of the crystalline transition metals which they contain. However, the direct effect of the structural disorder on the moments is very small. This points out the importance of chemical instead of structural disorder. The reduction is least in B-based glass and highest in P-based glass. The observed moments on TM-M glasses can approximately fitted to a formula(3.6).

$$\mu = \left(\mu_{TM} C_{TM} - C_B - 2C_{SiC} - 3C_P\right) / C_{TM}, \qquad (3.7)$$

Where μ_{TM} is the magnetic moment of TM-M atoms, taken as 2.6, 1.6 and 0.6 respectively in Bohr magneton for Fe, Co and Ni. C's are respective concentrations. This clearly demonstrates the change transfer from metalloid to d-band of transition metal and seems to suggest that 1, 2 or 3 electrons are transferred from each of B, Si (C, Ge) or P atom. The relative number of electrons donated can be listed as $-P_{13}C_7\rangle - S_{15}B_{10}\rangle - P_{16}B_6Al_3\rangle - P_{14}B_6\rangle - Si_9B_{13}\rangle - B_{20}$ based on the relative magnitudes of M_s.

Amorphous alloys are rather poor conductors, but their 3d-electrons are just as "itinerant" as in crystalline transition metal alloys. Only itinerant exchange between 3d moments is of importance in the transition metal-metalloid alloys. Itinerant exchange arises because the single site exchange taken together with the intersite electron hopping terms produce a correlation between moments on different sites. This mechanism depends on the band structure and can lead to ferromagnetism, antiferromagnetism or complex spin arrangements. The theoretical treatment of spin ordering in amorphous solids is a much more difficult problem than in regular crystalline lattices and has not been satisfactorily solved. If the molecular field approximation (MFA) is used, even though its use is doubtful, the paramagnetic Curie temperature can be expressed as

$$T_c = \left[2S(S+1)/3K\right]\sum_{ij} J_{ij}, \qquad (3.8)$$

where S is the spin number, K is Boltzmann's constant and J_{ij} is the exchange interaction between atoms at the position r_i and r_j, and can be expressed interms of the radial distribution function.

In the first, a unique constant exchange interaction between the magnetic atoms is assumed and the amorphous nature of the alloy is taken into account by calculating a random distribution of the local anisotropy field[3.7]. In the second approach to treating this problem, a distribution of exchange integrals is assumed in order to reflect the structural fluctuation in the amorphous alloy[3.8]. Both approaches predict that the M Vs T curve will flat below that for the crystalline counter part. The first model however predicts that amorphous alloys should exhibit a structureless Mössbauer spectrum, contrary to the observed spectra. Thus the second approach is preferred of the various theories the molecular field approach (MFA) and mean field theories.

3.2.1. Molecular Field Theory of Ferromagnetic Amorphous Materials

The simplest theory which can explain the phase transition from the ordered ferromagnetic phase (for $T < T_C$) to the disordered paramagnetic phase (for $T > T_C$) is the molecular field approximation (MFA). The original treatment as given by Weiss[3.9] was purely phenomenological, but in our discussion here, the approximation as applied to the Heisenberg exchange interaction for crystalline ferromagnets will be considered. This will help us to understand the changes that must be incorporated in MFA for its application to amorphous ferromagnets.

The Heisenberg Hamiltonian in the presence of an external field H is

$$\hat{H} = -\sum_{ij} A_{ij}\vec{J}_{ij}\vec{J}_{ij} - \sum_{j} g_j \mu_B \hat{J}_i^z H^z, \qquad (3.9)$$

where g is the lande 'g'-factor, μ_B is the Bhor magneton and describe the interaction of spin J_i on the i-th site with the spin J_j on the j-th site via the exchange interaction $A_{ij} = A\left(\hat{R}_i - \hat{R}_j\right)$, A_{ij} is a random variable with some distribution function law. In the simplest case where only one kind of magnetic atoms $g_i = g$ and any sign $J_i = J$ are used, we have

$$\hat{H} = -\sum_j \left\{ \frac{\sum_i A_{ij} \bar{J}_i}{g_j \mu_B} + H \right\} g_j \mu_B \hat{J}_j^z \qquad (3.10)$$

For $\hat{J}_i \rightarrow \left\langle \hat{\bar{J}} \right\rangle$ quantum statistical average,

$$\hat{H} = -\sum_j \left\{ \frac{A_{ij} \left\langle \hat{J}_i \right\rangle}{g_j \mu_B} + H \right\} g_j \mu_B \hat{J}_j^z \qquad (3.11)$$

Thus eq^n(3.11) can be written as

$$\hat{H}_{MFA} = -\sum_j \left(H_{exch}^j + H \right) g_j \mu_B \hat{J}_j^z, \text{ where exchange field } H_{exch}^j = \sum_i \frac{A_{ij} \left\langle \hat{J}_i \right\rangle}{g_j \mu_B}$$
$$= \sum_j H_{eff}^j g_j \mu_B \hat{J}_j^z \qquad (3.12)$$

where the effective field $H_{eff}^j = H_{exch}^j + H$. The energy of a magnetic atom at the j-th site in the effective field H_{eff}, is.

$$E_j = -H_{eff}^j g_j \mu_B \left\langle \hat{J}_j^z \right\rangle, \qquad (3.13)$$

where the Brackets represents a thermodynamic average. But we can write

$$\left\langle \hat{J}_j^z \right\rangle = \frac{\sum_{m_j=+J}^{m_j=+J} m_j e^{\frac{-E_j}{K_B T}}}{\sum_{m_j=-J}^{m_j=+J} e^{\frac{-E_j}{K_B T}}}$$
$$= J B_J \left[\frac{g \mu_B J}{K_B T} H_{eff}^j \right] \qquad (3.14)$$

The argument of the Brillouin function

$$\frac{g \mu_B J}{K_B T} \left[H_{exch}^j + H \right] = \frac{g \mu_B J}{K_B T} \left[\frac{\sum_i A_{ij} \left\langle \hat{J}_i \right\rangle}{g \mu_B} + H \right]$$
$$= \frac{J}{K_B T} \sum_i A_{ij} \left\langle \hat{J}_i^z \right\rangle + \frac{g \mu_B J}{K_B T} H$$

By introducing high temperature expansion (paramagnetic region), we get

$$B_J(x) = \frac{J+1}{3J}x$$

Thus we eq^n(3.14) can be written as

$$\left\langle \hat{J}_j^z \right\rangle = \frac{J(J+1)}{3J}\left[\frac{J}{K_B T}\sum_i A_{ij}\left\langle \hat{J}_i^z \right\rangle + \frac{g\mu_B J}{K_B T}H\right],$$

where $\left\langle \hat{J}_i^z \right\rangle$ represents upper bar mean. Configuration average with random distribution function can be written as

$$\left\langle \bar{\hat{J}}_j^z \right\rangle = \frac{J(J+1)}{3J}\left[\frac{J}{K_B T}\sum_i \overline{A}_{ij}\left\langle \bar{\hat{J}}_i^z \right\rangle + \frac{g\mu_B J}{K_B T}H\right].$$

After random approximation the value of J_j does not depend one site, thus $\left\langle \bar{\hat{J}}_j^z \right\rangle = \left\langle \bar{\hat{J}}^z \right\rangle$

and $\left\langle \bar{\hat{J}}_j^z \right\rangle\left[1 - \frac{J(J+1)}{3K_B T}\sum_i \overline{A}_{ij}\right] = \frac{J(J+1)\mu_B g}{3K_B T}H$, and $\left\langle \bar{\hat{J}}_j^z \right\rangle = \frac{\frac{J(J+1)\mu_B g}{3K_B T}H}{1 - \frac{J(J+1)}{3K_B T}\sum_i \overline{A}_{ij}}$

From the quantum theory of paramagnetism we can write the equation for spontaneous magnetism as

$$M(T) = Ng\mu_B\left\langle \bar{\hat{J}}^z \right\rangle$$

$$= \frac{Ng\mu_B \frac{J(J+1)\mu_B g}{3K_B T}H}{1 - \frac{J(J+1)}{3K_B T}\sum_i \overline{A}_{ij}}$$

$$= \frac{\frac{Ng^2\mu_B^2 J(J+1)}{3K_B T}}{1 - \frac{J(J+1)Z.\overline{A}}{3K_B T}}H \qquad (3.15)$$

where $\overline{A}$ is mean value of A_{ij} and Z is the number of nearest neighbours of the Pseudo crystal. After annealing amorphous materials become crystalline, and approximated. eq^n(3.15) can be written as Curie Weiss law for amorphous material as

$$\chi(T) = \frac{M(T)}{H}$$

$$= \frac{C}{T - T_c} \qquad (3.16)$$

Here, $C = \frac{Ng^2\mu_B^2 J(J+1)}{3K_B}$ and $T_c = \frac{J(J+1)Z.\overline{A}}{3K_B}$.

T_c is the Curie temperature at which the susceptibility tends to infinity. This means that M has a finite value when H is zero, which is an evidence of spontaneous magnetization. This spontaneous magnetization below the Curie temperature is shown in fig.-3.1, where the magnetization decreases from a saturated value $M = M_s(0)$ at T=0 to zero at $T = T_c$.

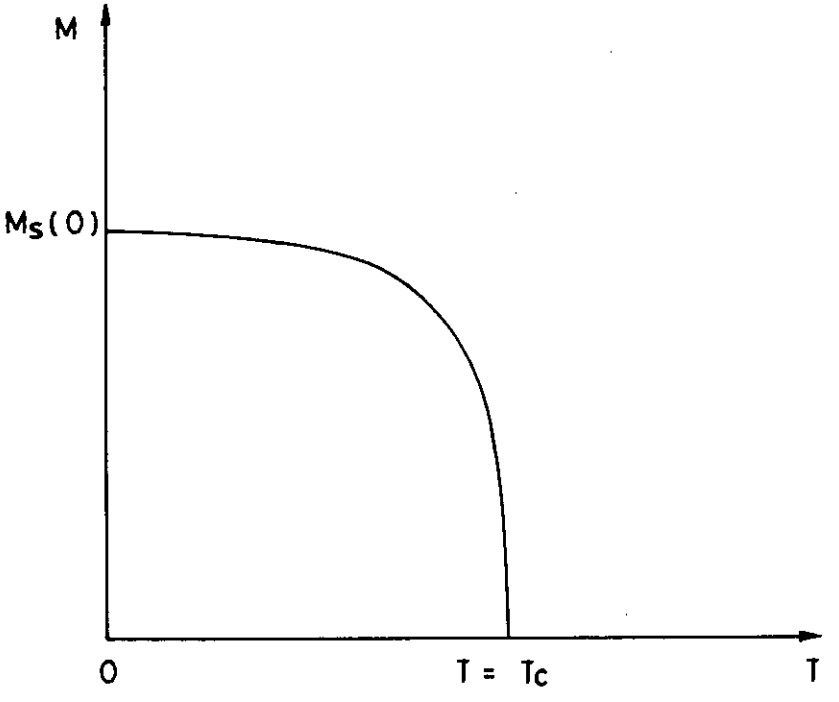

Fig-3.1. Spontaneous magnetization below the Curie temperature.

Now magnetization

$$\left\langle \hat{J}_i^z \right\rangle = J.B_J\left[\frac{g\mu_B J}{K_B T}\frac{\sum_i A_{ij}\left\langle \hat{J}_i^z \right\rangle}{g\mu_B}\right], \text{ when H=0} \qquad (3.17)$$

Without external field, A_{ij} = mean value part + fluctuating part

$$= \overline{A} + \Delta A_{ij}$$

Eq^{n}(3.17) can be written as

$$\left\langle \bar{\hat{J}}_j^z \right\rangle = JB_J\left[\frac{JZ\overline{A}}{K_B T}\left\langle \bar{\hat{J}}^z \right\rangle + \frac{J}{K_B T}\left\langle \bar{\hat{J}}^z \right\rangle \sum_i \Delta A_{ij}\right]$$

$$= JB_J\left[X + Y\sum_i \Delta A_{ij}\right] \qquad (3.18)$$

where $X = \frac{JZ\overline{A}}{K_B T}\left\langle \bar{\hat{J}}^z \right\rangle$ and $Y = \frac{J}{K_B T}\left\langle \bar{\hat{J}}^z \right\rangle$

Expanding by Taylor series,

$$B_J\left[X + Y\sum_i \Delta A_{ij}\right] = B(X) + \frac{B'(X)}{1!} Y\sum_i \Delta A_{ij} + \frac{B''(X)}{2!} Y^2\left(\sum_i \Delta A_{ij}\right)^2 + \ldots\ldots\ldots\ldots$$

The distribution functions for probability are

$$P\left(\sum_i \Delta A_{ij}\right) = \frac{1}{2}\left\{\delta\left[\sum_i \Delta A_{ij} - ZA\right] + \delta\left[\sum_i \Delta A_{ij} + ZA\right]\right\},$$

$$\overline{f\left(\sum_i \Delta A_{ij}\right)} = \int d\left(\sum_i \Delta A_{ij}\right).P\left(\sum_i \Delta A_{ij}\right) f\left(\sum_i \Delta A_{ij}\right),$$

$$\overline{B_J\left(X + Y\sum_i \Delta A_{ij}\right)} = \int d\left(\sum_i \Delta A_{ij}\right).P\left(\sum_i \Delta A_{ij}\right) B_J\left(X + Y\sum_i \Delta A_{ij}\right),$$

and we have neglected the higher order correlations by assuming that the fluctuation in A_{ij} are symmetric about A. Thus

$$\left(\sum_{ij} \Delta A_{ij}\right)^n = \begin{cases} 0 & \text{for n odd i.e. } n = 2k+1. \\ (Z\Delta)^n & \text{for n even i.e. } n = 2k. \end{cases}$$

$$\text{But}\left(\overline{\sum_{ij} \Delta A_{ij}}\right)^2 = \frac{1}{2}\left\{(ZA)^2 + (-ZA)^2\right\} = (ZA)^2.$$

and we can write eq^{n}(3.18) as

$$\left\langle \bar{J}^z \right\rangle = J\frac{1}{2}\left\{B_J(X + YZ\Delta) - B_J(X - YZ\Delta)\right\}, \qquad (3.19)$$

which can be solved for the reduced magnetization m. A simpler closed expression results, if we expand it in a Taylor series in the absence of the external field. Thus

$$m = \frac{M(T)}{M(0)} = \frac{\langle \bar{J}^z \rangle}{J}$$

$$= \frac{1}{2}\left\{ B_J\left[\frac{ZJ^2A}{K_BT} m + \frac{ZJ\Delta g\mu_B}{K_BT} m \right] + B_J\left[\frac{ZJ^2A}{K_BT} m - \frac{ZJ\Delta g\mu_B}{K_BT} m \right] \right\}$$

$$= \frac{1}{2}\left\{ B_J\left[\frac{3J}{J+1} \frac{m}{\tau}(1+\delta) \right] + B_J\left[\frac{3J}{J+1} \frac{m}{\tau}(1-\delta) \right] \right\}, \qquad (3.20)$$

where $\delta = \frac{\Delta}{A}$ and $\tau = \frac{T}{T_c}$

The temperature dependence of m as obtained from eq^n(3.20) is shown in fig-(3.2). A finite value of δ depresses the reduced magnetization curve compared to the curve for δ = 0 over the entire temperature range, as was later observed experimentally. No m(T) curve fits experimental data for a single value of δ.

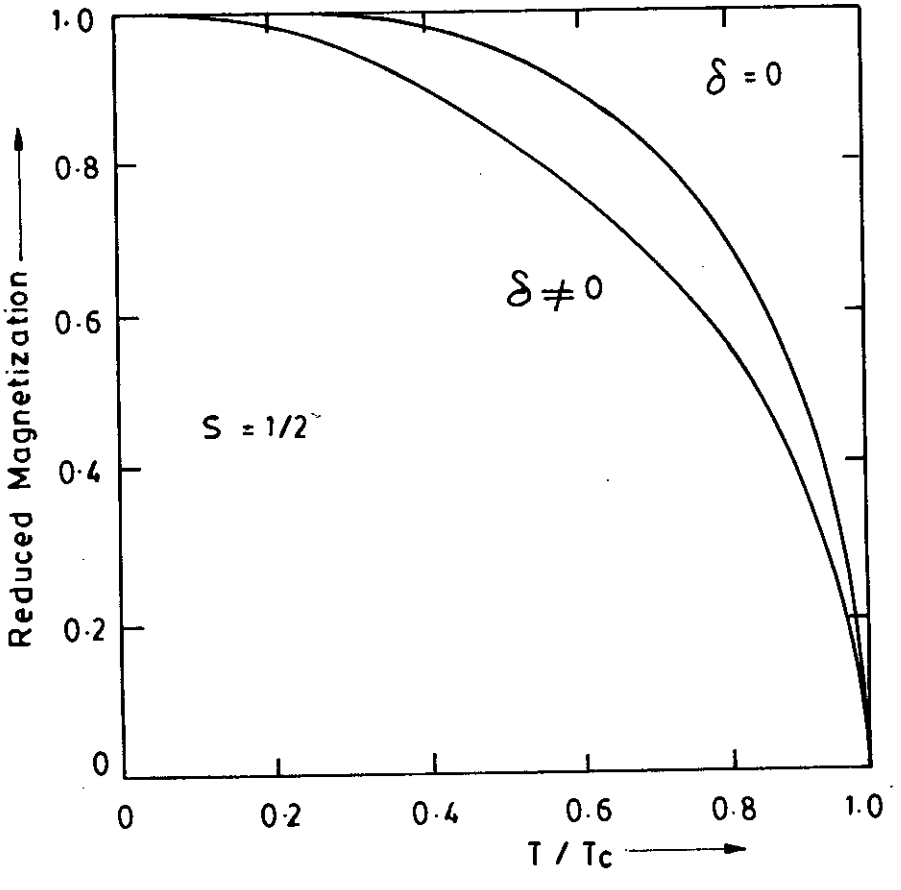

Fig-3.2. Reduced magnetization curves with $(\delta \neq 0)$ and without $(\delta = 0)$ fluctuations in the exchange interaction.

Considering that MFA does not accurately reproduce the m(T) curves for crystalline ferromagnets, this could hardly be expected. Given the above restriction on the applicability of the MFA, it is of value to investigate the effect of disorder within the framework of other effective field methods based on clusters of atoms. Such methods for crystalline magnets are well known[3.10], and here we will explore their applications to amorphous ferromagnets.

3.2.2. Mean-Field Theory for Temperature Dependence of the Magnetization.

The lack of a general analytic expression to predict the temperature dependence of M_s had led to the use of simple approximations allowing at a least a qualitative interpretation of the experimental data. The mean-field theory is based on the Heisenberg model by assigning to the i-th atom a magnetic moment

$$\mu_i(T) = \mu_i(0)\langle m_i \rangle, \tag{3.21}$$

where $\mu_i(0) = g_i \mu_B J_i$ and $\langle m_i \rangle = \frac{\langle J_i \rangle}{J_i}$; g_i and J_i are, respectively, the gyromagnetic factor and the total angular momentum of the i-th atom, where the leter is composed of the spin and orbital angular momenta. $\langle m_i \rangle$ represents the time averaged projection of the total angular momentum along the quantization axis and is defined by

$$\langle m_i \rangle = \frac{\sum_{m_i=-J_i}^{m_i=+J_i} m_i e^{-\left(\frac{E_i}{K_B T}\right)}}{\sum_{m_i=-J_i}^{m_i=+J_i} e^{-\left(\frac{E_i}{K_B T}\right)}}, \tag{3.22}$$

where

$$E_i = -\mu_i(0)\left(H + H^i_{exch}\right)m_i. \tag{3.23}$$

Here K_B denotes the Boltzmann constant. In the molecular field approximation the exchange field can be written in the form

$$H^i_{exch}(T) = \sum_j \frac{J_{ij}}{g_i g_j \mu_B^2} \mu_j(T), \tag{3.24}$$

where the J_{ij} represent the exchange constants and the summation in eq^{n}(3.24) can be performed leading to the Brillouin function

$$\langle m_i \rangle = B_{Ji}(Z_i) = \frac{2J_i+1}{2J_i}\coth\left(\frac{2J_i+1}{2J_i}Z_i\right) - \frac{1}{2}J_i\coth\left(\frac{Z_i}{2J_i}\right), \qquad (3.25)$$

where $Z_i = \frac{\mu_i(0)}{K_B T}\left(H + H^i_{exch}\right)$.

Assuming all moments of the same atomic species to be equal, the sublattice magnetization $M_i(T)$ is defined by

$$M_i(T) = Nx_i\mu_i(T), \qquad (3.26)$$

where N is the total number of magnetic atoms per unit volume and x_i is the fraction of the i-th species in the alloy. The saturation magnetization is given by

$$M_s(T) = \left|\sum_{i=1}^{r} M_i(T)\right|, \qquad (3.27)$$

where r is the number of subnet works.

Structural disorder causes fluctuations of the exchange interaction reported by Handrich(3.11) and Jäger(3.12). Restricting to nearest neighber exchange, eq^{n}(3.24) can be written as

$$H^i_{exch} = \frac{2}{Ng_i\mu_B}\sum_{j=1}^{r}\frac{n_{ij}\langle J_{ij}\rangle}{g_j\mu_B}(1+\Delta_{ij})M_j(T), \qquad (3.28)$$

where i and j now denote the subnetworks and n_{ij} are the number of nearest neighbours.

Assuming the exchange fluctuation Δ_{ij} to be small $(\Delta_{ij} \langle\langle 1)$, the Brillouin function can be expanded in a Taylor series, yielding in the absence of an external field for one-subnet work alloy by Handrich and Kaneyoshi(3.13)

$$M_s(T) = \frac{1}{2}M_s(0)\left\{B_J\left[Z(1+\Delta)\right] + B_J\left[Z(1-\Delta)\right]\right\} \qquad (3.29)$$

and for a two -subnet work by Jäger(3.12)

$$M_1(T) = \frac{1}{4} M_1(0)\left\{B_{J_1}\left[\lambda_{11}^{+} M_1(T) + \lambda_{12}^{+} M_2(T)\right] + B_{J_1}\left[\lambda_{11}^{-} M_1(T) + \lambda_{12}^{-} M_2(T)\right] + B_{J_1}\left[\lambda_{11}^{+} M_1(T) + \lambda_{12}^{-} M_2(T)\right] + B_{J_1}\left[\lambda_{11} M_1(T) + \lambda_{12} M_2(T)\right]\right\}$$

, ...(3.30)

where $\lambda_{ij}^{\pm} = \dfrac{n_{ij}}{N\mu_B^2 g_i g_j}\left\langle J_{ij}\right\rangle\left(1 \pm \overline{\Delta_{ij}}\right)$. (3.31)

A corresponding equation applies to $M_2(T)$. The average values $\overline{\Delta_{ij}}$ are obtained from $\left\langle \Delta_{11}^2 \Delta_{22}^2 \right\rangle = \overline{\Delta_{11}^2}\,\overline{\Delta_{22}^2}$. The mixed terms $\left\langle \Delta_{11}\Delta_{22} \right\rangle$ vanish because the fluctuations of J_{11} and J_{22} are independent. For $\overline{\Delta_{ij}} = 0$, these equations correspond to the molecular field equations applied to crystalline ferrimagnets. In this case $\left(\overline{\Delta_{ij}} = 0\right)$ and the Curie temperature can be expressed in terms of the λ_{ij} by

$$T_c = \frac{1}{2}\left\{T_{11} + T_{22} + \sqrt{(T_{11} - T_{22})^2 + 4T_{12}T_{21}}\right\}, \qquad (3.32)$$

where the T_{ij} are related to the λ_{ij} by

$$T_{ij} = \frac{N(J_i + 1)\mu_i^2(0)x_i}{3K_B}\lambda_{ij} \qquad (3.33)$$

The relations given in eq^{n}(3.29) and eq^{n}(3.30) are used to calculate the sublattice magnetizations regarding the exchange constants as adjustable parameters. The calculations reveal an increasing flattening exchange fluctuation parameter $\overline{\Delta}$ and a pronounced shift of the compensation temperature towards lower temperatures. The mean field theory does not account for spin-wave excitations at low temperatures and does not account for exchange fluctuations in the range of the Curie temperature.

3.2.2.1. Transition-Metal based Alloys.

The temperature dependence and the Curie temperature reflect the strength of the exchange coupling. The structural disorder in amorphous alloys induces an exchange fluctuation that causes a pronounced flattening of the $M_s(T)$ curves. The temperature curve for the amorphous alloy lies substantially below that for the crystalline compound. This reduction of M_s was explained interms of the mean field theory eq^{n}(3.29) using an exchange fluctuation parameter

$$\Delta = \frac{\sqrt{\left\langle \left(\sum_{ij} \Delta J_{ij}\right)^2 \right\rangle}}{\sum_{ij} J_{ij}}, \qquad (3.34)$$

which is defined according to the Δ_{ij} introduced in eq^{n}(3.28) and adapts values in the range $0.4 \leq \Delta \leq 0.6$. The experimental data lye typically below the theoretical curve at low temperature and above it at high temperatures. The calculated curve representing an overall fit was explained by Kaul[3.13] and Pan *et. al.*[3.14]. This inadequate description of the experimental data corresponds to the situation for crystalline alloys and has to be attributed to the mean-field approximations and the temperature independent treatment of Δ. In general, Δ is a function of temperature. Using the empirical relation[3.15].

$$\Delta = \Delta_0 \left[1 - \left(\frac{T}{T_c} \right)^2 \right], \tag{3.35}$$

deviation from the calculated line occur for $T \geq 0.2T_c$ to $0.4T_c$ due to the neglect of critical fluctuations or the temperature dependence of the spin-wave stiffness constant. In the corresponding crystalline compounds, deviations from the $T^{3/2}$ law occur for $T \geq 0.15T_c$. However, not all amorphous ferromagnets obey the $T^{3/2}$ dependence. In the case of Ni-based alloys, the weak itinerant ferromagnetism leads to a temperature dependence of M_s as given by

$$M_s^2(T) = M_s^2(0) \left[1 - \left(\frac{T}{T_c} \right)^{\eta} \right] \tag{3.36}$$

Amorphous alloys containing Co exhibit significantly higher T_c values due to the stronger Fe-Co exchange as compered to the Fe-Fe exchange. Amorphous Fe-Ni alloys show sharper fall of $m(T)$ around T_c indicating non local exchange interaction and long range co-operative phenomena. It should be noted that the pronounced sensitivity of the exchange interaction on the structural disorder gives rise to a dependence of T_c on the preparation conditions.

3.2.2.2. Low Temperature behaviour of M_s of Amorphous Ribbons

The mean field theories do not account for local magnetic excitations and thus cannot provide an accurate description of the low temperature behaviour of the magnetic properties. In the quasicrystalline approximation and the long wavelength limit, the spin-wave energy can be expressed by Keffer[3.16].

$$E_K = E_0 + DK^2 + FK^4 + \ldots\ldots\ldots\ldots, \tag{3.37}$$

where K is the wave vector of the spin-wave and D and F are the spin stiffness constants. The presence of spin-waves gives rise to a reduction of the average magnetization, leading to a temperature dependence of the form

$$M_s(T) = M_s(0)\left[1 - BT^{3/2} - CT^{3/2} - \ldots\ldots\right], \qquad (3.38)$$

where $M_s(0)$ is the saturation moment. The coefficients B and C are related to the spin-wave stiffness constant D by

$$B = \xi(3/2)\left(\frac{g\mu_B}{M_s(0)}\right)\left(\frac{K_B}{4\pi D}\right)^{3/2} \text{ and } C = \frac{3}{4}\pi\langle r^2\rangle\xi(3/2)\left(\frac{g\mu_B}{M_s(0)}\right)\left(\frac{K_B}{4\pi D}\right)^{3/2},$$

where g is the g-factor (~2.1), μ is the Bohr magneton, $\xi(3/2) = 2.612$ and $\xi(5/2) = 1.341$ are the zeta functions and $\langle r^2\rangle$ represents the average mean-square range of the exchange interaction. D is directly proportional to the exchange constants. The $T^{3/2}$ terms comes from quadratic dependence of spin-wave on wave vector. With increasing exchange strength, the slope of $M_s(T)$ versus $T^{3/2}$ decreases are expected from experimental results of alloys with increasing T_c.

3.2.2.3. High Temperature behaviour of M_s of Amorphous Ribbons

The over all temperature behaviour of reduced magnetization $m = \frac{M_s(T)}{M_s(0)}$ in TM-M glass goes to zero quite sharply at critical temperature T_c and in many glasses the phase transition is as sharp an in crystalline system. Near T_c, $M_s(T) = (T_c - T)^{\beta}$ where the β is a critical exponent. At intermediate temperature there is flattening, which is found in almost all TM-M glasses studied. The effect of high temperature has been treated in two different approaches. The first approach as given by Harris *et. al.*(3.17) considers a constant exchange interaction between are magnetic atoms and a random distribution of the local anisotropy field is considered which changes with temperature. The other approach is to consider a distribution of exchange integral is assumed in order to take into account the fluctuation in the amorphous alloys as taken by Handrich(3.18) . Both the approaches are unrealistic and infact no rigorous theory of the high temperature behaviour for amorphous materials has been developed. We have determined the experimental power low from the temperature variation of magnetization in the high temperature range.

3.3. Coercive force

There are several approaches to calculating the coercive force, H_c, in terms of the amorphous material parameters. The B-H curve for the as-quenched material will be a combination of two components. There will be a square part that arises from the 180^0 wall present near the centre of the ribbon. The remanence, B_r will be reduced due to the regions where the local anisotropy is not parallel to the applied field. For 180^0 walls, the coercive force can be written from dimensional analysis, as

$$H_c = \frac{4(AK_u)^{1/2}S}{M_s d}, \qquad (3.39)$$

where S is a constant determined by inclusion size and density surface roughness, fluctuations in anisotropy or other factors; A is the exchange constant, K_u is the anisotropy, d is the ribbon thickness and M_s is the saturation magnetization.

The most significant point of the preceding discussion is that it has been possible to describe the B-H curve and derive reasonable values of H_c without considering the amorphous nature of the material. Essentially all of the interesting magnetic properties can be examined in terms of simple models and domain configurations that do not differ in a fundamental way from similar explanations developed for magnetically soft crystalline materials.

In another approach Hasegawa[3.19] wrote

$$H_c = \frac{2K_u}{M_s} f \qquad (3.40)$$

we assume reversal by domain wall motion where $f = \frac{\sum \Delta X}{X}$. Here ΔX stands for the fluctuation in X within a region corresponding to the domain wall width.

Fujimori *et. al.*[3.20] assumed that the major contribution to the H_c arose from the strain-magnetostriction anisotropy fluctuations so that

$$H_c \propto \frac{\lambda_s}{M_s} \qquad (3.41)$$

3.3.1. Remanence-to- Saturation induction ratio

As in crystalline materials the remanence-to-Saturation ratio of a magnetic material is important theoretically and technologically. Its values is determined by the magnitudes and directions of anisotropies present. In amorphous alloys of the TM-M type the anisotropies in the as-quenched ribbons appear to be dominated by the strain magnetostriction interaction. Since the magnitude and the direction of the strain may vary with the details of the quenching the resultant anisotropy and thus $^{B_r}/_{B_s}$, would be expected to magnetically soften the amorphous ribbons. The maximum dc permeability, are often calculated as $^{B_r}/_{H_c}$, for a number of amorphous alloys in the as-cast state. Sample with high $^{B_r}/_{B_s}$ are particularly suited to devices such as switch cores, high-gain magnetic amplitudes and low-frequency inverters, where the square loop characteristic is needed.

3.4. Initial Permeability of Amorphous Ribbons

For application in small electronic device, the amorphous alloys have some what poorer losses and permeabilities than the conventional Fe-Ni alloys, but have better performance than the Fe-Co and Fe-Si alloys in other respects. Where the design optimization requires the lower cost of the amorphous alloys, their higher induction compared to the Fe-Ni alloys or their lower losses compered to the Fe-Co, Fe-Si and the Fe-Ni at higher frequencies, the use of the amorphous alloys will be favoured. The complex magnetic properties of initial permeability (μ_i) may be strongly affected by the presence of an electric current, particularly in ac condition. Moreover, the effects are rather different in as-quenched amorphous ribbons. The measurement of magnetic properties as a function of frequency and its analysis by means of the complex permeability formalism has recently led to the resolution of several aspects of the magnetizations process(3.21-3.23). The measurement of complex permeability gives us valuable information about the nature of the domain wall and their movements.

In dynamic measurements the eddy current loss is very important which occurs due to irreversible domain wall movements that are frequency dependent. A large number of possible mechanisms can contribute to the magnetic loss such as local variation of exchange energy, surface defects, compositional inhomogencities, anisotropy and magnetostriction (3.24-3.25), whose relative values are determined by grain size, grain orientation and thickness of the sample. The present goal of most of the recent amorphous ribbons researches is to fulfil this requirement. Before going into the complexity of initial permeability measurement, we discuss in short the theories and mechanism involved in frequency spectrum of initial permeability.

3.4.1. Theories of Permeability

The primary requirement is the highest possible permeability, together with low losses in the frequency range of interest. The initial permeability μ_i is defined as the derivative of induction B with respect to the internal field H in the demagnetization state

$$\mu_i = \frac{dB}{dH}, H \to 0, B \to 0 \qquad (3.42)$$

At microwave frequencies, and also in low anisotropic amorphous materials, dB and dH may be in different directions, the permeability then has a tensor character. In the

case of amorphous materials containing a large number of randomly oriented magnetic atoms the permeability will be scalar, at low frequencies with

$$B = \mu_0(H + M) \tag{3.43}$$

and the susceptibility $\chi = \frac{dM}{dH} = \frac{d}{dH}\frac{1}{\mu_0}(B - H)$

$$= \frac{1}{\mu_0}(\mu - 1) \tag{3.44}$$

The magnetic energy density

$$E = \frac{1}{\mu_0}\int H.dB \tag{3.45}$$

For time harmonic fields $H = H\sin\varpi t$, the dissipation can be described by a phase difference δ between H and B. In the case of permeability is namely defined as the proportional its constant between the magnetic field induction B and applied intensity H;

$$B = \mu H \tag{3.46}$$

This naive definition needs further sophistication's. If a magnetic material is subjected to an ac magnetic field as given below

$$B = B_0 e^{i\varpi t}, \tag{3.47}$$

then it is observed that the magnetic flux density B experiences a delay. The delay is caused due to the presence of various losses and is thus expressed as

$$B = B_0 e^{i(\varpi t - \delta)}, \tag{3.48}$$

where δ is the phase angle and marks the delay of B with respect to H. The permeability is then given by

$$\mu = \frac{B}{H} = \frac{B_0 e^{i(\varpi t - \delta)}}{H_0 e^{i\varpi t}}$$

$$= \frac{B_0 e^{-i\delta}}{H_0} = \frac{B_0}{H_0}\cos\delta - i\frac{B_0}{H_0}\sin\delta$$

$$= \mu' - i\mu'', \tag{3.49}$$

where $\mu' = \frac{B_0}{H_0}\cos\delta$ and $\mu'' = \frac{B_0}{H_0}\sin\delta$ (3.50)

The real part μ' of complex permeability μ as expressed in eq^{n}(3.49) represents the component of B which is in phase with H, so it corresponds to the normal permeability. If there are no losses, we should have $\mu = \mu'$. The imaginary part μ'' corresponds to that part of B which is delayed by phase angle 90^{0} from H. The presence of such a component requires a supply of energy to maintain the alternating magnetization, regardless of the origin of delay.

It is useful to introduce the loss factor or loss tangent $(\tan\delta)$. The ratio of μ'' to μ', as is evident from eq^{n}(3.50), gives

$$\frac{\mu''}{\mu'} = \frac{\left(B_0/H_0\right)\sin\delta}{\left(B_0/H_0\right)\cos\delta} = \tan\delta \qquad (3.51)$$

This tanδ is called the LOSS FACTOR. The Q-factor or quality factor is defined as the reciprocal of this loss factor, i.e.

$$Q = \frac{1}{\tan\delta} \qquad (3.52)$$

and the relative quality factor $= \frac{\mu_i}{\tan\delta}$ (3.53)

The behaviour of μ' and μ'' versus frequency is called the permeability spectrum. The initial permeability of a ferromagnetic or ferromagnetic substance is the combined effect of the wall permeability and rotational permeability mechanisms.

3.4.2. Wall Permeability

The mechanism of wall permeability arises from the displacement of the domain walls in small fields. Let us consider a piece of material in the demagnetized state, divided into weiss domains with equal thickness L by means of 180^{0} Bloch walls shown in fig-3.5. The walls are parallel to the Y, Z plane. The magnetization M_s in the domains is oriented alternately in the +Z or -Z direction. When field H with a component in the +Z direction is applied, the magnetization in this direction will be favoured. A displacement dx of the walls in the direction shown by the dotted lines will decrease the energy density by an amount: $\frac{2M_sH_zdx}{L}$

This can be described as a pressure $2M_sH_z$ exerted on each wall. The pressure will be counteracted by restoring forces, which for small deviations may by assumed to be kdx per unit wall surface. The new equilibrium position is than given by

$$d = \frac{M_s H_z dx}{L}$$

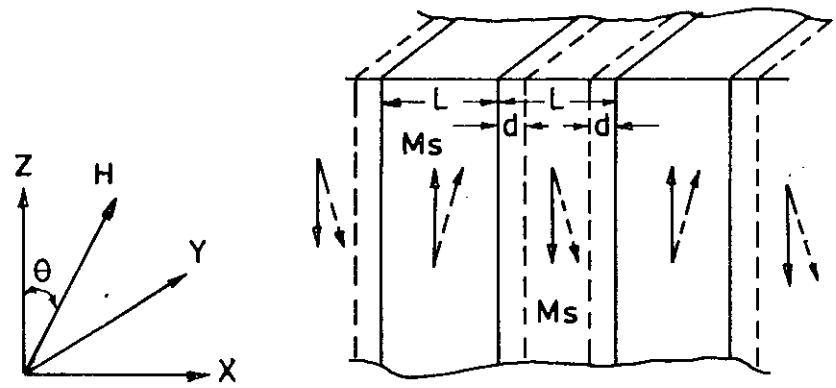

Fig.-3.5. Magnetization by wall motion and spin rotation

From the change in the magnetization

$$\Delta M = \frac{2M_s d}{L}$$

the wall susceptibility χ_w may be calculated. Let H make the angle θ with Z direction. The magnetization in the direction becomes

$$(\Delta M)_\theta = \frac{2M_s d}{L}\cos\theta, \text{ and with } H_z = H\cos\theta \text{ and } d = \frac{2M_s H_z}{K}.$$

We obtain

$$\chi_w = \frac{(\Delta M)_\theta}{H} = \frac{4M_s^2\cos^2\theta}{KL} \qquad (3.54)$$

3.4.3. Rotational Permeability

The rotational permeability mechanism arises from rotation of the magnetization in each domain. The direction of M can be found by minimizing the

magnetic energy E as a function of the orientation. Major contribution to E comes from the crystal anisotropy energy. Other contributions may be due to the stress and shape anisotropy. The stress may influence the magnetic energy Via the magnetostriction. The shape anisotropy is causes by the boundaries of the sample as well as pores, nonmagnetic inclusions and inhomogeneties. For small angular deviations α_x and α_y or M, where

$$\alpha_x = \frac{M_x}{M_s} \text{ and } \alpha_y = \frac{M_y}{M_s}$$

from the equilibrium Z-direction may be expressed as

$$E = E_0 + \frac{1}{2}\alpha_x^2 E_{xx} + \frac{1}{2}\alpha_y^2 E_{yy},$$

where it is assumed that x and y are the principal axes of the energy minimum. Instead of E_{xx} and E_{yy}, the anisotropy field $H_x^\wedge$ and $H_y^\wedge$ are often introduced. Their magnitude is given by

$$H_x^\wedge = \frac{E_{xx}}{2M_s} \text{ and } H_y^\wedge = \frac{E_{yy}}{2M_s},$$

where $H_x^\wedge$ and $H_y^\wedge$ represent the stiffness with which the magnetization is bound to the equilibrium direction for deviations in the x and y directions, respectively. The rotational susceptibilities $\chi_{r,x}$ and $\chi_{r,y}$ for fields applied along x and y directions, respectively are

$$\chi_{r,x} = \frac{M_s}{H_x^\wedge} \text{ and } \chi_{r,y} = \frac{M_s}{H_y^\wedge}$$

For cubic materials it is often found that $H_x^\wedge$ and $H_y^\wedge$ are equal. For $H_x^\wedge = H_y^\wedge = H^\wedge$ and a field H which makes an angle θ with the Z direction as shown in fig-3.5 the rotational susceptibility, $\chi_{r,c}$ in one crystallite becomes

$$\chi_{r,c} = \frac{M_s}{H^\wedge}\sin^2\theta \qquad (3.55)$$

A polycrystalline material consisting of a large number of randomly oriented grains of different shapes, with each grain divided into domains in a certain way, the rotational susceptibility χ_r of the material has to be obtained as a weighted average of $\chi_{r,c}$ of each crystallite, where the mutual influence of neighbouring crystallites has to be taken into account. If the crystal anisotropy dominates other anisotropies, then $H^\wedge$ will be constant throughout the material, so only the factor $\sin^2\theta$ from eq^n(3.55) has to be averaged. Snoek(3.26) assuming a linear averaging of $\chi_{r,c}$ and found

$$\chi_r = \frac{M_s}{3H^{\wedge}} \tag{3.56}$$

The total internal susceptibility

$$\chi = \chi_w + \chi_r = \frac{4M_s^2\cos^2\theta}{KL} + \frac{2M_s}{3H^{\wedge}}. \tag{3.57}$$

If the shape and stress anisotropies can not be neglected, $H^{\wedge}$ will be larger. Any estimate of χ_r will then be rather uncertain as long as the domain structure, and the pore distribution in the material are not known. A similar estimate of χ_w would require knowledge of the stiffness parameter k and the domain width L. These parameters are influenced by such factors as imperfection, porosity and crystallite shape and distribution which are essentially unknown.

3.5. Physical Origin of Uniaxial Anisotropy of Amorphous Ribbons

The theories that have been proposed to explain the magnetic anisotropy of the amorphous ribbons are basically the extension of the idea proposed for the origin of anisotropy in crystalline and disordered solids. In amorphous Fe, Ni and Co-based magnetic alloys we can assume the existence of disordered 3d shells where the Intra-atomic dipole-dipole interaction between the spin magnetic moments may depend on the direction of magnetization. The effect is similar to free elongated single domain particles giving rise to anisotropy energy[3.27]. Since anisotropy can be induced by spin orbit interaction, in an amorphous material this can happen by the excitation of the additional orbital states which depends on the direction of the magnetization in a disordered 3d shell.

The effect of magnetic annealing on anisotropy was first proposed by Bozorth[3.28] as due to magnetostrictive deformation which at high temperature gets relaxed through the plastic flow of boundaries and of inclusion, but when cooled gets locked up giving rise to elastic energy and hence magnetic anisotropy when this domains are rotated by the external field out of the original direction. Using this argument magnetostrictive anisotropy of $K_\lambda = -\frac{3}{2}\lambda_s\sigma$ has been proposed for amorphous magnetic materials[3.29], Chikazumi[3.30] proposed directional ordering due to distribution of atom pairs during the process of magnetic annealing, thus bringing about change in magnetoelastic energy. Kaya[3.31] on the other hand proposed shape anisotropy due to elongated ordered phase.

Another theory was proposed by Neel[3.32] and C. Kettel *et. al.*[3.33] for the mechanism of induced anisotropy by magnetic annealing, where due to precipitation of elongated particles in the matrix of spontaneous magnetization, surface density of free poles appear which gives anisotropy energy when magnetization vector is rotated perpendicular to the long axis. The anisotropy in amorphous magnetic materials is thus explained often as pair ordering[3.34], local co-ordination[3.35], shape anisotropy and shaped void formation[3.36] etc. However, if several kinds of anisotropy are mixed up in the magnetic specimen it is very difficult to give a quantitative analysis of its origin. In the light of the experimental evidence of positive magnetostriction in Fe-B amorphous ribbons and also the reduction of this magnetostriction due annealing[3.37]. We consider that our observed anisotropy is associated with magnetostriction which is induced by the strain during the preparation process. The

easy direction of magnetization is the length of the ribbon which is also the direction of strain for positive magnetostrictive materials.

3.5.1. Theories Based on the Localized Electron Model

In order to understand the origin of magnetic anisotropy in amorphous solids, we will first look at the theories developed for magnetic anisotropy of crystalline solids based on the localized electron model. Akulov[3.38] is the pioneer to drive the first theoretical expression for the temperature dependence of magnetic anisotropy constant K_1. Using a simple classical argument and assuming a system of independent spins, Akulov assumed that each spin had a free energy of the form $K_1 = \left(\alpha_1^2\alpha_2^2 + \alpha_2^2\alpha_3^2 + \alpha_3^2\alpha_1^2\right)$, where the direction cosines α_i refer to a particular spin. A simple statistical calculation gives the relationship

$$\frac{K_1(T)}{K_1(0)} = \left[\frac{M(T)}{M(0)}\right]^{10} \qquad (3.58)$$

between K_1 and the spontaneous magnetization M.

The number 10 arises from the structural combination of the direction cosines in the usual expression for the anisotropy energy, a combination dictated solely by the asymmetry of the crystal. The power law holds well for many insulators and rare-earth metals, for which the localized electron model is particularly applicable. But agreement with the experimental data for nickel and iron is not satisfactory; for example, in nickel the temperature variation of K_1 exhibits a dependence of the 50th power of the magnetization[3.39].

In a further classical treatment of magnetic anisotropy Zener[3.40], generalised the 10th power law to an $\frac{n}{2}(n+1)$ law assuming a system of independent spins. Zener showed that, if the anisotropy energy E_a is written in terms of spherical harmonics,

$$E_a = \sum_n k_n(T) Y_n^m(\alpha) \qquad (3.59)$$

$$\text{then} \quad \frac{k_n(T)}{k_n(0)} = \left[\frac{M(T)}{M(0)}\right]^{\frac{n}{2}(n+1)}$$

Here the $k_n(T)$ are linear combinations of the $K_1(T)$, and in particular

$$k_2(T) = K_1(T) + \frac{1}{11}K_2(T) + \ldots\ldots \text{and } k_3(T) = K_2(T) \qquad (3.60)$$

The two assumptions basic to Zener's derivation are:

(i) the existence of regions of sort-range order of spins around each atom, inside which the anisotropy constants are temperature independent. Thus the only effect of raising the temperature is to introduce small perturbations in the direction of the local magnetization.

(ii) the distribution of spins within each region is random so that the local anisotropy energy may be averaged over all directions.

3.5.2. Pair Model of Magnetic Anisotropy

Magnetic anisotropy describes the circumstance that the energy of a system changes with a rotation of magnetization. The relation between the change in energy of a system with the change in energy of atomic pairs is called the pair model of anisotropy. Van Vleck[3.41] first developed this theory. The most important interaction between the atomic magnetic moments is the exchange interaction. This energy is only dependent on the angle between the neighbouring atomic moments, independently of their orientation relative to their bond direction. In a view to explain magnetic anisotropy we may assume that the pair energy is dependent on the direction of the magnetic moment, ϕ, as measured from the bond direction. In general we express the pair energy by expanding it in Legendre polynomials,

$$w(\cos\Phi) = g + l\left(\cos^2\Phi - \frac{1}{3}\right) + g\left(\cos^4\Phi - \frac{6}{7}\cos^2\Phi + \frac{3}{15}\right) + \ldots\ldots \qquad (3.61)$$

The first term is independent of ϕ; hence the exchange energy is to be included in this term. The second term is called the dipole-dipole interaction.

If the pair energy were due exclusively to magnetic dipolar interaction, it should follow that

$$l = -\frac{3M^2}{4\pi\mu_0 r^3} \qquad (3.62)$$

The actual value of l can be evaluated from the uniaxial crystal anisotropy. In most cases the estimated value is 10^2 to 10^3 times larger than that given by eq^n(3.62). The origin of this strong interaction is believed to be the combined effect of spin-orbit interaction and exchange or coulomb interaction between the neighbouring orbits. That is if there are small amounts of orbital magnetic moment remaining unquenched by the

crystalline field, a part of the orbit will rotate with a rotation of the spin magnetic moment because of a magnetic interaction between the two, and the rotation of the orbit will, in turn, change the overlap of the wave function between the two atoms, giving rise to a change in the electrostatic or exchange energy. This type of interaction is termed as the anisotropic exchange. It should be noted here that the dipolar term of eq^{n}(3.61) does not contribute to the interaction energy E_a, since the spins are perfectly parallel. The dipole terms between the atomic pairs with different bond directions cancel out as long as their distribution maintains cubic symmetry. If, however, the crystal has a lower symmetry than the cubic crystal, as in a hexagonal crystal, the dipole-dipole interaction gives rise to magnetic anisotropy.

Van Vleck pointed out that the dipole-dipole interaction does give rise to cubic anisotropy since the perfect parallelism of the spin system is distributed by the dipolar interaction itself. Thus if I<0 and all the spins are parallel, the dipole-dipole interaction gives rise to a large pair energy for $\Phi = \frac{\pi}{2}$. In such a case, a more stable configuration of the spin pair will be an antiparallel alignment. Some of the spins will therefore take the anti parallel direction in an equilibrium state.

According to Van Vleck's calculation, the cubic anisotropy constants for an f.c.c. system due to dipole-dipole interaction are

$$K_1 = -\frac{9NI^2}{8SMH_m} \text{ at } T = 0^0 K, \qquad (3.63)$$

where S is the total spin quantum number, M the atomic magnetic moment, and H_m the molecular field. In the classical picture, K_1 should vanish by letting $S \to \infty$.

Now, since $NMH_m \approx 10^9 J/m^3$ and $NI \approx 10^7 J/m^3$, the order of magnitude of K_1 due to dipole-dipole interaction is

$$K_1 \approx \frac{(NI)^2}{NMH_m} \approx \frac{(10^7)^2}{10^9} \approx 10^5 J/m^3$$

This is sufficient to explain the magnitude of the observed anisotropy energy.

Judging from the origin of anisotropy, it would be practical to suppose that the anisotropy constant decreases with increasing temperature and disappears at the Curie point. Actually this does happen, and the temperature dependence is more drastic than that of spontaneous magnetization. Zener treated this problem in a simple way and explained the temperature dependence fairly well. He assumed that the pair energy is

given by eq^{n}(3.61) even for the thermally perturbed spin system, since the neighbouring spins maintain approximately in parallel alignment upto the Curie point, where, because of the strong exchange interaction, parallel spin clusters prevail in the spin system. Carr followed this method to calculate the crystal anisotropy constant for iron, nickel and cobalt[3.42].

Let $(\alpha_1,\alpha_2,\alpha_3)$ denote the direction cosines of the average magnetization, and $(\beta_1,\beta_2,\beta_3)$ the direction cosines of the local magnetization. Since we assume local parallelism in the spin system, the anisotropy energy should be given by the average of the local anisotropy energies, so that

$$E_\alpha(T) = K_1(0)\left\langle \beta_1^2\beta_2^2 + \beta_2^2\beta_3^2 + \beta_3^2\beta_1^2 \right\rangle, \tag{3.64}$$

where $K_1(0)$ is the anisotropy constant at $T = 0^0K$ and $\langle\ \rangle$ denotes the average over all possible orientations of local magnetization. Using the polar co-ordinates (θ,Φ), where θ is the angle between the local spin and the average magnetization, and Φ the azimuthal angle around the magnetization direction, we have

$$E_a(T) = K_1(o)\frac{\int_0^{\pi}\left[\left(\frac{1}{2\pi}\right)\int_0^{2\pi}\left(\beta_1^2\beta_2^2 + \beta_2^2\beta_3^2 + \beta_3^2\beta_1^2\right)\right]n(\theta)d\theta d\Phi}{\int_0^{\pi} n(\theta)d\theta}, \tag{3.65}$$

where n(θ)dθ is the number of spins which point in the solid angle between θ and (θ+dθ). Since

$$\frac{1}{2\pi}\int_0^{2\pi}\left(\beta_1^2\beta_2^2 + \beta_2^2\beta_3^2 + \beta_3^2\beta_1^2\right) = \frac{1}{5}\left[1 - P_4(\cos\theta)\right] + P_4(\cos\theta)\left(\alpha_1^2\alpha_2^2 + \alpha_2^2\alpha_3^2 + \alpha_3^2\alpha_1^2\right), \tag{3.66}$$

where $P_4(\cos\theta)$ is the fourth order Legendre polynomial. Thus eq^{n}(3.66) becomes

$$E_a(T) = K_1(0)\left\langle P_4(\cos\theta)\right\rangle\left(\alpha_1^2\alpha_2^2 + \alpha_2^2\alpha_3^2 + \alpha_3^2\alpha_1^2\right), \tag{3.67}$$

$$\text{where}\left\langle P_4(\cos\theta)\right\rangle = \frac{\int_0^{\pi} P_4(\cos\theta)n(\theta)d\theta}{\int_0^{\pi} n(\theta)d\theta} \tag{3.68}$$

This can be expressed in a polynomial series in $\frac{1}{\alpha} = \frac{kT}{MH_m}$ where H_m is the molecular field.

$$\left\langle P_4(\cos\theta)\right\rangle = 1 - \frac{10}{\alpha} + \frac{45}{\alpha^2} - \frac{105}{\alpha^3} + \ldots\ldots \tag{3.69}$$

On the other hand

$$M(T) = M(0)\left(\coth\alpha - \frac{1}{\alpha}\right) \approx M(0)\left(1 - \frac{1}{\alpha}\right) \tag{3.70}$$

so that

$$\left[\frac{M(T)}{M(0)}\right]^{10} \approx 1 - \frac{10}{\alpha} + \frac{45}{\alpha^2} - \frac{120}{\alpha^3} + \ldots\ldots \tag{3.71}$$

comparing eq^{n}(3.69) and eq^{n}(3.71) we get

$$\left[\frac{K_1(T)}{K_1(0)}\right] = \left[\frac{M(T)}{M(0)}\right]^{10} \tag{3.72}$$

eq^{n}(3.72) holds good for the temperature dependence of K_1 of iron. Carr also explained the temperature dependence of K_1 for nickel and cobalt by taking into consideration the effect of thermal expansion of the crystal lattice. But, in constant to zener's theory, Van Vleck obtained a much more gentle temperature dependence of magnetic anisotropy. Keffer (3.43) investigated this point and showed that the Zener's theory is valid at least at low temperature, while Van Vleck's theory is valid at high temperature.

3.5.3. Single-Ion Model of Magnetic Anisotropy

The orbital state of magnetic ions plays an important role in determining the magnetic anisotropy. The orbital state of the magnetic ion is influenced by a given crystalline field and the resultant orbital state gives rise to magnetic anisotropy. This phenomenon is described by the single-ion model of magnetic anisotropy. This model has been successful in interpreting the magnetic anisotropy of various anti-ferromagnetic and ferromagnetic crystals.

In free atomic states, every 3d electronic state has the same energy. In other words, their energy levels are degenerate. When the atom is placed in a cubic field, the orbital states of 3d electrons are split into two groups. One is the triply degenerate dε orbits, the spatial distributions of which are expressed by xy, yz or zx. The other is the doubly degenerate dγ orbits whose distributions are expressed by $2z^2 - x^2 - y^2$ and $x^2 - y^2$. Fig.-3.3 explains that the dε orbits extends to $\langle 110 \rangle$ directions, while the dγ orbits extend along the co-ordinate axes. In octahedral sites, the surrounding anions are found on the three co-ordinate axes, so the dγ orbits, which extend towards the anions, have a much higher energy than dε orbits, because of the electrostatic repulsion between anions and orbits. For tetrahedral sites dγ orbits are more stable than dε orbits (Fig-3.4).

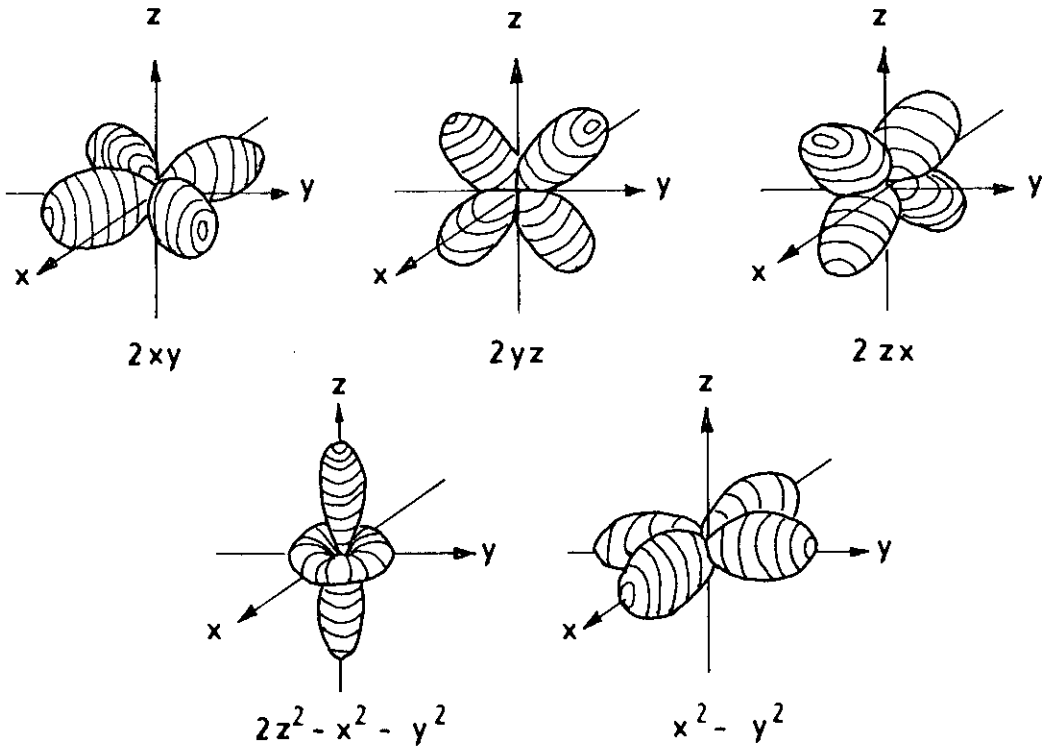

Fig-3.3. Spatial distribution of dε and dγ orbits

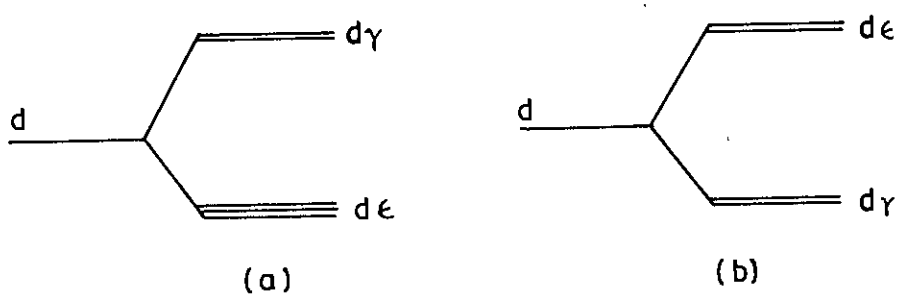

Fig-3.4 Energy levels of dε and dγ electrons in (a) octahedral and (b) tetrahedral sites.

Let us consider the case of the d electrons occupying the 3d energy levels. First let us assume that the magnetic ion only 3d electron. This electron will naturally occupy the lowest energy level. Now as the three dε levels have the same energy, the lowest orbital state is triply degenerate (triplet). Such an orbital degeneracy plays an important role in determining the magnetic anisotropy. If there are additional 3d electrons, they should occupy exclusively the plus spin levels, because the exchange interaction between these 3d electrons is much larger than the energy separation between the dγ and dε levels. In the case of $(3d)^3$, the three electrons occupy the three dε levels, so that the ground state is non-degenerate (singlet). For $(3d)^4$, three electrons occupy the dε levels and remaining one occupies one of the two dγ levels, thus the state is doubly degenerate (doublet). In the case of $(3d)^5$, all electrons occupy plus spin levels, so that the ground state is a singlet. When there are more than five electrons, first five fill up the plus spin levels while the remaining electrons occupy the minus spin levels in the same way as for the plus spin levels.

As for the Fe^{2+} ion, the sixth electron should occupy the lowest singlet state, so that the ground state is non-degenerate. On the other hand, the Co^{2+} ion has seven electrons, so that the last one should occupy the doublet. In such a case the orbit has the freedom to change its state in the plane which is normal to the trigonal axis, so that it has an angular momentum parallel to the trigonal axis. Now since the angular momentum is fixed in direction, it tends to align the spin magnetic moment parallel to the trigonal axis through the spin-orbit interaction. The energy of this interaction can be expressed as $-\lambda LS|\cos\theta|$, where λ is the spin-orbit parameter, L and S are the orbital and spin-angular momentum and θ is the angle between the magnetization and the trigonal axis. This model was first proposed by Slonczewski[3.44], who explained the magnetic annealing effect in Co ferrite by this model. He also explained the temperature dependence of the anisotropy constant of cobalt-substituted magnetite. In the normal, or non-magnetically annealed state, Co^{2+} ions should be distributed equally among the four kinds of octahedral sites each of which has its trigonal axis parallel to one of the four $\langle 111 \rangle$ directions, so that the cubic anisotropy can be obtained by averaging the anisotropy energy $-\lambda LS|\cos\theta_i|$ over four direction of trigonal axes.

If the ground orbital state is non-degenerate, we cannot expect any orbital angular momentum so long as the atom stays in the ground state; in other words, the orbital angular momentum is quenched by the crystalline field. In such a case we cannot expect an anisotropy as large as that of the Co^{2+} ion in an octahedral site. There are, however, various sources which result in a fairly small magnetic anisotropy, which is nevertheless sufficiently large to account for the observed values. Yosida and

Tachiki[3.45] calculated the various types of anisotropy and applied their results to the Mn, Fe and Ni ferrites, which contain Mn^{2+},Fe^{3+},$Fe^{2+}$and Ni^{2+} ions. Firstly, they found that the magnetic dipole-dipole interaction is too weak to account for the observed magnitude of anisotropy. The main source of anisotropy is thought to be the distortion of the 3d shell from spherical symmetry. In a distorted 3d shell the intra-atomic dipole-dipole interaction between the spin magnetic moments may depend on the direction of magnetization; this is similar to the dependence of the magneto static energy on the direction of magnetization in a fine elongated single domain particle, and gives rise to anisotropy energy.

The anisotropy is also induced through spin-orbit interaction. That is, some amount of orbital angular momentum can be induced by spin-orbit interaction by exciting additional orbital states. In a distorted 3d shell this excitation is dependent on the direction of magnetization, giving rise to anisotropy. Yosida and Tachiki showed that the anisotropy due to these mechanisms should vanish for $S = \frac{1}{2}, 1$ and $\frac{3}{2}$, where S is the total spin angular momentum, and that anisotropy of this type cannot be expected for Ni^{2+} and Co^{2+} ions. Accordingly, the main source of the anisotropy of Mn, Fe and Ni ferrites is considered to be the Mn^{2+},Fe^{3+} and Fe^{2+} ions. Since Ni^{2+} ion has no effect on the magnetic anisotropy in Ni ferrite, the difference in anisotropy energy between Fe and Ni ferrites must be explained by the anisotropy due to Fe^{2+} ions. Yosida and Tachiki also calculated the temperature dependence of the anisotropy constant for Mn ferrites and fitted the theory with experiment.

3.5.4. Theoretical Considerations for Uniaxial Magnetic Anisotropy in Amorphous Materials

Amorphous magnetic alloys because of their noncrystalline structure are expected to behave magnetically isotropic or to exhibit a low anisotropy. However in the case of ribbons produced by melt spinning technique intrinsic stresses are induced, which may cause a stress induced anisotropy. For most alloys a uniaxial anisotropy energy,

$$E_u = K_u \mathrm{Sin}^2\theta \text{ is observed,} \qquad (3.73)$$

where K_u is the magnetic anisotropy constant and θ is the angle between magnetization and the easy axis which is related to the direction of the stress. The magnitude of K_u depends on the degree of short-range order and the magnetic anisotropy per atom. In one-subnet work 3d based alloys, usually low anisotropies are

found originating primarily from the magnetostrictive coupling of the magnetization to the internal stresses[3.46] or due to pair ordering[3.47].

Pair ordering and dipolar interaction lead to a relation between K_u and the sublattice magnetizations that can be expressed in the form

$$K_u = \sum_{i \neq k} C_{ik} M_i M_k \qquad (3.74)$$

using the sublattice magnetizations inferred from the mean-field analysis, K_u is dependent on composition and temperature.

These anisotropies are associated with short-range pair ordering and interstitial or monoatomic ordering of the metalloids. The magnetostrictive effects in amorphous alloys originate from the magnetoelastic interactions associated with the local anisotropies and the local strains controlling the local direction of the magnetic moments. The origin of the local strains is discussed in terms of the Single-Ion model with random local axis[3.48-3.49]. These amorphous alloys are also susceptible to stress induced ordering as studied by Berry and Pritchet[3.50] using internal friction measurements. As in crystalline alloys, this ordering presumably occurs Via the interactions of the strain produced with the magnetostriction, indicating that the stress induced contribution

$$K_u^{\sigma} = -\frac{3}{2}\sigma\lambda_s \qquad (3.75)$$

where σ and λ_s denote the stress and saturation magnetostriction constants. It is thus concluded that stress induced directional ordering involves different atomic species or motions than those involved in magnetically induced ordering.

3.5.5. Exchange Anisotropy of Amorphous Materials

Evidence for ferromagnetic-antiferromagnetic "exchange anisotropy" has been found in the amorphous alloy by Sherwood et. al.[3.51]. Thus appears to be the first demonstrated example exchange anisotropy in an amorphous transition-metalloid alloy. This rises some interesting, and unanswered questions concerning the atomic arrangement necessary to develop this effect. The anisotropy in the TM-M alloys, and their type of magnetic ordering is determined by the exchange interaction and the strong single-ion anisotropy. The spins are coupled through the exchange interaction which can be one of the followings:

(i) direct exchange between itinerant 3d states.
(ii) indirect RKKY (Rudermann-Kittel-Kasuya-Yosida) exchange and
(iii) superexchange

The superexchange is a sensitive function of bond angle and bond length and therefore, can be very different in amorphous state compared to that in crystalline state. The substances is ferromagnetic in amorphous state, although it is antiferromagntic in crystalline phase[3.52]. The long-range nature of RKKY exchange is nearly washed out due to large reduction of the mean-free path of electron caused by both chemical and topological disorder[3.53]. The direct exchange is also short-range one and it is more so in disordered solids. In either of the causes, the coupling is described by Heisenberg model

$$H = -\sum_{ij} J(R_{ij}) S_i . S_j \qquad (3.76)$$

where $J(R_{ij})$ is the effective coupling and depends on the nearest neighbour distance R_{ij} As no two sites are equivalent in amorphous state R_{ij} is random resulting in a distribution of J . So a given spin couples with its nearest neighbours with varying magnitude of J and even with different sign of J also. If both positive and negative coupling with equal probability occure, the "frustration effect" appears[3.54]. The exchange is not isotropic, where superexchange predominates. The localized description of metallic glass is an approximation, nevertheless, like in crystalline system it provides an a qualitative understanding of magnetic phases.

3.5.6. Random Anisotropy Model of Amorphous Material

The simplest model Hamiltonian for an exchange coupled system with a fluctuating uniaxial anisotropy is given by

$$H = -\sum_{ij} J_{ij}(r_{ij}) S_i . S_j - \sum_i D_i (n_i . S_i)^2, \qquad (3.77)$$

where J_{ij} is the exchange integral between the spins S_i and S_j, D_i is the single ion anisotropy of the i-th ion , n is the unit vector defining local anisotropy at i-th sites. The easy axis direction varies randomly from site to site. Fluctuations of the anisotropy axes of an amorphous magnetic material lead to a non-linear magnetic structure. Alben et. al.[3.55] have shown that behaviour of an amorphous ferromagnet changes sharply

in ferromagnetically soft to magnetically hard material, when the anisotropy of the single-ion local anisotropy becomes comparable to the exchange interaction energy.

However, the calculation based on local anisotropy leads to values which are much lower than the experimental values. The reasons for this discrepancy lies in the technological factor introduced in the preparation process. Amorphous materials are therefore anisotropic on the macroscopic scale due to fluctuation of the composition and stress as caused by the preparation technique.

3.6. Mössbauer Spectroscopy Analysis of Amorphous Materials

Mössbauer spectroscopy yields information on the magnetic properties of individual atoms rather than on assemblies of atoms as in conventional magnetization measurements. Mössbauer spectroscopy is used for the identification of magnetic field distribution of magnetic atoms in amorphous ribbons by the evaluation of the collected spectra. This is a very useful technique for studying the hyperfine field distribution as affected by the nature and number of nearest magnetic neighbours in an amorphous alloy. As stated by Durand[3.56] the analysis of the data obtained for Fe-based amorphous alloys shows that iron atom needs as many as 6-8 nearest neighbouring iron atoms to assume a magnetic moment. Mössbauer spectroscopy has also been used to determine the average direction of magnetization by using the well known fact that for the ^{57}Fe, the intensities of the six lines of the hyperfine spectra have an area ratio 3:Z:1:1:Z:3, where $Z = 4/(1+\mathrm{Cot}^2\theta)$, θ being the angle between the direction of magnetic field at the nucleus and the direction of γ-ray emission[3.57]. In ^{57}Fe the strength of this magnetic field is H = 33T[3.58] at room temperature.

The value of Z varies from 0 for the axis magnetization in the sample plane to 4 for the axis of magnetization in the sample plane. Results by Chien and Hasegawa[3.59] indicated that the magnetization stayed nearly completely in the atoms of the ribbons for the as-prepared samples. The hyperfine field obtained from the Mössbauer spectra is assumed to be proportional to the magnetization compered to some amorphous ribbons. In order to determine the variation of the magnetic moment in iron, as well as to see how well the hyperfine field on iron nuclei is defined, we carried out Mössbauer effect studies on our samples. For the melt-spun samples, a "Cold-front" moves through the melt and solidifies the melt. Although this front is moving very fast at the quenching rate of about $10^{6}{}^{0}C/s$, the atoms retain a high mobility for a short while during which the alloys are prepared by the chemical reduction method. The atoms are probably reduced to singles at this time and are built on the top of already frozen atoms. These atoms may not rearrange easily.

3.6.1. Mössbauer Parameters

Nuclear transitions emit γ-radiations, which are not preceded by phonon transitions. These zero phonon γ-transitions take place between the excited and ground state nuclear energy levels of the nucleus which is bound in a solid matrix as reported

by Mössbauer[3.60]. Therefore, the nucleus is no longer isolated, but fixed with the lattice. In this situation the recoil energy may be less than the lowest quantized lattice vibrational energy and consequently the γ-ray energy may by emitted without any loss of energy due to the recoil of nucleus. This is known as the Mössbauer effect. The important parameters which can be measured using Mössbauer spectroscopy are described here.

The hyperfine parameters describe the interaction of the nucleus with the surrounding atomic electrons. These parameters give information about the nature of the chemical bonds, electric field gradient and magnetic ordering moments.

The Hamiltonian for the interaction between the nucleus and the surrounding changes may be written as[3.61]

$$H = E_0 + M_1 + E_2 + \ldots\ldots, \qquad (3.78)$$

where E_0 represents electric monopole coulombing interaction between nuclear charge and the electron clouds which affects the nuclear energy levels, M_1 refers to magnetic dipole interaction between the nuclear magnetic moment and the effective magnetic field at the nucleus and E_2 represents the electric quadrupole interaction between electric field gradient at the nucleus and the electric quadrupole moment of the nucleus. Higher order terms are usually very small and can be neglected.

3.6.1.1. Isomer Shift

Hyperfine interactions for the ^{57}Fe nucleus is shown in fig.-3.6. The Mössbauer transition energy will now be slightly different in the two materials and this will appears as a shift in the Mössbauer spectrum as shown in fig-3.6(a). This shift is known as the isomer shift (IS), and is proportional to the difference in the electron densities at the nuclear sites in the two materials. The IS measures the S-electron density at the nucleus. Experimentally, the IS is the shift of the centre of gravity of the spectrum from the zero velocity position. This effect was first observed by Kistner and Sunyar[3.62]. This shift of centre of gravity can be due to the isomer shift and second order Doppler shift. The second order Doppler shift arises due to the temperature difference between source and absorber.

The IS arises from the fact that a nucleus has a finite volume and S-electrons spend a fraction of their time inside the nuclear region. The nuclear charge thus

interacts electrostatically with the S-electron charge. As a result of this interaction the nuclear energy levels get shifted by a small amount, the shift depends upon the chemical environment. Although, we cannot measure this energy change directly, it is possible to compare values by means of a suitable reference which can be either the γ-ray source or another standard absorber. The observed range of IS is within an order of magnitude of the natural linewidth of the transition i.e. 10^{-8} to 10^{-9} ev.

Let us consider that the absorber and source lattice are different in chemical composition so that electronic wave functions at the nuclei differ in the two lattices. This would cause differential shifts in the energy of the γ-rays from the source nuclei and the absorber nuclei. This difference in the energy can be written as(3.63)

$$\begin{aligned} IS &= \Delta E_A - \Delta E_s \\ &= \left(\frac{2\pi}{5}\right) Ze^2 \left(R_{ex.}^2 - R_g^2\right) [\ |\psi(0)|_A^2 - |\psi(0)|_s^2\ ] \\ &= \left(\frac{4\pi}{5}\right) Ze^2 R^2 \left(\frac{dR}{R}\right) [\ |\psi(0)|_A^2 - |\psi(0)|_s^2\ ], \end{aligned} \qquad (3.79)$$

where $dR = R_{ex} - R_g$ and $R = \frac{R_{ex} + R_g}{2}$, here R_{ex} and R_g are the nuclear radii of the excited and ground states, R is the average charge radius and $|\psi(0)|_A$ and $|\psi(0)|_S$ refer to the electron densities at the nuclei of absorber and the source respectively.

The expression shows that the IS is the product of two parameters: (1) $\frac{dR}{R}$, a nuclear parameter and (2) $|\psi(0)|_A^2 - |\psi(0)|_s^2$, an atomic or chemical parameter. IS can be positive or negative, depending on whether $\frac{dR}{R}$ is positive or negative, and $|\psi(0)|_A^2 > |\psi(0)|_s^2$ or $|\psi(0)|_A^2 < |\psi(0)|_s^2$.

So far we have consider that only S-electrons posses non-vanishing wave functions at the nucleus(3.64). However, it is known that when relativistic effects are taken into account not only S but also $P_{1/2}$ electrons have a non-zero charge density at the nucleus. But its contribution to IS is negligible because $|\psi_{P_{1/2}}(0)|^2$ is small in the vicinity of the origin and secondly the occupancy of $P_{1/2}$ states of the atomic orbitals in the source and observer are identical; furthermore, the mutual screening of S and $P_{1/2}$ can also be neglected. Thus only the S-electrons have a finite density at the nucleus.

IS provides important information concerning the nature of the chemical bond because the outer electrons (valence electrons) would be most affected by changes in chemical surrounding and consequently the changes in the outer S electron densities would contribute most to IS. Using the IS data it is possible to derive information about the oxidation state and spin state of Mössbauer atom in different compounds. Let us consider iron as Mössbauer atom. Since their atomic configuration differ only by a d-electron which does not itself contribute noticeably to the charge density $|\psi(0)|^2$, the effect arises indirectly via the 3S-electrons. The electrostatic potential which they experience there depends on the screening effects of inner electrons. Thus adding a d-electron reduces the attractive coulomb potential and causes the 3S-electron wave function to expand, reducing its charge density at the nucleus. Thus increasing the d-electron density decreases the electronic charge density at the nucleus resulting in an increases in the IS. For ^{57}Fe, since (dR/R) is negative, it can be seen from eq^{n}(3.79) that increase in charge density $|\psi(0)|^2_A - |\psi(0)|^2_s$ at the nucleus reduces the IS.

There is a well defined range for IS for different oxidation states of an atom for high spin complexes. For of an atom, the IS relative to iron metal are 0.8 to 1.5mm/s for divalent iron and 0.2 to 0.5mm/s for trivalent iron(3.63-3.65). A large change in IS is observed when the co-ordination number changes from 6 to 4. IS for octahedral Fe^{3+} high spin complexes because in octahedral site co-ordination number is 6, whereas in tetrahedral site the co-ordination number is 4. As we known, increasing the sheered electrons at octahedral Fe^{3+} nucleus causing more IS at octahedral Fe^{3+} site than at tetrahedral Fe^{3+} site.

3.6.1.2. Electric Quadrupole Splitting

The interaction of the quadrupole moment of a nucleus with an electric field gradient (EFG) established at its site by the surrounding environment causes quadrupole splitting in nuclear levels(3.60-3.66). An oblate (flattened) nucleus has a negative quadrupole moment while a prolate (elongated) one has a positive moment. Nuclei whose spin is φ or $\frac{1}{2}$ are spherical symmetric and have zero quadrupole moment and thus the ground state of ^{57}Fe with $I = \frac{1}{2}$ does not exhibit quadrupole splitting.

The diagonalized EFG tensor at the nuclear sites is completely specified by the three components, viz., $\delta^2V/\delta x^2$, $\delta^2V/\delta y^2$ and $\delta^2V/\delta z^2$; denoted by V_{xx}, V_{yy} and V_{zz},

respectively, where V is the electrostatic potential. Further V_{zz} the principal component, is chosen to be EFG so that $|V_{zz}|>|V_{xx}|\geq|V_{yy}|$. On applying the constraint imposed by laplace eq$^{n}(\nabla^2 V=0)$, the number of independent components are reduced to two, which can be chosen as;

$$q=\frac{V_{zz}}{e} \text{ and } \eta=\frac{(V_{xx}-V_{yy})}{V_{zz}} \tag{3.80}$$

η is known as asymmetry parameter and can take values between 0 and 1; q is called the field gradient parameter. The Hamiltonian of the interaction between a nuclear quadrupole moment (eQ) and the EFG (eq) can be written as(3.60)

$$H=-\frac{e^2qQ}{4I(2I-1)}\left[3I_z^2-I(I+1)+\frac{\eta}{2}(I_+^2+I_-^2)\right], \tag{3.81}$$

where I_+ and I_- are the raising the lowering operators, respectively and I_z is Z component of nuclear spin. Eq^{n}(3.81) has tbe eigenvalues.

$$E=-\frac{e^2qQ}{4I(2I-1)}\left[3m_I^2-I(I+1)\right]\left[1+\frac{\eta^2}{3}\right]^{1/2}, \tag{3.82}$$

where $m_I = I, I-1, \ldots\ldots\ldots\ldots, -I$

In ^{57}Fe, the first excited level with $I=3/2$ splits into two sub-levels (corresponding to $m_I=\pm 3/2 \text{ and } \pm 1/2$) having the energy difference known as quadrupole splitting(3.63). m_I values are the components of the angular momentum along the Z-axis it is clear that the $m_I=\pm 1/2$ states lie at lower energy than the $m_I=\pm 3/2$ states. If the electric field gradients is positive in sign the effect is as shown in fig-3.6b, since the quadrupole split spectrum is symmetric about the centroid. For nuclei other than ^{57}Fe, involving spins greater than $I=3/2$, the quadrupole split spectrum is more complicated.

$$\Delta E=\frac{1}{2}e^2qQ=\frac{1}{2}eQV_{zz}, \tag{3.83}$$

If electric field is not axially symmetric i.e. $V_{xx}\neq V_{yy}\neq V_{zz}$ then the splitting involves the asymmetry parameter η.

$$E=\frac{1}{2}e^2qQ\left(1+\frac{\eta^2}{3}\right)^{1/2} \tag{3.84}$$

The transition $\pm 3/2 \rightarrow \pm 1/2$ is called π-component and the transition $\pm 1/2 \rightarrow \pm 1/2$ is referred to as the σ-components. For a particular orientation i.e.

$$\frac{I_\pi}{I_\sigma} = \frac{3(1+\mathrm{Cos}^2\theta)}{5-3\mathrm{Cos}^2\theta}, \qquad (3.85)$$

where θ is the angle between V_{zz} axis and the direction of emission of γ-rays.

The quantity e^2qQ or qQV_{zz} is usually called quadrupole coupling constant and the sign of this quantity gives the sign of quadrupole interaction. The sign of coupling constant can be determined by the following methods. First for single crystals the sign can be obtained by measuring doublet intensity ratio I_π/I_σ in the Mössbauer spectra recorded with different orientation with respect to γ-direction. Another method is based on magnetic field perturbation on the quadrupole split pattern[3.67-3.69]. In the presence of a strong magnetic field the quadrupole doublet lines $(\pm 3/2 \text{ and } \pm 1/2)$ further split into a triplet and a doublet. If the doublet lies at a higher energy than the triplet, e^2qQ is positive and if it lies at a lower energy, e^2qQ is negative.

Now in brief we describe here the origin of electric field gradient at the nucleus. In general, there are two fundamental sources which contribute to effective EFG at the nucleus.

(1) Charges on distant atoms or ions surrounding the Mössbauer atoms in noncubic symmetry constitute lattice contribution denoted by $(V_{aa})_{lat.}$. As a matter of fact, the Mössbauer atom distort in the presence of a non-cubic charge distribution of the surrounding crystal lattice in such a way as to amplify the lattice quadrupole interaction. The net lattice contribution can be written as $(1-\gamma_a)(V_{aa})_{lat.}$, where γ_a is sternheimer antishielding factor. $(1-\gamma_a)$ which has been estimated to be of the order of 10 for iron compounds.

(2) A non-spherically symmetric valence cell of the Mössbauer atoms gives rise to valence contribution. Sternheimer has shown that valence contribution to EFG $(V_{aa})_{val.}$ is also modified due to screening of the valence electrons from the nucleus by inner cell electrons and actual valence contribution can be written as $(1-R)(V_{aa})_{val.}$, where R is sternheimer shielding factor[3.70-72]. Thus the total effective EFG at the Mössbauer nucleus may be written as

$$V_{aa} = (1-\gamma_a)(V_{aa})_{lat.} + (1-R)(V_{aa})_{val.}. \qquad (3.86)$$

In case the legend environment around the iron has cubic symmetry,

$$(V_{aa})_{lat.} = (V_{aa})_{val.} = 0$$

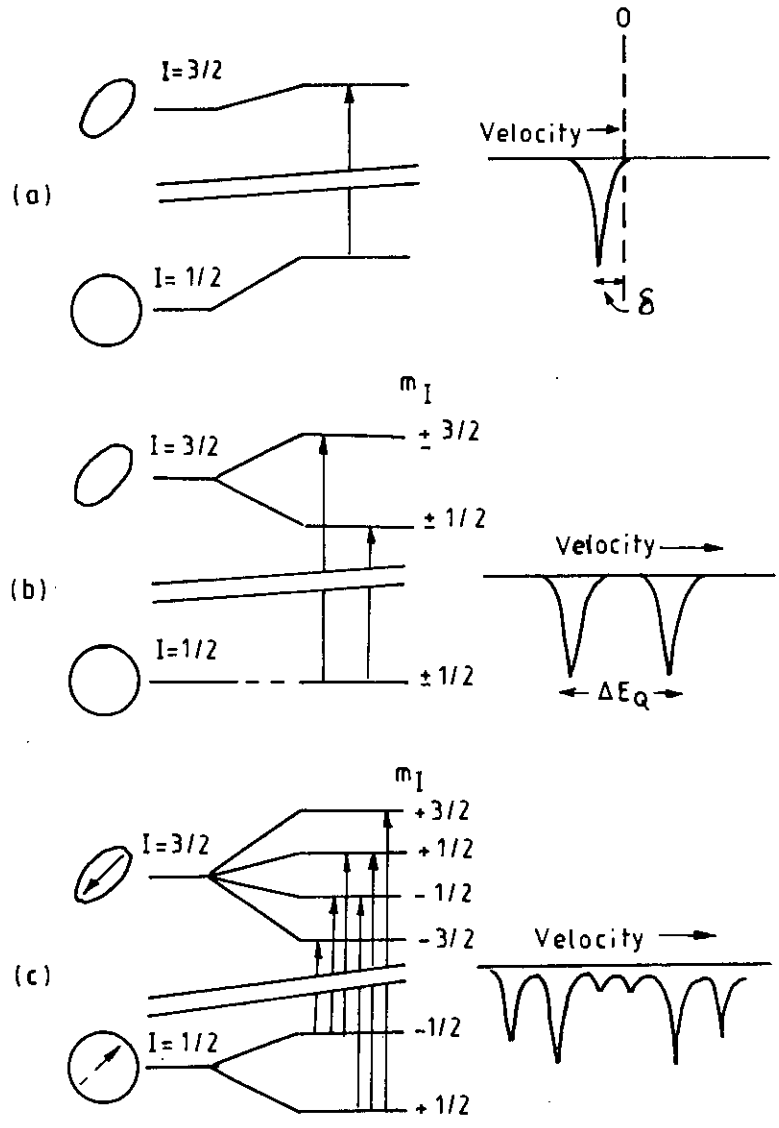

Fig-3.6. Hyperfine interactions for the ^{57}Fe nucleus. On the extreme left of each diagram are shown the unperturbed nuclear levels, the $I = \frac{3}{2}$ state being 14.4 KeV above the $I = \frac{1}{2}$ ground state. The effect of increasing the S-electron density at the nucleus is shown in (a). Relative to the hypothetical point charge nucleus, the energies of both states are increased, but the more voluminous ground state is affected most.

3.6.1.3. Magnetic Hyperfine Interaction

The interaction of the nuclear magnetic dipole moment μ with the magnetic field H at the nucleus gives rise to zeeman splitting of the nuclear levels with spins I (I >o) into (2I+1) sublevels. This field H may originate either within the atom itself or within the crystal by exchange interaction, or it may be an externally applied field. The Hamiltonian of the magnetic interaction is (3.60)

$$H_{\mu} = -\vec{\mu}.\vec{H} = -g\mu_N \vec{I}.\vec{H} \qquad (3.87)$$

where μ_N is the number magneton $\left(\frac{e\hbar}{2m_N C}\right)$, g is the nuclear g-factor and m_N is the mass of the nucleus.

The energy levels obtained as a consequence of the interaction are

$$E_m = \frac{-\mu_N H m_I}{I} = -g\mu_N H m_I \qquad (3.88)$$

where m_I is the magnetic quantum number representing the Z-component of I,

$$m_I = I, I-1, I-2, \ldots\ldots\ldots\ldots, -I$$

In the case of ^{57}Fe, according to selection rules $\Delta m = 0, \pm 1$, the possible allowed transitions are shown in fig-3.6(c). The relative line intensities in a spectrum containing magnetic spilt, six lines will be 3:Z:1:1:Z:3 where $Z = \frac{4}{1+\cot^2\theta}$, θ being the angle between the direction of magnetic field at the nucleus and the direction of γ-ray emission(3.57). In ^{57}Fe the strength of this magnetic field is H = 33KG at room temperature. The internal magnetic field at the nucleus has its origin from the spin and radial and angular distribution of the electron density in the atom. The magnetic field is given by(3.60-3.63)

$$H = -\frac{8}{3}n\mu_B \left|\psi_{\uparrow}(0)\right|^2 \vec{S} - 2\mu_B \left\langle \vec{l} \right\rangle \left\langle \frac{1}{r^3} \right\rangle - 2\mu_B \frac{\left\langle 3\left(\vec{r}.\vec{\Delta}\right)\vec{r} - r^2\vec{S} \right\rangle}{r^5}, \qquad (3.89)$$

where μ_B is Bohr magneton, S and l are operators for the spin and orbital moment of the electron and $\left|\psi_{\uparrow}(0)\right|^2$ is the electron density at the nucleus with +½ spin projection.

The first term in this expression is known as Fermi contact term which describes the contact magnetic interaction between the S-electrons and a nucleus. Only

S-electrons contribute to the Fermi contact term since the S-electron have a non-zero charge density at the nucleus. The field resulting from this source is very large compared to that from other sources. The Fermi contact field mainly arises from the polarization of the spins of paired S-electrons by the unpaired 3d electrons via exchange attraction that exists between electrons of like spins[3.73-3.75]. The inner core electrons (1S and 2S) produce a large negative field, whereas 3S and 4S electrons produce smaller positive fields resulting in a net negative field almost of the nuclei[3.76].

The second term in the above expression is known as orbital current field and it is produced due to an interaction of the unquenched orbital moment of electrons with the nuclear magnetic moment. The third term known as Dipolar field arises due to the dipole-dipole interactions operating between the electron spin and the nuclear magnetic moment.

For observing a well resolved Zeeman splitting in the Mössbauer spectrum, two conditions have to satisfied

$$\tau_0 > \tau_L \text{ and } \tau_S > \tau_L, \qquad (3.90)$$

where τ_0 is the life time of the nuclear excited state, τ_S is the electron spin correlation time and τ_L is the larmour precession time of the nucleus. The first conditions states that the Zeeman splitting must be larger than the natural line width. The second condition states the relationship between the spin correlation time and nuclear Larmour precession time. In paramagnetic systems the spin correlation time is so small, of the order of 10^{-12} to 10^{-14} sec, that during on Lamour precession, the electron of spin undergoes several fluctuations and hence the nuclei will not experience any hyperfine field to precess around and hence no magnetic splitting will be absorbed. In magnetically ordered systems, the strong exchange interaction helps to increase the spin correlation times, thus the direction of the hyperfine field is steady and the nucleus spin processes round it to lift the degeneracy of the nuclear levels yielding hyperfine split spectrum.

CHAPTER-4 EXPERIMENTAL DETAILS

4.6.5. The High Temperature Oven
4.6.6. Calibration of the Torque Magnetometer
4.7.0. Experimental Procedure for Mössbauer Spectrometer
4.7.1. Instrumentation
4.7.2. Velocity Drive System
4.7.3. γ-Source
4.7.4. Detection System
4.7.5. Pre-amplifier and Amplifier
4.7.6. Single Channel Analyser
4.7.7. Data Storage System
4.7.8. Description of the Workdone
4.7.9. Calibration of ^{57}Fe absorber sample for measurement of Mössbauer parameters
4.7.10. Computer Analysis of the Data

4.1. The Differential Thermal Analysis

4.1.1. Introduction

The differential thermal analysis (DTA) is an important technique for studying the structural change occurring both in solid and liquid materials under heat treatment. These changes may be due to dehydration, transition from one crystalline variety to another, destruction of crystalline lattice, oxidation, decomposition etc. The principle of DTA consists of measuring the heat changes associated with the physical or chemical changes that occur when a standard substance is gradually heated. This technique can also be used to identify magnetic ordering of amorphous ribbons. In order to discuss the possible applications of DTA in amorphous materials, we briefly define the various temperatures, that are useful in characterizing an amorphous alloy.

The glass transition temperature T_g is defined as the temperature at which the alloy passes from the "Solid" to the "Liquid" state. For our purposes, it is sufficient to describe T_g as the temperature at which atomic mobility is great enough to allow diffusive atomic rearrangement to occur in a matter of minutes. The crystallization temperature T_x defined as the temperature at which crystallization occurs with long range ordering and is usually determined by DTA technique by a heating rate of $\approx 10^0 C$ / min. Metallic glass ribbons usually are ductile in the "as-quenched" condition, but may often be embrittled by exposure to elevated temperature. The DTA technique has been used in determining T_g and T_x of our amorphous ribbons with composition $Fe_{90-x}Si_xB_{10}$ [x = 6, 8, 10, 12 and 14], $Ni_{80-x}Fe_xB_{20}$ [x = 20, 30, 40 and 50] and $Co_{80-x}Fe_xSi_{10}B_{10}$ [x = 0, 2, 4, 6 and 8].

4.1.2. The principle of Differential Thermal Analysis

The DTA technique was first suggested by Le Chatelier[4.1] in 1887 and was applied to the study of clays and ceramics. DTA is the process of accurately measuring the difference in the temperature between a thermocouple embedded in a sample and a thermocouple in a standard inert material such as aluminium oxide, while both are being heated at the uniform rate. The difference of temperature is measured that arise due to the phase transition or chemical reactions in the sample involving the evolution of heat or absorption of heat due to exothermic reaction or endothermic reaction. The exothermic and endothermic reactions are generally shown in the DTA trace as positive

and negative deviations respectively from the base line. DTA curves indicate a continuos thermal record of reactions occurring in a sample.

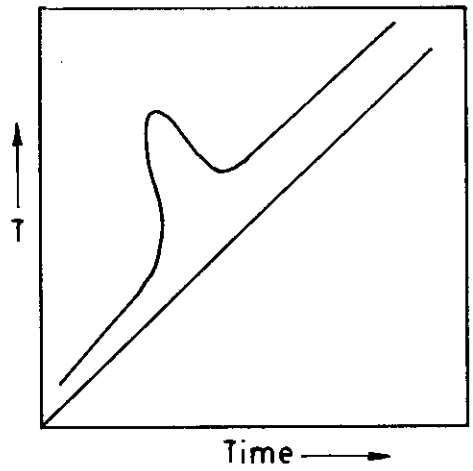

Fig-4.1(a) Heating curve of sample and reference substance

When a sample and reference substance are heated or cooled at a constant rate under identical environment, their temperature difference are measured as a function of time and temperature as shown in fig-4.1(a). The temperature of the reference substance, which is thermally inactive rises uniformly when heated while the temperature of the sample under study changes anomalously when there is a physical or a chemical change in it at a particular temperature. For an exothermic reaction there is a peak in the temperature versus time curve due to the additional heat supplied by the specimen accompanied by the reaction. When the reaction is over the sample temperature gradually catch up the temperature of the inactive specimen. The temperature difference ΔT is detected, amplified and recorded by a peak as shown in fig-4.1(b).

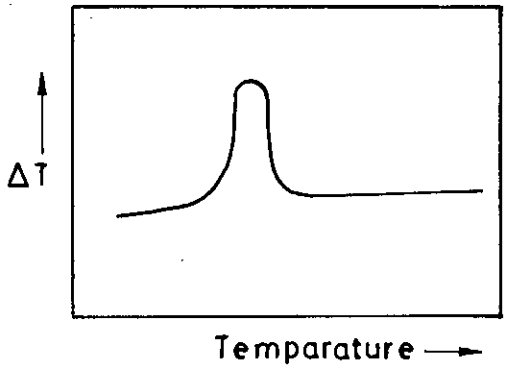

Fig-4.1(b) DTA curve

For any endothermic reaction or change the active specimen absorbs heat which is reflected in the corresponding trough in temperature versus time curve. The temperature in the sample holder is measured by a thermocouple, the signal of which is compensated for the ambient temperature and fed to the temperature controller. This signal is compared with the program signal and the voltage impressed to the furnace is adjusted. Thus the sample and reference substance are heated or cooled at a desired rate. The temperature in the sample holder is digitally displayed on the DT-30 and is also recorded on the recorder.

4.1.3. Apparatus

The apparatus for the differential thermal analysis consists of a thin walled refractory specimen holder made of sintered alumina with two adjacent cubical compartments of exactly the same size, 1cm in length, as shown in fig-4.2. Of these one is for the inert reference material and the other for the test material. The compartments are separated by a 1mm wall. The specimen holder is placed in the cavity of the heating block which is operated in the centre of the cylindrical refractory tube of an electrical furnace. This supplies a uniform heating rate. The furnace (9″X6″X9″ deep) is peaked with calcined china clay. The input of current into the furnace is secured through the secondary of a Variac transformer, which controls the current. Fine chromelalumel wires (28 gauge) are used for thermocouples. A cold junction is used for thermocouple leads and the e.m.f. is recorded almost continuously, while the temperature of the inert material is measured at 3 minute intervals. It is essential to use perfectly dry materials, as otherwise errors will be introduced in the analysis. Approximately 0.1gm anhydrous alumina is used in the reference cup and the sample weights varies over a range 0.05 to 0.125gm; depending on their density. A heating rate of 10^0c per minute of the furnace is conveniently choosen, and this gives satisfactory results in most cases. A block diagram of DTA as shown in fig-4.3.

The thermal analysis runs generally for 1 to 1.5 hrs. Thermal analysis curves are obtained by plotting heating temperature and the difference between the temperatures of the test and reference substances. From these plots the reaction temperature could be determined. Under standard conditions of the experiment; characteristic curves for different compositions of Ni-based, Fe-based and Co-based amorphous ribbons. T_g and T_x points are indicated, by sharp exothermic peaks.

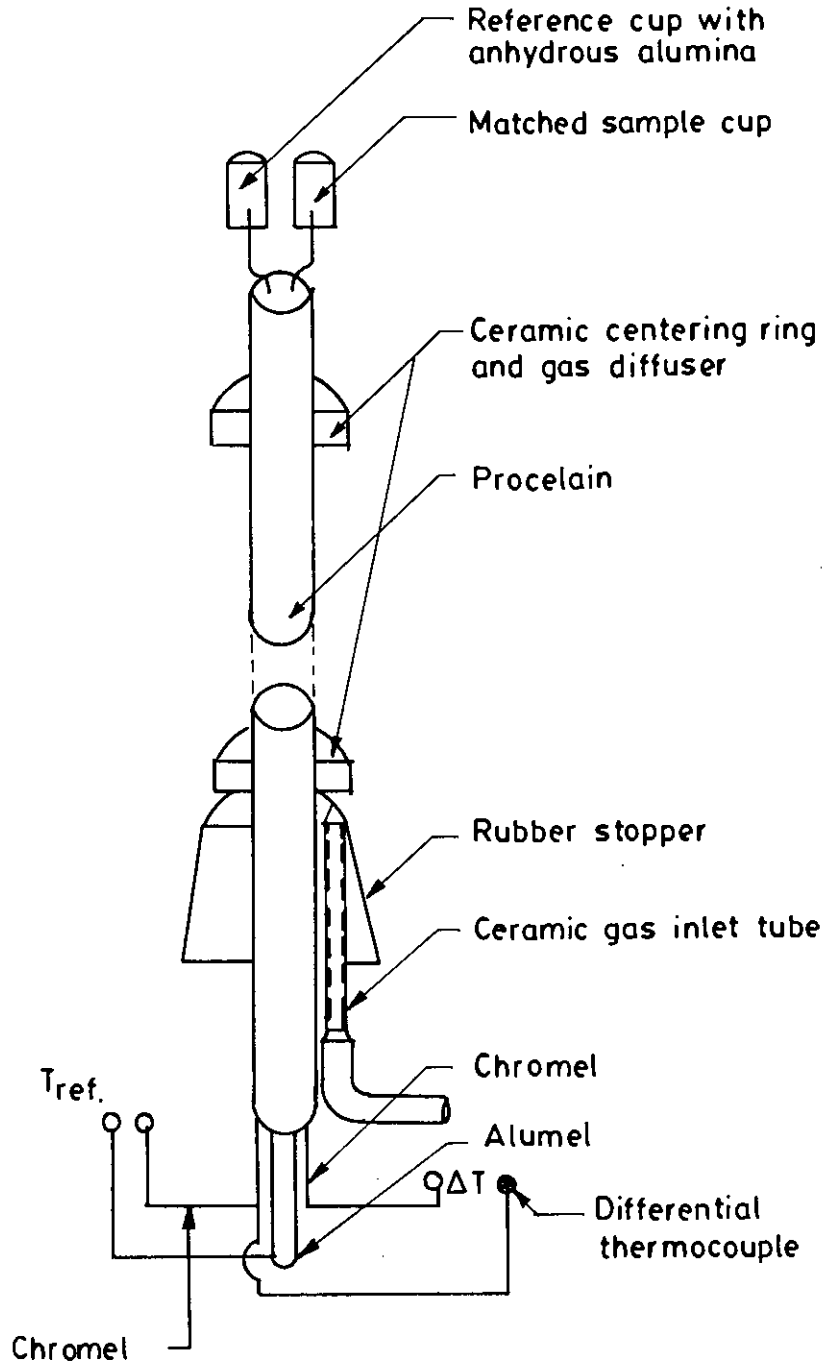

Fig.-4.2. DTA Thermocouple assembly

All experiments are run at atmospheric pressure in continuous flow of a purified inert gas argon. Gausses are normally purged into the furnace chamber at the lower end through a purification train in which oxygen and water are removed by heated copper wool and exhausted from the top into a condensate trap for collecting the condensable volatile products.

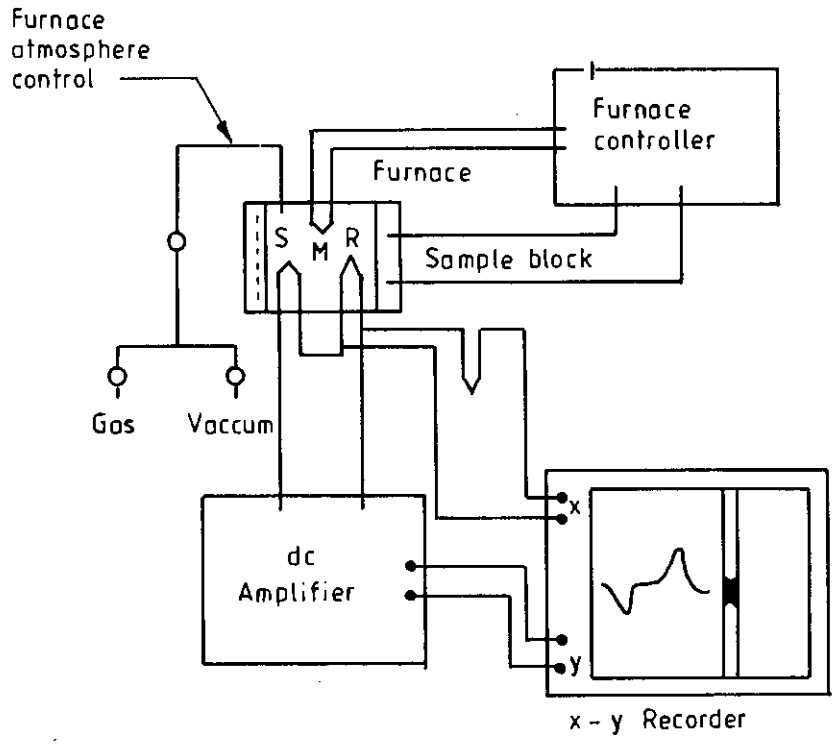

Fig.-4.3. Block diagram of a differential analysis equipment, (S) sample thermocouple, (R) reference thermocouple, (M) monitor thermocouple.

4.2. Curie temperature determination from temperature dependence of A.C. permeability.

The Curie temperature which is measure of exchange interaction between the magnetic atoms is quite complicated in the case of amorphous alloys and is very much an experimental parameter. Because, theories are helpful only as a guide in rationalising the results obtained experimentally. So, the determination of Curie temperature (T_c) accurately is of great importance.

Our experimental set up for T_c measurement is shown in fig.-4.4. we made use of the excellent experimental facilities available at Magnetic Material Division, AECD. The temperature dependence of A.C. permeability was measured by using induction method. A laboratory built technique using an oven in which a heating wire is wound bifillerly and two identical induction coils are wound in opposite directions such that the current induced flux in the two coils cancel each other. The whole set up is introduced in an oven. By varying temperature, A.C. permeability of the amorphous samples of toroidal shapes as a function of temperature was measured. When the magnetic state inside the amorphous sample changes from ferromagnetic to paramagnetic, the permeability falls sharply. From the sharp fall at specific temperature the T_c is determined. This is the basic principle used in our experimental set up.

As shown in the fig.-4.4, the circuit consists of two parts. The primary part consists of a low frequency generator, a multimeter and a resistance in series. The signal generator generates an alternating signal of frequency up to 200KHz. A voltage drop occurs at the resistance of value 390 ohm. This voltage drop is measured by the voltmeter. The secondary part of the coil comprises of only voltmeter. The voltage induced in the secondary coil is measured by the voltmeter.

An A.C. current i flowing through the primary of the toriodal ring shape sample produces a magnetizing field. The dynamic field H within the primary is given by the relation

$$H = \frac{0.4 N_1 i\sqrt{2}}{\bar{d}}, \qquad (4.1)$$

where N_1 is the total number of turns in the primary of the toriodal ring and $\bar{d}$ is given by

$$\bar{d} = \frac{d_1 + d_2}{2}$$

where d_1 and d_2 are the inner and outer diameter of the toroidal sample. Magnetic induction B calculated from the relation

$$B = \frac{E \times 10^8}{4N_2 fS}, \tag{4.2}$$

where N_2 is the number of turns in the secondary of the toroidal rings, f is the frequency of the balance the differential flux area of the cross-section of the toroidal ring is given by $S = dh$ where $d = \frac{d_2 - d_1}{2}$ and h is the height of the toroidal sample. Finally permeability is measured by the relation

$$\mu = \frac{B}{H} = \frac{E.\bar{d} \times 10^8}{4fN_1N_2S \times 0.4i\sqrt{2}} \tag{4.3}$$

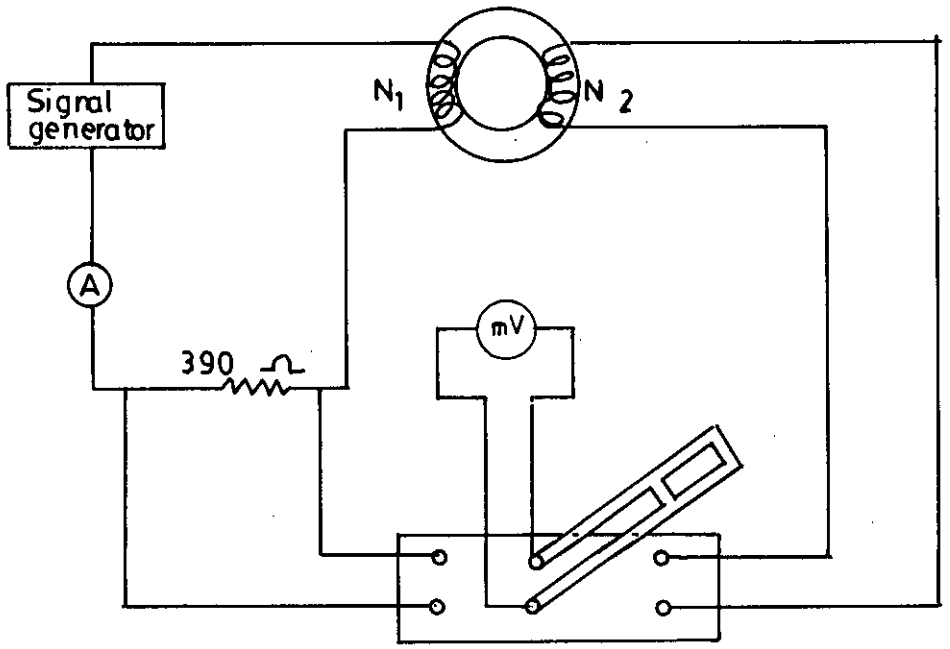

Fig.-4.4. Schematic diagram for the experimental set up for determination of Curie temperature.

At first we wind wires in the toriadal sample to make primary and secondary coils. The number of turns in each coil is 10. The sample thus wound is kept in a little oven with a thermocouple placed at the middle. The thermocouple measures the temperature inside the oven and also the sample. The sample is kept just in the middle part of the cylindrical oven so that gradient is minimized. The temperature of the oven is raised slowly. If the heating rate is very fast then temperature of the sample may not follow the temperature inside the oven and there can be misleading information on the temperature of sample. The thermocouple showing the temperature in that case will be erroneous. Due to the closed winding wires the sample may not receive the heat at once. So, a slow heating rate is used to eliminate this problem. Also heating adjustment of amorphous sample ensures accuracy in the determination of T_c. The oven was kept thermally insulated from the surroundings.

4.3.0. Determination of maximum permeability, maximum induction, Coercive force and Remanence

4.3.1. Ballistic technique

The ribbons were wound into the toriodal cores having 13 to 15mm outer diameter and 10mm inner diameter. Static magnetic properties were measured using the Ballistic method. The saturation magnetic induction (B_s), remanence (B_r), the ratio B_r/B_s and coercive force (H_c) have been determined for the as-cast ribbons from the experimental hysteresis loops. The toriodal ring shaped specimens were magnetized, so that no free poles are developed and the demagnetizing field is zero. Experimental circuit diagram is shown in fig-4.5.

A current I flowing through the primary of the toriodal core produces a magnetizing field H within the primary of the toriodal ring. This field is given by the relation

$$H = \frac{0.4 N_1 I}{\bar{d}}, \qquad (4.4)$$

where N_1 is the total number of turns in the primary of the toriodal ring, $\bar{d}$ is the average diameter of the toriodal ring and is given by $\bar{d} = \frac{d_1 + d_2}{2}$, where d_1 and d_2 are the inner and outer diameter of the toroidal sample.

To determine the ballistic galvanometer constant C_Ψ, a standard solenoid is used and is given by the formula

$$C_\Psi = \frac{0.8\pi N_1' N_2'' Si}{l\alpha} \qquad (4.5)$$

$$= 60.37,$$

where the number of turns in the primary of the solenoid N_1' is 500, the number of turns in the secondary of the solenoid N_2'' is 1700, length of the solenoid l is 89cm, diameter of the solenoid d is 3.9cm, area of cross-section of the solenoid S is $\pi d^2/4$ and a current of 10mA through the primary of the solenoid (i = 10mA) produces a galvanometer deflection α = 47 division. B is calculated by the relation

$$B = \frac{\alpha'}{2N_2 A} C_\Psi, \qquad (4.6)$$

where α' is deflection in the ballistic galvanometer for different values of the current and N_2 is the total number of turns in the secondary of the toriodal ring. Due to sudden change in induction in the primary flux is linked with the secondary the galvanometer

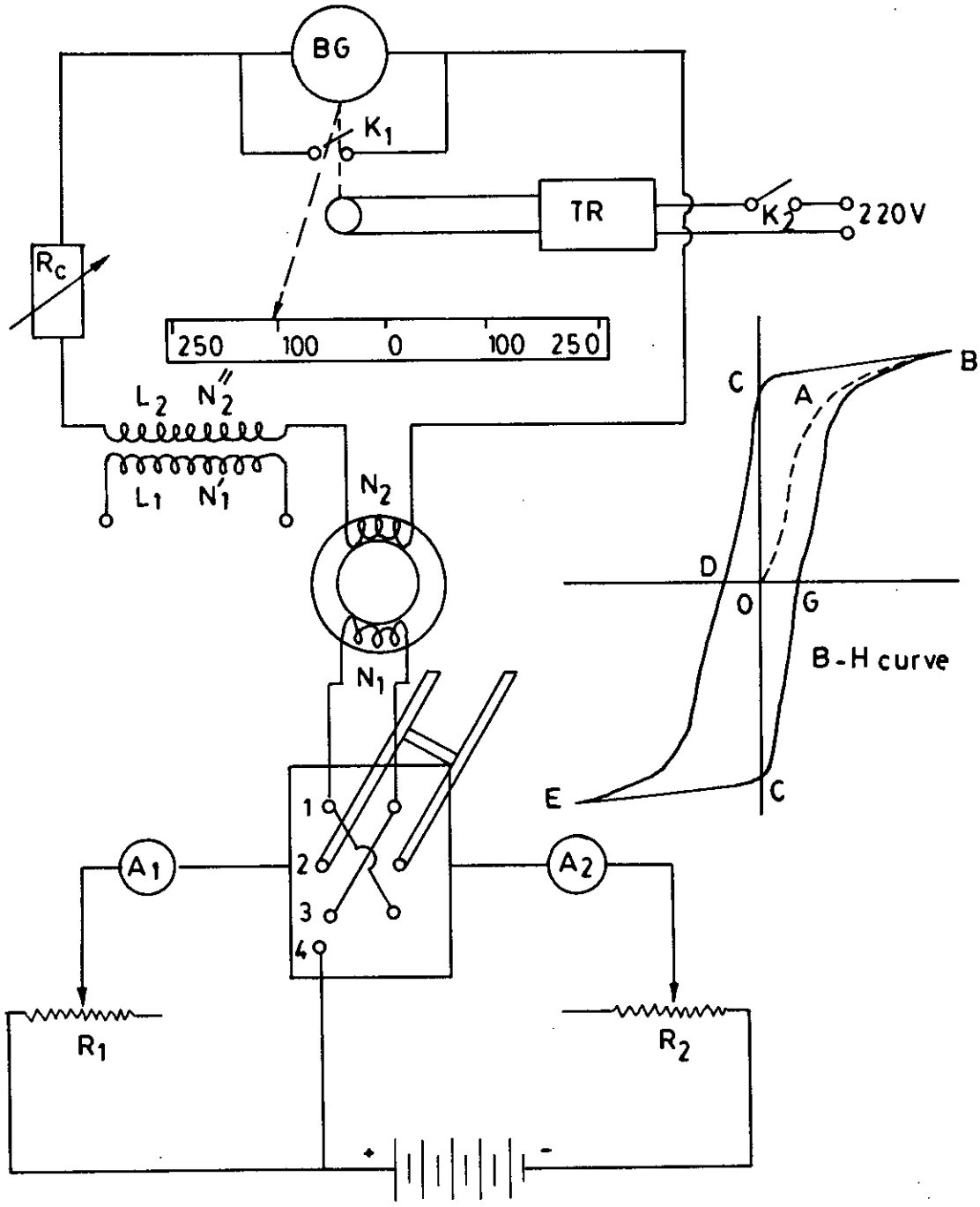

Fig.-4.5. Experimental circuit diagram for B-H curve measurement.

records a deflection, the magnitude of which is proportional to the change in induction in the primary.

$$\Delta B = \frac{\Delta \alpha}{2N_2 A} C_\Psi \qquad (4.7)$$

The operation is repeated with increasing value of the resistance R_2, so that each new current is less then its previous value. The current and the corresponding galvanometer deflection for each new operation is noted. The zero current point is reached in this way at the remanence point. B and H for each value of the current is determined by

$$B = B_{max.} - \Delta B \qquad (4.8)$$

The cross-conducting strip of the commutator is the removed and the resistance to the commutator is shown in circuit diagram-4.5. The experiment is repeated with decreasing values of R_2 until the current reaches the maximum negative value giving the coercive force from the intersection of the CDE curve with the field axis. The remanence and the coercive force are thus determined from the B-H loop trace. The maximum permeability and the maximum induction are determined from the initial magnetization curve.

The important magnetic parameters that characterize ribbons of various compositions $Fe_{90-x}Si_x B_{10}$, $Ni_{80-x}Fe_xB_{20}$ and $Co_{80-x}Fe_xB_{10}Si_{10}$ are determined by using the B-H loop tracing technique.

4.4.0. Experimental Techniques for Measuring Complex Permeability

4.4.1. Real and Imaginary Components of Complex Permeability

Determinations of permeability normally involve the measurements of the change in self inductance of a coil in the presence of the magnetic core. The behaviour of a self inductance can now be described as follows. If we have an ideal lossless air coil of inductance L_0, on insertion of magnetic core with permeability μ, the inductance will become μL_0. The complex impedance Z of this coil can then be expressed as

$$\begin{aligned} Z &= R + iX = i\varpi L_0 \mu \\ &= i\varpi L_0 (\mu' - i\mu''), \end{aligned} \qquad (4.9)$$

where the resistive part is

$$R = \varpi L_0 \mu'' \qquad (4.10)$$

and the reactive part is

$$X = \varpi L_0 \mu' \qquad (4.11)$$

The r.f. permeability can be derived from the complex impedance of a coil in eq^{n}(4.9). The core is taken in the toroidal form to avoid demagnetizating effects. The quantity L_0 is derived geometrically as shown in section-4.4.3.

4.4.2. Preparation of the samples for permeability measurements

The amorphous ribbons were wound into toroidal cores having outer and inner diameters within 13 to 15mm and with the ratio of outer and inner diameter always kept less than 1.2 in order to improve the homogeneity of the applied field, as also to reduce the possibility of an inhomogeneous inductance response. A low capacitance coil with 8 to 10 turns was wound around the toroids to allow the application of magnetic fields over a wide range of amplitudes. While measuring the permeability of the amorphous ribbon cores at high frequency, the high electric resistance of these materials generally precludes the trouble some skine effect found with ribbons. However, the cross section of the amorphous ribbon core to be measured may have to be kept small in order to avoid dimensional resonance phenomena. To avoid an increase in resistance owing to skin effect, braided copper wire is used at frequencies higher than 100KHz. The thickness of the separate wire stands being adapted in the measuring

frequency of up to about 13MHz. The thumb rule is that, the wire thickness in microns must be smaller than the wavelength in meters.

At higher frequencies the capacitance arising from the winding gives inaccurate values R and L_s. It is, therefore, necessary to keep the capacitance of the winding as low as possible. Frequency response characteristics were then investigated on these ring shaped specimens as a function of frequency.

4.4.3. Frequency Characteristics of Amorphous Materials

The frequency characteristics of the amorphous ribbon samples, i.e. the permeability spectra, were investigated using an Hewlett Packart Impedance Analyzer of model No.-4192ALF. The measurement of inductances were taken in the frequency range 0.5KHz to 13MHz. The values of measured parameters obtained as a function of frequency and the real and imaginary parts of permeability and the loss factor. μ' is calculated by using the following formula

$$L_s = L_0\mu' \text{ or } \mu' = \frac{L_s}{L_o} \qquad (4.12)$$

and

$$\tan\delta = \frac{\mu''}{\mu'} \text{ or } \mu'' = \mu'\tan\delta, \qquad (4.13)$$

where L_s is the self-inductance of the sample core and

$$L_0 = \frac{\mu_0 N^2 S}{\bar{d}}, \qquad (4.14)$$

where L_0 is the inductance of the winding coil without the sample core and N in the number of turns of coil (here N=8), S is the area of cross-section as given bellow

$$S = dh \text{ where } d = \frac{d_2 - d_1}{2}, \text{ and h= height}$$

and $\bar{d}$ is the mean diameter of the sample given as follows

$$\bar{d} = \frac{d_1 + d_2}{2}$$

The relative quality factor is determined for the ratio $\mu_i/\tan\delta$.

4.5.0. Experimental set-up for Measurements of Magentization

4.5.1. The Principle of Vibrating Sample Magnetometer

All magnetization measurements have been made on EG and G Princeton Applied Research Co. make vibrating sample magnetometer (V.S.M.)[4.2-4.3]. The principle of V.S.M. is as follows: when the sample of a magnetic material is placed in a uniform magnetic field, a dipole moment proportional to the product of the sample susceptibility times the applied field is induced in the sample. If the sample is made to undergo a sinusoidal motion, an electrical signal is induced in suitably located stationary pick-up coils. This signal which is at the vibrating frequency, is proportional to the magnetic moment, vibration amplitude and vibration frequency. In order to obtain the reading of the moment only, a capacitor is made to generate another signal for comparison which varies in its moment, vibration amplitudes and vibration frequency in the same manner as does the signal from the pick-up coil. These two signals are applied to the two inputs of a differential amplifier, and because the differential amplifier passes only difference between the two signals, the effect of vibration amplitude and frequency changes are cancelled. Thus only the moment determines the amplitude of the signal at the output of the differential amplifier. This signal is in turn applied to a Lock-in amplifier, where it is compared with the reference signal which is at its internal oscillator frequency and is also applied to the transducer which oscillates the sample rod. Thus the output of the Lock-in amplifier is proportional to the magnetic moment of the sample only avoiding any noise of frequency other that of the signal. The Lock-in action yields an accuracy of 0.05% of full scale. The absolute accuracy of this system is better than 2% and reproducibility is better than 1%. Least measurable moment is 5×10^{-4} emu.

Variable magnetic field is achieved with a Newport Electromagnet Typen 177 with 17.7cm diameter pole pieces. The magnet is mounted on a graduated rotating base. The standard model is modified to provided an adjustable pole gap in order that the highest possible field strength is available. The field can be varied from 0 to 9KG. The field is measured directly by using Hall probe.

4.5.2. Mechanical Design of the V.S.M.

The various mechanical parts of the magnetometer are shown in detail in the fig.-4.6. The base B of the V.S.M. is a circular brass plate of 8mm thickness and 250mm diameter. A brass tube T of 25mm outer diameter and 0.5mm thickness runs normally through the base such that the axis of the tube and the centre of the plate coincide. The base and the tube are joined together by soft solder. The tube extends 60mm upward and 24mm downward from the base. There is a vacuum port on the lower part of the tube 120mm below

Electrical connections from the audio amplifier to the speaker and from the reference coil system to the phase-shifter are taken via the perspex feed-through. By connecting the vacuum port of the tube T to a vacuum pump the sample environment can be changed. The speaker SP is fitted 25mm above the tube T with the help of our brass stands. The lower ends of stands are screwed to the base plate while the rim of the speaker is screwed on the tops of the stands. The speaker has a circular hole of 10mm diameter along the axis of it. An aluminium disc having female threads in it is fitted to the paper cone with araldite. The aluminium connector having male threads on it and attached to the drive rod assembly fits in the aluminium disc and thus the drive rod assembly is coupled to the speaker. The drive rod assembly consists of two detachable parts which are joined together by means of aluminium threaded connectors. Each part is a thin Pyrex glass tubing of 4mm diameter. The upper part has a small permanent magnet P situated 100mm below the aluminium connector attached to it. At the lower end of the drive rod assembly a perspex sample holder having quite thin wall can be fitted tightly with the sample in it. A few perspex spears are also attached to the driver rod throughout its length. The spacers guide the vibration of the sample only in the vertical direction and stops sidewise vibration or motion. The total length of the drive rod assembly is 920mm up to base. The lower end of the tube T is joined to a brass extension tube L by a threaded coupling and an o'ring seal. Another thin tube K made of german silver and of 8mm inner diameter runs through the extension tube L from the compiling point C to about 50mm below the sample position. Above the base there is a hollow brass cylinder M of 180mm length and 130mm inner diameter, having 40mm wide collars at its both ends. The lower collar seats on an o'ring seal which is situated in a circular groove in the base plate. On the upper collar, there rests an aluminium top N with an o'ring seal. The brass cylinder M has a side port VP. This is again a brass tube of 41mm diameter and 43mm length. The port has a collar at the end away from the cylinder. A perspex vacuum feed-through is fitted at its end with o'ring seal. This port is connected to the cylinder by soft solder.

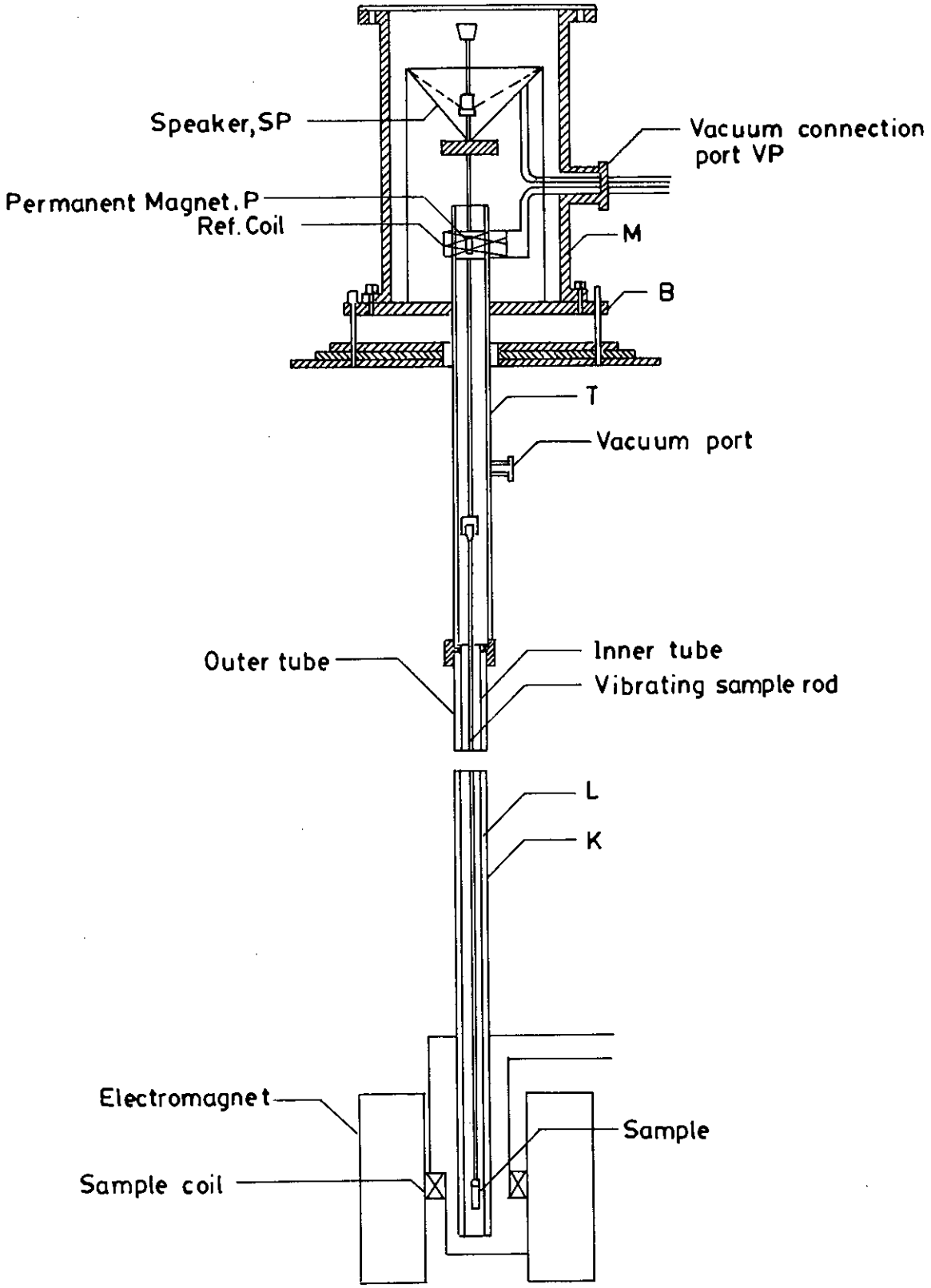

Fig.-4.6. Mechanical construction of the vibrating sample magnetometer.

The base plate of the V.S.M. rests on three levelling screws above a brass frame which in turn rests on an iron angle bridge. The bridge is rigidly fitted to the sidewall of the room. The brass frame is provided with arrangements with the help of which it can be moved in two perpendicular directions in the horizontal plane.

The levelling screws are used to make the drive rod vertical and to put the sample at the centre of the pole-gap between the sample coils. The sample can also be moved up and down by the levelling screws.

4.5.3. Electronic Circuits of the V.S.M.

The function of the associated electronic circuits are:

(i) To permit accurate calibration of the signal output obtained from the detection coils.

(ii) To produce a convenient AC output signal which is directly related to the input and which can be recorded.

(iii) To produce sufficient amplification for high sensitivity operation.

The block diagram of the electronic circuit used for the V.S.M. consists of a mechanical vibrator, a sine wave generator, an audio amplifier, a ratio transformer, a phase-shifter, a Lock-in amplifier, a pick-up coil system, a reference coil system and an electromagnet as shown in fig.-4.7.

The sample magnetized by the electromagnet generates an e.m.f. in the pick-up coils PC. The strength of this signal is proportional to the magnetization of the sample. The vibrating permanent magnet also generates an e.m.f. of fixed amplitude in the surrounding reference coils. This reference signal is stepped down with the help of a ratio transformer so that its amplitude is equal to that the sample signal. The two signals are then brought in phase and put to the Lock-in amplifier.

The Lock-in amplifier works as a null dector. The ratio transformer reading is to be calibrated using spherical shape sample S of 99.99% pure nickel.

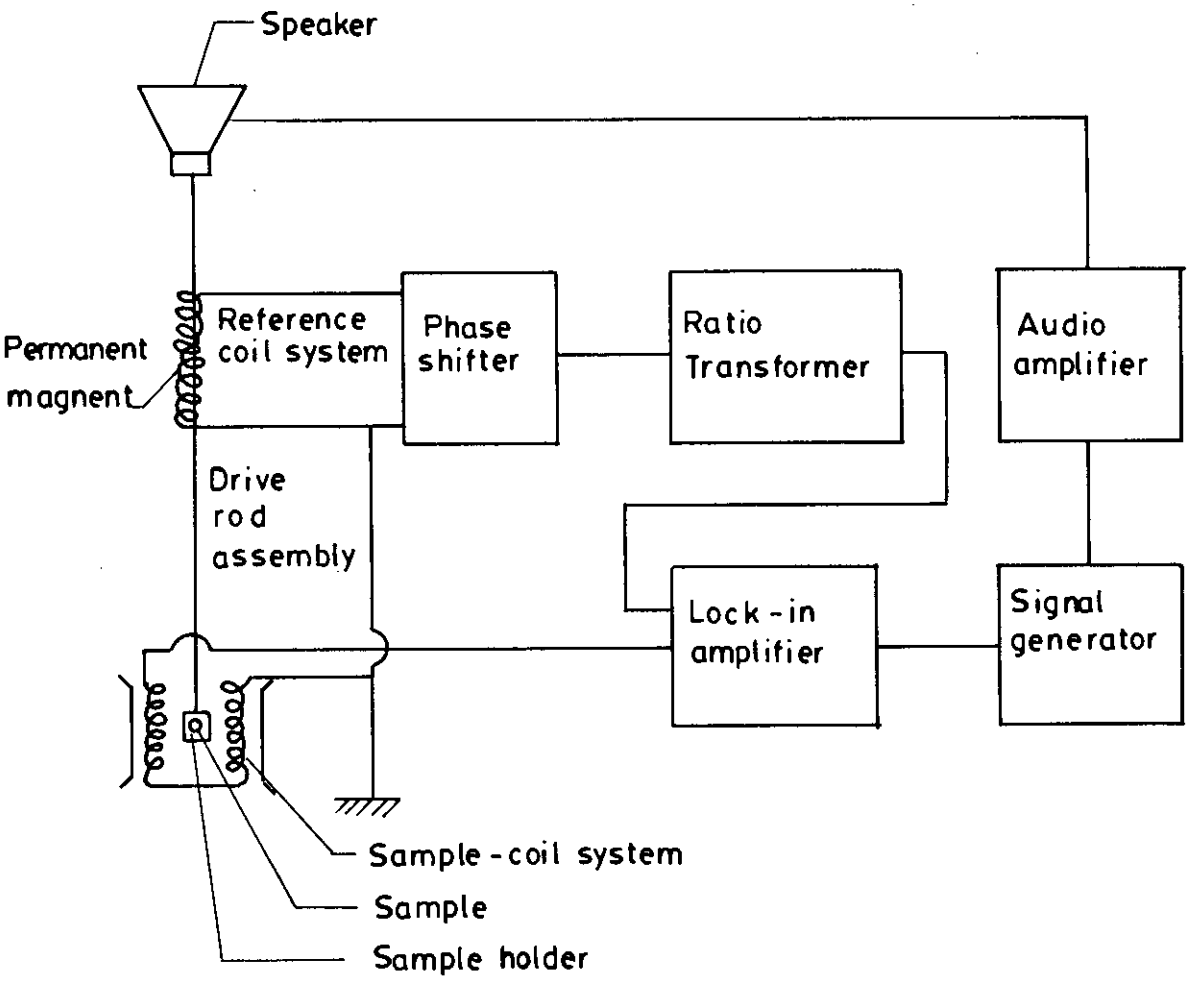

Fig.-4.7. Schematic diagram of the electronic system of the V.S.M.

4.5.3.1. Sensitivity limits

Limits of sensitivity are determined by signal to noise ratio at the input circuit, where noise is defined as any signal not arising from the magnetic moment of the sample. The major sources of noise are the Johnson noise of the wire used for the pick-up coils, and the magnetic responses of the sample holder, which superimposes undesired signals in phase with the wanted signal. Use of a minimum mass of weakly diamagnetic material for a sample holder, carefully checked to contain no ferromagnetic impurities, is essential to minimize this coherent noise contribution. Corrections for the small magnetic contribution of the sample holder can then be made by measurements with the sample removed. This correction is much less then the equivalent case with a moving coil system.

Our standard sample used for calibration was spherical shaped specimens of mass 0.0584gm. The different field susceptibility $\Delta x \cong 5 \times 10^{-10}$ could be observed after synchronous phase detection with band width $\cong 2 \times 10^{-2}$ cps. The other tests used was small current at 81Hz or an alternating current 81Hz passed through the coil which remained stationary.

4.5.3.2. Stability Tests Differential Measurements

With only the Lock-in amplifier and the oscilloscope as a null detector, it was found that the 0.0584gm Ni-sample signal could be balanced reproducibly. Such reproducibility indicated that the long time drifts caused by the combined effects of vibration, amplitude changes and frequency changes a bridge sample position and other effects were negligible. Chosen synchronous phase detector added differential changes about one-tength the size that could be recorded reproducibly.

4.5.3.3. Vibration Amplitude

The pick-to-pick vibration amplitude has been varied from less than 0.1mm upto 1.0mm in order to examine errors caused by amplitude changes. Such tests show that the measured magnetic moment varied by less than ±0.5% over these range of amplitude, although at higher variation of amplitudes, because of the larger signals involved.

4.5.3.4. Image Effects

Image effects were also examined with a small vibrating coil carrying a dc current. The image effect was no greater than ±1% for fields upto 5KG produced in an air gap of 3.6cm. Undoubtedly, there is an image induced in the magnet poles. It appears, however, that when the sample is vibrated, the effective image vibration is reduced by eddy current shielding.

4.5.3.5. Vibration Frequency

The vibration frequency is not critical. High frequency operation is limited by the driving mechanism and capacitive shunting in the detection coils. Frequencies of 100Hz or less permit the use of inexpensive components and minimize eddy current shielding by the vacuum chamber. The measurements are completely independent of eddy currents in the surrounding parts, if measurements and calibration are made at the same temperature. The thickness of conducting parts has been minimized, so that the temperature dependence of penetration depth is less than 1%

4.5.3.6. Vibration Problems

Mechanical coupling between the vibrating system and the fixed detection coils must be avoided. Although the coils are arranged for minimum sensitivity to external vibration, a noticeable background signal is obtained when the vacuum chamber contacts the detection coils. Such mechanical effects are difficult to eliminate electronically, because the spurious background signal has the same frequency as the sample signal and maintains a constant phase differences with respect to the sample signal. Usually the magnetometer and detection coils are both supported by the magnetic coupling, so that some mechanical coupling may be noticed at highest sensitivity.

4.5.4. High Temperature Magnetization Measurements

Magnetization measurements at temperatures above room temperature were done using a high temperature oven assembly (EG and G. Princeton Applied Research Co.). The oven consists of an electrically heated outer tube assembly with vacuum and reflective thermal insulation. The heater consists of an integral bifilar wounding heating coil with a resistance of 80 ohms. The winding is therefore non inducting. The sample holder consists of a quartz tube extension attached to a sample cup.

During operation of the high temperature assembly evacuation is accompanied by continuos flow of nitrogen gas to eliminate reaction of the sample with oxygen. A chromal-alumel thermocouple is used as a temperature sensor and the lughest temperature that can be achieved is 500^0C.

4.5.5. X-Y Recorder

All the measurements of temperature dependence of magnetization were plotted using LISEIS make X-Y Recorder model LY18100. The magnetic moment from V.S.M. and temperature form the potential differences in volts taken from panel meter are plotted on X-Y recorder. Magnetic moment can also be plotted as a function of time. A graph paper remains struck on an electrically charged plate during the plotting in X and Y scales are calibrated and can be reduced or enlarged as per need.

4.5.6. Calibration of the V.S.M.

There are usually two methods of calibration of a vibrating sample magnetometer(V.S.M.)

(i) by using a standard sample and

(ii) by using a coil of small size whose moment can be calculated from the magnitude of the d.c. current through it.

We have calibrated our V.S.M. using a 0.0584gm spherical sample of 99.99% pure nickel. The sample was made spherical with the help of a sample shaping device. The saturation magnetic moment of the sample has been calculated using the available data. The ratio transformer reading is obtained by actual measurement from the relation

$$M = KK', \tag{4.15}$$

where M is magnetic moment, K′ is saturation ratio transformer reading and K is V.S.M. calibration constant. But

$$M = m\sigma, \tag{4.16}$$

where σ is the specific magnetization and m is the mass of the sample. From eq^{n}(4.15) and eq^{n}(4.16) calibration constant is given by

$$K = \frac{m\sigma}{K'}. \tag{4.17}$$

The accuracy of this calibration, however, depends on the reliability of the standard nickel sample; the accuracy of the ratio transformer and the gain of amplifier. The equipment has been operated repeatedly with the same standard sample and stability has been found to be within 1 part in 100.

The absolute accuracy of the instrument depends on the knowledge of the magnetic properties of the calibration standard and reproducibility of sample position. When the substitution method of calibration is used, the major error ±1% is introduced by the estimation of standard nickel sample. The relative accuracy of this instrument depends on accurate calibration of the precision resistor divider net work.

The total error here can be kept less than 0.5%. A typical calibration curve of magnetic field Vs ratio transformer reading is shown in fig.-4.8

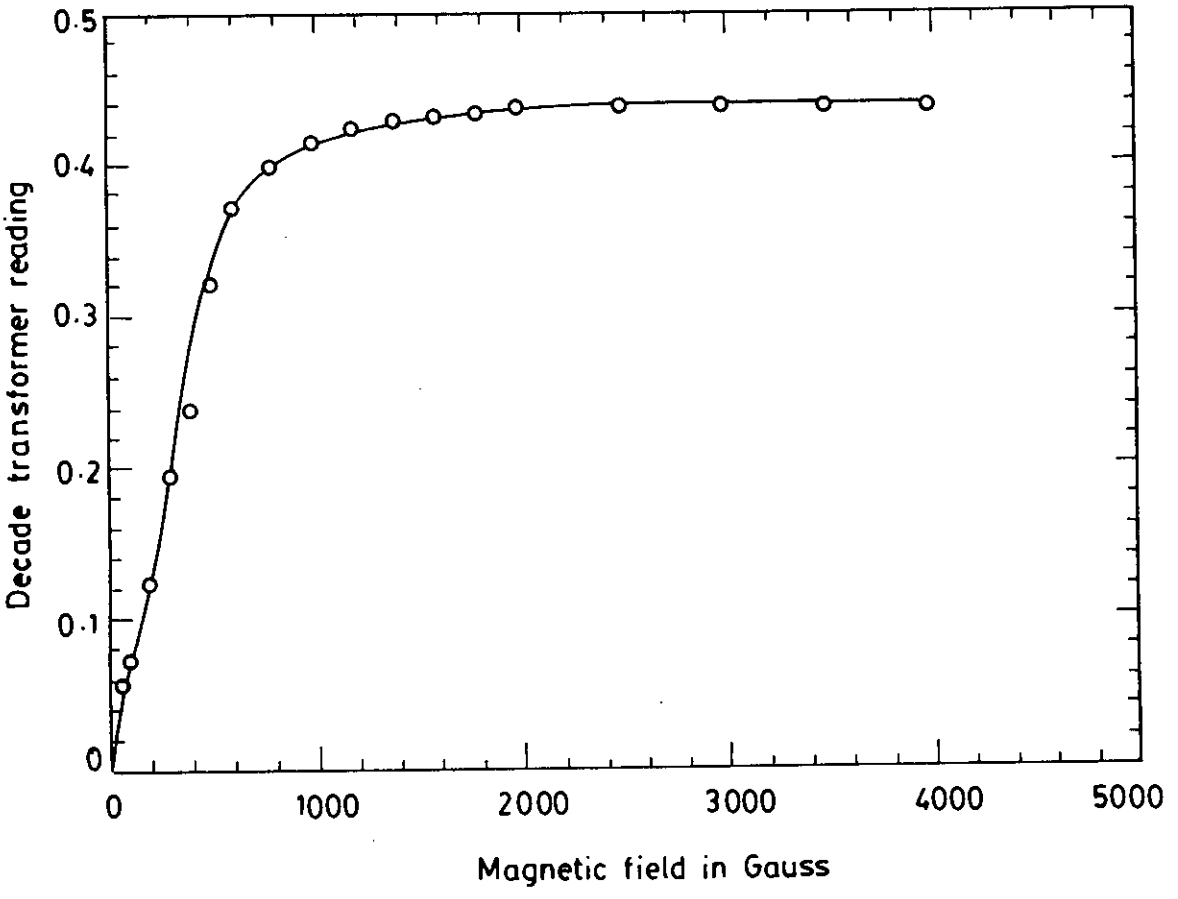

Fig.-4.8. Calibration curve of magnetic field Vs. decade transformer reading (V.S.M.)

4.5.6.1. Calibration Data

(i) Reference signal with phase shifter and decade transformer in connection:

$$V_{ref_1} = \frac{1}{0.01} \times \frac{10\mu V}{20} \times 19$$
$$= 9.5\mu V \times 100 = 0.95 mV$$

(ii) Reference signal with decade transformer in connection:

$$V_{ref_2} = \frac{1}{0.01} \times 11\mu V = 1.1 mV$$

(iii) Reference signal with direct connection:

$$V_{ref_3} = 13 \times 0.1 mV = 1.3 mV$$

Saturation decade transformer reading for pure Ni at $20^0 C$ is given as $K' = 0.4386$
Specific magnetization for pure Ni at $20^0 C$ is given by $\sigma_s = 54.75 \, ^{Am^2}/_{Kg}$
Mass of the pure Ni-sample $m = 0.0584 \times 10^{-3} Kg$
Magnetic moment $M = m\sigma = 3.1975 \times 10^{-3} Am^2$
and hence V.S.M. calibration constant is found as

$$K = \frac{m\sigma}{K'} = 7.29 \times 10^{-3} Am^2$$

4.6.0. Experimental Set-up for Anisotropy Measurements

4.6.1. Principle of the Torque Magnetometer

The apparatus used is a sensitive Torque magnetometer with a Proportional Integrating Differentiating (P.I.D.) regulator following the technique used by B.Westerstrandh et.al.(4.4). This apparatus allows measurements of the torque as a function of direction cosines of the magnetic with respect to crystallographic axes. A laser source provides a coherent light beam of constant intensity which falls symmetrically on two photo-diodes and illuminates them equally. Any deviation of the beam from the symmetric position due to the rotation of the mirror fixed on the specimen attached to this holder produces an out of balance photocurrent. This photocurrent is fed in to the P.I.D. regulator which produces a compensating current and sends it to the compensating coil placed in a permanent magnetic field.

To avoid any spuratic torque due to the image effect in the pole pieces, the specimen is placed in the central position between the poles of a rotatable magnet. The centre of the sample is made to coincide with the axis of the rotatable magnet and this is ensured by the exact repetition of the torque value at every 180^0 rotation of the field. A circular specimen was cut from the amorphous ribbon to provide maximum symmetry about the axis of the rotating field. Torque against angle showed reasonable reproducibility for forward and reverse rotation of the field.

4.6.2. Mathematical Formulation of Torque Analysis

The inherent property of a magnetic material in a static magnetic field is to align itself in order to minimise its energy. The energy variation with respect to sample orientation is represented by a torque exerted on the sample. The torque L exerted along an axis perpendicular to the magnetic field is related to the total anisotropy energy E_a given by

$$L = -\frac{dE_a}{d\varphi}, \qquad (4.18)$$

where, φ is the angle between a fixed direction in the sample and the direction of the magnetic field. Thus it is evident that by measuring the torque from a sample in a magnetic field we can gain information about the magnetic anisotropy energy of a material. For ferromagnetic substances the anisotropy constants can be deduced from a

Fourier analysis of the torque data as a function of the angle φ between the magnetic field and a direction fixed in the crystal.

Akulov[4.5] showed that E_a can be expressed in terms of a series expansion of the direction cosines of M_s (saturation magnetization) relative to the crystal axes in a cubic crystal, let M_s make angles a, b, c with the crystal axes and let $\alpha_1, \alpha_2, \alpha_3$ be the cosines of these angles, then

$$E_a = K_0 + K_1\left(\alpha_1^2\alpha_2^2 + \alpha_2^2\alpha_3^2 + \alpha_3^2\alpha_1^2\right) + K_2\left(\alpha_1^2\alpha_2^2\alpha_3^2\right) \qquad (4.19)$$

where K_0, K_1, K_2.....are the anisotropy constants. The first term, K_0, is independent of angle and is usually ignored, because normally we are interested only on the change in energy E_a when the M_s vector rotates from one direction to another. When K_2 is zero, the direction of easy magnetization is determined by the sign of K_1. If K_1 is positive, then $E_{100} \langle E_{110} \langle E_{111}$, and $\langle 100 \rangle$ is the direction of easy magnetization. If K_1 is negative, $E_{111} \langle E_{110} \langle E_{100}$, and $\langle 111 \rangle$is the direction of easy magnetization. For nickel K_1 is negative and for iron K_1 is positive.

The anisotropy energy expression for a hexagonal crystal can be written as

$$E_a = K_0 + K_1 \mathrm{Sin}^2\theta + K_2 \mathrm{Sin}^4\theta + \ldots\ldots\ldots \qquad (4.20)$$

The in-plane anisotropy energy usually shows uniaxial symmetry by the magnetic torque curve and can be expressed may be written neglecting K_2

$$E_a = K_u \mathrm{Sin}^2\theta, \qquad (4.21)$$

where K_u is the magnetic anisotropy constant, θ is the angle between magnetization and the easy axis.

The anisotropy constants were determined by measuring the torque as a function of angle of the magnetic field with respect to the easy direction. A Sinθ curve was obtained which was later Fourier analyzed using a computer program. For uniaxial anisotropy the energy E of a system can be written as

$$E = K_{u1} \mathrm{Sin}^2\theta + K_{u2} \mathrm{Sin}^4\theta, \qquad (4.22)$$

where K_{u1} is the first anisotropy constant and K_{u2} is the second anisotropy constant. Form Fourier analysis it is shown that the K_{u2} value is negligible. In amorphous materials there is an induced anisotropy due to the preparation technique. Instead of

presuming uniaxial anisotropy before calculation, the uniaxiality of the amorphous ribbons were confirmed empirically.

Since the torque on the specimen per unit volume is given by

$$L = -\frac{dE}{d\theta} \tag{4.23}$$

We get eq^{n}(4.22)

$$L = -(K_{u1} + K_{u2})\mathrm{Sin}2\theta + (K_{u2}/2)\mathrm{Sin}4\theta \tag{4.24}$$

From eq^{n}(4.24) K_{u1} and K_{u2} are now determined from the Fourier co-efficient

$$A_2 = -(K_{u1} + K_{u2}) \text{ and } A_4 = \frac{K_{u2}}{2} \tag{4.25}$$

and solving $K_{u1} = -(A_2 + 2A_4)$

Thus the uniaxial anisotropy K_u is given by

$$K_u = A_2 + 2A_4 \tag{4.26}$$

4.6.3. Design and Working Principle of the Torque Magnetometer

A simple form of torque compensation can be achieved by suspending the sample from a fibre with known torsional constant. When a magnetic field is applied, the torque from the crystal will twist the fibre, thus we can measure, by how much we have to rotate the upper point of suspension of the fibre to bring the crystal back to its original position.

Instead of rotating the torsion fibre a balancing torque can be generated with a compensation coil in a static magnetic field. The torque from the coil is proportional to the current through the coil over a wide range of currents. Thus we can measure the current needed for the crystal to maintain its orientation.

The principle drawing of a torque magnetometer with an automatic compensation system is shown in fig.-4.9. The sample is rigidly connected to a mirror and the compensation coil. The whole assembly is freely suspended in a thin quartz fibre and the coil is located in a field produced by a pair of permanent magnets. Now if laser beam is shined on the mirror, the image of the beam will move as soon as some

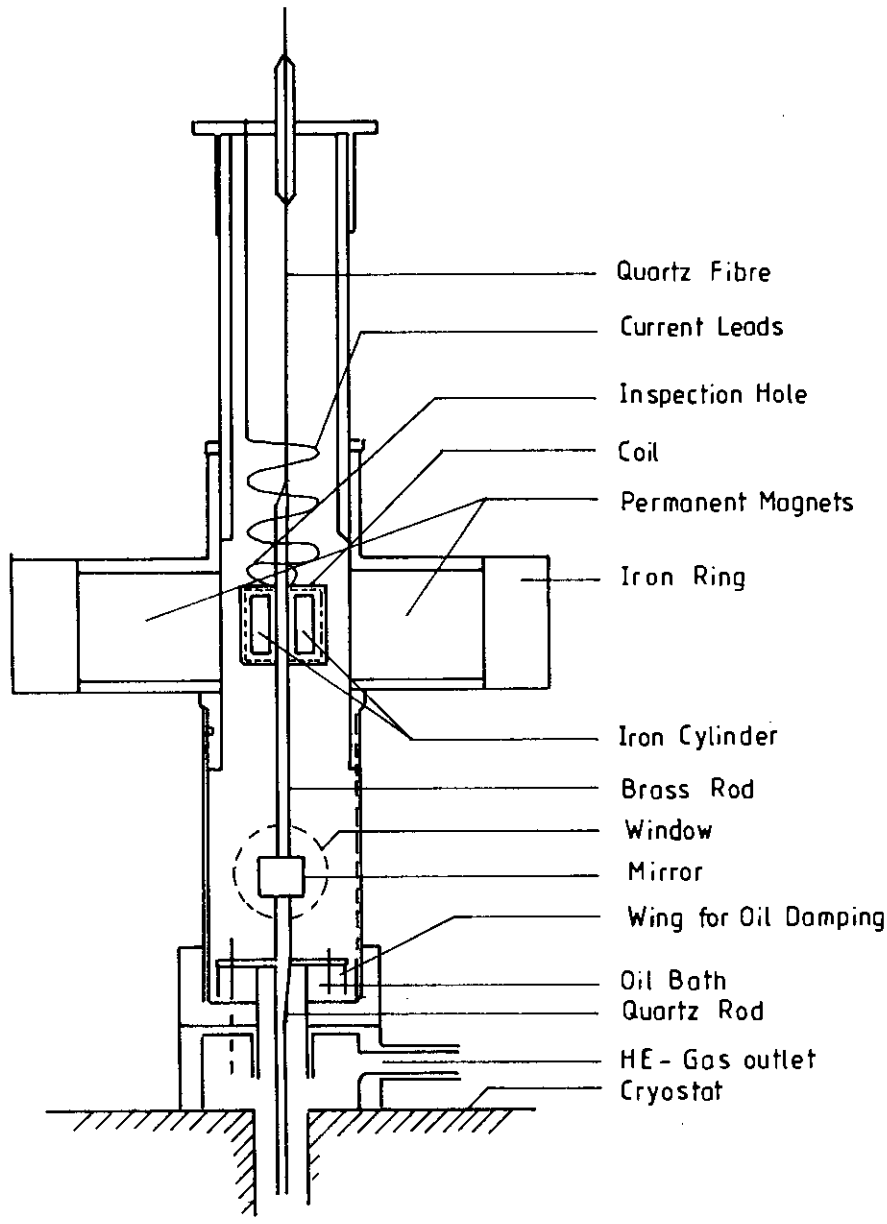

Fig.-4.9. Cross section of the upper part of the torque magnetometer.

torque acts on the crystal and thus turns the mirror. The principle is to let a phto-detector detect the movement of the reflected beam via an amplifier generating a current through the compensation coil which inhibits the motion of the suspension.

The simplest tupe of electronic compensation system with a photosensitive feedback have been designed[4.4]. The simplest way is to let the current through the compensation coil to be directly proportional to the signal from the detector. Such a feedback system is often referred to as a proportional(P) regulator. If a torque acts on the crystal the turning of the mirror gives rise to a deflection of the beam shining on the detector, and the deflection from the centre of the detector can be made small by increasing the amplifier gain. Nevertheless the contribution from the rigidity of the suspension may seriously affect measurements of small torques. Neither the gain of the feedback could be increased too much since the system will then become unstable. To improve the stability we have used the oil damping. The viscosity of the oil damps oscillations so that we can increase the amplifier gain. To enhance the electronic damping a differentiating amplifier has been used in parallel with the proportional amplifier and hence improve the stability of the system. This type of compensation system can be characterised as a proportional differentiating regulator (PID). Since large deflection of the suspended system is a problem, the introduction of a differentiating unit allows a very high gain and a small angular deflection.

4.6.4. The Sample Suspension

The sample is mounted at the end of a thin quartz rod. Quartz is a suitable material for this purpose as it is diamagnetic and has a low thermal conductivity. The upper end of the quartz rod is attached to a brass rod, to which the mirror and the compensating coils are fixed. The whole assembly is suspended by a quartz fibre. The quartz fibre is very suitable because of its large tensile strength and small torsional constant. Typical values of the torsional constant are 5×10^{-7} to 10×10^{-7} $^{Nm}/_{rad.}$. The elasticity in the longitudinal direction is very low, which prevents low frequency oscillation along the axis of suspension. The compensation coils have 10 layers of 100 turns of 0.06mm copper wire. To minimise influence from the stiffness of the copper wire, the leads to the coils have been spiralized. Below the coil there is, besides the mirror, an arrangement for oil damping, effective against self oscillations.

4.6.5. The High Temperature Oven

The high temperature oven is constructed following the method devised by Dr. Per Nordblad and Late Prof. Leif Lundgren of the Department of Technology, Uppsala University, Sweden. The schematic diagram of the oven is shown in fig.-4.10. The most important feature in the construction of the oven is that the inner stainless steel tube extends throughout the oven and the thermocouple unit is introduced from the bottom end with the thermocouple junction placed immediately below the sample.

The heater is wound directly on the inner tube. The heater consists of a MgO insulated chromel-Constantan thermocouple with a stainless steel cover (O.D. 1mm, length 1.3mm, manufactured by OMEGA Corp.). This thermocouple is flexible and to obtain a firm contact between the heater and the inner sample tube, the thermocouple is first wound on a tube with a some what smaller diameter, and the resulting spiral is afterwards squeezed on to the sample tube. The thermal contact between the heater and the sample tube is improved by adding some silver paint. The lower ends of the heater wires are electrically connected by means of silver paint. Copper wires, connecting an external power supply, are soft soldered on the upper ends of the heater wires. The silver paint is dried out at ordering atmosphere by passing some current through the heater. The advantages to use this Chromel-Constantan thermocouple as a heater for this oven are that it is readily available, non-magnetic, insulated, easily formed, and gives a bifilar winding and close thermal contact with the sample tube. The heater has a resistance of 75 ohms at room temperature.

Five radiation shields, consisting of 50μm stainless steel foils are located outside the heater. These are tied directly on to the heater using reinforced glass fibre thread. The outer tube is at the bottom end connected to the inner tube via a phosphor-bronze bellow, in order to allow for the difference in length of the two tubes at higher temperature. O-ring coupling are used throughout to eable easy disassembling of the oven in case of any fault.

Both the oven and the thermocouple are adjustable in height with respect to the sample. This gives a possibility to find a position of the sample in the warmest region of the oven which gives a minimum temperature gradient between the sample and the thermocouple junction. The temperature gradient $\frac{\nabla T}{T - T_0}$ over 10mm of length in the warmest part in the oven is approximately 0.1% and independent of the temperature.

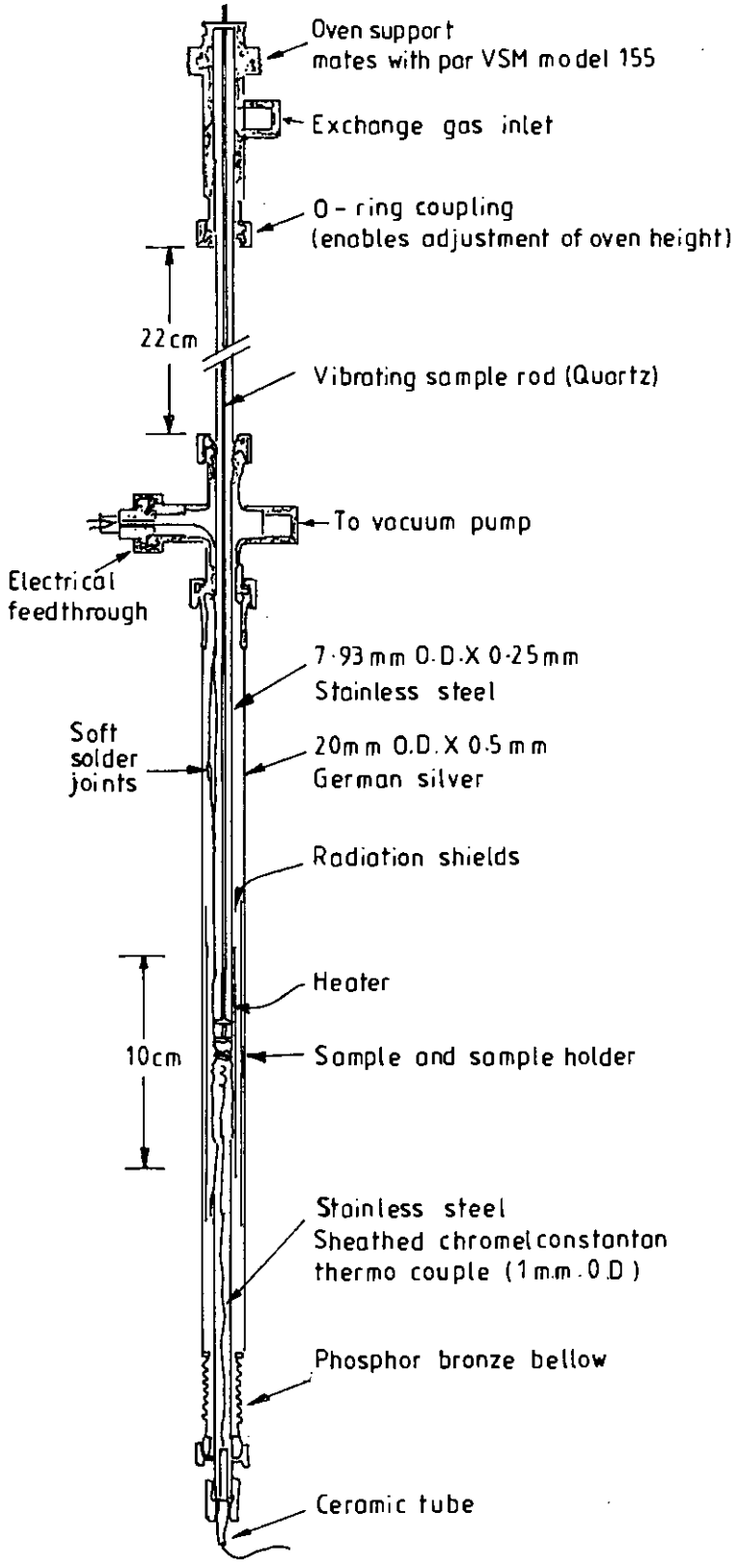

Fig.-4.10. Schematic diagram of the high temperature oven

The special characteristics of the oven are:

(i) The oven can be heated from room temperature to 1043K in less than 15minutes with a temperature difference between thermocouple and sample of less than 1K at the final temperature;

(ii) At a constant heating or cooling rate of 5K/minute a temperature difference of the order of 1K is established;

(iii) Due to small thermal mass of the oven, it cools from 1150K to 600K in about 30 minutes which enables a fast interchange of sample.

4.6.6. Calibration of the Torque Magnetometer

For the calibration of the torque magnetometer a thin nickel single crystal disc is used. The disc is of mass 45mg and is oriented in such a way that the (100) crystallographic plane lies on the plane of the disc. The sample is glued to a sample holder and is suspended from a thin quartz fibre connected to a brass spindle. The sample is thin placed in between the poles of an electromagnet. A 3.0KG magnetic field which is strong enough to saturate the nickel specimen is applied along the plane of the disc and measurements of torque is taken at every 10^0 angular rotation for a complete 360^0 rotation of the magnetic field. A total of 36 data points are obtained for a complete rotation of the magnetic field. The whole process of measurements is repeated for an applied magnetic field 0.775KG to 3.775KG. Fig.-4.11 shows the torque curve at 25^0C of a nickel disc oriented in the (100) crystallographic plane.

The measured data are entered in a computer programme for Fourier analysis. The Fourier coefficients are equated with the standard equation for the torque curve. Thus from the known mass of the disc and the known value of the anisotropy constant for nickel at room temperature, the calibration constant of the torque magnetometer is determined.

$$1\text{volt} = 4.755 \times 10^{-7}\,\text{joule}$$

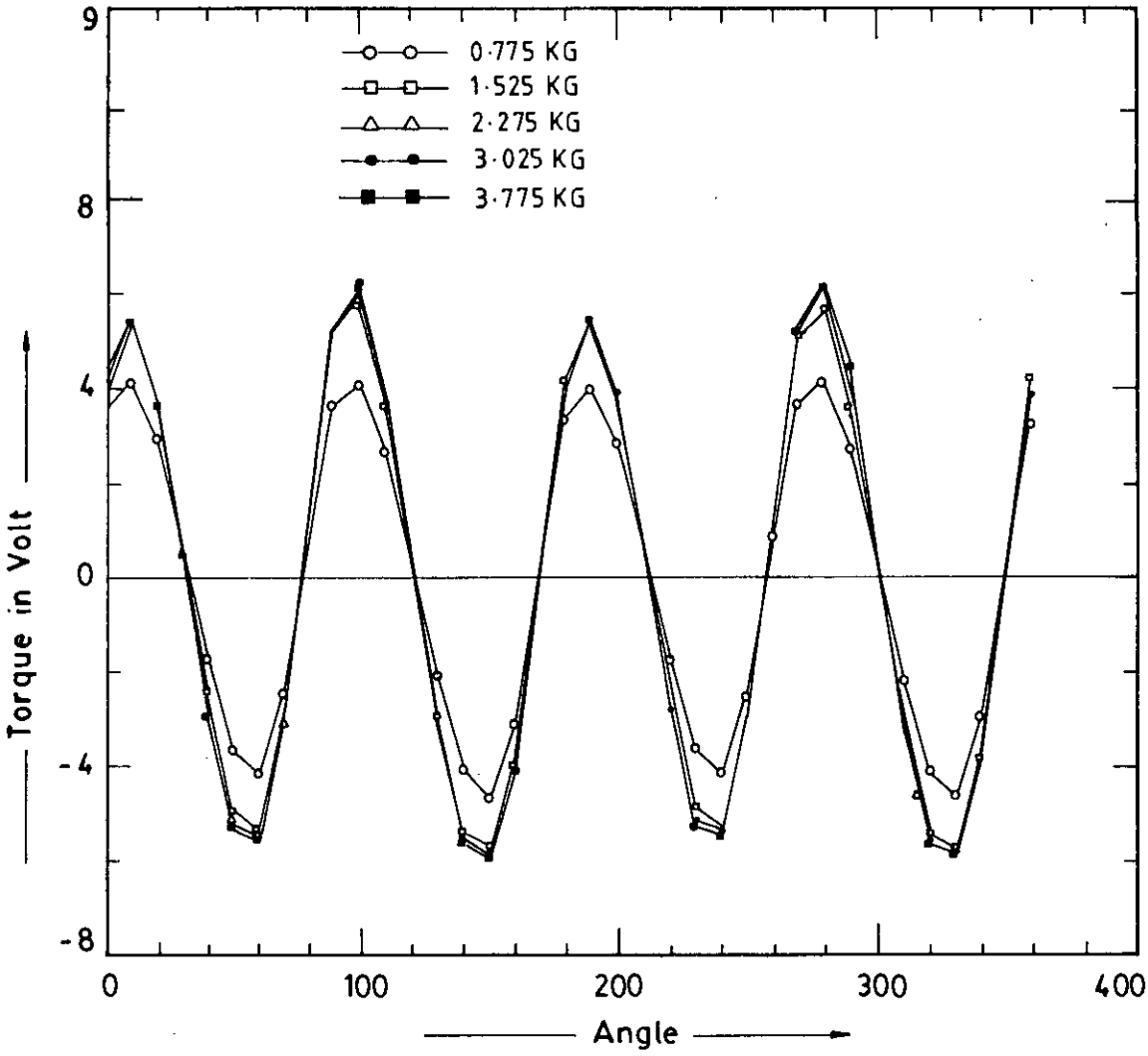

Fig.-4.11. Torque curve for a single crystal of Nickel disc in (110) crystallographic plane at 25^0C

4.7.0. Experimental Procedure for Mössbauer Spectrometer

4.7.1. Instrumentation

Mössbauer measurement can be made in two different geometries, transmission and scattering configurations. In the present work only transmission geometry was used. In transmission type measurements, the intensity of γ-rays transmitted through a thin absorber are measured with the help of a suitable detector like proportional counter. γ-ray source is driven electromagnetically by a transducer so as to Doppler shift the energy of emitted γ-rays by small and known amounts. The absorption Mössbauer spectrum is obtained by counting transmitted γ-rays as a function of the source to absorber velocity.

The experimental set-up consists of three parts, an electromechanical velocity drive system, a detection system and a data storage system. The Block diagram of the experimental set-up is shown in fig.-4.12.

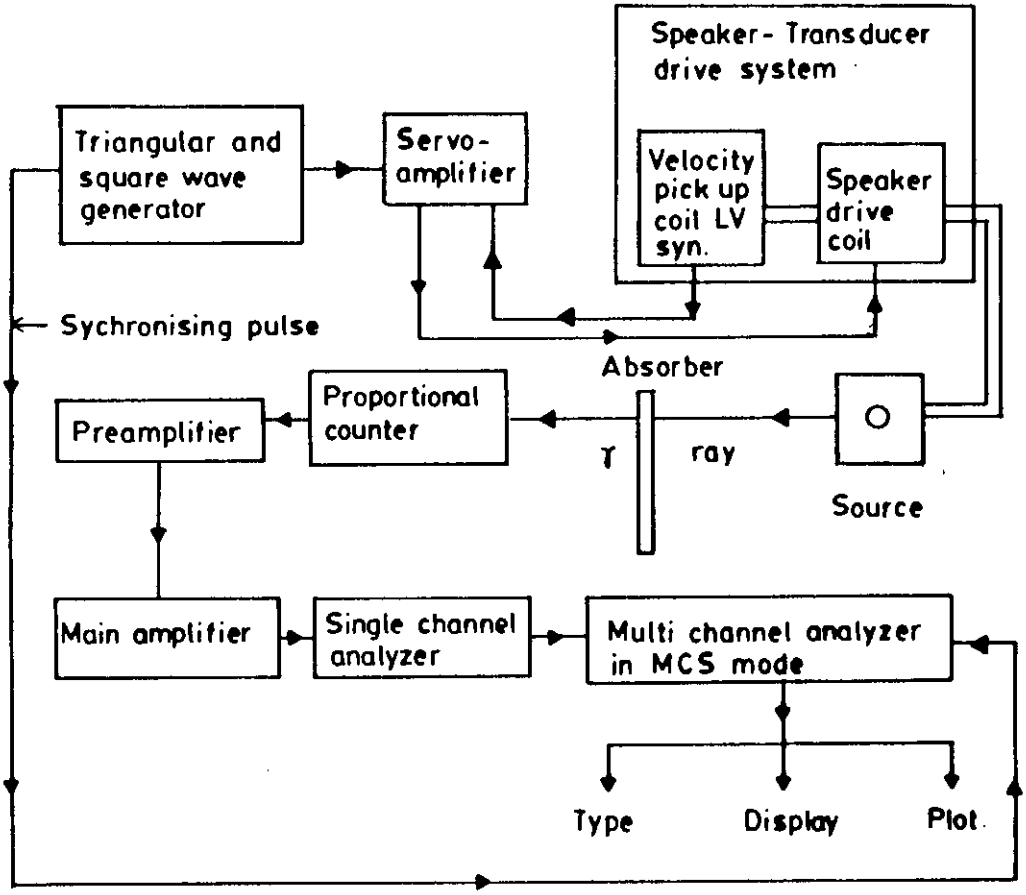

Fig.-4.12. Block diagram of the experimental set-up

The work reported here is based on Mössbauer spectroscopy of 14.4KeV γ-rays. For this ^{57}Co embedded in Rh matrix was used as the source. It emits 14.4KeV γ-radiation nuclear level decay scheme depicted in fig.-4.13. The half life of the source is 270 days.

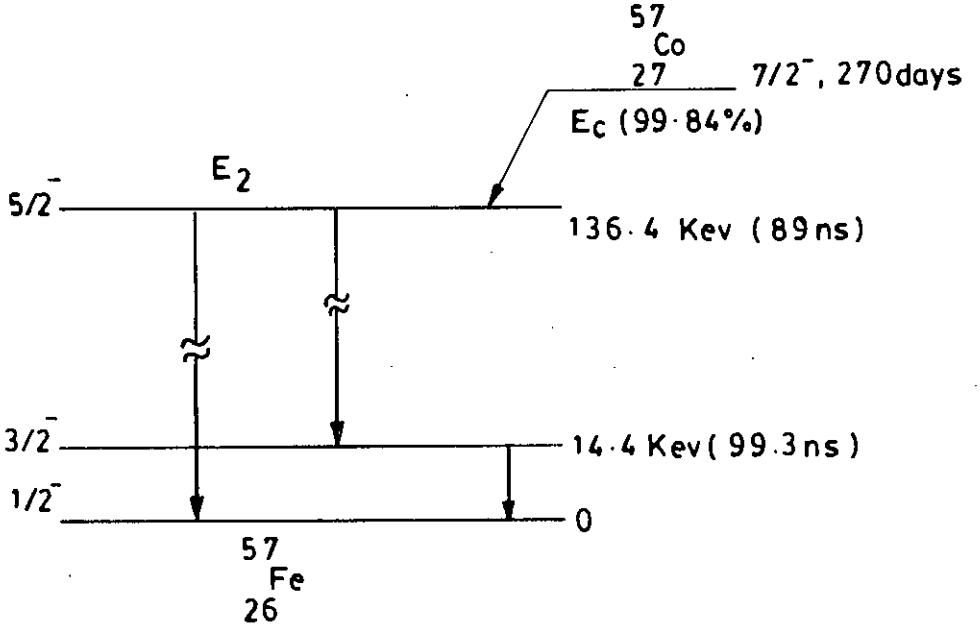

Fig.-4.13. Nuclear level decay scheme of ^{57}Co Mössbauer isotope

4.7.2. Velocity Drive System

In order to provide a Doppler motion to the source with respect to stationary observer or vice-versa a velocity drive system is used. In the present work Doppler motion is given to the source. For this an electromechanical system is used. It comprises of a velocity transducer and its related electronics(4.6). It works fairly linear by upto a velocity of ±25mm / s. To run this in constant acceleration mode this is connected to computer and a power amplifier. Triangular wave is fed as a reference signal to one of the transducer coils acting as a pick up coil. Also due to transducer motion a signal is induced at this pick up coil. Also due to transducer motion a signal is induced at this pick up coil subtracts from the reference generating an error signal, which is amplified, integrated and then applied to a complimentary circuit to push-pull power amplifier which drives the coil. In this way self sustained motion of the drive is obtained. Pulses of a repetition rate equal to that of the frequency of a triangular wave

formed from the leading edge of the square wave obtained by differentiation of the triangular wave. These pulses are used to start and stop signals for scanning of 512 channels. Here synchronisation is achieved with the help of computer.

4.7.3. γ-Source

A good Mössbauer source should have high recoil free electrons, long life time and narrow line width. In the present work, Mössbauer studies using ^{57}Fe have been reported. The γ-ray of 14.4KeV emitted by it is used. Characteristics are as follows Matrix: Rhodium; Matrix size: 8mm diameter; Matrix thickness: 6μm; Source strength: 10mCi and Half life: 270days. More details are given in Table-4.1. Decay scheme for ^{57}Co is given in fig.-4.13.

Table-4.1. Properties of ^{57}Fe isotopes.

Isotope abundance (%)	2.19
Transition energy (KeV)	14.39
Spin and Parity I_g I_e	 $\frac{1}{2}^-$ $-\frac{3}{2}^-$
Excited state half life (sec)	9.8×10^{-8}
Internal conversion co-efficient	9.00
Cross-section $\left[cm^{-2}\right]$	2.43×10^{-18}
Magnetic moment $\mu_g(nm)$ $\mu_e(nm)$	 0.09024 -0.154
Quadrupole moment $Q_g(barns)$ $Q_e(barns)$	 0.0 0.285
Natural width (KeV)	4.655×10^{-12}
Observable width $w_0(mm/s)$	0.194
Recoil energy $E_R(eV)$	1.956×10^{-3}
Recoil free fraction of ^{57}Fe in Rh matrix (at 300K)	0.72

4.7.4. Detection System

For 14.4KcV γ-rays a proportional counter gives good performance with a high efficiency and a fairly good resolution. Proportional counter has got a very poor efficiency for 122KeV and 136KeV γ-rays. During this work, we havc used a Krypton filled proportional counter which yielding 20% energy resolution. For further routing the signal to detect it, a preamplifier, an amplifier and a single channel analyser were used.

4.7.5. Pre-amplifier and Amplifier

The signal from the proportional counter is only 2mV. In order to select proper energy pulses using a single channel analyser and to feed them to a multichannel analyzer for storage, pulses of ~2V height are required. This would need a high gain amplifier. The proportional counter output is at an impedance of ~1MΩ. This has to be reduced to a few ohms in order to reduce the noise level. For this purpose the proportional counter output is fed to a preamplifier first, and its output is then fed to the amplifier(4.7). The pre-amplifier serves as an impedance matching device.

4.7.6. Single Channel Analyser

In order to select 14.4KeV pulses a single channel analyser is used. Since height of the detector pulse is proportional to the γ-energy, a pulse height discriminator (or analyser) is employed. It yields the output pulse only if the linear input pulses fall between prescribed upper and lower levels, the so-called window. Further details of the circuit performance may be found in reference (4.8).

4.7.7. Data Storage System

The spectrum reported in this work has been recorded in constant acceleration mode and so the data have been collected in multiscaling mode. For this a multi channel analyser (MCA) has been used. This MCA works in time scaling mode and each channel opens for a constant dwell time ranging from 0.2msec to 2msec. It has in all 1024 channels and has an option of using a minimum of 128 or integral multiple

number of channels. The memory storage is magnetic type. We have used 512 channels. A synchronisation is to be maintained between velocity amplitude of the drive and the channel number of MCA. The data are collected into two groups. First group of 256 channels pertains to positive Doppler velocities and the second group of remaining 256 channels which is mirror image of the first pertains to negative Doppler velocities. The representative spectrum of ^{57}Fe absorber is shown in fig.-4.14.

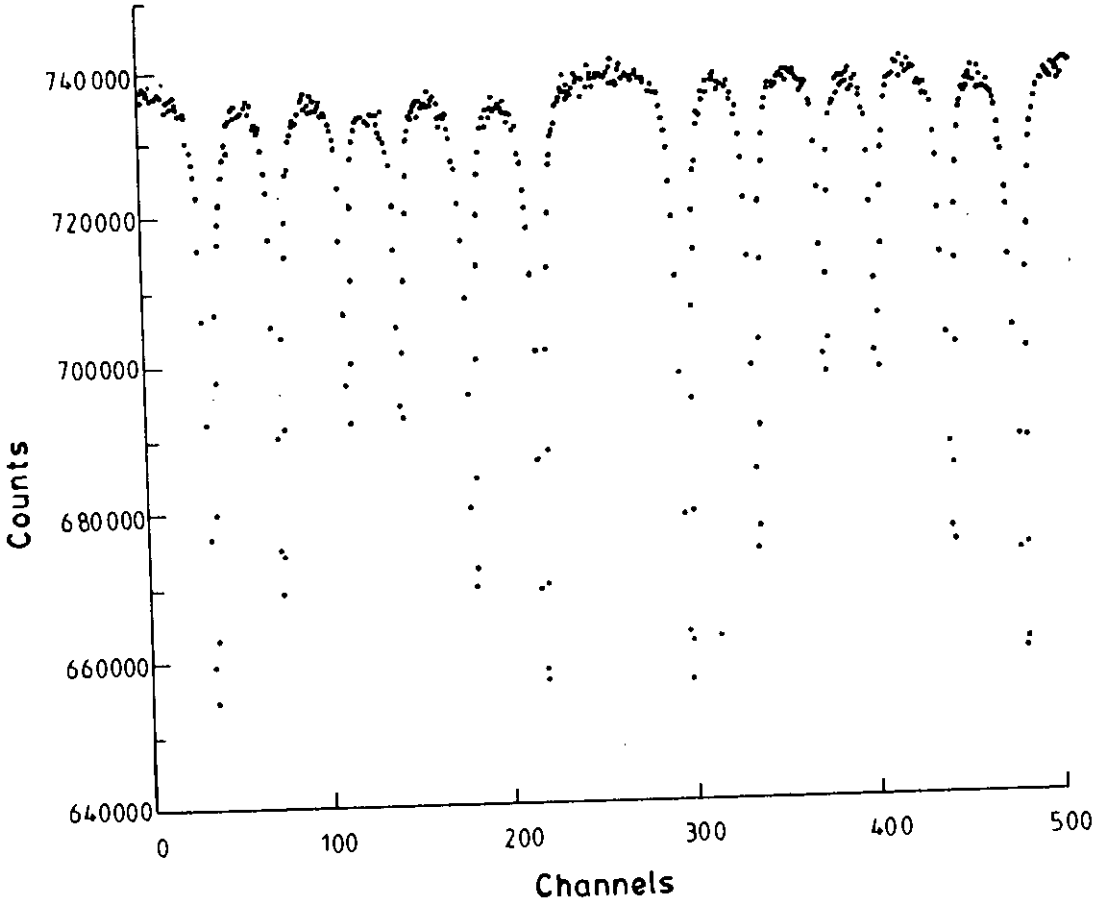

Fig.-4.14. Room temperature Mössbauer transition spectrum for relative counts Vs. channels of ^{57}Fe absorber.

4.7.8. Description of the workdone

Using the above Mössbauer set-up, with ^{57}Co as source and Natural Iron (^{57}Fe) as absorber, a Mössbauer spectrum is observed. For this we have used an exactly similar single channel analyser as discussed. Absorber is placed infront of the source at a distance of 10cm. Velocity of the drive is set to 0.3cm/s. Then using the MCA, counts are obtained in 512 channels. Then a graph between no. of counts versus velocity is plotted. In order to calculate the velocity per channel, velocity between peaks are given in literature as in fig.-4.15. Using these standard values, velocity per channel is calculated.

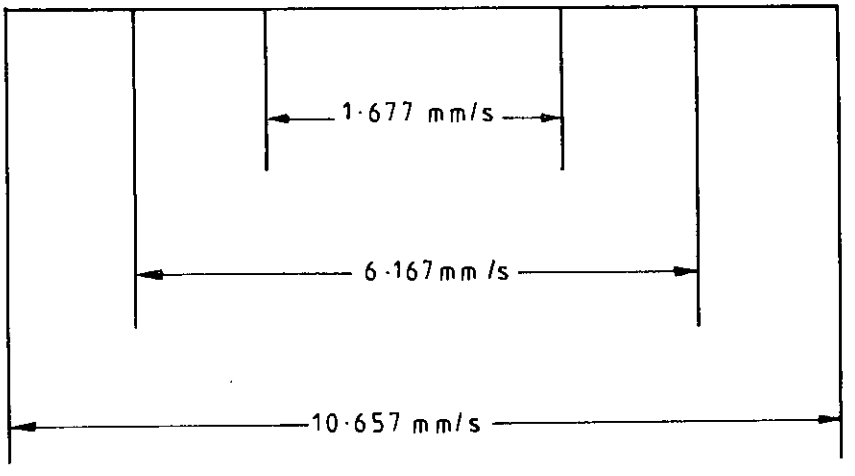

Fig.-4.15. Standard velocity between peaks of ^{57}Fe absorber

4.7.9. Calibration of ^{57}Fe absorber sample for measurement of Mössbauer parameters

Using the Mössbauer set-up spectrum for ^{57}Fe absorber is obtained. The number of counts versus velocity of the source is plotted in fig.-4.16. Energies corresponding to the velocities are also denoted in the same figure.

We see that there are two groups of spectra which are mirror image of each other, containing six lines each. In the case of ^{57}Fe, there is infact an internal magnetic field acting at ^{57}Fe nucleus. This causes the upper $-\frac{1}{2}$ level to splite to four levels and the lower $-\frac{1}{2}$ level splits into two levels. Using the selection rule $\Delta m = 0, \pm 1$, for transition to occur, one gets six possible transitions. The source in Rh-matrix is a single

line source. Hence in order to match the source energy to each of the six allowed energy difference, in Iron metal absorber, one has to give six different velocities to the source. This is automatically achieved in constant acceleration mode.

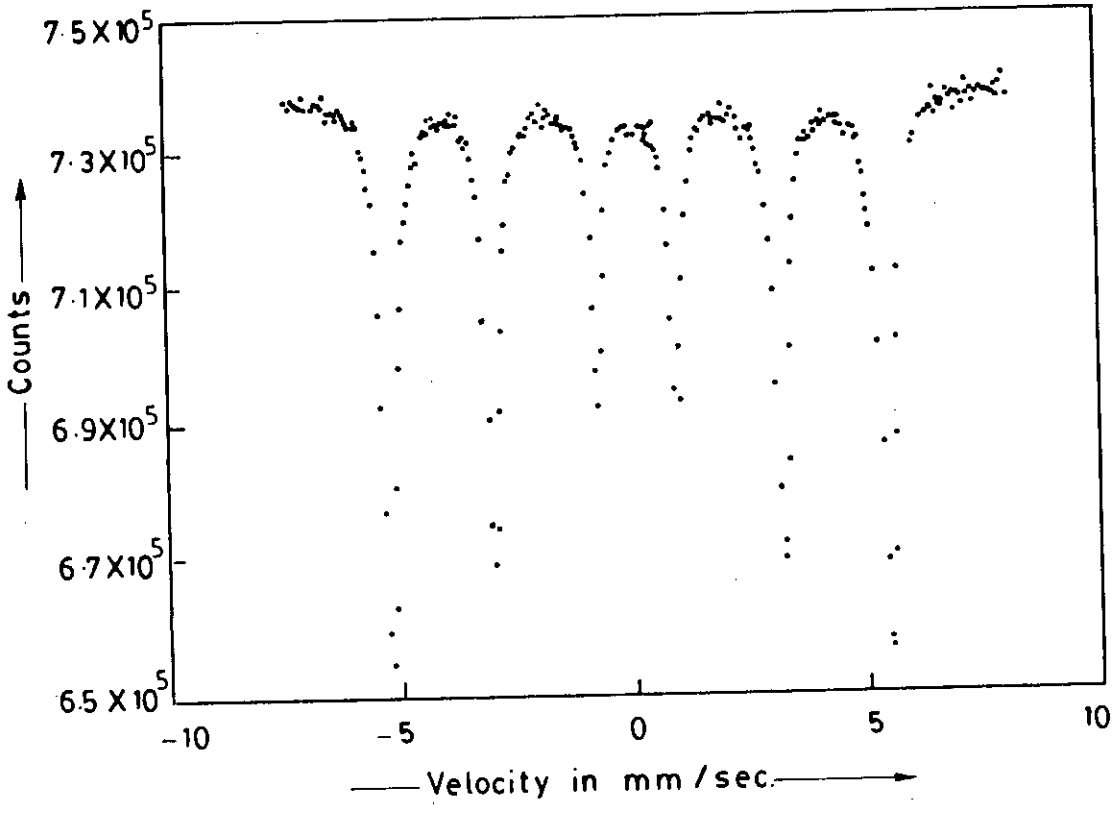

Fig.-4.16. Room temperature Mössbauer transition spectrum for relative counts versus velocity of ^{57}Fe absorber.

4.7.10. Computer Analysis of the Data

All the Mössbauer spectra have been resolved into Lorentzian components. For this a tested computer program developed by Ericsson[4.9] and Kamal[4.10] has been used. This program is written in FORTRAN-IV language which does a least Chi-square (χ^2) spectra curve fitting for over lapping Lorentzian lines. A non-linear variable

matrices minimization technique is used iteratively to optimize the parameters of the theoretical function by minimizing χ^2 for the spectral data. First using the calibration spectrum of ^{57}Fe recorded at the same drive setting at which the sample spectrum is recorded, one linearizes the data and the two groups (mirror image of each other) are folded, resulting in improved statistics. Also the parabolic effect in the base line, caused by the periodic parabolic displacement of the source, gets cancelled as a result of the folding. This folded set of data is then used for analysis. The fitting is done in terms of the parameters of isomer shift (IS), quadrupole splitting (E_Q), internal hyperfine field (H_{hf}), full width half maximum (FWHM), probability distribution curve and absorption percentage of the components in a magnetic pattern. Finally the experimental spectrum and the fitted function is plotted on screen to decide about the goodness of fitting.

CHAPTER-5 RESULTS AND DISCUSSION OF Fe-BASED AMORPHOUS RIBBONS

5.1. Differential Thermal Analysis of Iron-Silicon-Boron ribbons as affected by silicon content

5.2. Curie Temperatures of the Amorphous Ribbons

5.2.1. Curie Temperature Measurements of Amorphous Iron-Silicon-Boron Ribbons

5.3. Determination of Maximum permeability, Maximum induction, Coercive force and Remanence of Fe-based Amorphous Ribbons

5.4. Dynamic Magnetic Properties of Fe-based Amorphous Ribbons

5.5.0. Specific Magnetization of Fe-based Amorphous Ribbons

5.5.1. Specific Magnetization at Room Temperature

5.5.2. Temperature Dependence of Specific Magnetization of Fe-based Amorphous Ribbons

5.6. Stress Induced Anisotropy of Fe-based Amorphous Ribbons

5.6.1. Temperature Dependence of K_u

5.7. Experimental Results and Analysis of Mössbauer Parameters for Fe-based Amorphous Ribbons

5.0. Results and Discussion of Fe-based Amorphous Ribbons.

5.1. Differential Thermal Analysis of Iron-Silicon-Boron ribbons as affected by silicon content.

Iron-Silicon-Boron amorphous ribbons with composition $Fe_{90-x}Si_xB_{10}$ [x = 6, 8, 10, 12 and 14] are potentially important commercial materials with low magnetostriction and are candidates for electromagnetic devices for power application at high frequencies. In particular, studies of early glass transition temperature T_g and crystallization temperature T_x are determined by DTA at a heating rate of 10^0c/min. Structural relaxation in Fe-B-Si alloys has enabled us to explain changes in the electromagnetic energy loss behaviour due to heat treatment. Our work on the ferromagnetic glasses of this alloys provide information on the crystallization kinetics T_g, T_x and T_x' due to variation of the Si-content.

The DTA trace of amorphous Iron-Silicon-Boron of composition $Fe_{82}Si_8B_{10}$ is shown in fig-5.1. The three anomalies observed in the temperature VS time curve were at 448^0c, 555^0c and 605^0c respectively. Both the peaks which correspond to release of heat at these temperatures correspond to crystallographic ordering of the atoms. Fig-5.2 shows the DTA traces of the different amorphous ribbons with composition $Fe_{90-x}Si_xB_{10}$. The amorphous samples produced showed T_g well below T_x, so that there was sufficient mobility of the atoms without the possibility of crystallization. The numerical values of T_g, T_x and T_x' for all the samples are shown in Table-5.1.

Table-5.1

$Fe_{90-x}Si_xB_{10}$	T_g	T_x	T_x'
x = 6	458^0c	545^0c	595^0c
x = 8	488^0c	555^0c	605^0c
x = 10	525^0c	564^0c	600^0c
x = 12	545^0c	568^0c	600^0c
x = 14	550^0c	570^0c	600^0c

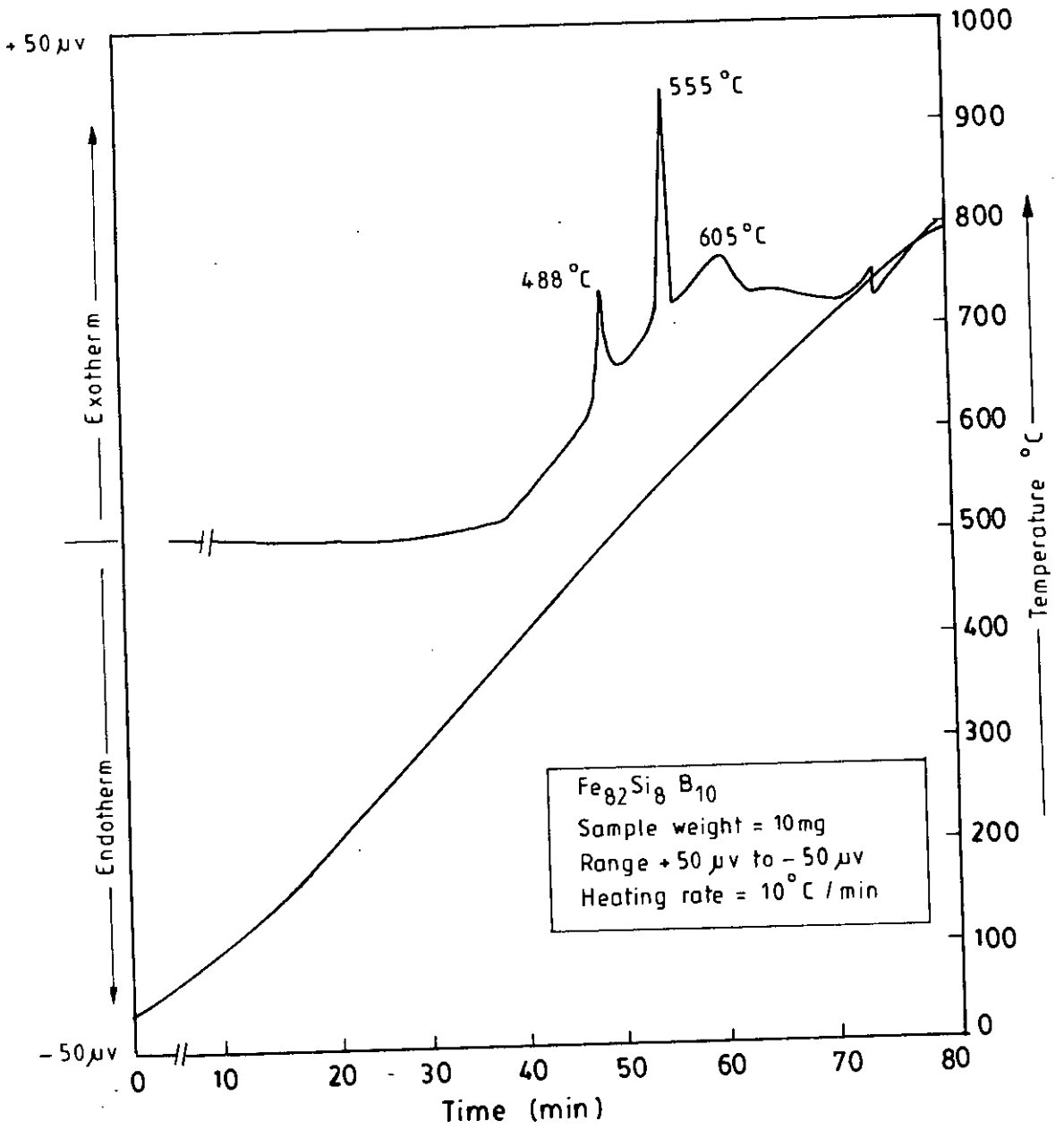

Fig.-5.1. DTA graph of amorphous ribbon with composition $Fe_{82}Si_8B_{10}$

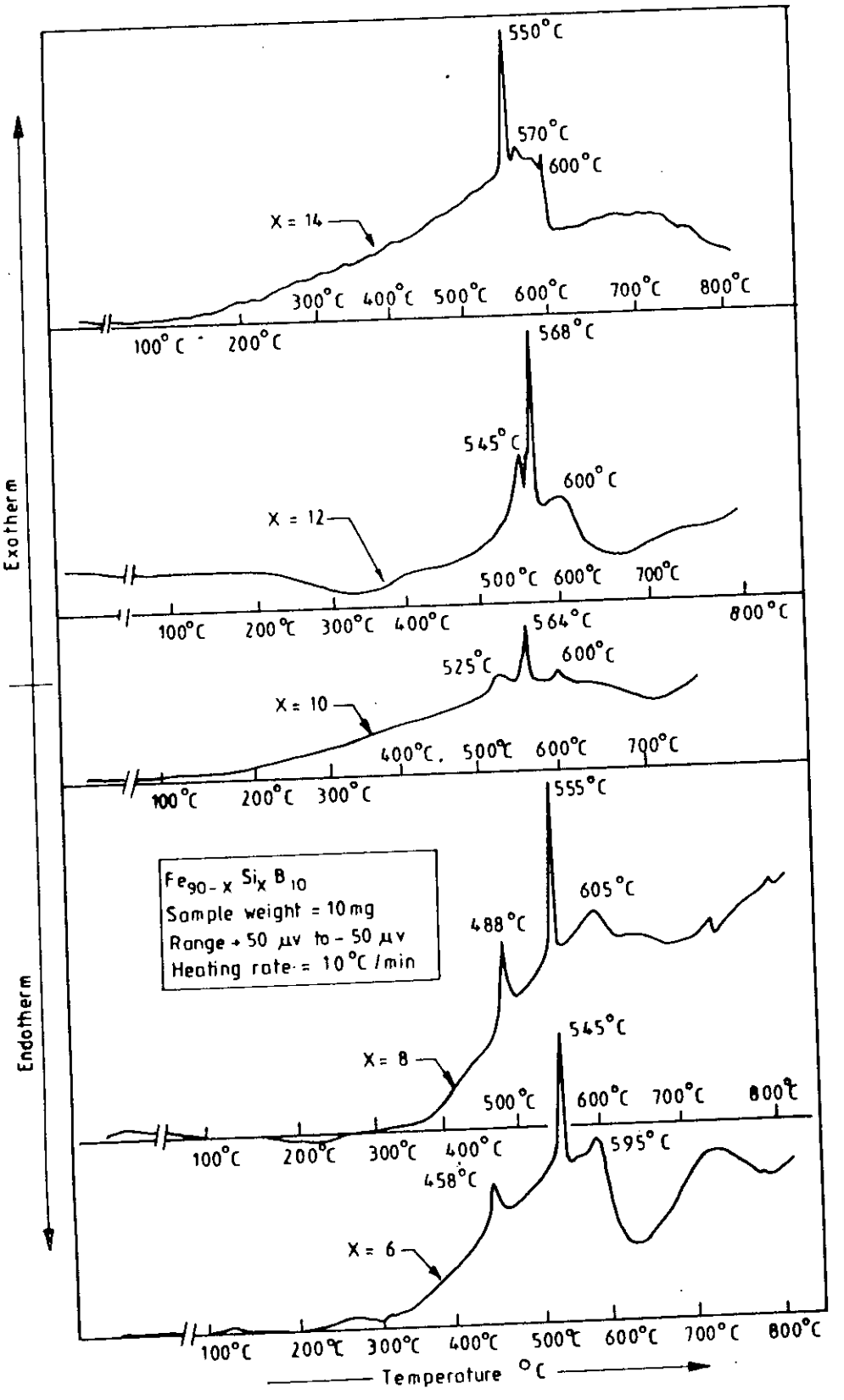

Fig.-5.2. Determination of T_g, T_X and T_x' from DTA graph of amorphous ribbons with composition $Fe_{90-x}Si_xB_{10}$ [x=14, 12, 10, 8 & 6].

Fig-5.3 shows the dependence of T_g, T_x and T_x' on silicon content. T_g is increases with silicon content and reaches to a saturation value for 12 atomic percentage of silicon. T_x also increase slightly with the increase of Si-content. The secondary crystallization temperature T_x' remains unchanged with the addition of Si-content. These results are important in the selection of composition for making amorphous ribbons to be used as core materials.

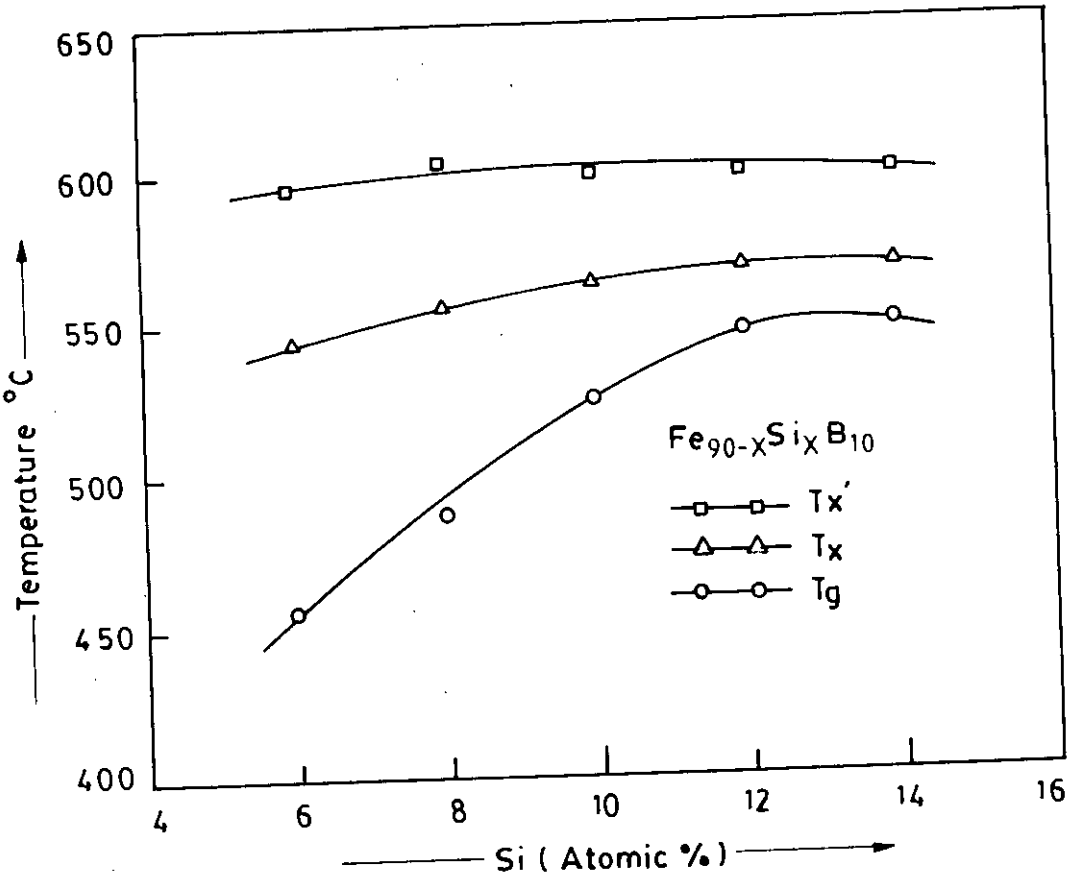

Fig.-5.3. Variation of T_g, T_X and T_x' due to change in the silicon content in $Fe_{90-x}Si_xB_{10}$ amorphous ribbons.

5.2. Curie Temperatures of the Amorphous Ribbons

The curie temperature T_c is a basic parameter in the study of magnetic phase transitions in ferromagnetic alloys. It is well known that T_c of an alloy in the crystalline and the amorphous state differ, and in spite of chemical and structural disorder, an amorphous ferromagnet, most offen, demonstrate a well defined ferromagnetic ordering temperature T_c which has been confirmed by magnetization versus temperature curves, Mössbauer effects and specific heat measurements(5.1). It is demonstrated that T_c determined for the magnetization VS temperature curve do not provide unambiguous results due to structural disorder and chemical disorder. The accurate determination of the Curie temperature of the amorphous materials is quite difficult, because one has to have adequate knowledge of the relaxation process that generally take place during the heating of the sample. During the measurement of the Curie temperature the heating rate should be adjusted in such a way that, no crystallization can take place.

It is shown that for temperatures below 100°c no noticeable effects in glassy materials are produced(5.2). Curie temperature has been estimated from the μ Vs T curve, where T_c corresponds to the temperature at which dM/dt attains a maximum value. It is interesting to note that the sharp fall of permeability at T_c enables us to determine T_c unambiguously. From the experiences during the course of this work it is found out that the heating rate should be above 10°c/min. to determine T_c of an amorphous sample in this system. It is also noticed that a higher T_c and a lower heating rate fails to determine T_c, because, the longer time initiate nucleation of crystallites which hampers the determination of T_c of the perfect amorphous state. The sharp fall of the A.C. initial permeability at T_c indicates that the material is quite homogeneous from the point of view of amorphousity. It is also observed from this curve that the permeability increases with temperature and attains the maximum value just before T_c, which we consider to be due to Hopkinson effect, as described by Kersten *et. al.*(5.3).

5.2.1. Curie Temperature Measurements of Amorphous Iron-Silicon-Boron Ribbons

Amorphous Iron-Silicon-Boron ribbons of composition $Fe_{90-x}Si_xB_{10}$ [x = 6, 8, 10, 12 & 14] have been chosen for the determination of the Curie temperature (T_c), using the μ Vs.T curves. Temperature dependence of A.C. initial permeability of the samples subjected to a heating rate of 12°C / min. and the constant frequency of 30KHz

was used for exciting current from a signal generator as shown in fig.-5.4. The numerical values of T_c's for all the samples are shown in Table-5.2.

Table-5.2.

$Fe_{90-x}Si_xB_{10}$	x = 6	x = 8	x = 10	x = 12	x = 14
T_c	357°C	387°C	421°C	434°C	448°C

Fig.-5.4. shows that the A.C. initial permeability of Fe-Si-B amorphous system increases with decreasing silicon content and has the maximum value at 8At.% of silicon. Beyond this point there is a decrease in the permeability.

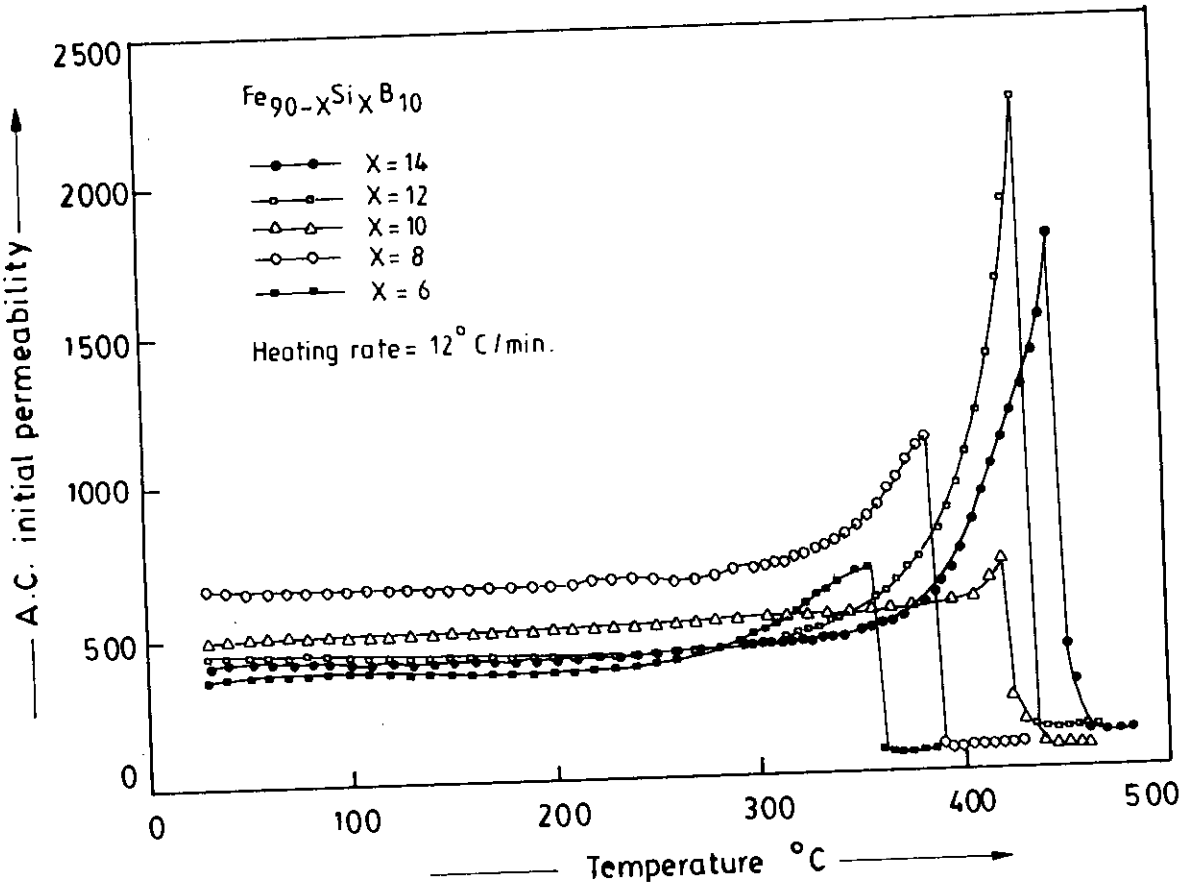

Fig.-5.4. T_c determination from temperature dependence of A.C. initial permeability of amorphous ribbons with composition $Fe_{90-x}Si_xB_{10}$.

Fig.-5.5. shows the dependence of T_c on the silicon content. It is observed that T_c increases with increasing silicon content. In the first place the addition of silicon as a

third element makes the alloy system more complex. This complexity of the chemical bonds between the constituent atoms should increase the relaxation time for the transformation from amorphous to crystalline state. Secondly, the diffusion of the silicon atoms into the interstitial positions bring about an increase in density.

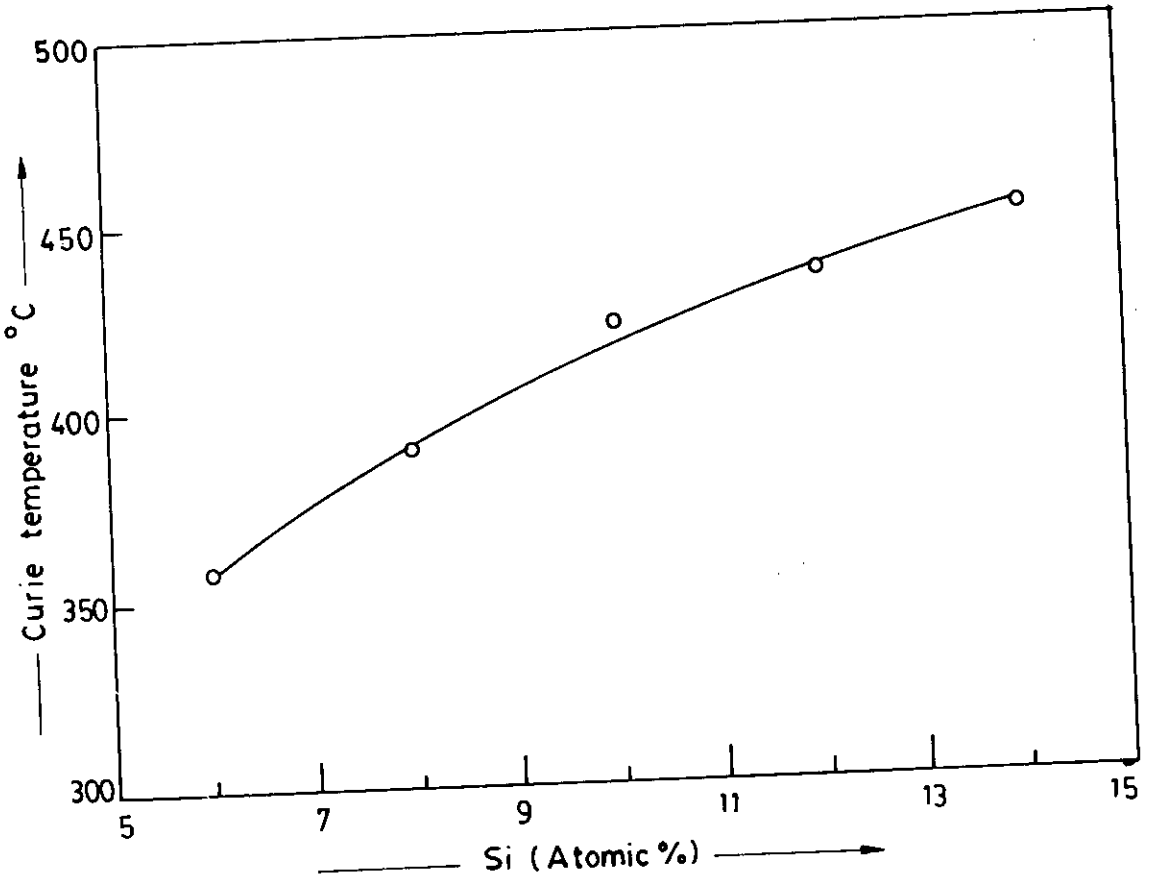

Fig.-5.5. Variation of T_c due to change in the silicon content in $Fe_{90-x}Si_xB_{10}$ amorphous ribbons.

Unambiguous and sharp values of T_c, obtained from our measurements, support the fact that, in spite of chemical and structural disorder, ferromagnetic glass have well defined magnetic ordering temperature. A quantitative understanding of magnetism in amorphous solids is very difficult and is as yet an unsolved problem, because, the chemical and structural disorder change all the important parameters like magnetic moment and exchange integral of the system. However, the coupling of the moments in an amorphous system arising from single site exchange, which takes place by the inter site hoping electrons, produce a correlation between the moments at different magnetic atoms. Since the exchange interaction in amorphous transition metal metalloid alloys is assumed to be of RKKY type, the magnitude of exchange integral is quite likely to

depend on the interatomic distance between the magnetic atoms. Our observed increase of T_c with increasing silicon content can be understood, in principle, as arising from the dependence of J_{ij} on r_{ij}. The equation guiding the mechanism can be written as

$$T_c = \left[2S(S+1)/3K\right]\sum_{ij} J_{ij}(r_{ij}), \qquad (5.1)$$

assuming a molecular field approximation, where S is the spin number, K is Boltzmann constant and J_{ij} is exchange integral between atoms at position r_i and r_j. The results reported by Durand *et. al.*(5.4) on the Fe-P-B alloys shows that with fixed concentrations of P, there is an increase of T_c with increasing boron. This is quite in keeping with the results, that there is an increase in T_c when iron atoms are replace by silicon atoms with the number of boron atoms remaining fixed.

5.3. Determination of Maximum Permeability, Maximum induction, Coercive force and Remanence of Fe-based Amorphous Ribbons

Amorphous Iron-Silicon-Boron ribbons having composition $Fe_{90-x}Si_xB_{10}$ [x = 6, 8, 10, 12 & 14] are of great interest as a soft magnetic material for their static measurements. For static magnetic characteristics like saturation magnetic induction (B_s), coercive force (H_c), maximum permeability (μ_m) and the ratio (B_r/B_s) have been obtained for the as-cast ribbons from the experimental hysteresis curves. The ribbons were wound into the toroidal ring cores having 13 to 15mm outer diameter and 10mm inner diameter. In the as-quenched state these magnetic materials show very soft magnetic properties with rectangular hysteresis curves. From the hysteresis curves of amorphous Fe-based ribbons with 10At.% boron and 6 to 14At.% of Si as glass forming materials, static magnetic characteristics have been measured using a low static field up to 34A/m for all the compositions. The coercive force and the hysteresis losses are controlled by the process of magnetization reversal and thus depends on magnetic domain nucleation, irreversible rotation of magnetic domains and domain wall motion. The remanence $B_r \cong 0.86$ to $0.89B_s$ and $H_c \cong 4.6$ to 7.8A/m have been observed in Fe-based $Fe_{90-x}Si_xB_{10}$ amorphous ribbons. The results of our observation are shown in summary from in Table-5.3.

Table-5.3

$Fe_{90-x}Si_xB_{10}$	x =6	x = 8	x =10	x =12	x =14
$H_c(A/m)$	7.8	4.6	5.0	5.6	6.8
$B_r(mT)$	763.98	731.61	722.74	702.68	716.52
$B_s(mT)$	859.04	850.86	837.32	817.66	803.90
B_r/B_s	0.89	0.86	0.86	0.86	0.89
μ_m	29,467	36,484	33,723	32,195	30,670

Numerous intrinsic and extrinsic properties and the conditions which determine the magnetic B-H hysteresis curves are shown in fig.-5.6(a) and fig.-5.6(b). The saturation induction B_s is an intrinsic property and is typically dominated by the alloy composition and structure. Structural defects have minor effects. All other characteristics of the B-H curves depend on numerous properties and factors affecting the reversal of magnetization during a change of the applied magnetic field. For example, a low magnitude of the stress induced anisotropy constant K_u leads to a low coercive force H_c required for magnetically soft materials, because spin rotation is independent of the lattice. Therefore, amorphous metals, which have no crystal lattice and low induced magnetic anisotropy behave as ideal soft magnetic materials.

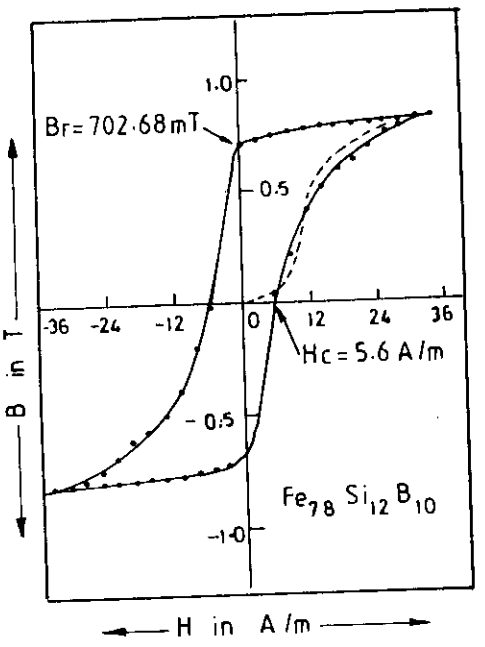

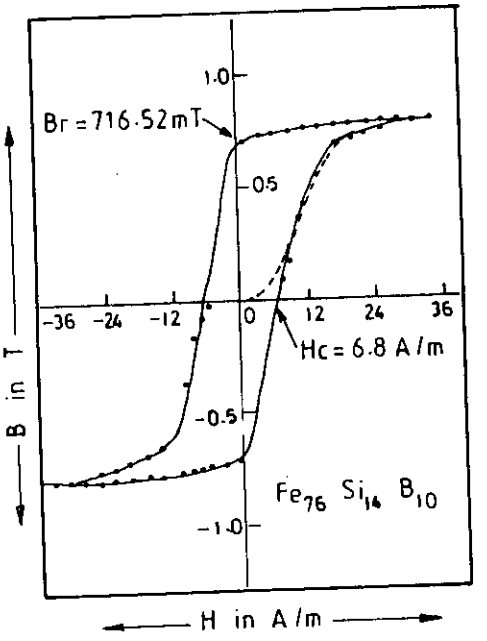

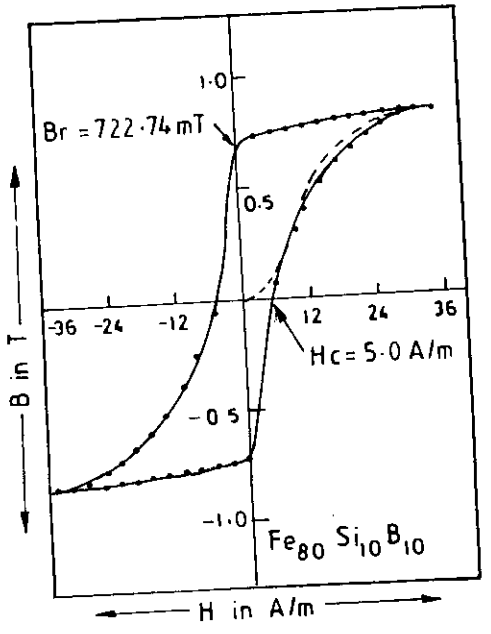

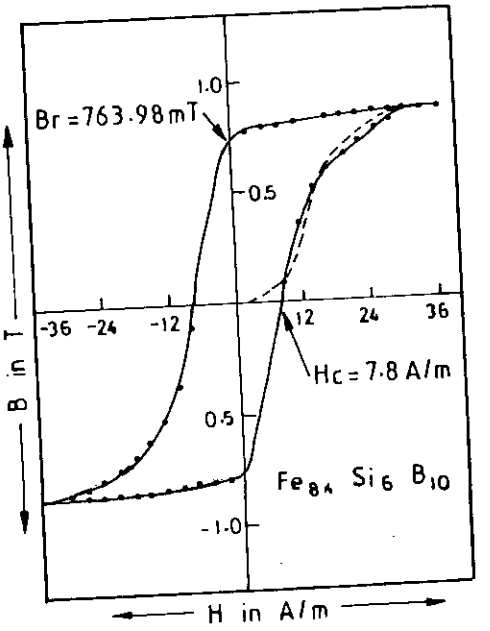

5.6(a). Hysteresis curve of amorphous ribbons with composition $Fe_{90-x}Si_xB_{10}$.

[x = 14, 12, 10 & 6]

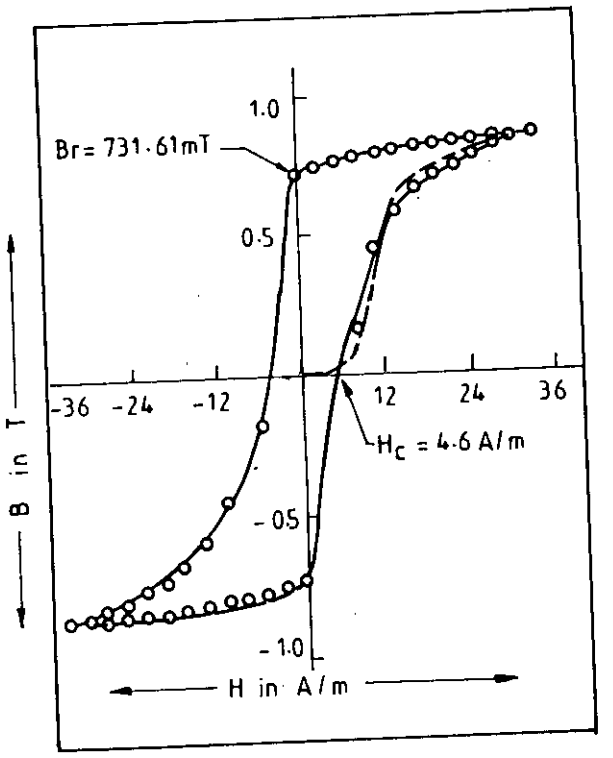

Fig.-5.6(b). Hysteresis curve of the amorphous ribbon with composition $Fe_{82}Si_8B_{10}$

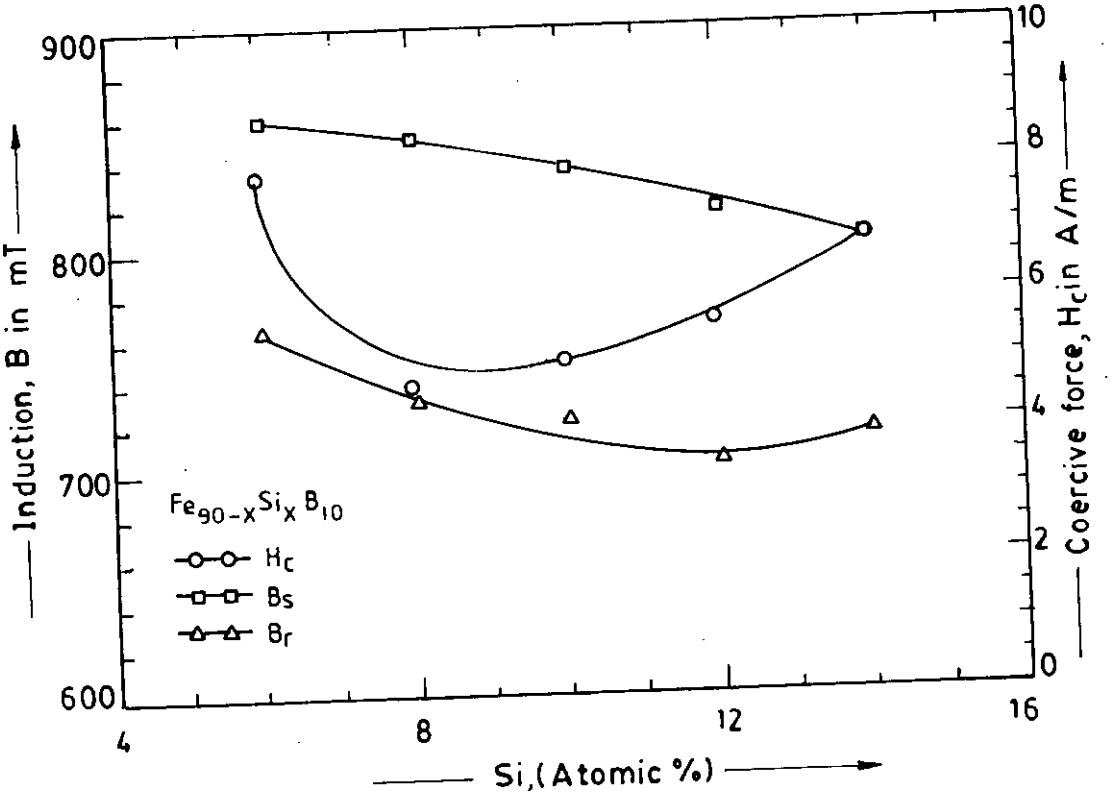

Fig.-5.7. Magnetic induction and coercive force variation with atomic percent of silicon content of amorphous ribbons with composition $Fe_{90-x}Si_xB_{10}$.

Fig.-5.6(a) and fig.-5.6(b) in combination with Table-5.4 represent the design parameters H_c, B_r, B_s, B_r/B_s and μ_m.

The rectangular shapes of the hysteresis curves show that materials are magnetically very soft and need very low field for saturation magnetization. The smooth nature of the experimental data which feat the hysteresis curve show the domain wall movements. One special feature of the initial magnetization curve represented by the doted line. Fig.-5.7 shows the variation of B_r, B_s and H_c of $Fe_{90-x}Si_xB_{10}$ alloy system, where x varies from 6 to 14 atomic percentage. It is observed that B_s decreased slowly with increasing percentage of silicon, and B_r decreased slowly up to increasing 12 atomic percentage of silicon and then increased with the increase of silicon. The H_c of the alloy system initially decreases with decreasing silicon up to 8 atomic percent and then increases with decrease of the Si-content.

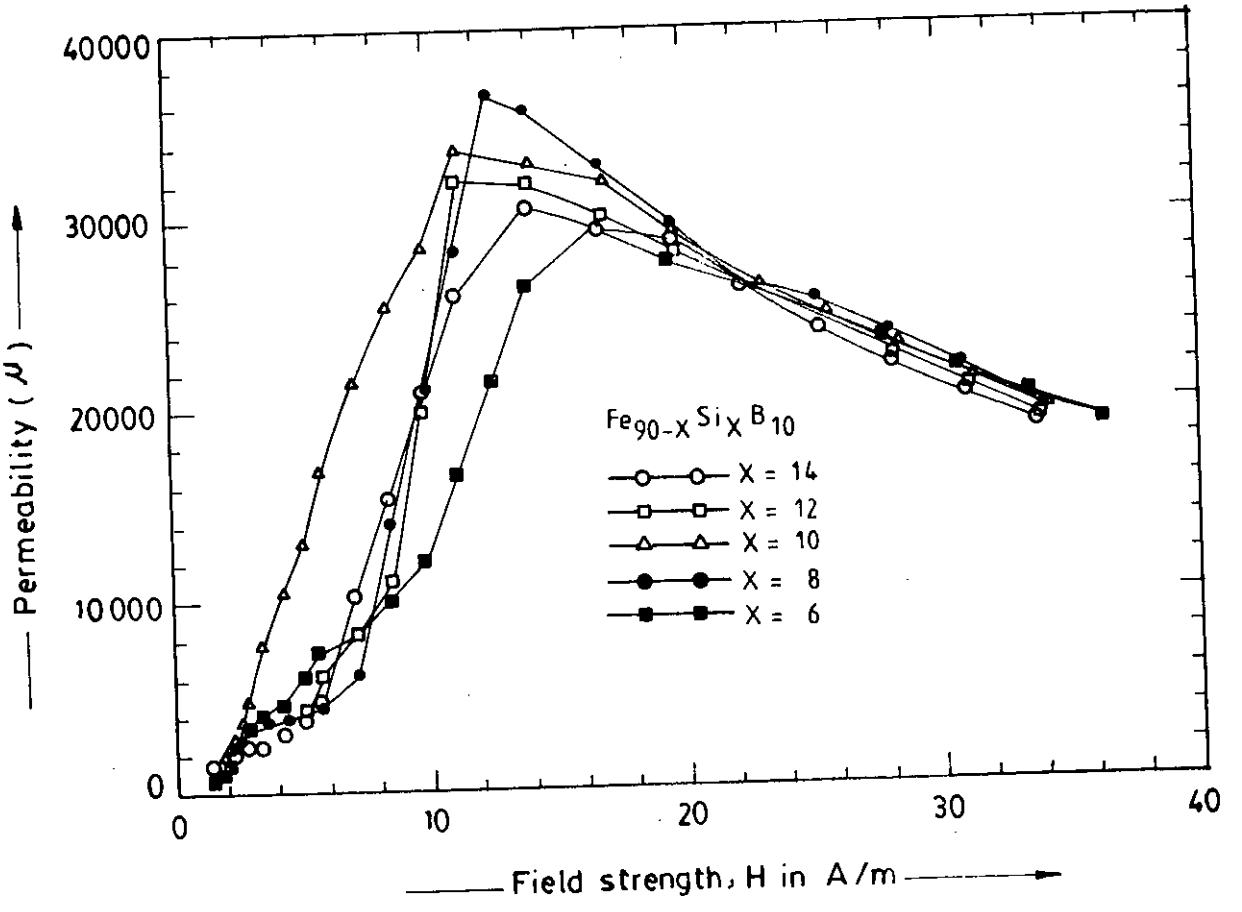

Fig.-5.8. Permeability versus static magnetic field of amorphous ribbons with composition $Fe_{90-x}Si_xB_{10}$

Permeability due to static external field from 0.4 to 34A/m for the ribbons with composition $Fe_{90-x}Si_xB_{10}$ are shown in fig.-5.8. The maximum permeability occurs at different fields 16.79, 12.66, 11.44, 11.37 and 14.15A/m for the compositions $Fe_{84}Si_6B_{10}$, $Fe_{82}Si_8B_{10}$, $Fe_{80}Si_{10}B_{10}$, $Fe_{78}Si_{12}B_{10}$ and $Fe_{76}Si_{14}B_{10}$ respectively, and hence corresponding values of μ_m are shown in Table-5.3. The μ_m values are very high and are nearly the same for all the compositions. Thus μ becomes independent of H at values of H for which $d\mu/dH = 0$ and the operating point should be close to the field that corresponds to maximum permeability and this will ensure high value of permeability and the field independence of the permeability.

5.4. Dynamic Magnetic Properties of Fe-based Amorphous Ribbons.

Dynamic magnetic properties of as-quenched Iron-Silicon-Boron system with composition $Fe_{90-x}Si_xB_{10}$ [x = 6, 8, 10, 12 & 14] have been determined using the impedance analyzer. The dynamic measurements of these amorphous alloys have been carried out to determine the frequency dependence of complex permeability, loss factor $(\tan\delta)$ and relative quality factor $\left(\mu/\tan\delta\right)$. The initial permeability (μ_i) of the amorphous ribbons, which is extrapolated to zero frequency and for vanishing magnetic field is estimated. Since the permeability cannot be measured without applying some field, the μ_i of the amorphous ribbons at very low frequency in our dynamic measurement, is assumed as a limiting case that corresponds to a static field. The μ_i of the ribbons with composition $Fe_{90-x}Si_xB_{10}$ is calculated from the low A.C. magnetic field dependence of permeability in the limit of frequency 0.5KHz and vanishing magnetic field as shown in fig.-5.9. The results are shown in Table-5.4.

Table-5.4.

$Fe_{90-x}Si_xB_{10}$	x =14	x =12	x =10	x = 8	x = 6
μ_i	524	547	566	571	394

As shown in fig.-5.9, the μ_i in the vanishing magnetic field region for all the ribbons, except for the composition $Fe_{78}Si_{12}B_{10}$, remain almost constant for slight variation of the field. Initial permeability is controlled by the irreversible part of the domain motion and the preparation technique determines the defects and the associated energy barriers to domain wall motion. Another accurate way to determine the μ_i value is for plot the imaginary part of the complex permeability (μ'') against the real part of the complex permeability (μ'). For any applied field, this representation shows a semicircle for the high frequency range. For low frequencies , if the applied field is lower than or equal to the propagation field, a short; vertical spike is observed. The μ_i value is determined from the semicircle's diameter i.e. from the intersection of the semicircle with the μ' axis. In the representative fig.-5.10, the results for the as-quenched sample with composition $Fe_{80}Si_{10}B_{10}$ is given. The calculated parameter of all the samples shown in Table-5.4 agree well with the values determined by extrapolation technique.

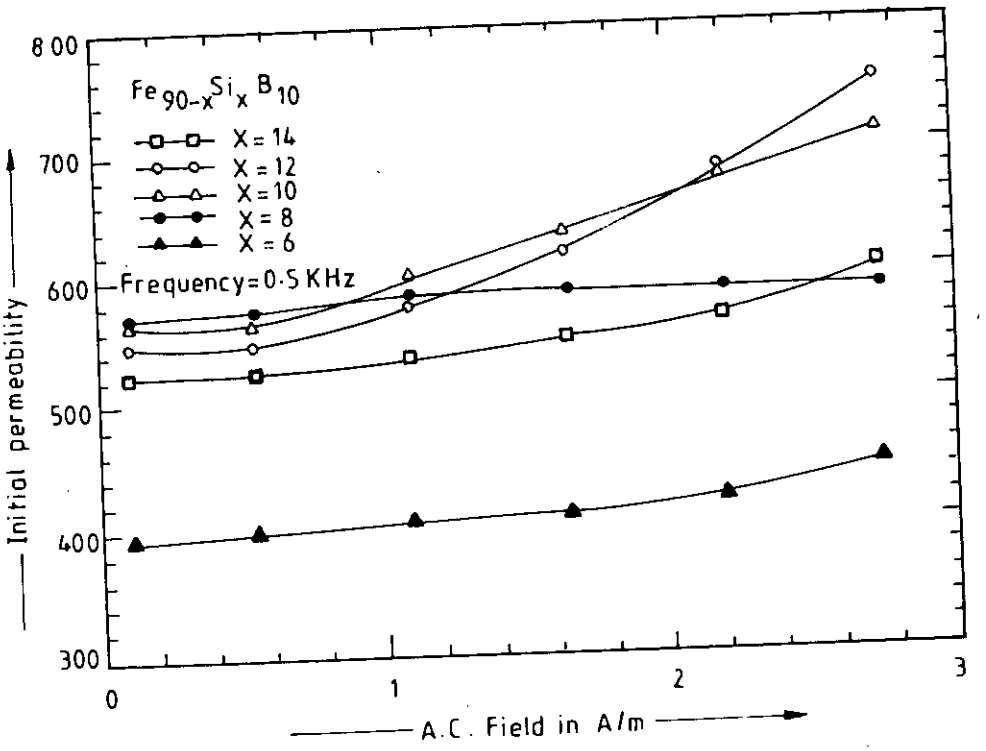

Fig.-5.9. Permeability versus A.C. magnetic field of amorphous ribbons with composition $Fe_{90-x}Si_xB_{10}$

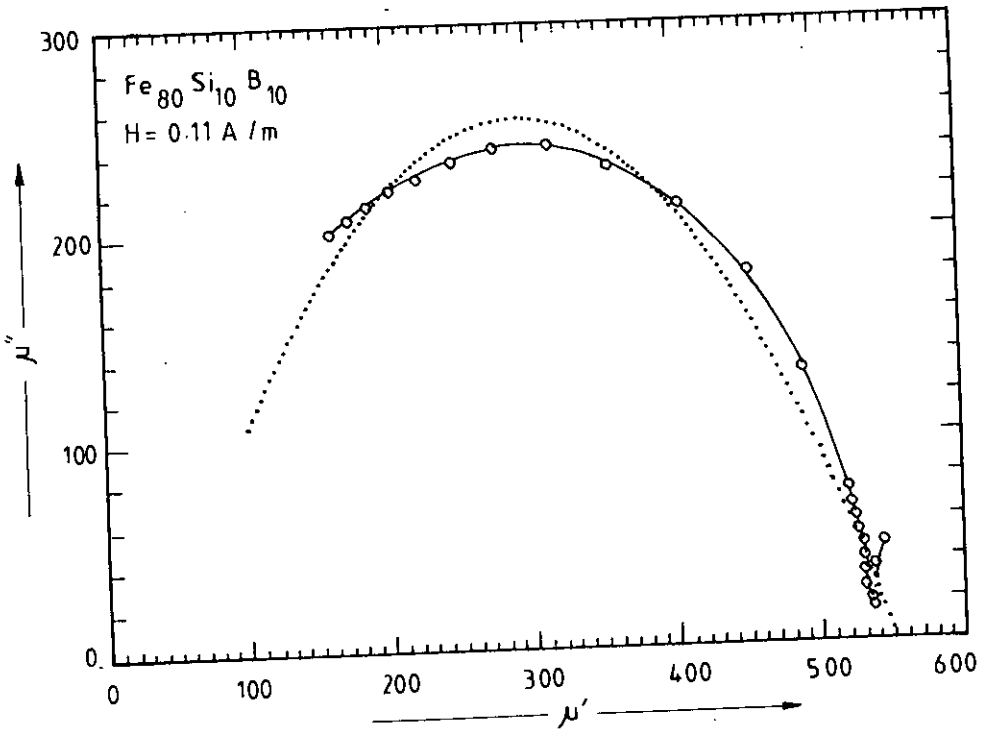

Fig.-5.10. Complex permeability μ'' Vs μ' plot for the as-quenched sample with composition $Fe_{80}Si_{10}B_{10}$

Fig.-5.11 shows that the μ_i of Fe-Si-B amorphous system increase with decreasing of Si-content upto 8At.%, and beyond this point there is a decreases with decreasing Si-content. The increase in the initial permeability upto 8 At.% of silicon may by explained as due to the decrease in magnetostriction as occurs in crystalline Fe-Si alloy. The decrease μ_i when the percentage of Si is increased beyond 8 At.%, is explained as due to the decrease in the magnetic moment arising from the dilution of the magnetic system. One does not ofcourse expect identical behaviour for amorphous and crystalline solids. But we find the general trend to be similar

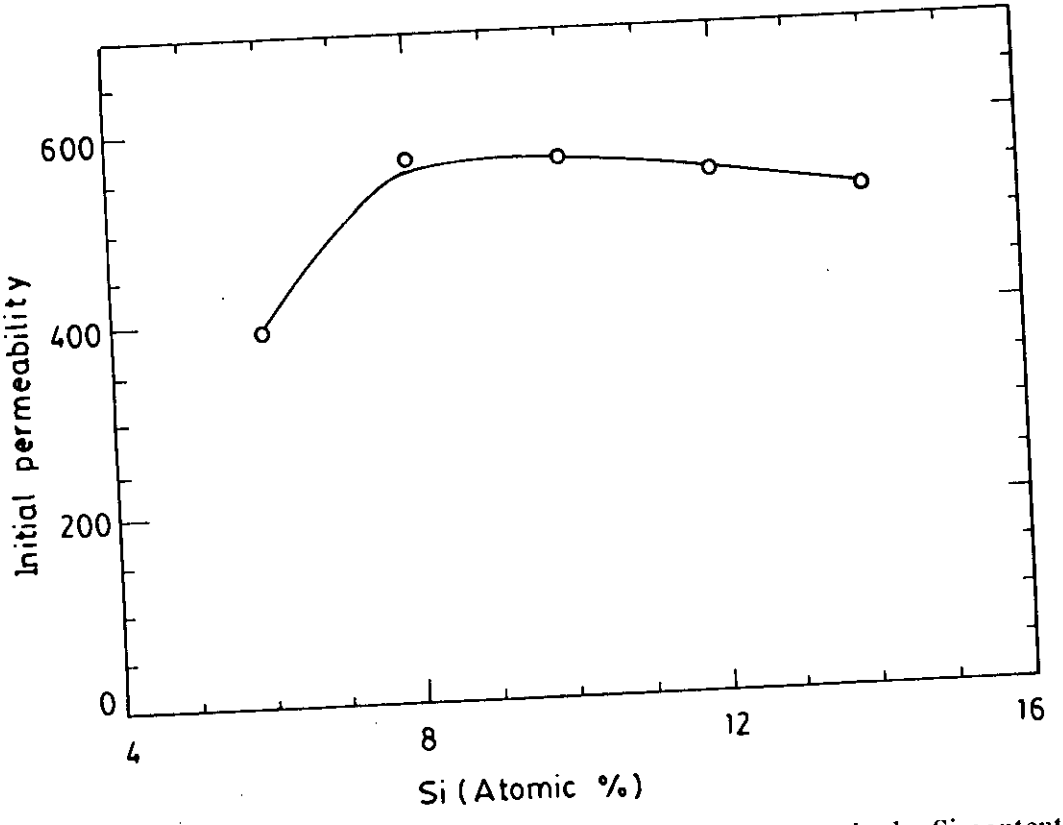

Fig.-5.11. Variation of initial permeability due to change in the Si-content in $Fe_{90-x}Si_xB_{10}$ amorphous ribbons.

The measurements were performed at room temperature using an A.C. fields with a very low constant value of H = 0.1A/m and frequency range from 0.5KHZ to 13MHz. The frequency dependence of the real part of complex permeability is shown in fig.-5.12. The flat region up to the frequency 1 to 3MHz indicates that except the ribbon with composition $Fe_{78}Si_{12}B_{10}$, all the other four samples of composition $Fe_{76}Si_{14}B_{10}$, $Fe_{80}Si_{10}B_{10}$, $Fe_{82}Si_8B_{10}$ and $Fe_{84}Si_6B_{10}$ respectively appear to be very suitable as core materials at low fields.

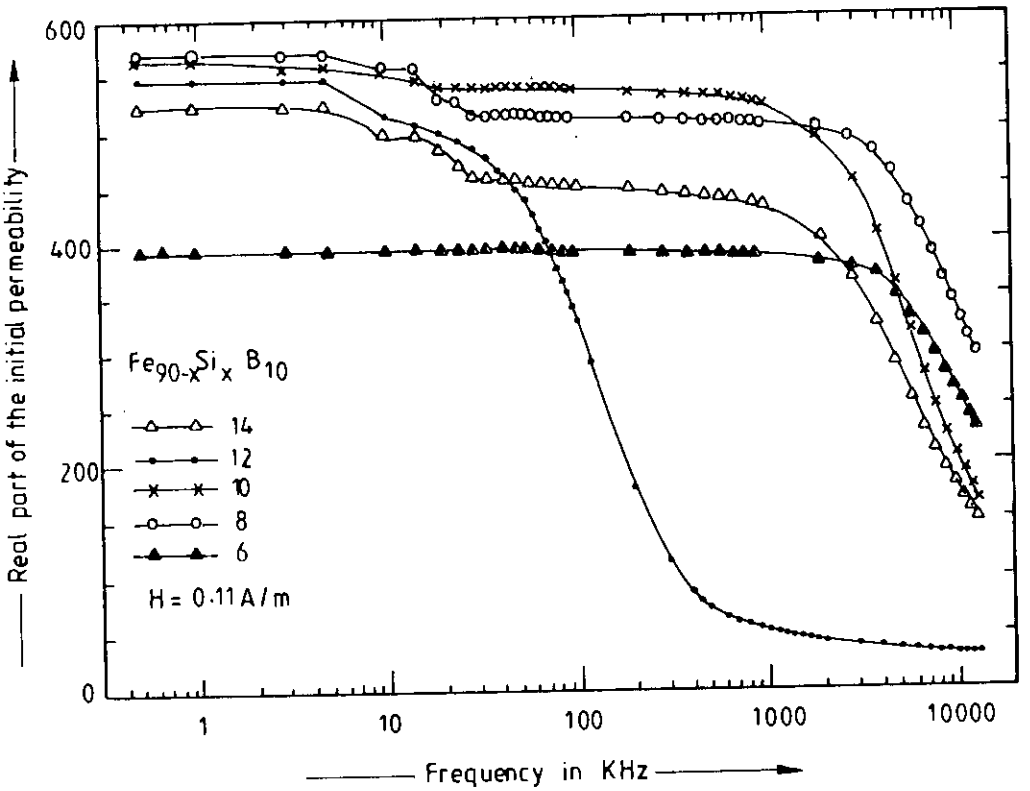

Fig.-5.12. Frequency dependence of the real part of complex permeability of amorphous ribbons with composition $Fe_{90-x}Si_xB_{10}$.

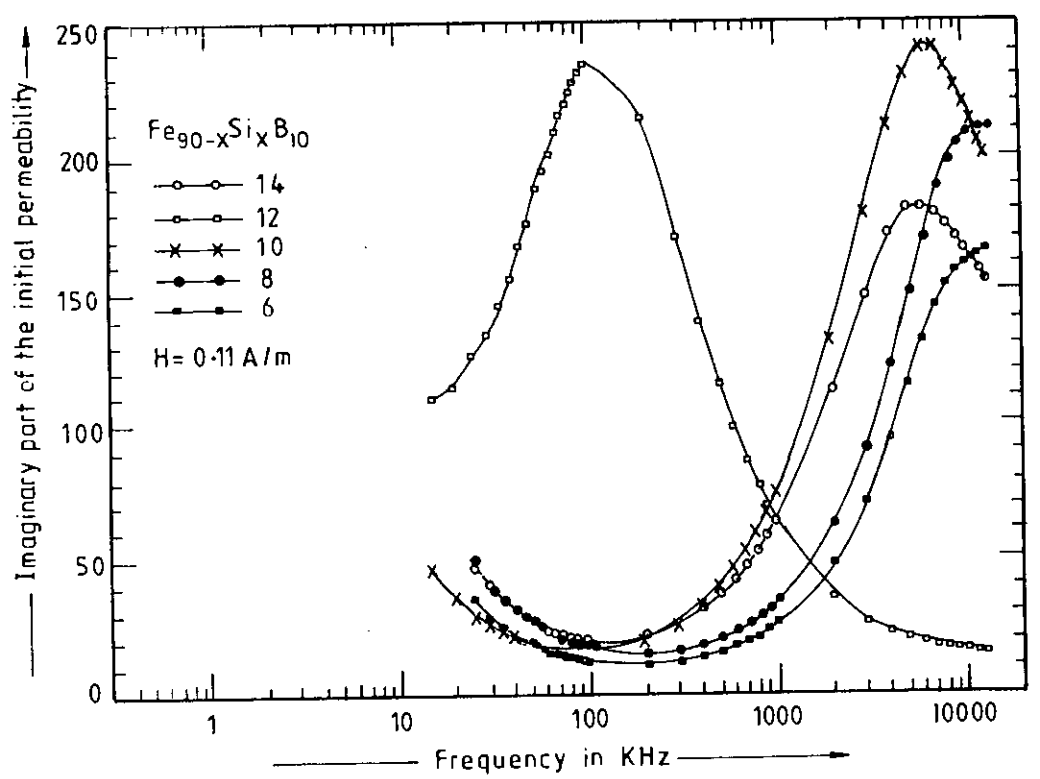

Fig.-5.13. Frequency dependence of the imaginary part of complex permeability of amorphous ribbons with composition $Fe_{90-x}Si_xB_{10}$

The imaginary part of the complex permeability and loss factor for different compositions over the frequency range 0.5KHz to 13MHz are shown in fig.-5.13 and fig.-5.14 respectively. The origin of the loss factors can be attributed to various domain defects[5.5], which include nonuniform and nonrepetitive domain wall motion, domain wall bowing, localized variation of flux density and nucleation and annihilation of domain walls. The principle cause of eddy current loss in amorphous ribbons is attributed to non sinusoidal and repetitive motion of domain walls. At low frequencies the loss is controlled by hysteresis losses and at high frequency the flux penetration becomes low and loss is controlled mainly by interaction between the grains.

The results show that the effects of grain size, grain orientation and specimen thickness are important. The precipitation of very small percent of particles improve the high frequency losses and permeability[5.6]. The Si-content has important effect and except the ribbon with composition $Fe_{78}Si_{12}B_{10}$, the other four samples having composition $Fe_{76}Si_{14}B_{10}$, $Fe_{80}Si_{10}B_{10}$, $Fe_{82}Si_8B_{10}$ and $Fe_{84}Si_6B_{10}$ show almost identical behaviour in their performances and have low loss factors at frequencies up to 3MHz.

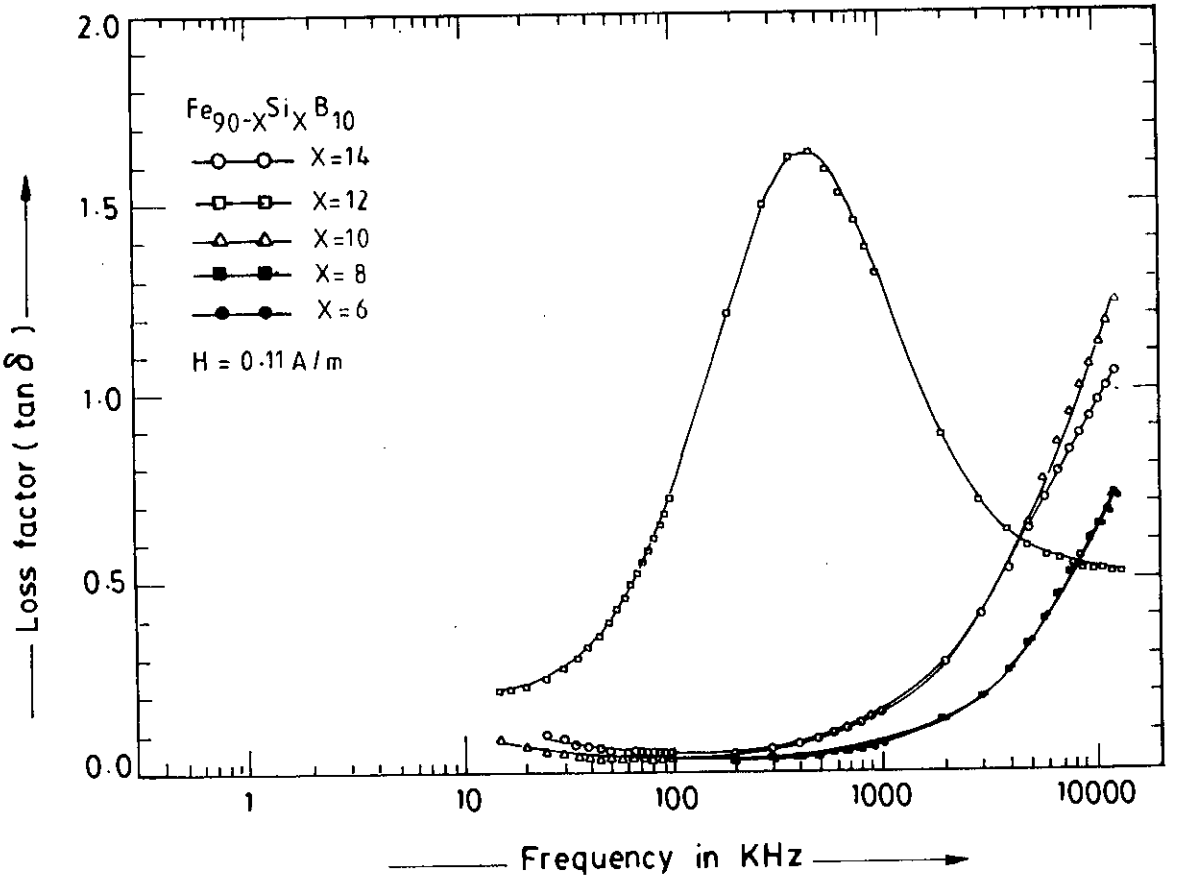

5.14. Frequency dependence of loss factors of amorphous ribbons with composition $Fe_{90-x}Si_xB_{10}$

The frequency dependence of relative quality factor is shown in fig.-5.15. The relative quality factors as controlled by the real part of the complex permeability have quite high values in the range 45KHz to 800KHz for the two ribbons having composition $Fe_{82}Si_8B_{10}$ and $Fe_{84}Si_6B_{10}$, this range is from 20KHZ to 500KHZ for the ribbons having composition $Fe_{76}Si_{14}B_{10}$and $Fe_{80}Si_{10}B_{10}$. These four ribbons, as a result, have low loss factors. The other ribbon with composition $Fe_{78}Si_{12}B_{10}$ have high loss factors and its relative quality factors is observed to be poor.

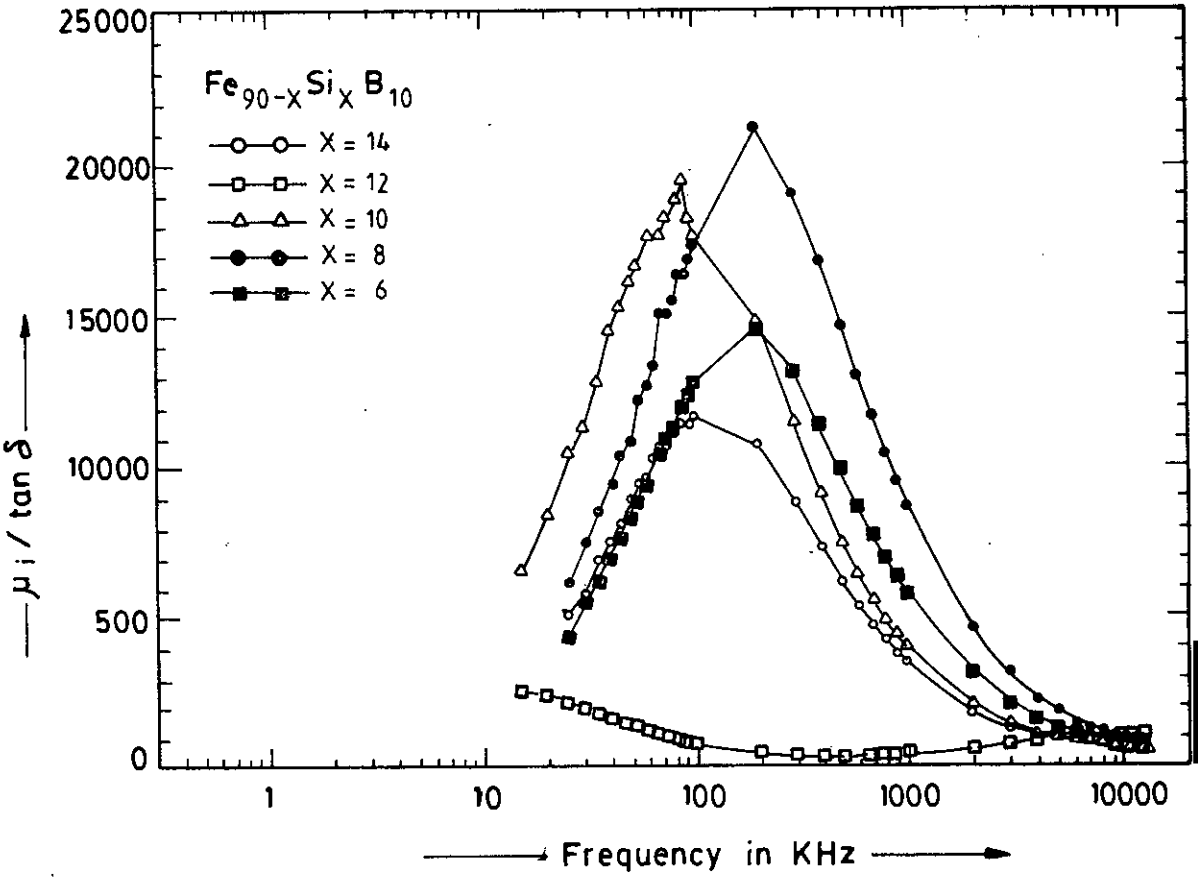

5.15. Frequency dependence of the relative quality factor of amorphous ribbons with composition $Fe_{90-x}Si_xB_{10}$.

Fig.-5.16 shows the effect of annealing on the initial permeability (μ_i) of amorphous ribbons with composition $Fe_{90-x}Si_xB_{10}$. The initial permeability of all the sample as affected by annealing at different temperatures with annealing time of one

hour in each case is measured at low frequency (1KHz) and in very low field (H = 0.1A/m). μ_i increases with annealing temperature and goes to maximum for the annealing temperature 400^0C for the ribbons having composition $Fe_{76}Si_{14}B_{10}$ and $Fe_{78}Si_{12}B_{10}$, and then decreases sharply when the annealing temperature is further increased. For the other two samples with compositions $Fe_{80}Si_{10}B_{10}$ and $Fe_{82}Si_8B_{10}$the corresponding maximum annealing temperature is found to be 350°C and for the sample with composition $Fe_{84}Si_6B_{10}$ the maximum annealing temperature 300°C. The significant increase in the μ_i of the annealed samples as observed with respect to the as-quenched samples, is explained as due to the removal of local strain and energy barriers in the sample. For annealing temperatures which are above the Curie temperature, the absence of domain walls leads to a random distribution of the short range order configuration and hence, to a significant decrease in domain wall pinning.

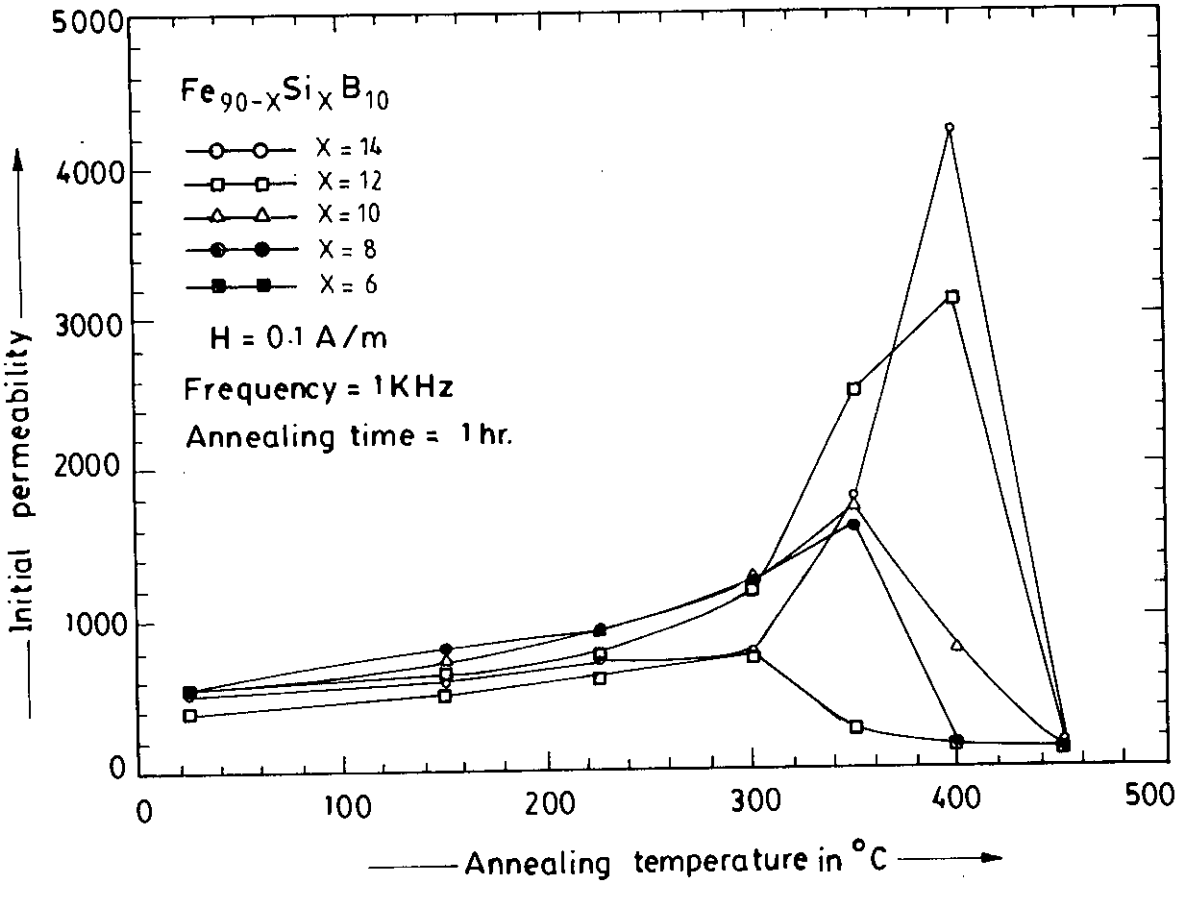

Fig.-5.16. Initial permeability versus annealing temperature of amorphous ribbons with composition $Fe_{90-x}Si_xB_{10}$.

5.5.0. Specific Magnetization Measurement of Fe-based Amorphous Ribbons

The magnetization of thin Iron-Silicon-Boron ribbons is measured as a function of magnetic field using a V.S.M.(5.7). The ribbon samples were cut into circular shapes, weighed and glued to a standard sample mount. The magnetometer was used as a field measuring device which was not affected by the presence of sample for its low susceptibility. The lock-in action of V.S.M. yields an accuracy of 0.05% of the full scale. The absolute accuracy of this system is better than 2% and the reproducibility is better than 1%. Least measurable moment is 5×10^{-4} emu. The proportionality constant accounting for the particular coil geometry and susceptibility is obtained by calibration with a high purity circular disk shaped nickel sample. The sample has a saturation moment of about $54.75 Am^2/Kg$ with a saturation flux of about 4KG. A relative accuracy of about 1% is obtained with the double coils, the absolute accuracy depends on the calibration method.

5.5.1. Specific Magnetization at Room Temperature

The Specific magnetization of these Fe-Si-B ribbons with composition $Fe_{90-x}Si_xB_{10}$ [x = 6, 8, 10, 12 & 14] in as quenched condition is measured, using a V.S.M. The magnetization process of the amorphous ribbons with different fields are shown in fig.-5.17. The saturation magnetization for these ribbons have higher values for higher percentage of iron. This is quite understandable from the consideration of higher contribution of magnetic moments in iron-rich ribbons. It is observed that while the ribbon with composition $Fe_{80}Si_{10}B_{10}$ reaches its saturation value around 3.0KG field, $Fe_{78}Si_{12}B_{10}$ requires 2.5KG, $Fe_{76}Si_{14}B_{10}$ requires 2.0KG, $Fe_{82}Si_8B_{10}$ requires 3.5KG and $Fe_{84}Si_6B_{10}$ requires 3.7KG. Magnetization is also evaluated as a function of field to find the dependence of magnetization on the domain structure. The saturation specific magnetization (σ_s) for different samples as calculated are shown in Table-5.5.

Table-5.5.

$Fe_{90-x}Si_xB_{10}$	x = 6	x = 8	x = 10	x = 12	x =14
σ_s in Am^2/Kg at room temp.	162.97	159.92	156.91	148.88	134.21
$\sigma_s(0)$ in Am^2/Kg at 0K	168	166	163	150	136
T_c	358^0C	388^0C	418^0C	434^0C	444^0C

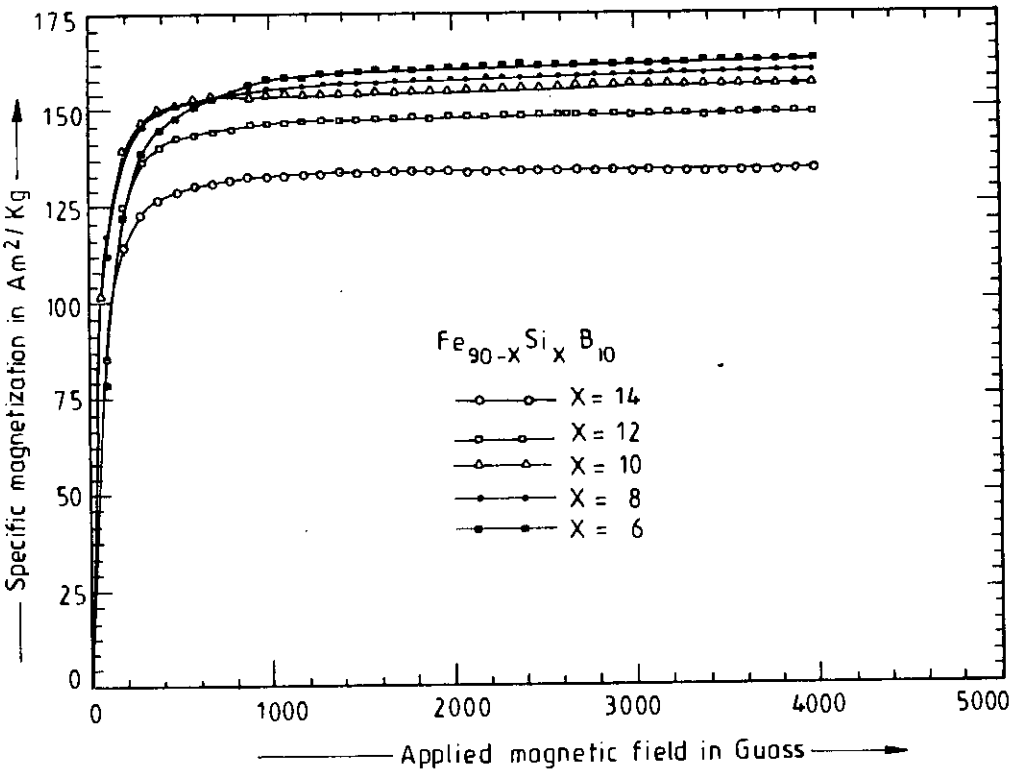

Fig.-5.17. Specific magnetization versus magnetic field of amorphous ribbons with composition $Fe_{90-x}Si_xB_{10}$.

The σ_s decreases with increasing Si-content, as shown in fig.-5.18. This is agreement with the moment per atom of the Fe-Si-B system where the moment is reduced due to the effect of electron transfer from the metalloid atoms to the Fe atoms. These results agree reasonably well with the rigid band model using the moment $2.6\mu_B$ for Fe and assigning an integral number of electron transfer from the metalloids, this number being 1 for B and 2 for Si. This can be well studied by Mössbauer spectroscopy, because the influence of the local environment on the iron moment is directly reflected in the hyperfine field distribution as shown section-5.7.

Magnetic saturation can be achieved only for Fe-based alloys. In this case, the local anisotropy is small and the next nearest neighbour exchange coupling leads to ferromagnetic order. The critical composition for the disappearance of ferromagnetism can be estimated from the extrapolation of the fall off curve of σ_s with the addition of

Si, where the nearest neighbour coupling is no longer dominant and an intermediate range occur, giving rise to a significant portion of antiferromagnetic interaction.

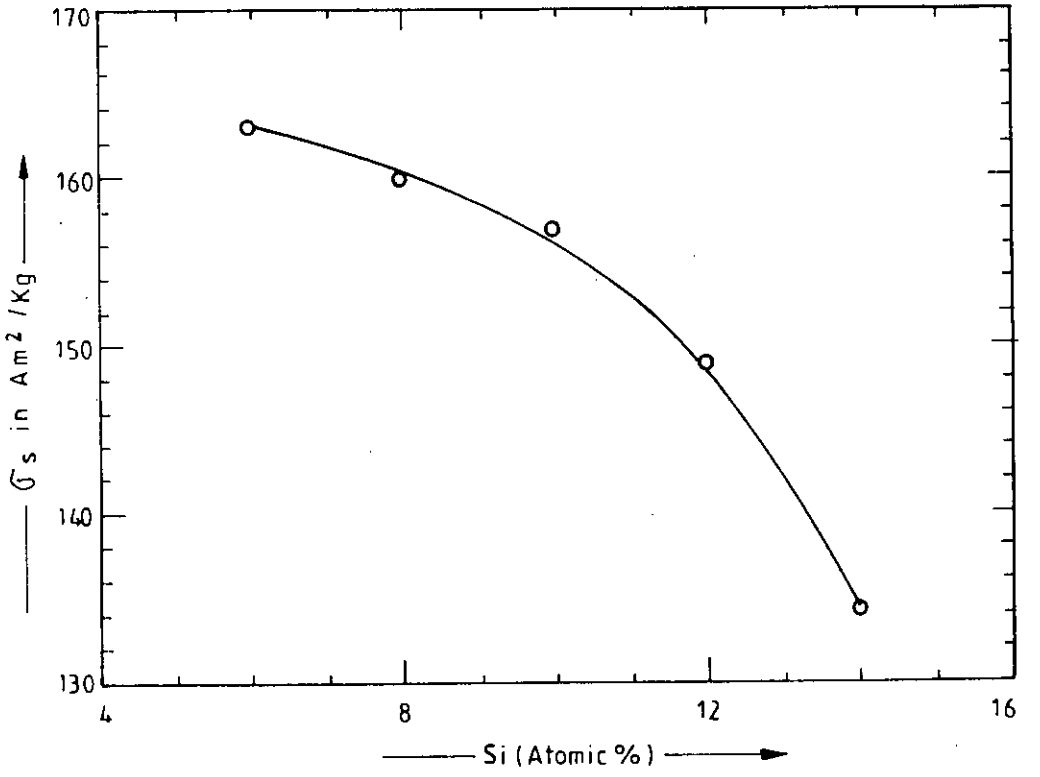

Fig.-5.18. Variation of saturation specific magnetization due to change in the Si-content in $Fe_{90-x}Si_xB_{10}$ amorphous ribbons.

5.5.2. Temperature Dependence of Specific Magnetization of Fe-based Amorphous Ribbons.

The effect of variation of temperature on specific saturation magnetization for amorphous ribbons with composition $Fe_{90-x}Si_xB_{10}$ are shown in fig.-5.19. The high temperature range, where the effect of clustering is important for the transition from the magnetically ordered state to the paramagnetic regime is shown in fig.-5.19. T_c corresponds to the temperature at which the internal magnetic field almost vanishes. Results for T_c by this method agrees with the values obtained from temperature dependence of initial permeability as discussed in section-5.2; fig.-5.5.

T_c depends on the transitionmetal spin value and the exchange constant. The disorder structure causes variation in the nearest neighbour distance and the number of nearest neighbours producing local fluctuations of the magnetic moment and the exchange coupling. Random fluctuations of the exchange coupling constant leads to an increase of T_c, provided the ferromagnetic coupling is maintained.

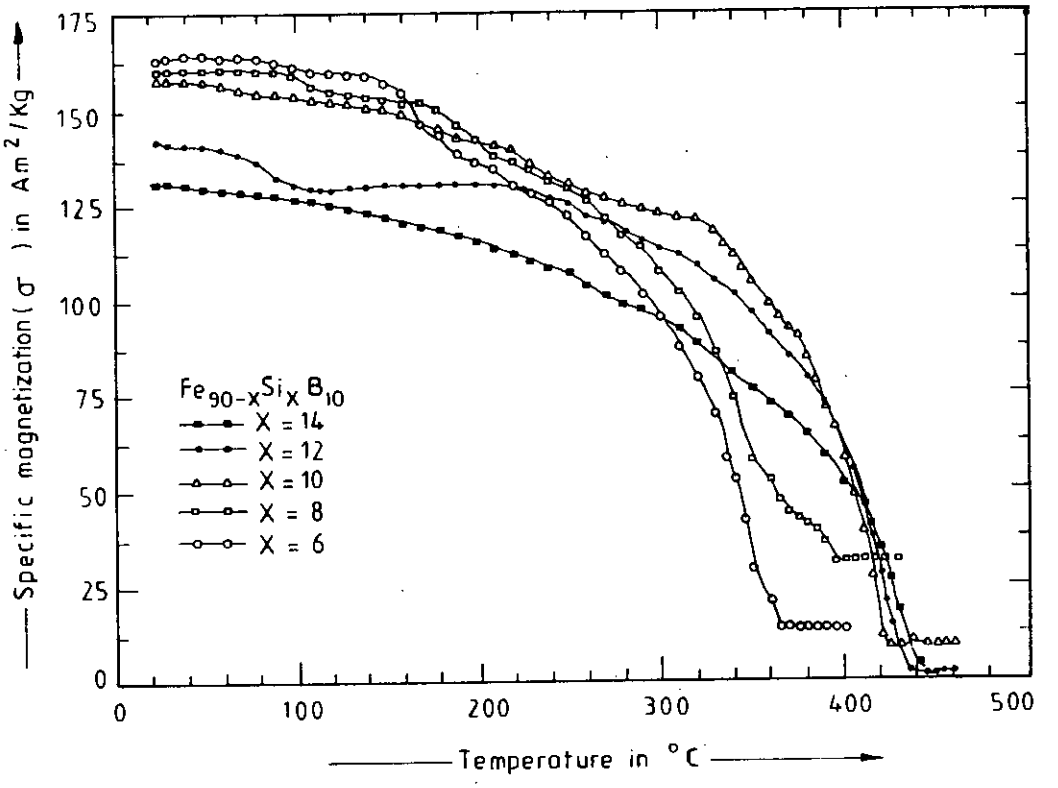

Fig.-5.19 Specific saturation magnetization as a function of temperature for $Fe_{90-x}Si_xB_{10}$ amorphous ribbons.

A typical temperature dependent saturation specific magnetization measured with H=4KG is shown in fig.-5.19. Saturation specific magnetization, $\sigma_s(0)$ at T=0 are obtained by extrapolating to 0K, the $\sigma_s(T)$ values measured at various temperature. The extrapolated values $\sigma_s(0)$ for different ribbons are value as shown in Table-5.5.

Plots of experimental data with mean field results of reduced magnetization $m = \frac{\sigma_s(T)}{\sigma_s(0)}$ with reduced temperature $= \frac{T}{T_c}$ for different Si content are shown in fig.-5.20. This description of the experimental data corresponds to the mean field approximation and the temperature independent treatment. Fig.-5.20 shows that the

fluctuations in the exchange interaction, hence the reduced magnetization arises from structural disorder. The full lines were calculated from the mean field theory, which are in good agreement with the experimental results for various Fe-Si-B ribbons. The best fit thus obtained is ofcourse no indication for high accuracy of the extracted values for the exchange constant. Reduced magnetization $m = \frac{\sigma_s(T)}{\sigma_s(0)}$ versus $\frac{T}{T_c}$ curves for amorphous ribbons with composition $Fe_{90-x}Si_xB_{10}$ lie substantially below that for crystalline iron. There is no complete theoretical understanding of this behaviour at present, a number of effective field approaches can be advanced to interpret the experimental data.

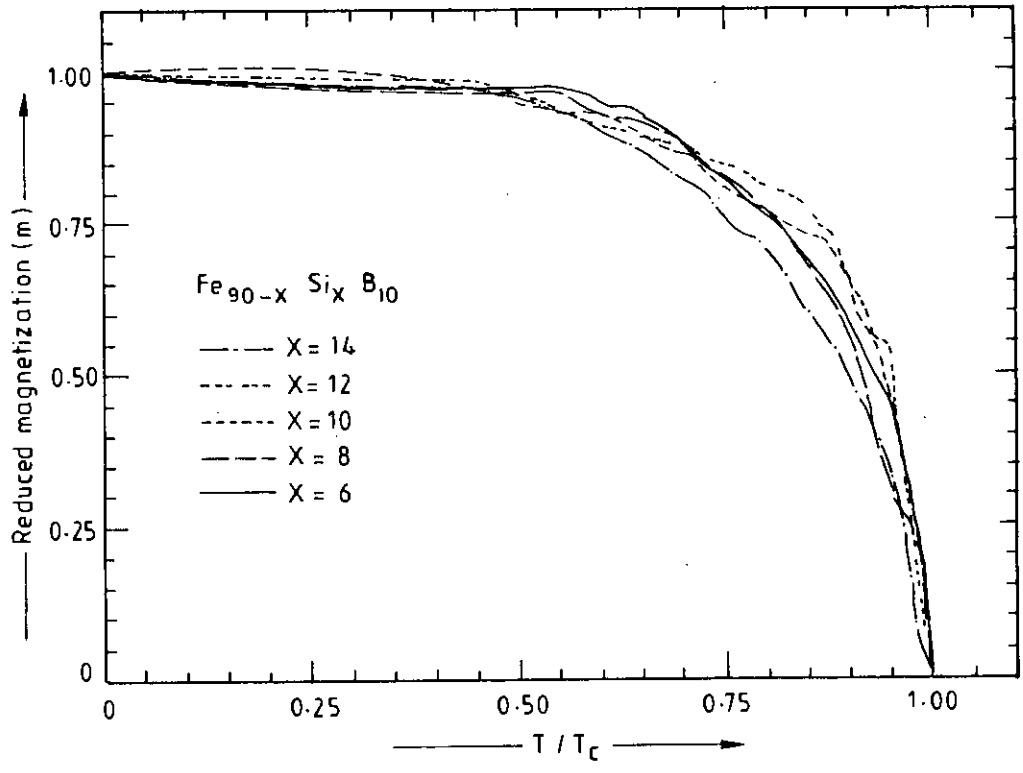

Fig.-5.20. Reduced magnetization $m = \frac{\sigma_s(T)}{\sigma_s(0)}$ versus $\frac{T}{T_c}$ for amorphous ribbons with composition $Fe_{90-x}Si_xB_{10}$

5.6. Stress Induced Anisotropy of Fe-based Amorphous Ribbons

The apparatus used is a standard Torque Magnetometer with proportional-integrating differentiating compensation which allows continuous registration of the torque as a function of the direction of the field. The laser source provides a coherent beam of constant intensity thus making the system free from light noise. To avoid any spuratic torque due to the image effect in the pole pieces, the specimens were pleased in the central position. The centre of the sample was made to coincide with the axis of the magnetometer and this is ensured by the exact repetition of the torque value at every 180^0 rotation of the field. A perfectly circular shape was cut from the ribbon to provide maximum symmetry about the axis of the rotating field. Samples were prepared as circular discs to avoid any shape anisotropy and associated demagnetizing effect. Torque against angle showed perfect reproduction for forward and reverse rotation of the field and for different samples cut from the same ribbon.

The field dependence of the torque versus angle curves are measured for as-quenched Fe-Si-B ribbons with composition $Fe_{90-x}Si_xB_{10}$ [x = 6, 8, 10, 12 & 14]. The representative torque versus angle curve of the field dependence of anisotropy of amorphous ribbon with composition $Fe_{82}Si_8B_{10}$ increases with increasing field as shown in fig.-5.21. This is explained as due to the competing contribution from Fe atoms to anisotropy energy. We assume that the origin of magnetic anisotropy in these ribbons, formed by melt spinning technique, is magnetostrictive strain. This concept is supported by the fact that the induced anisotropy developed in these ribbons is unidirectional and is coincident with the moving direction of the roller.

Amorphous ribbons have no crystalline structure and therefore are not likely to have magnetocrystalline anisotropy normally. However the Fe-Si-B system has a positive magnetostriction arising from the preparation technique and is attribute to the presence of Fe atoms which has positive magnetostriction in the bulk state. When a material with positive magnetostriction is strained it develops an easy direction of magnetization along the strain axis. In our prepared specimens the strain is induced along the length due to the tension on the ribbon produced by the centrifugal force. It is explained that for high percentage of Fe the magnetostrictive effect of Fe and the corresponding anisotropy will dominate(5.8).

It is, however, not possible to find any quantitative relation between anisotropy and composition in the case of amorphous materials, because the contribution of

different magnetic atoms through their random configurations in the amorphous state is too complicated. Our results are thus explained only in a qualitative way, considering the origin of anisotropy as due to magnetostrictive strain induced technically during the preparation process.

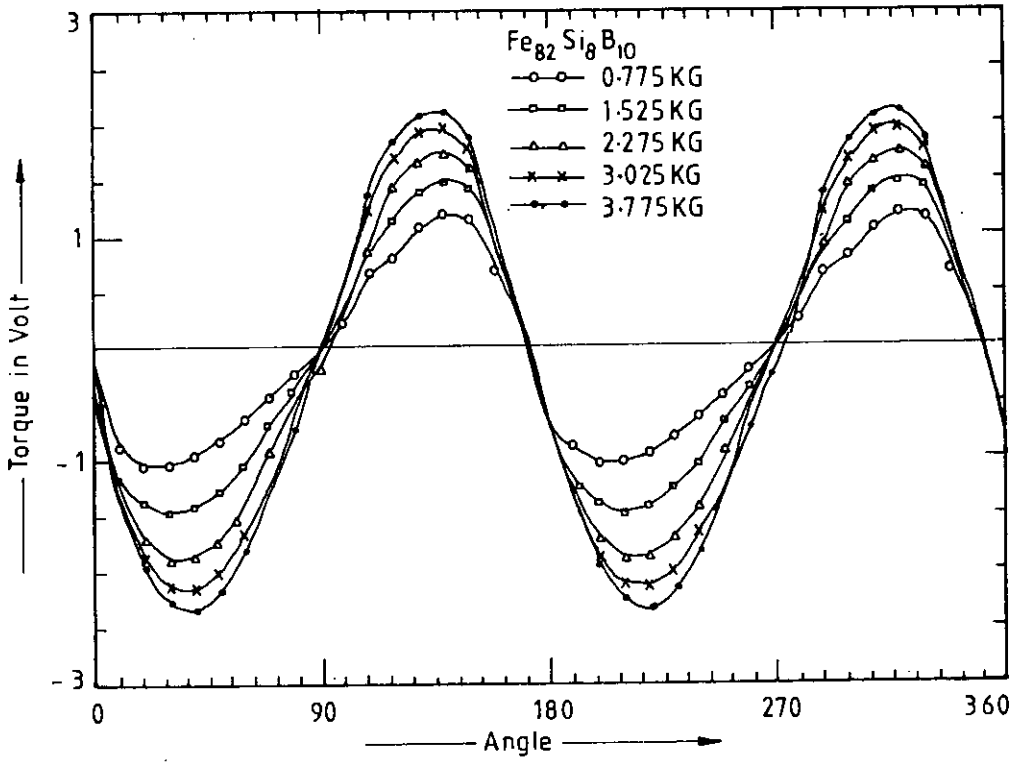

Fig.-5.21. Field dependence of torque versus angle for amorphous ribbon with composition $Fe_{82}Si_8B_{10}$

The uniaxial anisotropy (K_u) constants calculated from the torque versus angle curves by Fourier analysis for each set of temperature and field. The sensitivity of the torque magnetometer is calibrated to be $1\text{Volt} = 4.755 \times 10^{-7}\text{J}$ and by the use of different scale of sensitivity. Fourier coefficient as determined from the torque versus $\frac{1}{H}$ curve for different values of the angle between the preparation axis of the ribbon and the applied field, and by extrapolation of the field up to $H \to \infty$ are shown in fig.-5.22 and fig.-5.23.

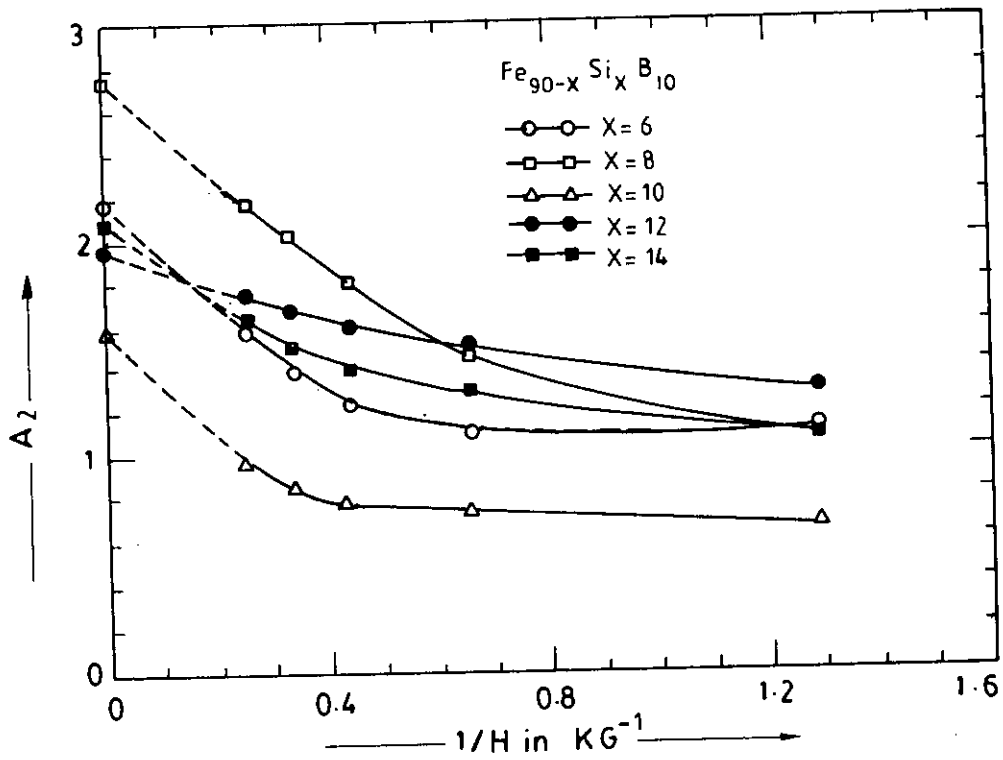

Fig.-5.22. Fourier coefficient for infinite field by extrapolation from A_2 versus $\frac{1}{H}$ curve for different composition of $Fe_{90-x}Si_xB_{10}$

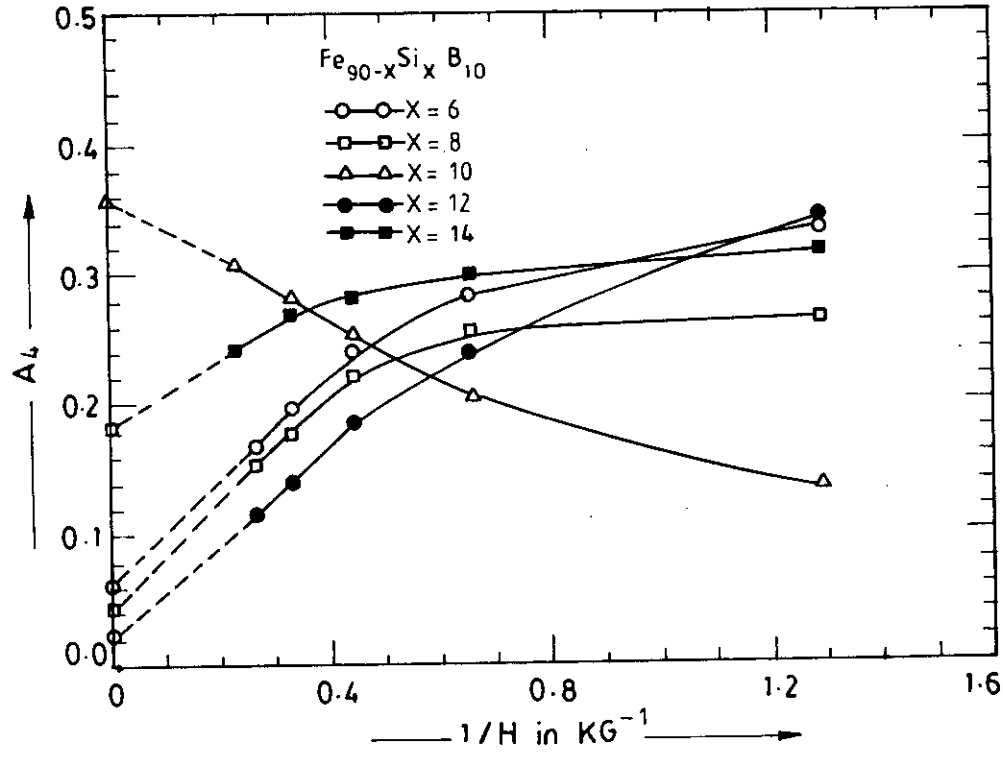

Fig.-5.23. Fourier coefficient for infinite field by extrapolation from A_4 versus $\frac{1}{H}$ curve for different composition of $Fe_{90-x}Si_xB_{10}$

Experimental values of the anisotropy constant K_u for different composition of $Fe_{90-x}Si_xB_{10}$ ribbons for different field are shown in fig.-5.24. The anisotropy constants are obtained by extrapolation K_u values against $\frac{1}{H}$ as shown in fig.-5.25. The results are shown in Table-5.6.

Table-5.6

$Fe_{90-x}Si_xB_{10}$	x =6	x = 8	x =10	x = 12	x = 14
K_u in J/m^3 at room temp.	3119	2025	2153	2263	2482
K_u in J/m^3 at 0K	3950	2700	2650	2400	3200
T_c	360^0C	390^0C	420^0C	440^0C	450^0C

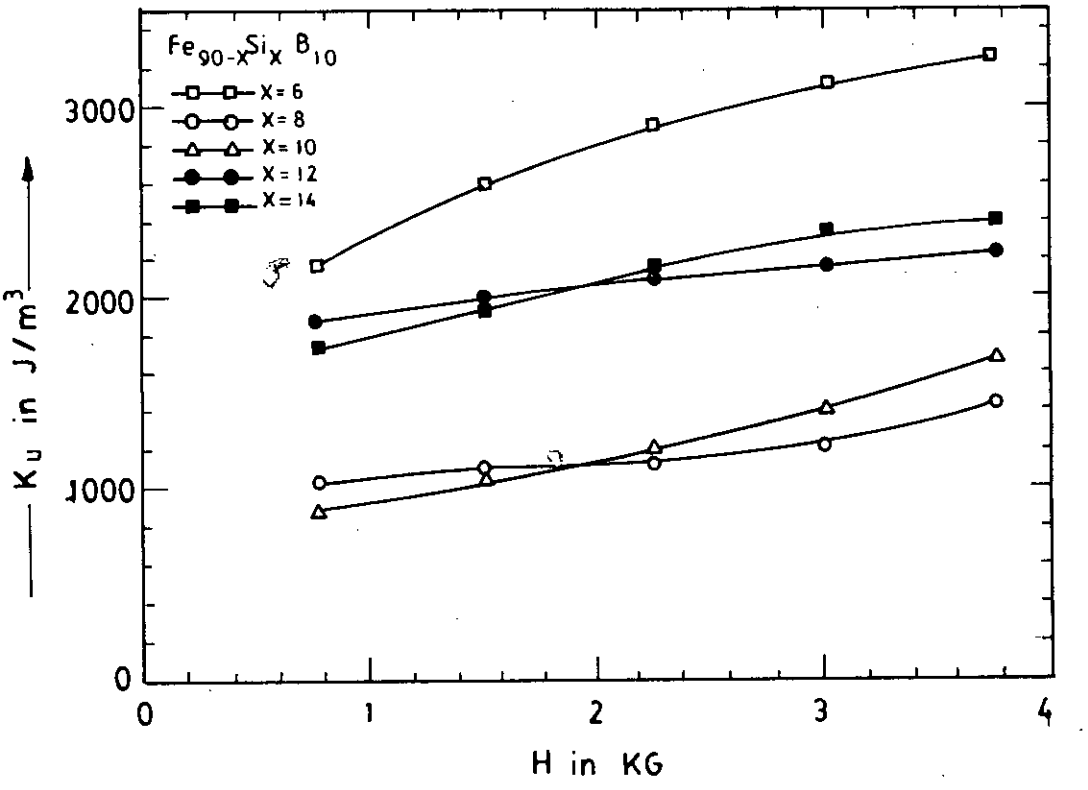

Fig.-5.24. Field dependence of experimental values of K_u for different composition of $Fe_{90-x}Si_xB_{10}$

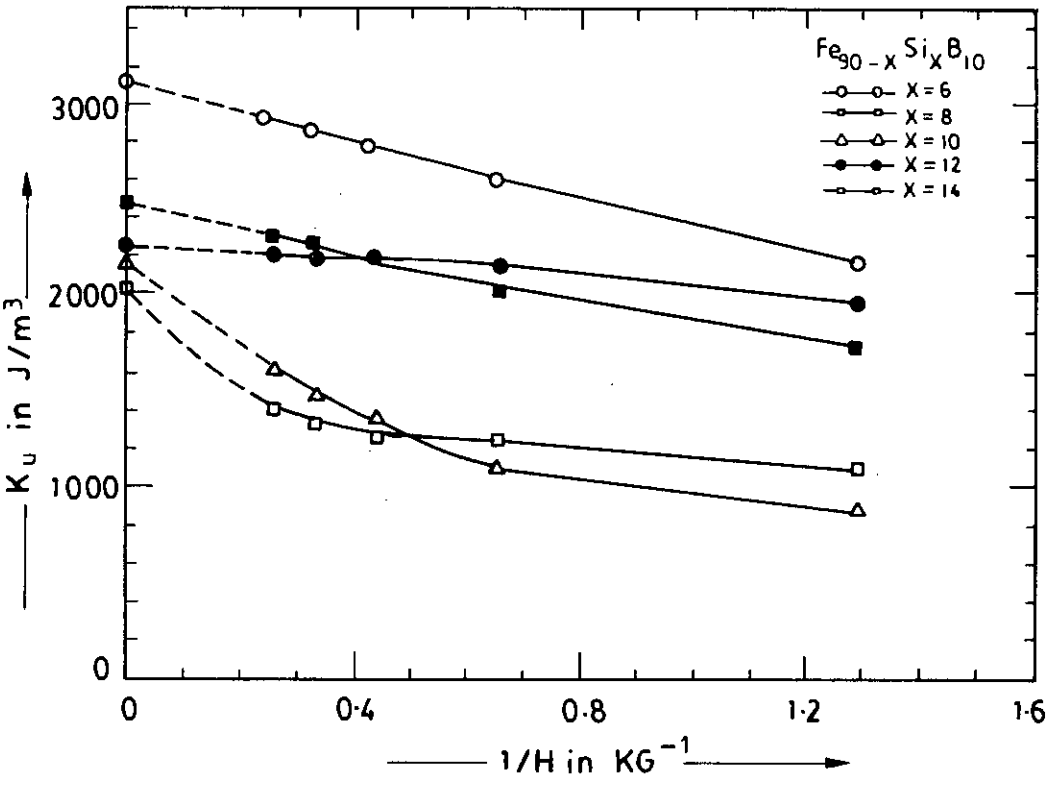

Fig.-5.25 Extrapolated value of K_u for infinite field for different composition of $Fe_{90-x}Si_xB_{10}$

The compositional dependence of stress induced anisotropy constants with silicon contents are shown in fig.-5.26, which shows the minimum value of K_u at 8 atomic percent of silicon and then goes on increasing with increasing value of Si up to 14 atomic percent of Si. This result agree with the results of the dependence of coercive force on composition as in fig.-5.7. K_u controlled by H_c in $Fe_{90-x}Si_xB_{10}$ amorphous ribbons. Higher coercivities arise from elastic stress centres, because they represent much stronger obstacles for domain movement through the magnetostrictive coupling, than the effect of anisotropy on initial permeability. The amorphous ribbon with composition $Fe_{82}Si_8B_{10}$ has the minimum value of $H_c = 4.6 A/m$, and minimum value of $K_u = 2025 J/m^3$, giving the maximum value of $\mu_i = 571$, thus indicating the importance of stress induced on the softness of the amorphous ribbons. K_u in ribbons are associated with short range pair ordering and interstitial or monoatomic ordering of the metalloids silicon and boron.

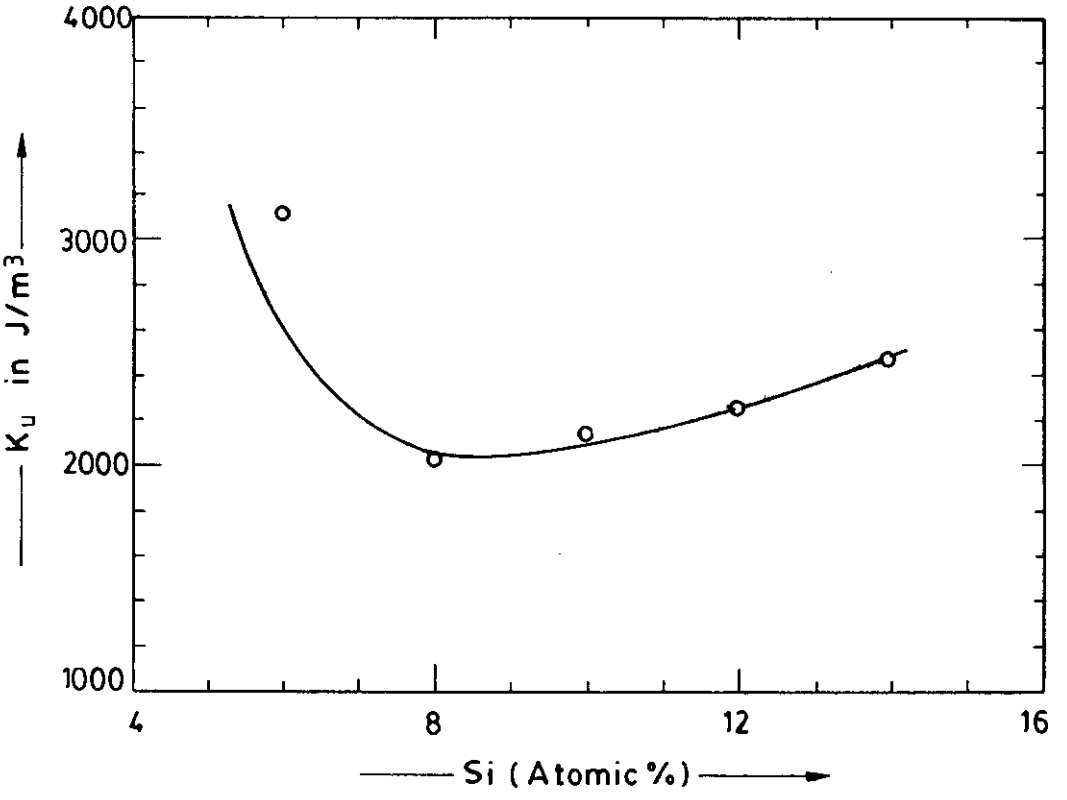

Fig.-5.26 Compositional dependence K_u of amorphous ribbons with composition $Fe_{90-x}Si_xB_{10}$

5.6.1. Temperature Dependence of K_u

The anisotropy constant K_u strongly depends on composition. The temperature dependence of anisotropy constant of amorphous ribbons of composition $Fe_{90-x}Si_xB_{10}$ for Si content is shown in fig.-5.27. There is almost monotonous decrease of anisotropy with the increase of temperature, for all the samples the fall being sharper for the sample with 6 At.% of Si. Although these results are of interest from a practical viewpoint they are difficult to interpret quantitatively interms of directional order theory because of the uncertainty as to the temperature dependence of K_u and the uncertainty as to whether equilibrium was achieved at any temperature. Directional order theory predicts a decrease in K_u with increases temperature and vanishes at Curie temperature. We have extrapolated to K_u zero value to calculate the ferromagnetic transition temperature T_c as shown in Table-5.6. This results are nearly the same as the value of T_c measured from the temperature dependence σ_s and μ_i values. The

anisotropy constant K_u is calculated in J/m^3 for different temperature as shown in Table-5.7.

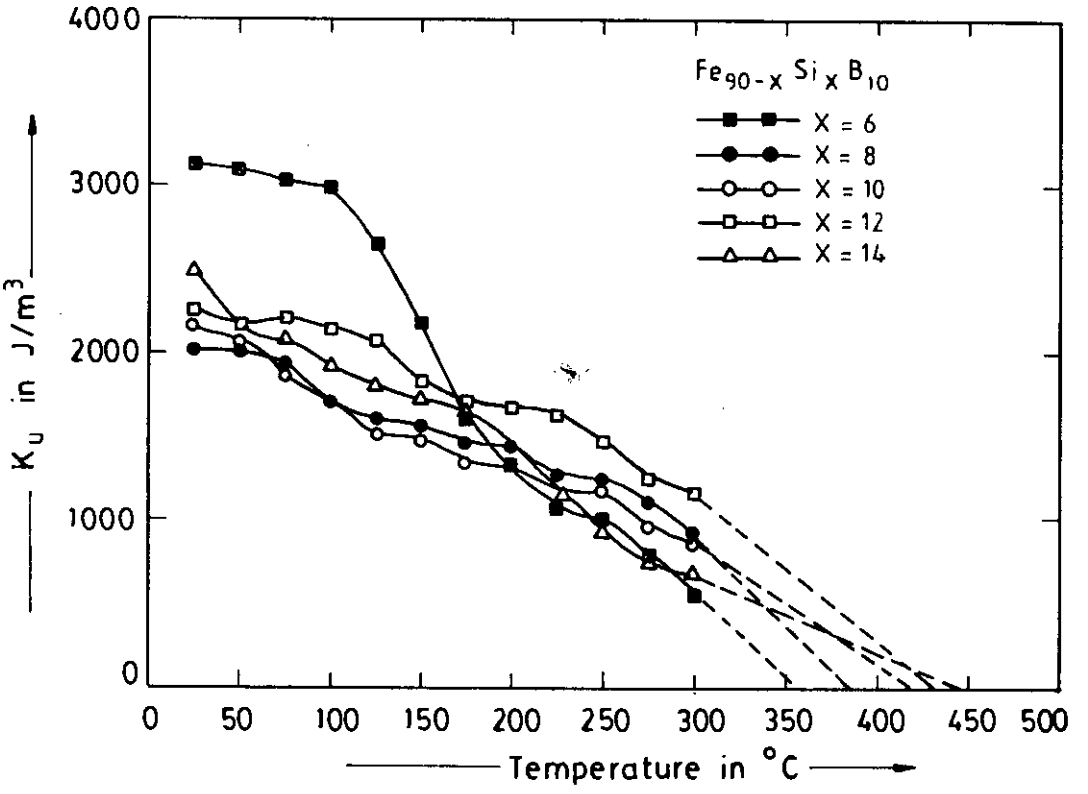

Fig.-5.27 Temperature dependence of K_u of amorphous ribbons with composition $Fe_{90-x}Si_xB_{10}$

Table-5.7.

$Fe_{90-x}Si_xB_{10}$	x = 6 K_u in J/m^3	x =8 K_u in J/m^3	x =10 K_u in J/m^3	x =12 K_u in J/m^3	x =14 K_u in J/m^3
25^0C	3119	2025	2153	2263	2482
50^0C	3092	2010	2065	2163	2116
75^0C	3024	1924	1858	2150	2075
100^0C	2984	1687	1708	2140	1912
125^0C	2645	1594	1521	2074	1800
150^0C	2175	1565	1483	1830	1729
175^0C	1611	1458	1342	1719	1658
200^0C	1335	1436	1323	1675	1444
225^0C	1067	1271	1173	1633	966
250^0C	1009	1235	1169	1469	926
275^0C	791	1113	967	1252	743
300^0C	567	919	873	1165	682

The stress induced anisotropy, $K_u(0)$ at T=0 is obtained by extrapolating the temperature dependence curve of $K_u(T)$ to 0K. The extrapolated values $K_u(0)$ for different ribbons of composition $Fe_{90-x}Si_xB_{10}$, are shown in Table-5.6.

The corresponding curves for $\ln\left[\frac{K_u(0)}{K_u(T)}\right]$ versus $\ln\left[\frac{\sigma_s(0)}{\sigma_s(T)}\right]$ for the amorphous ribbons with composition $Fe_{90-x}Si_xB_{10}$ follow straight lines as shown in fig.-5.28(a) to fig.-5.28(e). The temperature dependence of K_u is an interesting property for understanding these materials. According to Zener the effect of temperature upon K_u aries solely from the introduction of local deviations in an elementary region and resultants from a large number of independent deviations. The influence of these local deviations upon the K_u is most conveniently expressed by representing the magnetic energy as a series of surface harmonics. The coefficient of n harmonic is found to vary as follows: $n = \frac{\ln\left[\frac{K_u(0)}{K_u(T)}\right]}{\ln\left[\frac{\sigma_S(0)}{\sigma_S(T)}\right]}$. The K_u arising from the disorder caused by randomly oriented easy axes follows a power law; $\frac{K_u(T)}{K_u(0)} = \left[\frac{\sigma_s(0)}{\sigma_s(T)}\right]^n$ where $2<n<4$. The values of n are shown in Table-5.8.

Table-5.8

$Fe_{90-x}Si_xB_{10}$	x =6	x =8	x =10	x =12	x =14
n	3.29	1.88	3.08	3.27	4.12

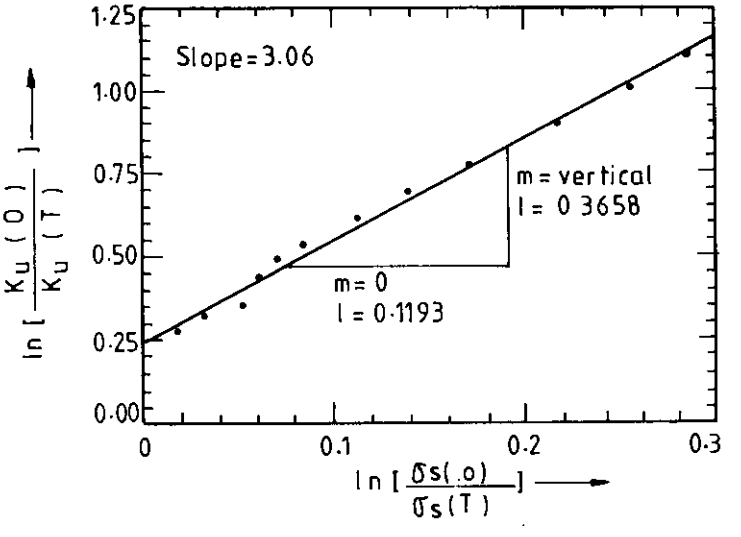

Fig.-5.28(a) $\ln\left[\frac{K_u(0)}{K_u(T)}\right]$ versus $\ln\left[\frac{\sigma_S(0)}{\sigma_S(T)}\right]$ curve of the amorphous ribbon with composition $Fe_{80}Si_{10}B_{10}$

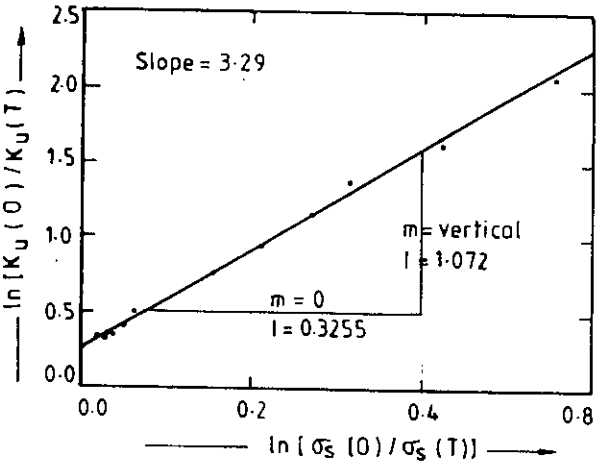

(b) Composition $Fe_{84}Si_6B_{10}$

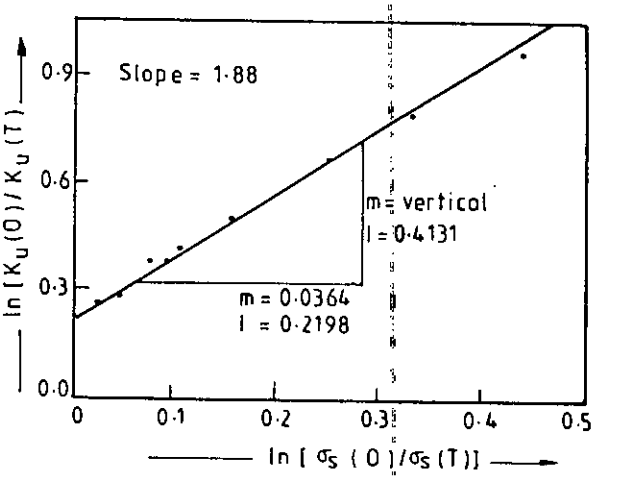

(c) Composition $Fe_{82}Si_8B_{10}$

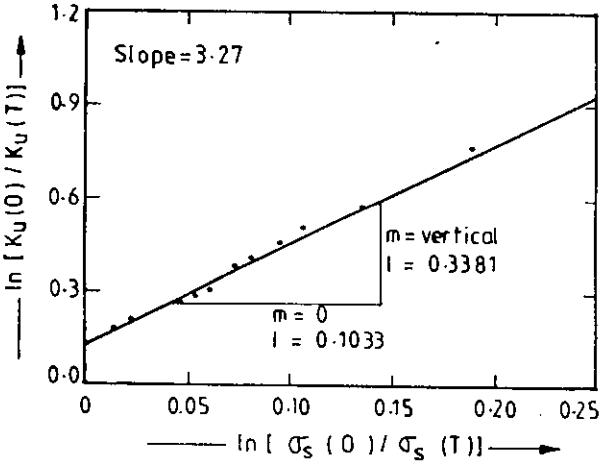

(d) Composition $Fe_{78}Si_{12}B_{10}$

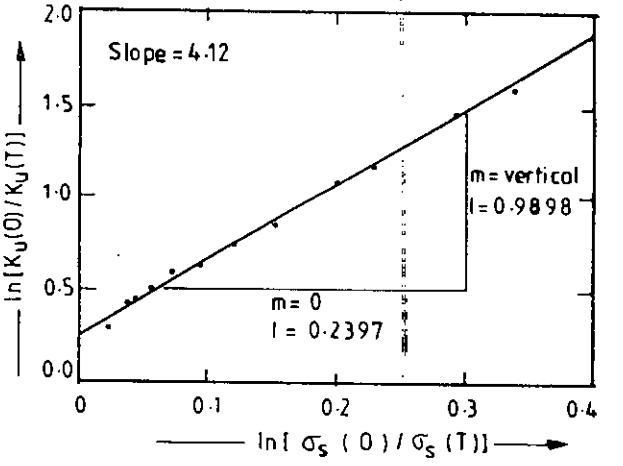

(d) Composition $Fe_{76}Si_{14}B_{10}$

Fig.-5.28(b) to (e) $\ln\left[\frac{K_u(0)}{K_u(T)}\right]$ versus $\ln\left[\frac{\sigma_s(0)}{\sigma_s(T)}\right]$ curves of amorphous ribbons with composition $Fe_{90-x}Si_xB_{10}$ [x = 6, 8, 12 &14]

5.7. Experimental Results and Analysis of Mössbauer Parameters for Fe-based Amorphous Ribbons.

The Mössbauer spectroscopy technique in constant acceleration mode has been used to study hyperfine structure of soft magnetic material of amorphous ribbons with composition $Fe_{90-x}Si_xB_{10}$ [x = 6, 8, 10, 12 & 14] in amorphous state. The experiments were performed at room temperature in transmission geometry, using ^{57}Co in a rhodium matrix. Pure ^{57}Fe thin foil has been used as the reference material for standarization of results. The number of counts versus velocity of the source is plotted in fig.-4.16. The data are collected into two groups. Each group is of 256 channels and the second group gives a mirror image spectrum of the first group. The representative spectrum of amorphous ribbon with composition $Fe_{80}Si_{10}B_{10}$ is shown in fig.-5.29.

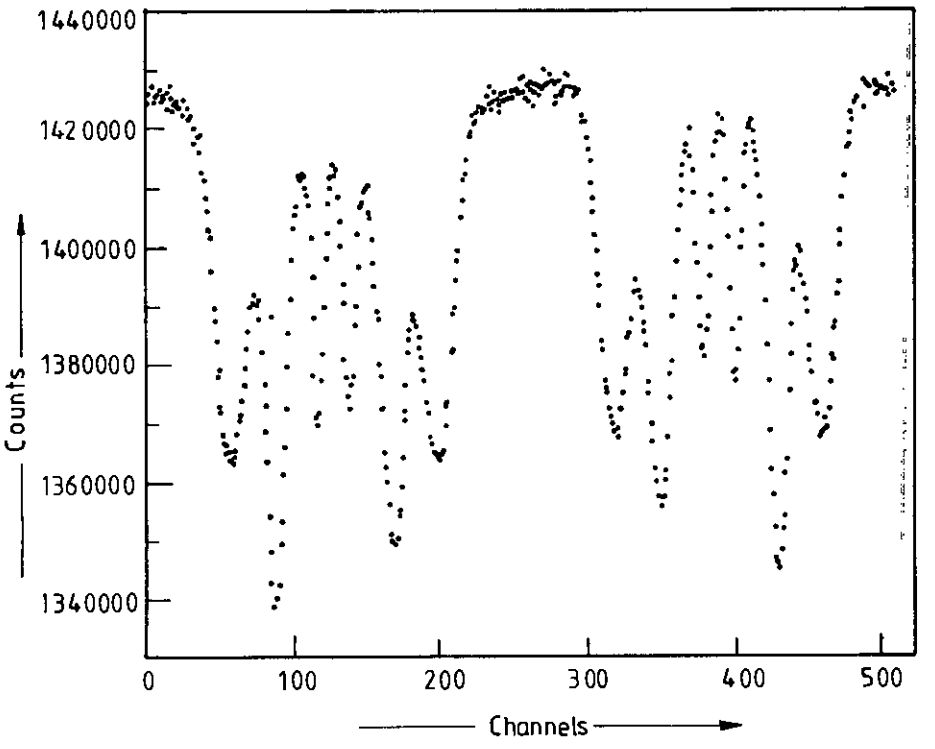

Fig.-5.29 Room temperature Mössbauer transition spectrum for relative counts versus channels of the as-quenched amorphous ribbon with composition $Fe_{80}Si_{10}B_{10}$

We linearize the data and the two groups are folded resulting in improved statistics. The parabolic effect in the base line, caused by the periodic parabolic

displacement of the source, gets cancelled as a result of the folding. This folded set of data is then used for analysis and the representative origin graph with composition $Fe_{80}Si_{10}B_{10}$ is shown in fig.-5.30. The fitting is done in terms of the Mössbauer parameters of Isomer shift (IS), qudrupole splitting (E_Q), internal hyperfine magnetic field (H_{hf}), line width as measured by full width half maximum (FWHM) and percentage of absorption of the components in magnetic pattern.

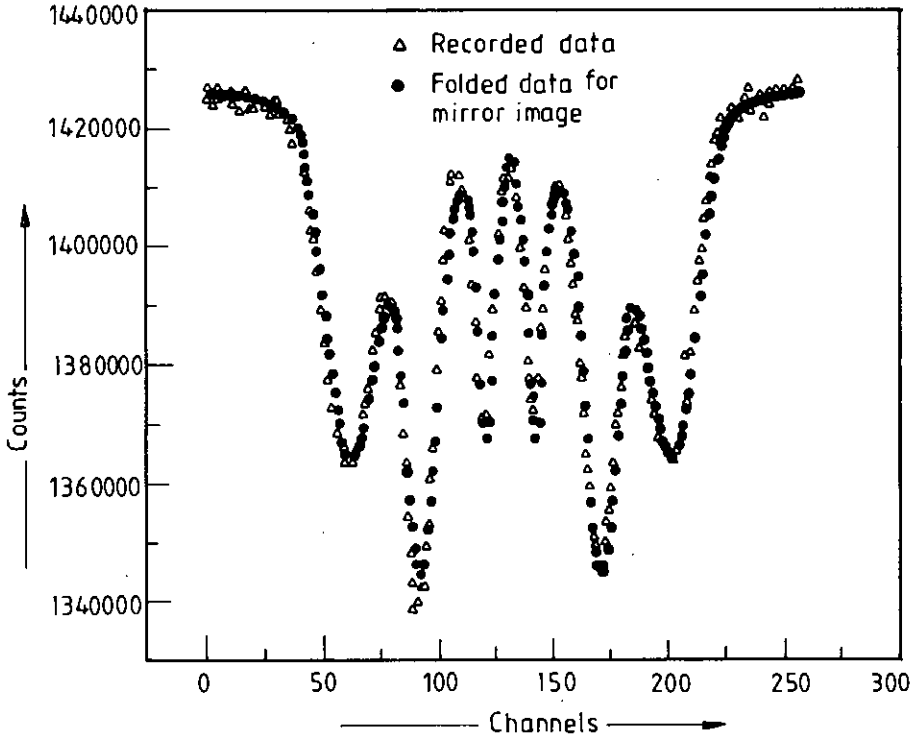

Fig.-5.30 The origin graph with composition $Fe_{80}Si_{10}B_{10}$ from the folded set of data.

In this case of ^{57}Fe there is an internal magnetic field acting at ^{57}Fe nuclei. This causes the upper $-\frac{1}{2}$ level to split to two levels. Using the selection rule $\Delta m = 0, \pm 1$ for transitions to occur, we get six possible transitions. In order to match the source energy to each of the six different velocities of the source. This is automatically achieved in constant acceleration mode. Room temperature Mössbauer spectra, typical of as-prepared amorphous ribbons, are obtained and the changes in the spectra corresponding to the different compositions of the system $Fe_{90-x}Si_xB_{10}$ [x = 14, 12, 10 & 8] are shown in fig.-5.31. Fig.-5.32 shows the spectrum for the sample $Fe_{84}Si_6B_{10}$.

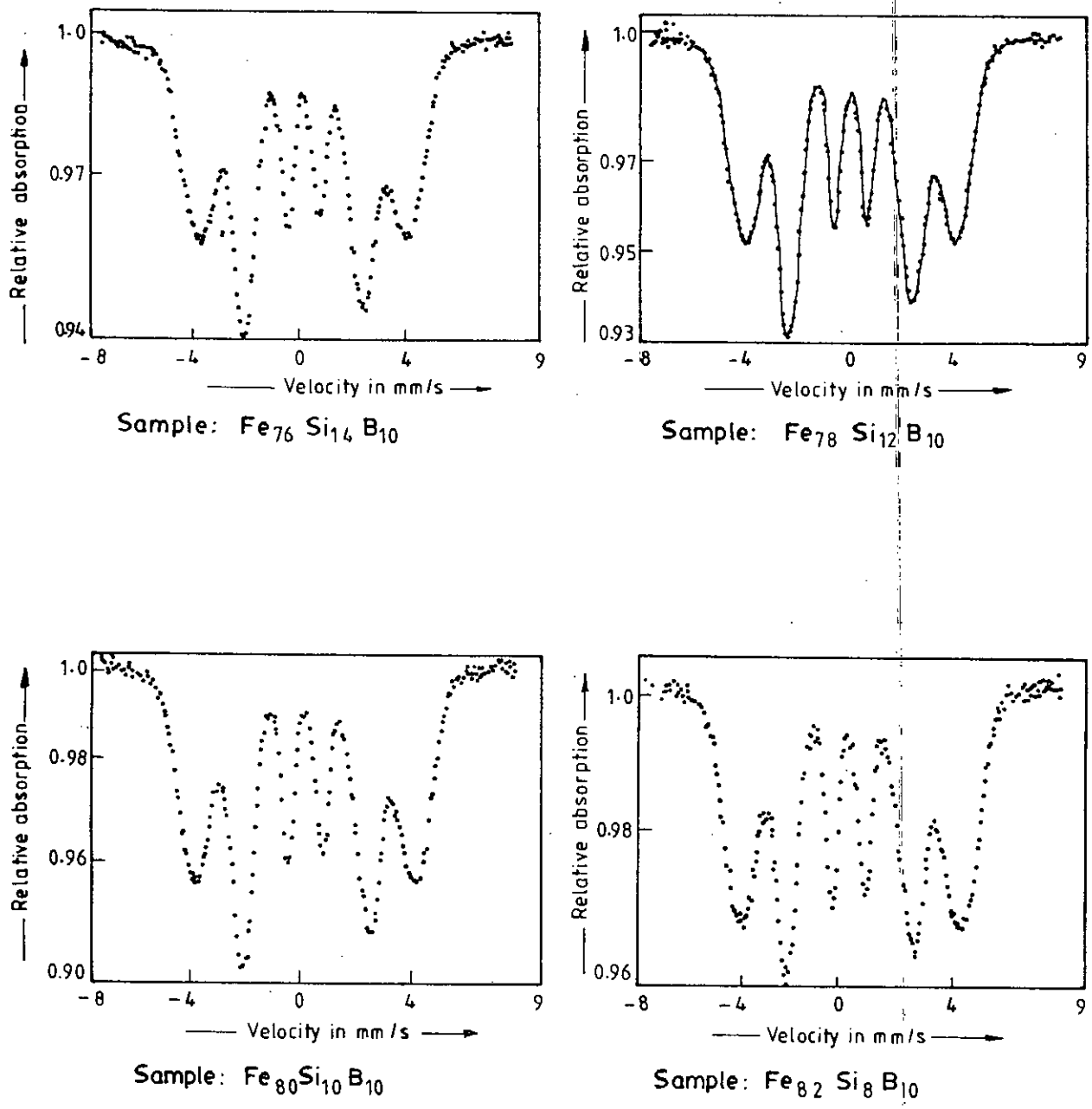

Fig.-5.31 Room temperature Mössbauer spectra of as-quenched amorphous ribbons with composition $Fe_{90-x}Si_xB_{10}$ [x = 14, 12, 10 & 8]

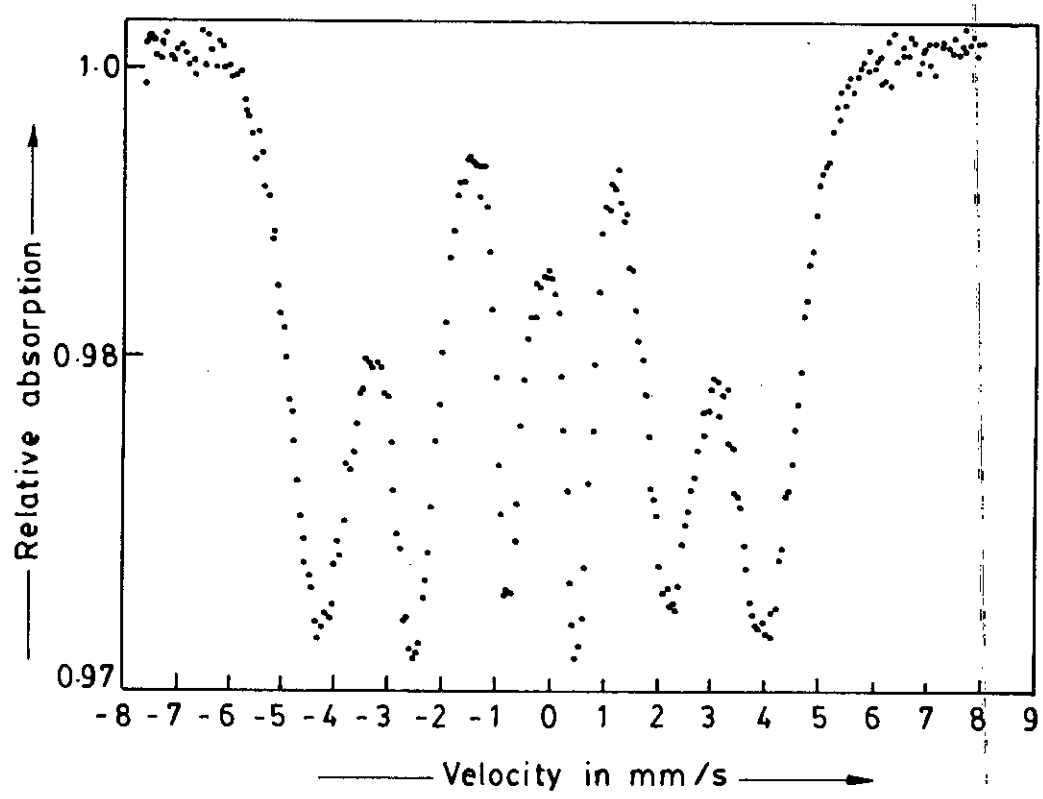

Fig.-5.32 Room temperature spectra of the as-quenched amorphous ribbon with composition $Fe_{84}Si_6B_{10}$.

A comparison of the spectrum of pure iron with those of the amorphous ribbons of different compositions shows the shift in the spectral lines and their broadening. This is caused by the change in the number of nearest neighbour iron atoms and also there interatomic distances. The numerical values of IS, E_Q, FWHM, H_{hf} and absorption percentages are shown in Table-5.9.

Table-5.9.

Sample	IS, mm/s ±0.005	E_Q mm/s ±0.005	H_{hf} Tesla ±0.1T	FWHM mm/s, ±0.01	Absorption %
Pure ^{57}Fe foil	.....	0.058	33	0.18	11.38
$Fe_{76}Si_{14}B_{10}$	0.242	0.175	24.07	1.20	4.76
$Fe_{78}Si_{12}B_{10}$	0.213	0.213	24.61	1.00	5.32
$Fe_{80}Si_{10}B_{10}$	0.206	0.175	24.98	1.083	5.27
$Fe_{82}Si_8B_{10}$	0.114	0.058	25.53	1.05	3.89
$Fe_{84}Si_6B_{10}$	0.338	0.213	25.71	1.083	2.74

The coulombic interaction alter the energy separation between the ground state and the excited state of the nuclei, thereby causing a slight shift in the position of the observed centroid of the spectrum, which are different for various amorphous ribbons with different compositions giving rise to isomer shifts. The velocity scale is calibrated by a room temperature measurement on a thin natural iron foil sample. The IS's are given relative to the centroid of this spectrum as shown in Table-5.9. IS of all the samples are given relative to the centroid of this spectrum. The centroids for the ribbons are calculated relative to the centroid of these spectra from the centroids of the velocity scale of a thin ^{57}Fe foil sample. The IS's of the iron atoms in amorphous ribbons with composition $Fe_{90-x}Si_xB_{10}$ is observed to be in the range 0.114 to 0.338mm/s, indicating that the iron atoms behave as trivalent ions in this system.

Quadrupole splitting is the electric quadrupole interaction between the quadrupole moments of the nuclei and the electric field gradient at the nucleus due to the asymmetric distribution of charges on the ions. This provide information on the nature of chemical bond. The E_Q of the iron atom in the amorphous ribbons with composition $Fe_{90-x}Si_xB_{10}$ is observed in the range o.058 to 0.213mm/s as shown in Table-5.9.

Absorption percentage, as compared with pure iron, decreases in Fe-Si-B ribbons. These absorption percentage slightly decreases with decreasing Si-content except for $Fe_{76}Si_{14}B_{10}$. These results are shown in Table-5.9. The effect of change in the composition of Fe-Si-B amorphous system on the transition line width as measured by FWHM is also shown in Table-5.9. The experimental FWHM of pure ^{57}Fe foil is 0.18mm/s, FWHM of the amorphous ribbons broadening is 5.5 to 6.5 times.

Using these standard results, the experimental spectra for the as-prepared samples of Fe-Si-B ribbons of different composition have been obtained by the best fit for the distribution of the hyperfine field. This is carried out by FORTRAN IV language which does a least χ^2 spectra fitting for over lapping Lorentzian lines. The curve through the experimental spectra is the best fit obtained by using the best fit with a probability distribution of hyperfine fields as shown in fig.-5.33. This solid curve indicating the probability distribution of magnetic H_{hf} has been observed as a single peak which corresponds to amorphous state. The results of average magnetic hyperfine field (H_{hf}) of the as-quenched amorphous ribbons with composition $Fe_{90-x}Si_xB_{10}$ are show in Table-5.9. The H_{hf} is increases with decreasing Si-content as shown in fig.-5.34.

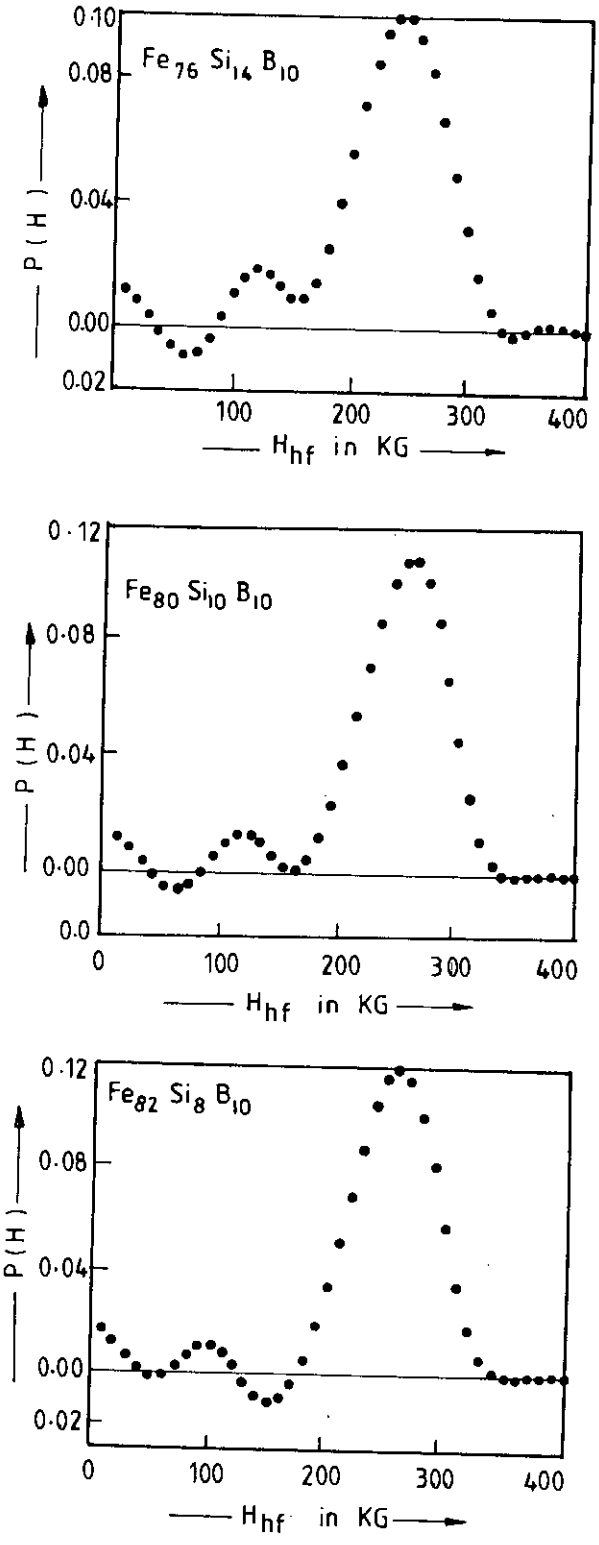

Fig.-5.33 The best fit curves of magnetic hyperfine field distribution for amorphous ribbons with composition $Fe_{90-x}Si_xB_{10}$ [x = 14, 10 & 8]

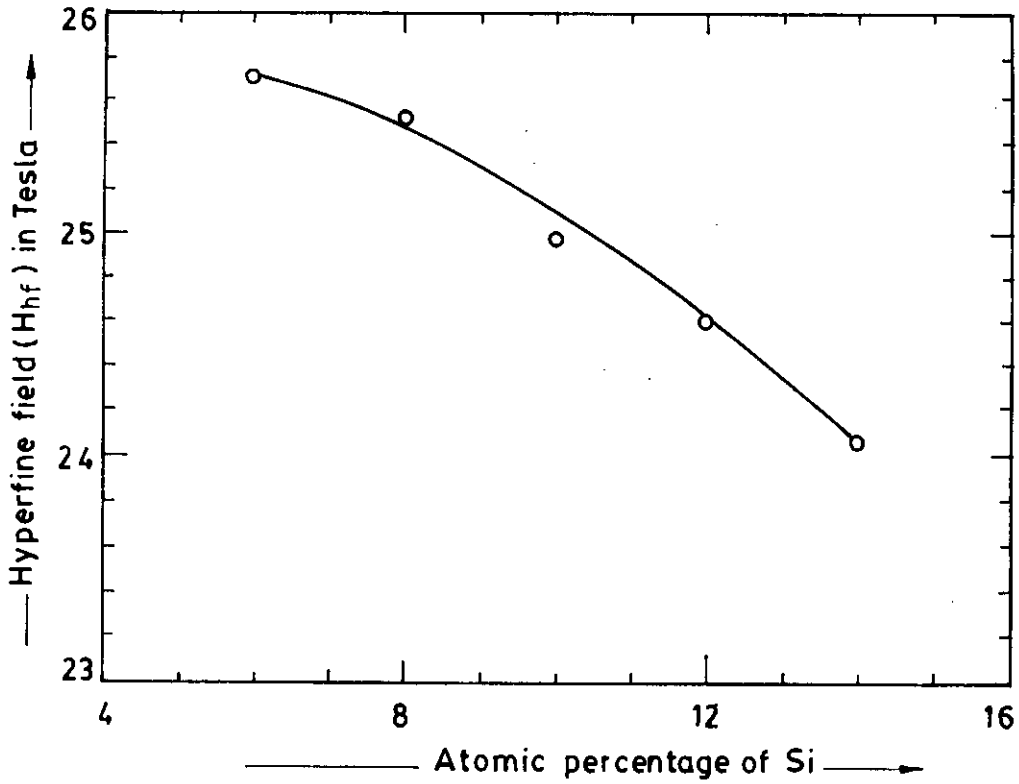

Fig.-5.34 Variation of internal hyperfine field due to change in the Si-content in $Fe_{90-x}Si_xB_{10}$ amorphous ribbons.

The H_{hf}, IS and E_Q for the sample with composition $Fe_{80}Si_{10}B_{10}$ have not changed by annealing at temperatures up to $300^0 C$ for one hour. The numerical values of IS, E_Q, FWHM, H_{hf} and the absorption percentage of annealed amorphous ribbon with composition $Fe_{80}Si_{10}B_{10}$ are shown in Table-5.10.

Table-5.10

sample $Fe_{80}Si_{10}B_{10}$	IS, mm/s ±0.005	E_Q, mm/s ±0.005	H_{hf}, Tesla ±0.1T	FWHM mm/s, ±0.01	Absorption %
At room temperature	0.206	0.175	24.98	1.083	5.27
$200^0 C$(1hr.)	0.231	0.117	25.53	1.083	4.72
$300^0 C$(1hr.)	0.125	0.117	25.71	1.083	4.98

The results of IS, E_Q, H_{hf} and FWHM of the annealed sample $Fe_{80}Si_{10}B_{10}$ are nearly the same as those of the as-quenched ribbon. Just slight gives the H_{hf} shows a increase with annealing temperature. The Effect of annealing is shown by the fitting the results to a solid curve for the distribution of magnetic H_{hf} of amorphous ribbon with composition $Fe_{80}Si_{10}B_{10}$ as shown in fig.-5.35.

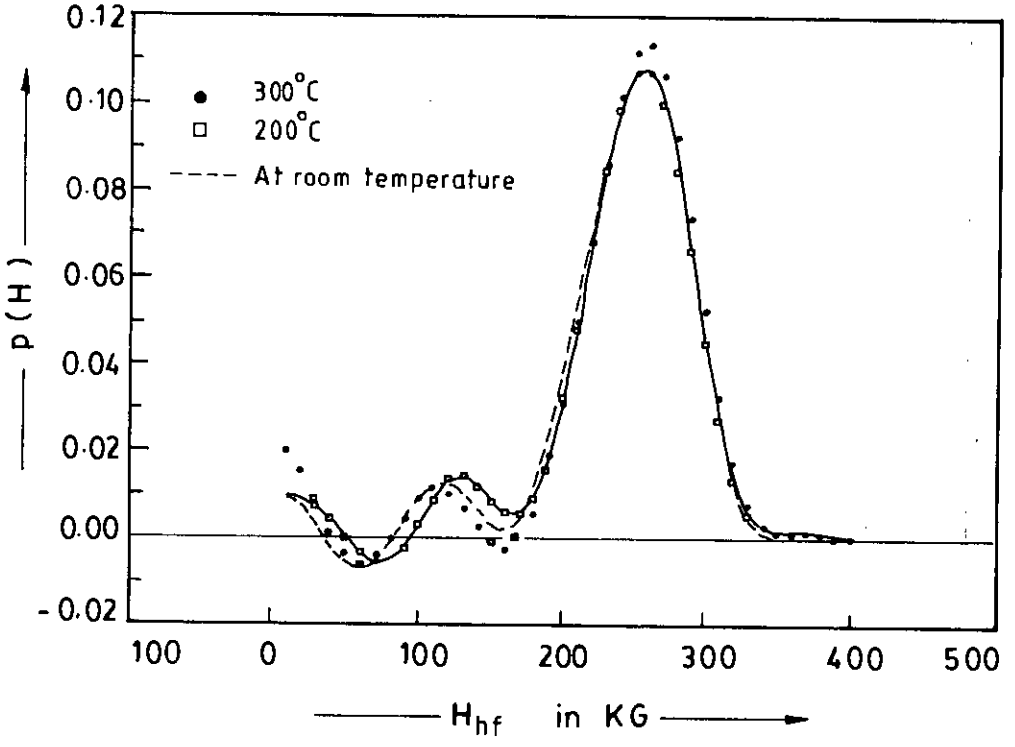

5.35 Effect of annealing on the distribution of magnetic hyperfine fields of amorphous ribbons with composition $Fe_{80}Si_{10}B_{10}$.

Fig.-5.35 shows that annealing did not alter the amorphousity, and the average hyperfine field changes very slightly due to annealing. It has been observed that although very small change is observed in the average hyperfine fields due to annealing, the change in the distribution of the hyperfine field is more appreciable.

CHAPTER-6 RESULTS AND DISCUSSION OF Ni-BASED AMORPHOUS RIBBONS

6.1. Differential Thermal analysis of amorphous Nickel-Iron-Boron ribbons as affected by Nickel content

6.2. Curie temperature measurements of amorphous Nickel-Iron-Boron Ribbons

6.3. Determination of Maximum permeability, Maximum induction, Coercive force and Remanence of Ni-based Amorphous Ribbons

6.4. Dynamic Magnetic Properties of Ni-based Amorphous Ribbons

6.5. Specific Magnetizations of Ni-based Amorphous Ribbons

6.5.1. Temperature Dependence of Specific Magnetization of Ni-based Amorphous Ribbons

6.6. Stress Induced Anisotropy Measurements of Ni-based Amorphous Ribbons

6.6.1. Temperature Dependence of K_u

6.7. Results and Analysis of Mössbauer parameters for Ni-based Amorphous Ribbons

6.0. Results and Discussion of Ni-based Amorphous Ribbons.

6.1. Differential Thermal Analysis of amorphous Nickel-Iron-Boron ribbons as affected by Nickel content

Nickel-Iron-Boron amorphous ribbons with compositions $Ni_{80-x}Fe_xB_{20}$ [x= 20, 30, 40 and 50] are of special interest, because these magnetic elements having different structures in their crystalline states and opposite magnetostrictions provide opportunities for tailoring the magnetic properties by change of composition. The glass transition temperature T_g, the crystallization temperature T_x and the secondary crystallization temperature T_x' of the amorphous alloys are determined by DTA at a heating rate of 10^0C / min. In fig-6.1 T_g, T_x and T_x' are shown which corresponds to respective exothermic picks of the alloy composition $Ni_{50}Fe_{30}B_{20}$. Fig-6.2 shows the DTA curves, of the different samples. The large peaks in these curves correspond to the crystallization temperatures, while the simple hum like peaks correspond to the glass transition temperatures.

It is observed that both T_g and T_x decrease as the nickel content increases. The decreases of T_x with nickel content may be explained as due to the increase of the melting point with the increases of the nickel content. The difference between T_x and T_g is found to be nearly the same for all composition, being in the range 20^0C to 30^0C. This difference in ΔT signifies that all the alloy composition are not eutectic, rather they deviate form the eutectic composition. In the above mentioned graph the third peak shows that the secondary phase transformation take place almost at the same temperature for all the alloy compositions under study. In fig-6.2 the results are presented in summarised form for a comparison to be drown between the samples of different compositions. The numerical values of T_g, T_x and T_x' for all sample are shown in Table-6.1.

Table-6.1

$Ni_{80-x}Fe_xB_{20}$	T_g	T_x	T_x'
x = 50	450^0C	480^0C	575^0C
x = 40	435^0C	455^0C	575^0C
x = 30	400^0C	422^0C	575^0C
x = 20	395^0C	415^0C	575^0C

Fig-6.3 shows the dependence of T_g, T_x and T_x' on composition and nickel content.

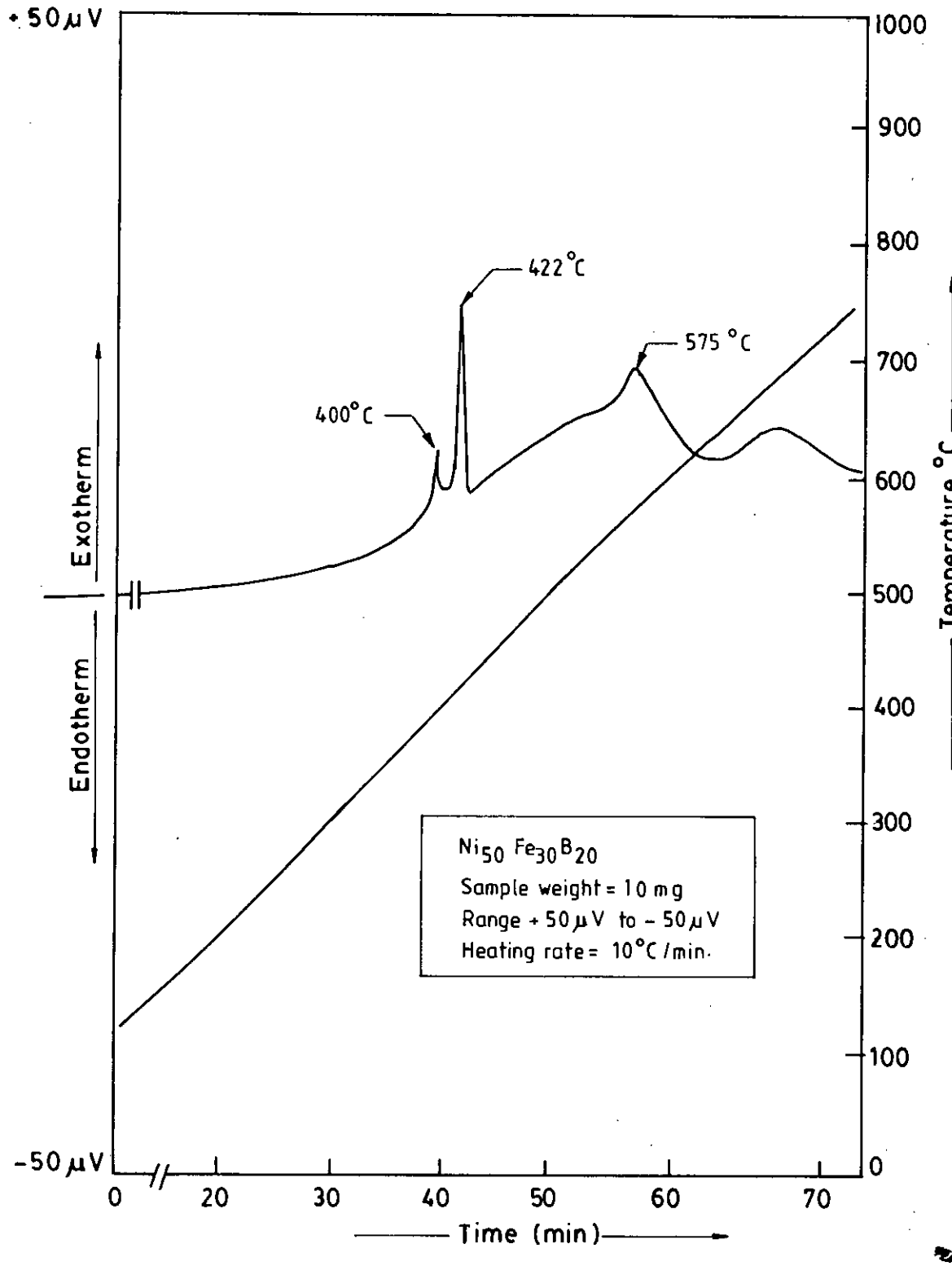

Fig.-6.1 DTA graph of the amorphous ribbon with composition $Ni_{50}Fe_{30}B_{20}$.

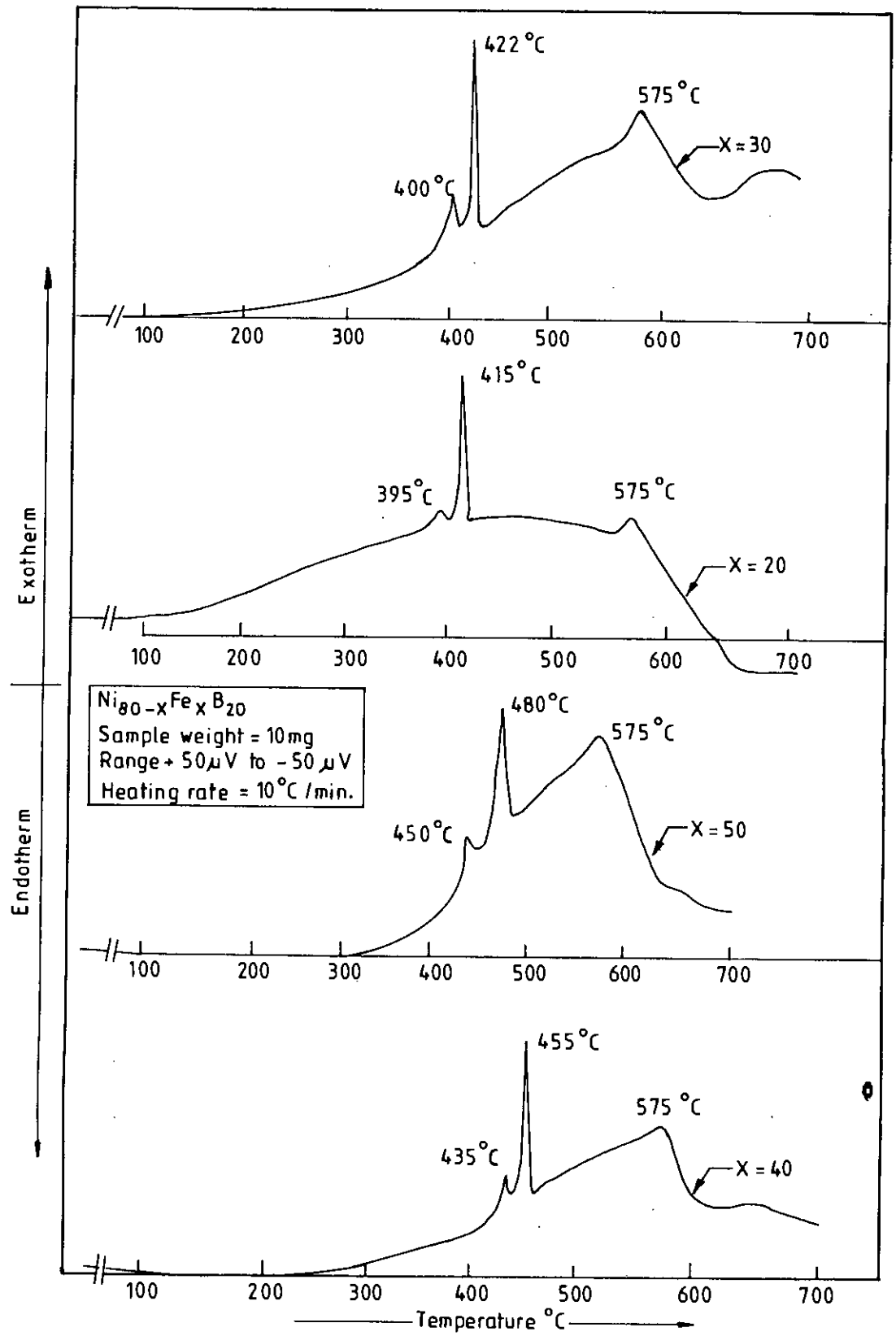

Fig-6.2 Determination of T_g, T_x and T_x' from DTA graph of amorphous ribbons with compositions $Ni_{80-x}Fe_xB_{20}$ [x = 20, 30, 40 & 50

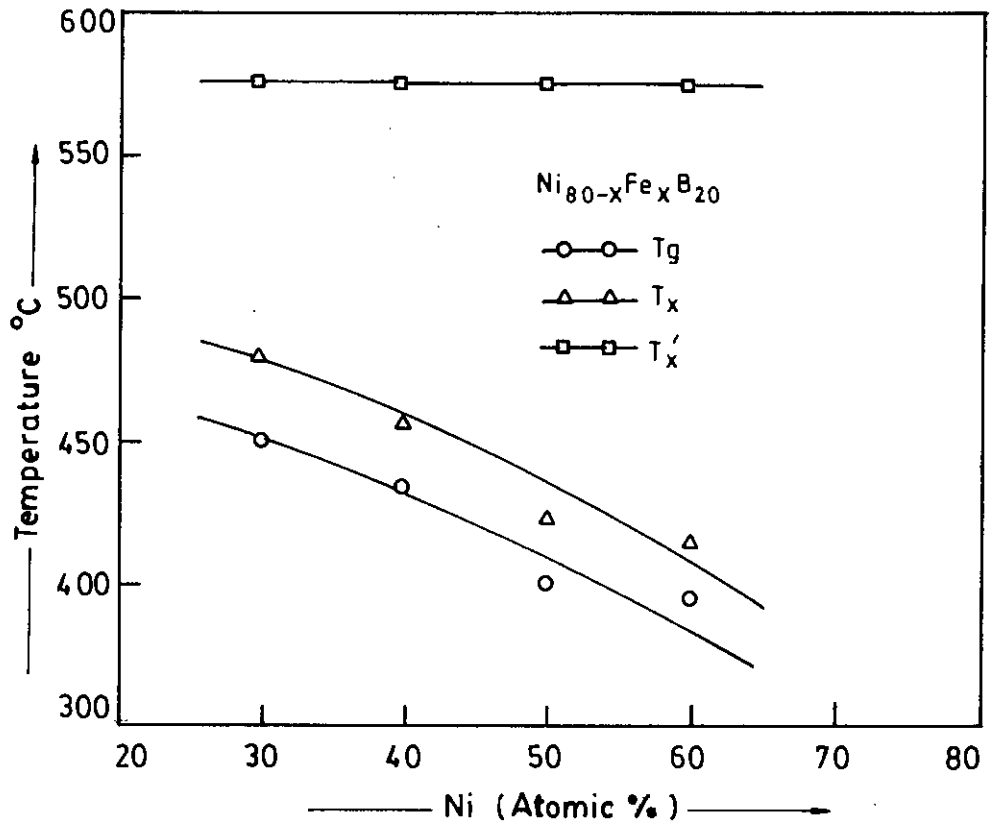

Fig.-6.3 Variation of T_g, T_x and T_x' due to change in the nickel content in $Ni_{80-x}Fe_xB_{20}$ amorphous ribbons.

6.2 Curie temperature measurements of amorphous Nickel-Iron-Boron ribbons

Amorphous Nickel-Iron-Boron ribbons having composition $Ni_{80-x}Fe_xB_{20}$ [x = 20, 30, 40 and 50] have been chosen for the determination of Curie temperature, using the μ VS T curves. The T_c corresponds to temperature at which the sharp fall of permeability occurs. Temperature dependence of permeability of the samples subjected to a heating rates of 12^0C / min. are shown in fig-6.4. The numerical values of T_c's for all the samples are shown in Table-6.2.

Table-6.2

$Ni_{80-x}Fe_xB_{20}$	x = 50	x = 40	x = 30	x = 20
T_c	445^0C	413^0C	333^0C	261^0C

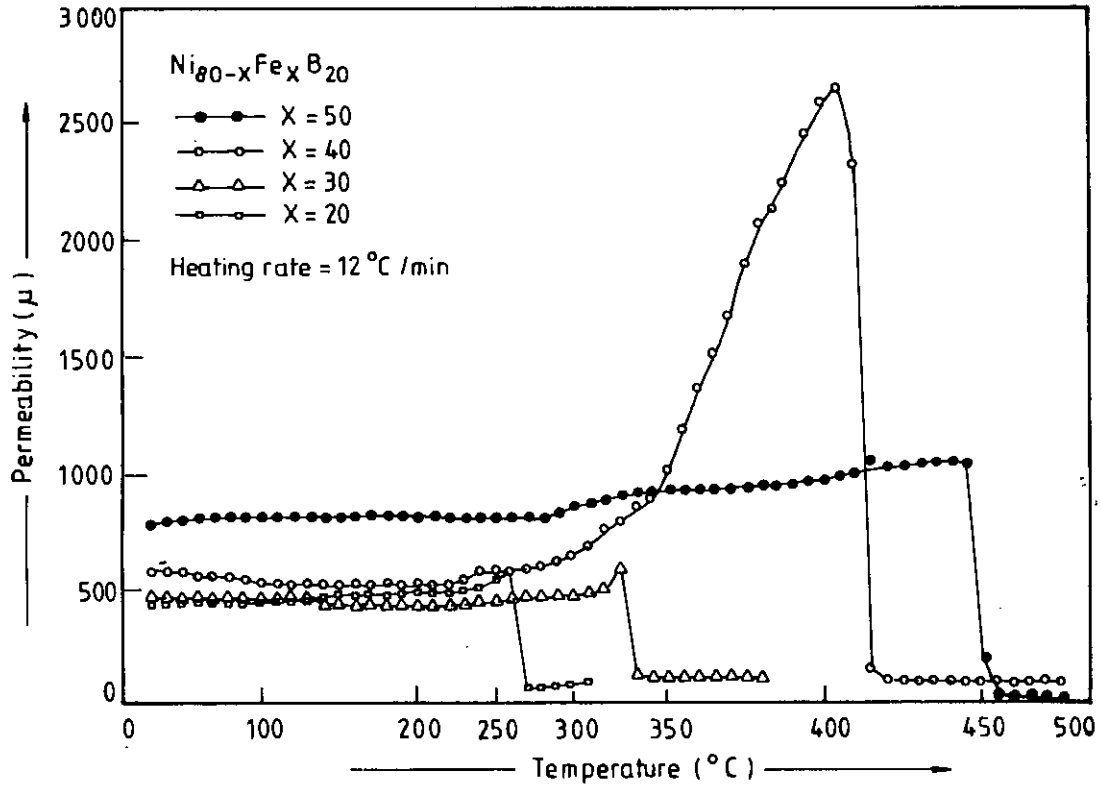

Fig.-6.4. T_c determination from temperature dependence of permeability of amorphous ribbons with composition $Ni_{80-x}Fe_xB_{20}$.

Although the chemical disorder appears to be largely responsible for reduction of Curie temperature T_c in amorphous ribbons, the effect of non-crystallineity is also significant. The dependence of T_c on the composition and the nature of the metalloids is not very systematic. T_c's of amorphous Nickel-Iron-Boron ribbons with composition $Ni_{80-x}Fe_xB_{20}$ decrease with the increase of Nickel content as shown in fig-6.5. Addition of Ni to replace Fe, with fixed concentration of boron, decreases T_c rather slowly for low concentration, but for higher concentration of Ni T_c falls sharply. It is noticed that T_c decreases monotonically with increasing Nickel content. It is explained as arising from the weakening of the exchange interaction between the magnetic atoms due to the replacement of Fe atom by Ni atoms.

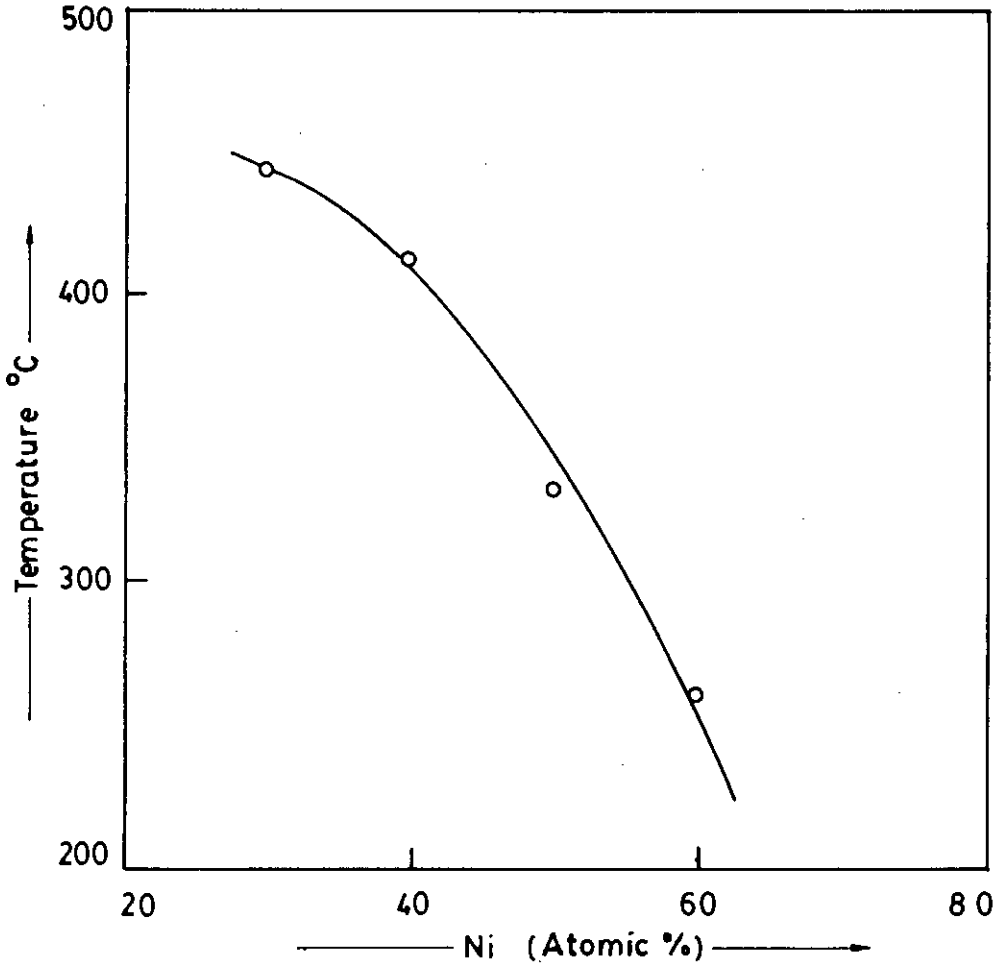

Fig.-6.5 Variation of T_c due to change in the Ni-content in $Ni_{80-x}Fe_xB_{20}$ amorphous ribbons.

6.3. Determination of Maximum Permeability, Maximum induction, Coercive force and Remanence of Ni-based Amorphous Ribbons.

Amorphous Nickel-Iron-Boron ribbons are of great interest as a soft magnetic material for their static applications. Amorphous ribbons of Nickel-Iron-Boron alloys having composition $Ni_{80-x}Fe_xB_{20}$ [x = 20, 30, 40 and 50] have been chosen for static magnetic characteristics like saturation magnetic induction (B_s), remanence (B_r), Coercivity (H_c),maximum permeability (μ_m) and the ratio (B_r/B_s). The ribbons were wound into the toroidal cores having 13 to 15mm outer diameter and 10mm inner diameter. In the as-quenched state these magnetic materials show very soft magnetic properties with rectangular hysteresis loops. In order to gain information which will help the development of advanced soft magnetic materials, a detailed study of the processes associated with the magnetization in such materials is required.

As-quenched ribbons of amorphous Nickel-Iron-Boron alloy system have been studied experimentally to determine B_s, B_r, H_c and μ_m from the hysteresis curves by varying the applied field up to 32A/m. The coercive field and the losses are controlled by the process of magnetization reversal, which depends on magnetic nucleation, irreversible rotation of magnetic domains and domain wall motion. But at the same time the saturation magnetic induction B_s and the remanence B_r are much reduced. The remanence $B_r \cong 0.85$ to $0.90B_s$ and H_c = 3.6 to 6.8A/m have been observed in $Ni_{80-x}Fe_xB_{20}$ amorphous ribbons. The results of our observation are shown in summary form in Table-6.3.

Table-6.3.

$Ni_{80-x}Fe_xB_{20}$	x = 50	x = 40	x = 30	x = 20
$H_c(A/m)$	5.1	6.8	5.8	3.6
$B_r(mT)$	242.5	231.5	202.5	170.0
$B_s(mT)$	286.58	255.96	233.95	196.1
B_r/B_s	0.85	0.90	0.87	0.87
μ_m	12,794	9,346	11,350	13,621

Fig-6.6 shows the hysteresis curve for $Ni_{80-x}Fe_xB_{20}$ [x = 20, 30, 40 and 50]. The rectangular shapes of the hysteresis curves show that materials are magnetically very soft and need very low field for saturation magnetization.

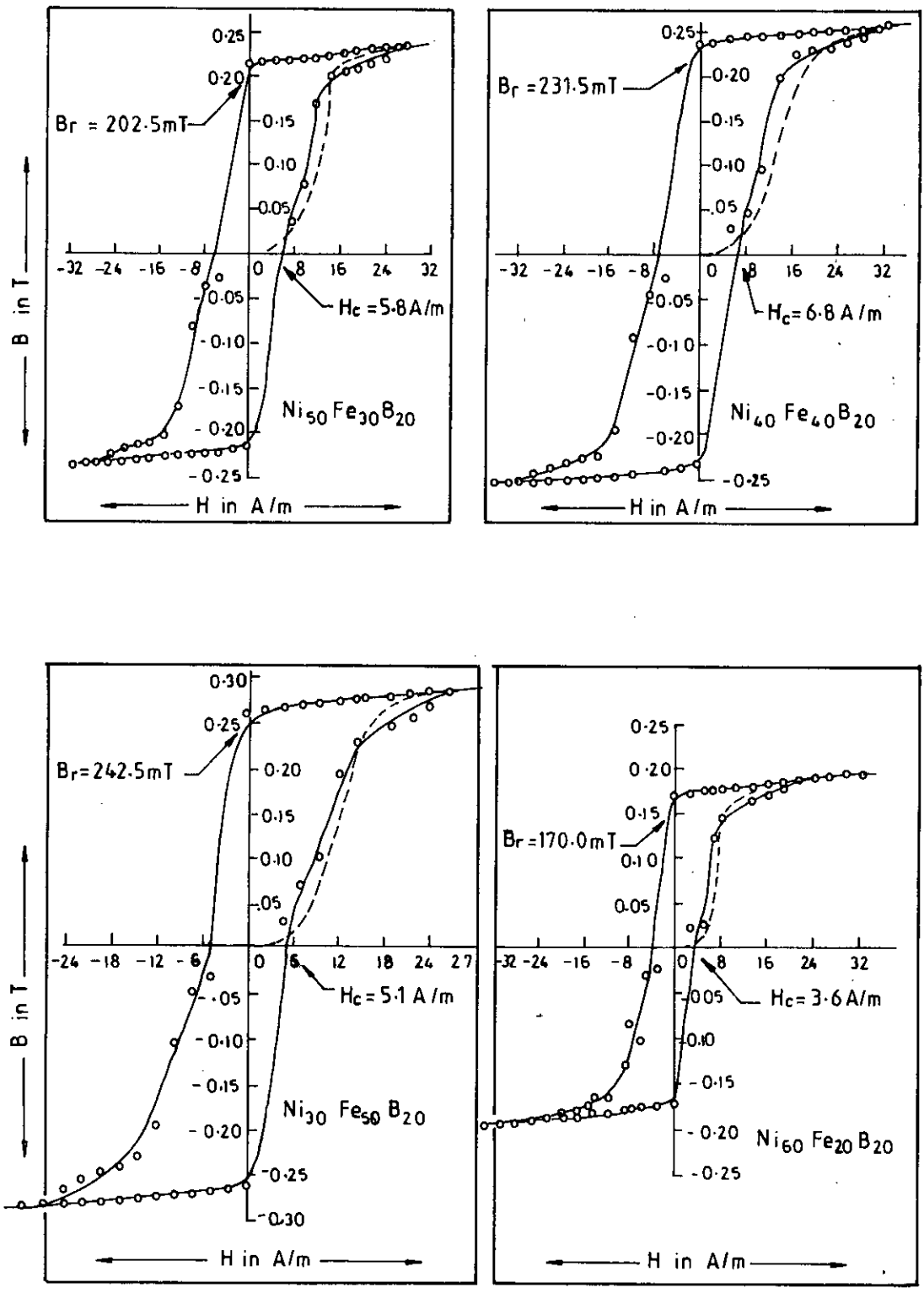

Fig.-6.6 Hysteresis curves of amorphous ribbons with composition $Ni_{80-x}Fe_xB_{20}$

The smooth nature of the experimental data which feat the hysteresis curve show that the domain wall movements have least Barkhausen noise. One special feature of the initial magnetization curve represented by the doted line is that a higher field is needed during the first magnetization cycle. This is explained by assuming that pinning effect decreases in successive magnetization cycles. The comprehensive results are shown in fig-6.7.

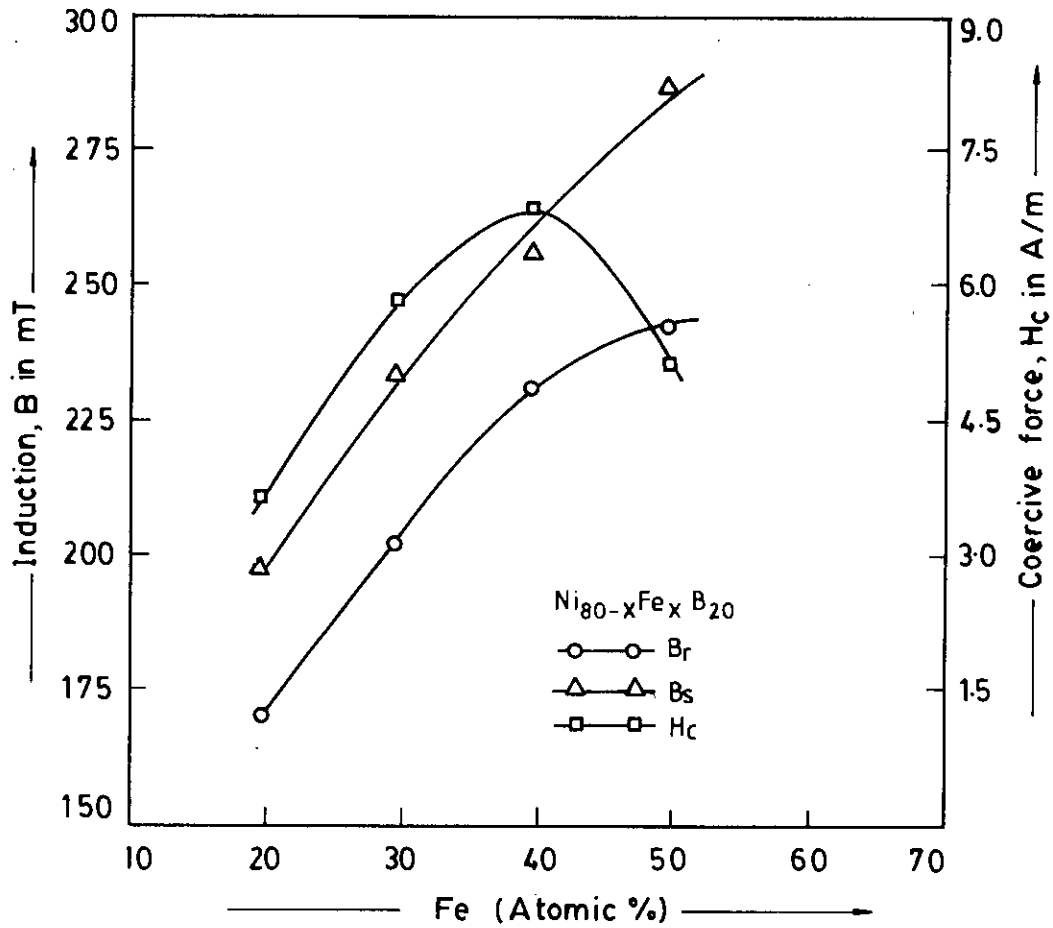

Fig.-6.7 Magnetic induction and coercive force variation with atomic percent of Fe-content in amorphous ribbons with composition $Ni_{80-x}Fe_xB_{20}$.

From Table-6.3, we find that with increasing percentage of iron B_s, B_r and H_c increase allmost monotonically with the exception of $Ni_{30}Fe_{50}B_{20}$ sample in which case coercivity decreased in spite of high percentage of Fe. As expected, the maximum permeability of these samples decreased with increasing Fe content,

consistently with the corresponding coercivity values. The maximum permeability of 13,621 was obtained for $Ni_{60}Fe_{20}B_{20}$ which shows that this particular composition is most suitable for soft amorphous magnets. The values of $^{B_r}/_{B_s}$ remains more or less constant for all the samples showing that magnetization mechanism is similar for all the compositions..

Since iron and Nickel have opposite values of magnetostriction, it is expected that their combination will give interesting effects on their alloys. The mechanism involved in these amorphous materials is very complicated, because no two magnetic sites are, in the strict sense, identical and their magnetic moment can vary from point to point. Also the variation of concentration due to the preparation technique involved produce stress induced anisotropy which again depends to co-ordination number of each magnetic site.

Permeability due to static external field from 0.5A/m to 35A/m for the ribbons with different compositions are shown in fig-6.8. The maximum permeability occurs at different fields 5.8, 14.95, 15.1 and 17.6A/m for compositions $Ni_{60}Fe_{20}B_{20}$, $Ni_{30}Fe_{50}B_{20}$, $Ni_{50}Fe_{30}B_{20}$ and $Ni_{40}Fe_{40}B_{20}$ respectively and their corresponding values of μ_m are shown in Table-6.3. The field corresponding to the peaks of the permeability curves are different for different compositions, the minimum field corresponds to the maximum percentage of nickel. This shows that even in the amorphous state the permalloy characteristics is maintained.

Magnetostriction and anisotropy along with surface defects (6.1), volume pinning effect of domain walls(6.2) and relaxation effects due to local structural rearrangements and clusters of chemical short range ordered(6.3) regions-all contribute to coercivity. However, we consider that magnetostriction is the major origin of coercivity in our specimens. Thus the variation of coercivity with composition is explained as originating from the complex combination of magnetostriction arising from iron and nickel atoms and the anisotropy introduced by the magnetostrictive strains in the ribbons during the preparation process. Since the initial permeability depends very much on the magnetic field, these materials cannot be used in low fields, where permeability although maximum is highly field dependent. One should rather choose the operating field at a relatively higher value where the permeability is more independent of the field.

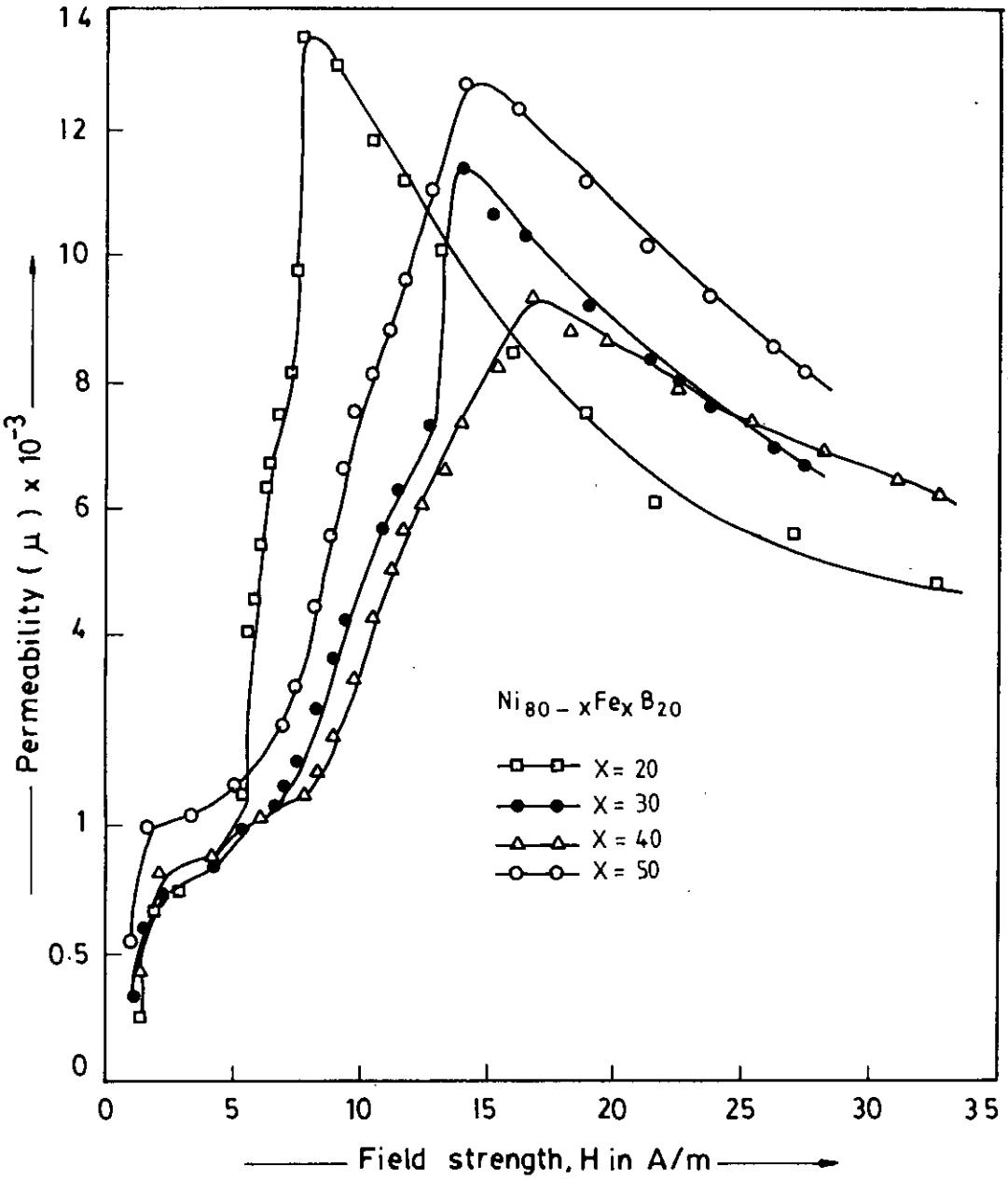

Fig.-6.8 Permeability versus static magnetic field for amorphous ribbons with composition $Ni_{80-x}Fe_xB_{20}$

6.4. Dynamic Magnetic Properties of Ni-based Amorphous Ribbons

Dynamic magnetic properties of as-quenched Nickel-Iron-Boron system with composition $Ni_{80-x}Fe_xB_{20}$ [x = 20, 30, 40 & 50] have been determined using an impedance analyzer. At room temperature the frequency and field dependence of the complex permeability $\mu = \mu' - i\mu''$ and the Core losses of the tape wound cores were measured by an impedance analyzer up to 13MHz and relative quality factor ($\mu_i/\tan\delta$) and the loss factors have been determined from the direct value $\tan\delta = (\mu''/\mu')$.

The initial permeability (μ_i) of the amorphous ribbon, which is extrapolated to zero frequency and for vanishing magnetic field, is estimated. Since permeability cannot be measured without applying some field, the initial permeability for the vanishing field is estimated by extrapolation of the initial permeability of the amorphous ribbons at very low frequency in our dynamic measurement. It is assumed that the limit of low frequency corresponds to static field. The μ_i of the ribbons with composition $Ni_{80-x}Fe_xB_{20}$ is calculated from the low A.C. magnetic field dependence of permeability in the limit of frequency 0.5KHz and in a vanishing magnetic field as shown in fig.-6.9. The results are shown in Table-6.4.

Table-6.4

$Ni_{80-x}Fe_xB_{20}$	x = 50	x = 40	x = 30	x = 20
μ_i	481	422	382	444

As shown in fig.-6.9, the initial permeability in the vanishing field region for all the ribbons except the one with composition $Ni_{30}Fe_{50}B_{20}$, remains almost constant with slight variation of the field. The ribbon of composition $Ni_{30}Fe_{50}B_{20}$ shows a large increase in the permeability with field even in the low field region which is quite interesting and is rather complicated. This shows that special barriers to domain wall motion exist for this particular composition. The results are shown in Table-6.4. Initial permeability is controlled by the irreversible part of the domain wall motion, and the preparation technique determines the defects and the associated energy barriers. It is difficult to explain the values of these parameters quantitatively, because of the various contributing factors.

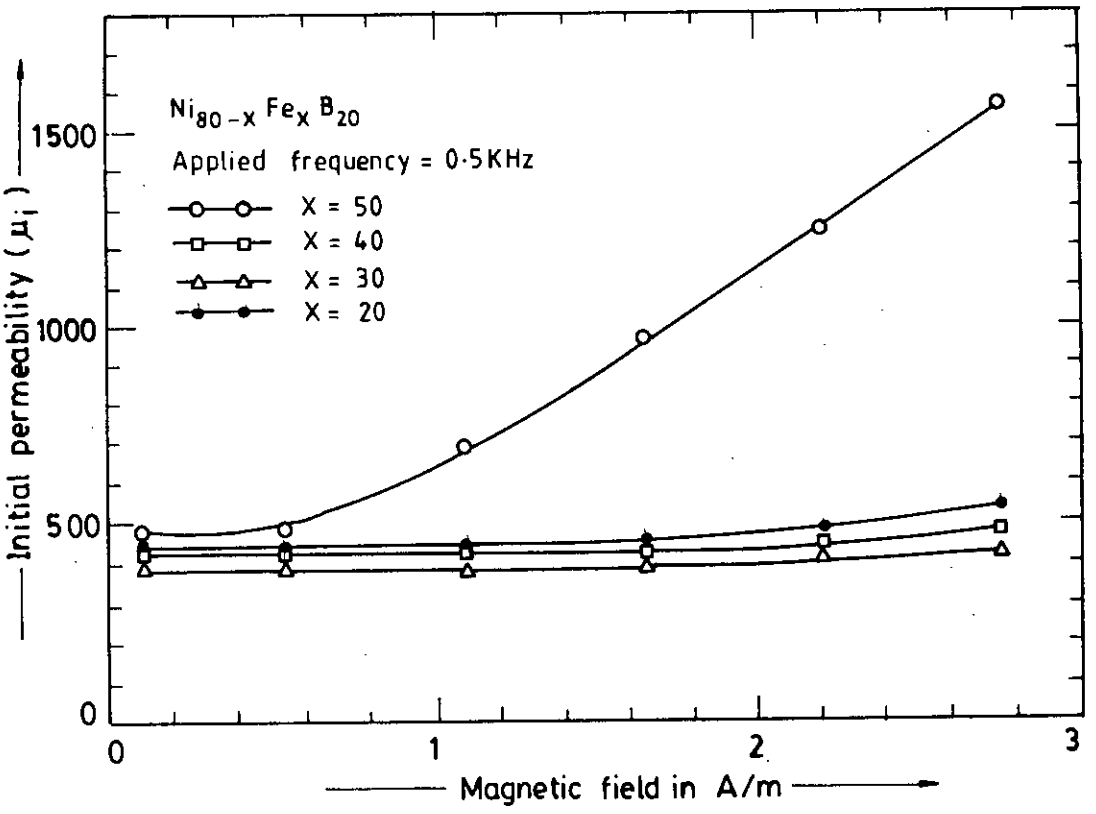

Fig.-6.9 Permeability versus A.C. magnetic field of amorphous ribbons with composition $Ni_{80-x}Fe_xB_{20}$

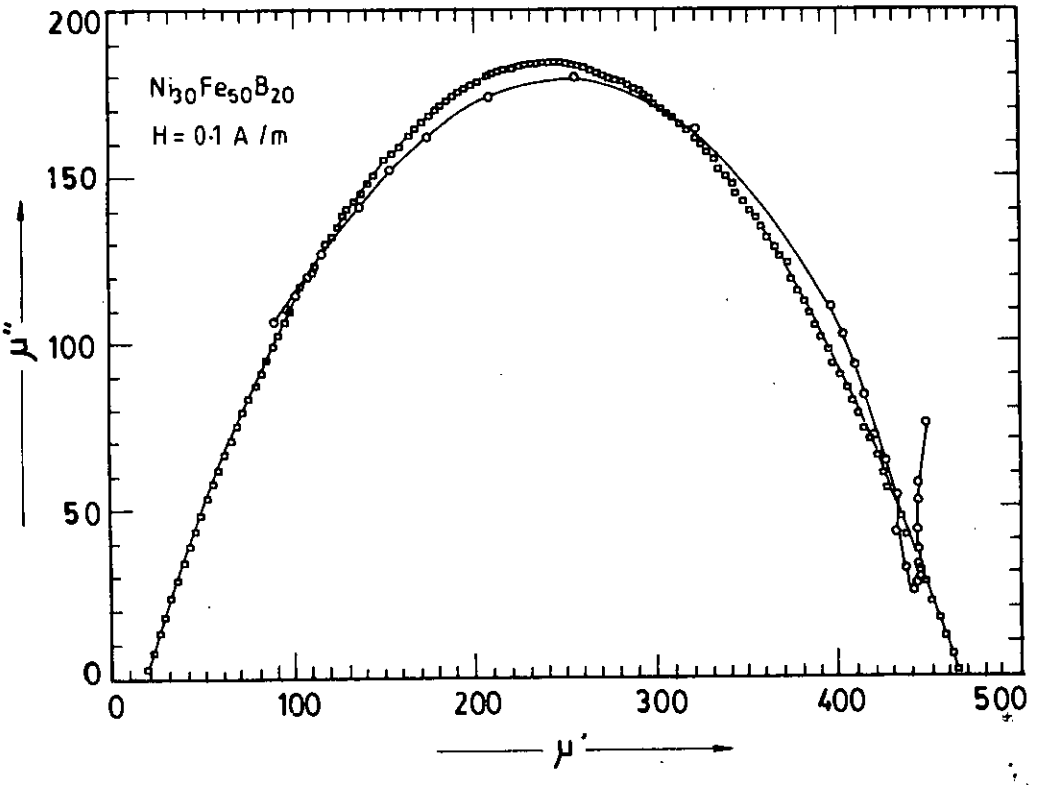

Fig.-6.10 Complex permeability μ'' Vs μ' plot for the as-quenched sample with composition $Ni_{30}Fe_{50}B_{20}$

Another supporting method for the accurate determination of μ_i is to plot the imaginary part of complex permeability (μ'') against the real part of complex permeability (μ'). For any applied field, this representation shows a semicircle for the high frequency to the low frequency. The μ_i value is determined from the semicircle's diameter which intersects the μ' axis corresponding to a low applied field H=0.1A/m. Fig.-6.10 gives the representative results of the as-quenched sample with composition $Ni_{30}Fe_{50}B_{20}$. This fig.-6.10 produces a short vertical spike, and the evaluation of the permeability corresponds exclusively to the relaxation, separating it from the low frequency dispersion. The high frequency end of the semicircle does not coincide with the origin of experimental data, presumably due to the existence of an additional dispersion.

Fig.-6.11 shows that μ_i of Ni-Fe-B amorphous system decreases with decreasing Fe-content upto 30At.% of Fe, beyond this point there is an increase of μ_i with decreasing Fe-content.

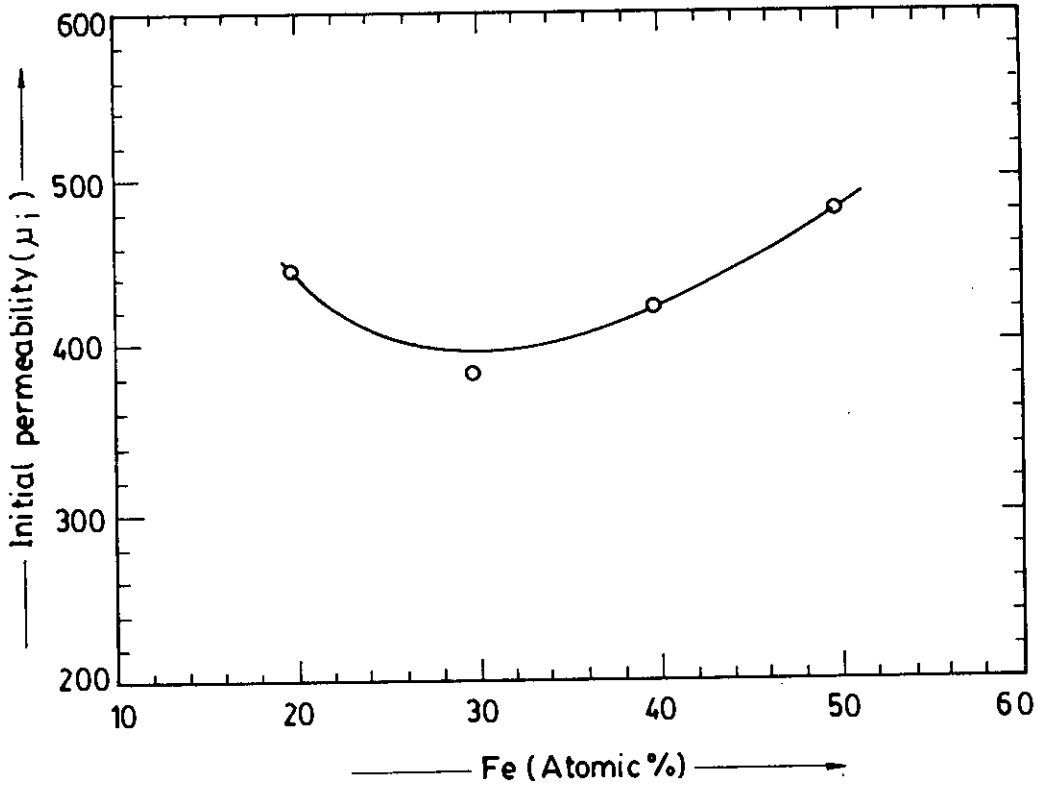

Fig.-6.11 Variation of initial permeability due to change in the Fe-content in amorphous ribbons with composition $Ni_{80-x}Fe_xB_{20}$.

The measurements were performed at room temperature using an ac fields with a very low constant value of H = 0.1A/m and a frequency from o.5KHz to13MHz. From the real part and the imaginary part of the complex permeability, the quality factors as a function of frequency have been calculated for different compositions. The frequency dependence of the real part of complex permeability is shown in fig-6.12. The flat region up to the frequency 3MHz indicates that except the ribbon with composition $Ni_{60}Fe_{20}B_{20}$, all the other three samples of composition $Ni_{30}Fe_{50}B_{20}$, $Ni_{40}Fe_{40}B_{20}$ and $Ni_{50}Fe_{30}B_{20}$ respectively are very suitable as Core materials at low fields.

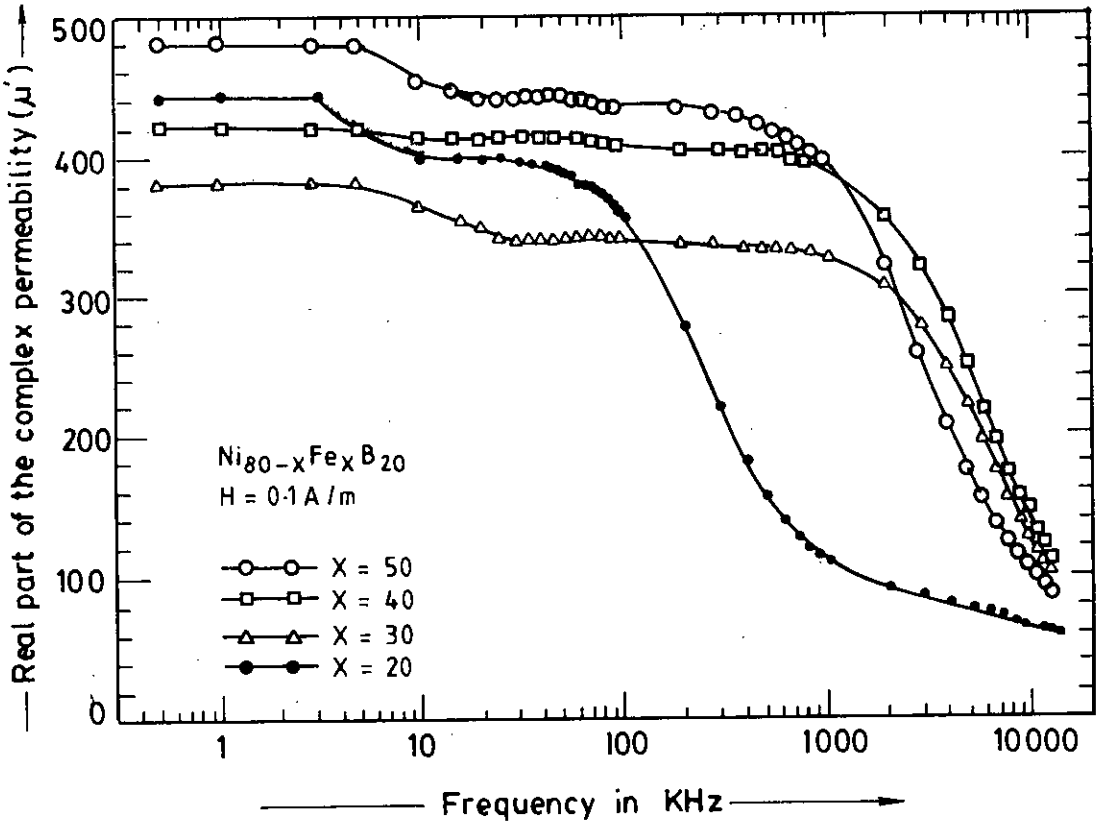

Fig.-6.12 Frequency dependence of the real part of complex permeability of amorphous ribbons with composition $Ni_{80-x}Fe_xB_{20}$

The imaginary part of the complex permeability and loss factor for different compositions over the frequency range 0.5KHz to 13MHz are shown in fig-6.13 and fig-6.14 respectively. The origin of the loss factors can be attributed to various domain effects, which include nonuniform and nonrepetitive domain wall motion, domain wall bowing, localized variation of flux density and nucleation and annihilation of domain walls. The principal cause of eddy current loss in amorphous ribbons is attributed to non sinusoidal and repetitive motion of domain walls.

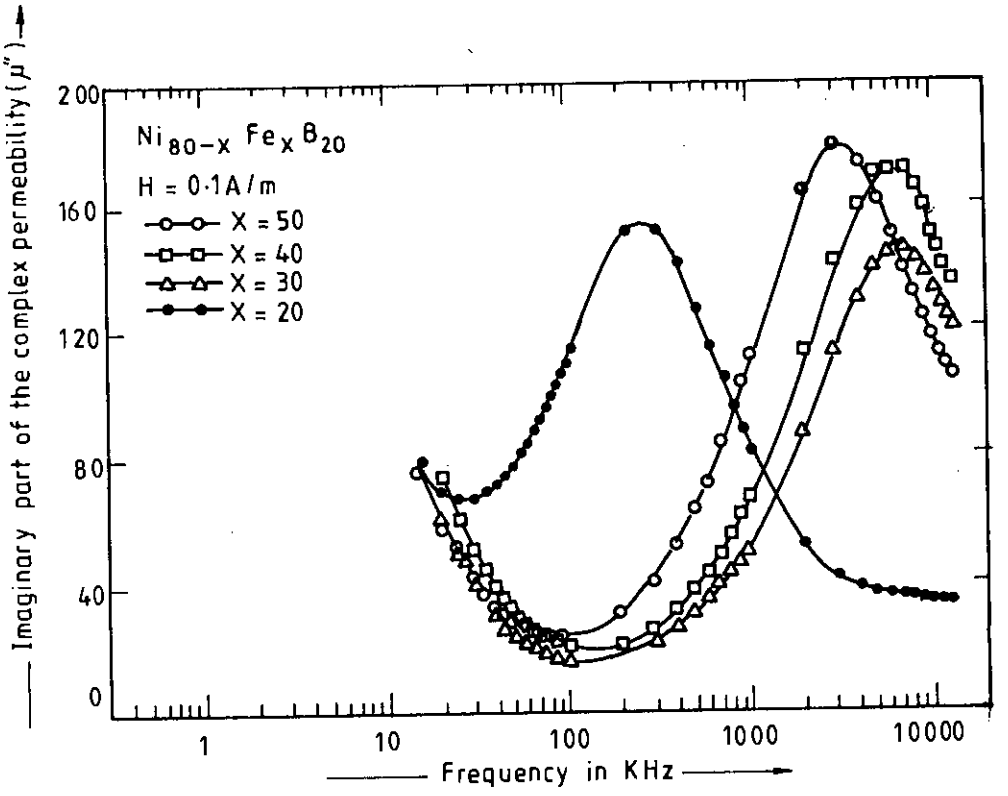

Fig.-6.13 Frequency dependence of the imaginary part of complex permeability of amorphous ribbons with composition $Ni_{80-x}Fe_xB_{20}$

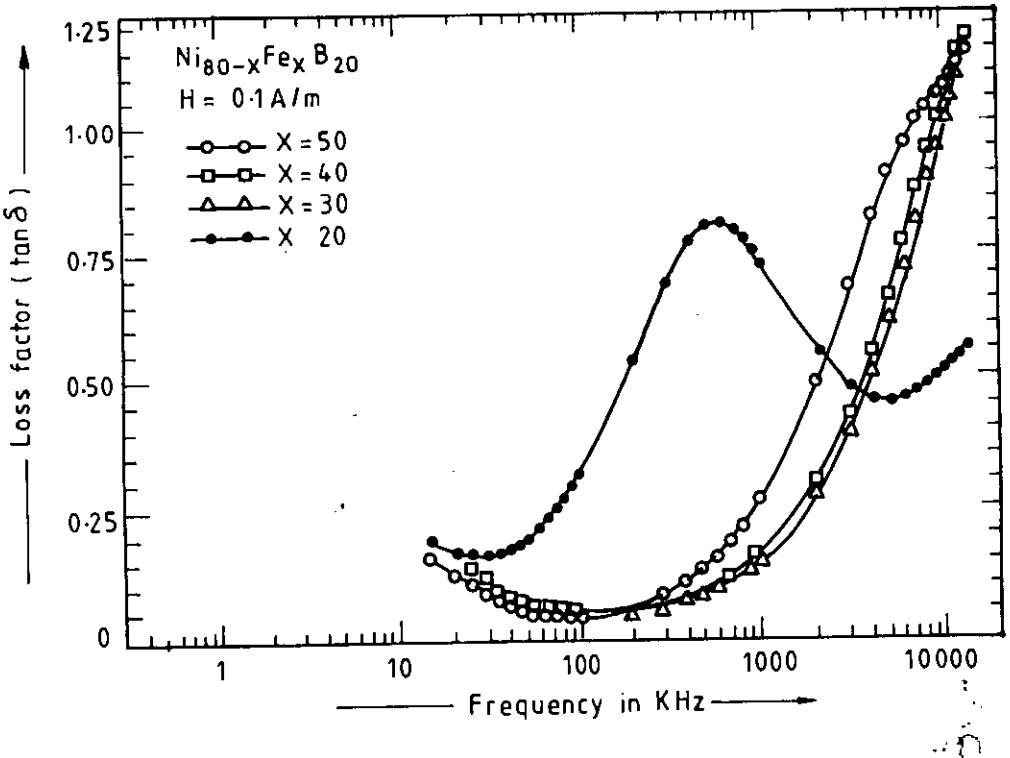

Fig.-6.14 Frequency dependence of loss factors of amorphous ribbons with composition $Ni_{80-x}Fe_xB_{20}$

At low frequencies the loss is controlled by hysteresis and eddy current losses and at high frequency the flux penetration becomes low and loss is controlled mainly by interaction between the grains. As a result grain size, grain orientation and specimen thickness become important. It has been reported before that the precipitation and specimen thickness become important factors. The precipitation of very small percent of particles improve the high frequency losses and permeability (6.4). The Nickel content has important effect in this case. Except the ribbon with composition $Ni_{60}Fe_{20}B_{20}$, the other three materials having composition $Ni_{50}Fe_{30}B_{20}$, $Ni_{40}Fe_{40}B_{20}$ and $Ni_{30}Fe_{50}B_{20}$ respectively are almost identical in their performances and have low loss factors in frequencies up to 2MHz.

The frequency dependence of relative quality factors are shown in fig.-6.15. The relative quality factors as controlled by the real part of the complex permeability have quite high values in the range 15KHz to 3MHZ for all the three ribbons, having low loss factors as mentioned before.

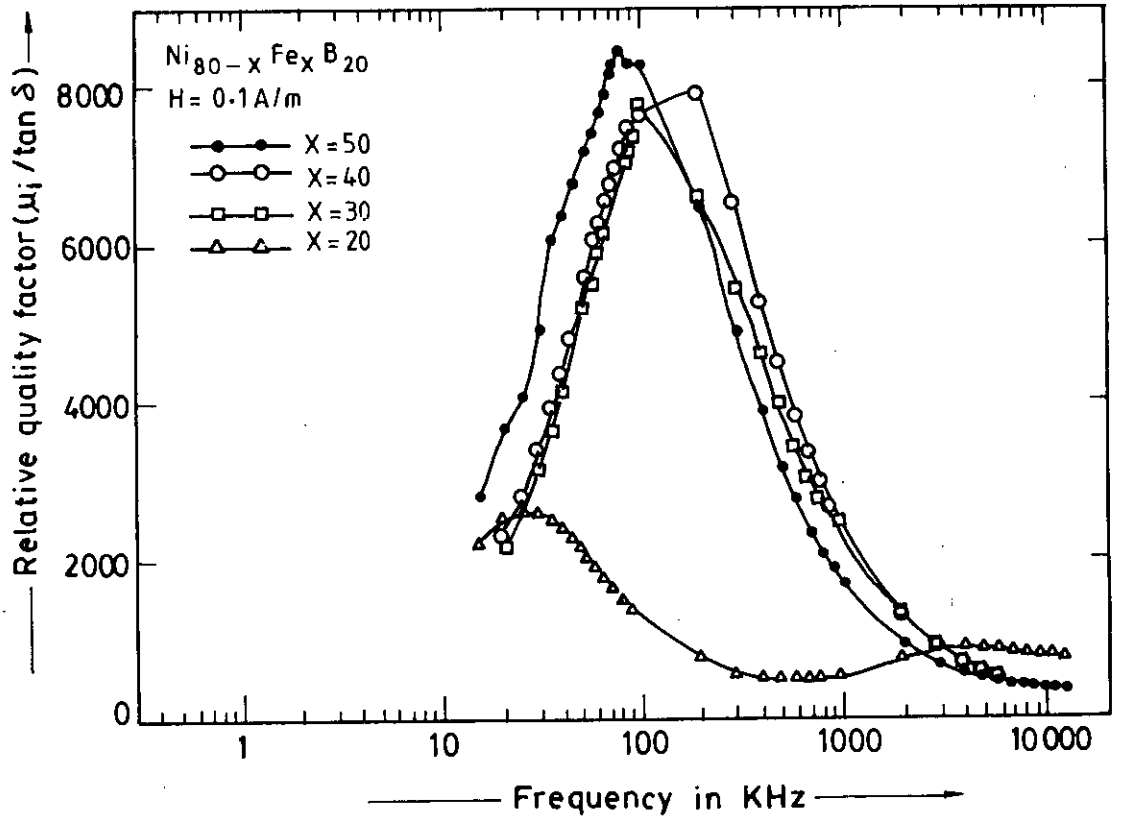

Fig.-6.15 Frequency dependence of relative quality factor of amorphous ribbons with composition $Ni_{80-x}Fe_xB_{20}$

Fig.-6.16 shows the annealing effect of μ_i of amorphous ribbons with composition $Ni_{80-x}Fe_xB_{20}$. μ_i of all the samples are studied for their dependence on annealing temperature at very low field H=0.1A/m at low frequency (1KHz). All samples are annealed at a constant annealing time of one hour. In general the value of μ_i increases with the annealing temperature which are different for different samples, and then decreases with further increase of the annealing temperature. The initial increase is explained as due to the removal of pinning centres and the final decrease in μ_i is explained as due to the nucleation of crystallites and their growth.

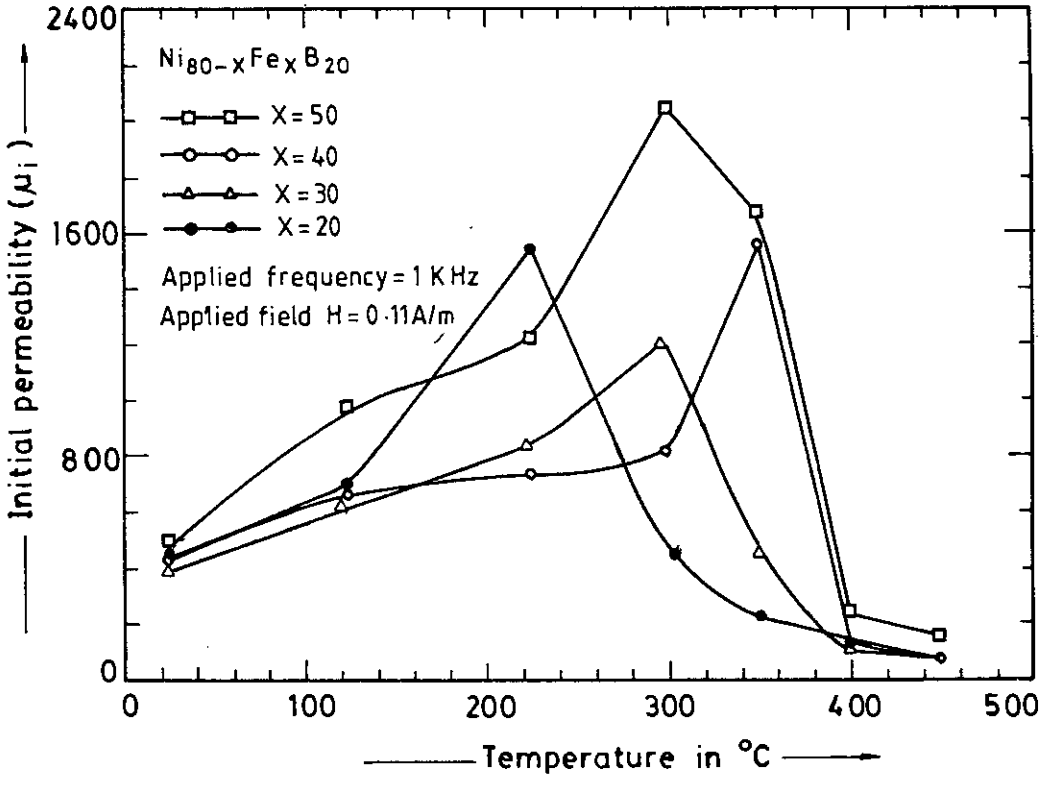

Fig.-6.16 Initial permeability versus annealing temperature of amorphous ribbons with composition $Ni_{80-x}Fe_xB_{20}$.

6.5 Specific Magnetization Measurements of Ni-based Amorphous Ribbons.

The specific magnetization of Ni-Fe-B ribbons with composition $Ni_{80-x}Fe_xB_{20}$ [x = 20, 30 40 & 50] in as-quenched condition is measured using a V.S.M. The specific magnetization process as a function of field are shown in fig.-6.17. The saturation magnetization for these ribbons have lower values for increasing replacement of Fe by Ni. It is observed that while the ribbon with composition $Ni_{30}Fe_{50}B_{20}$ reaches its saturation value around 1.9KG field, the ribbon with composition $Ni_{40}Fe_{40}B_{20}$ requires 1.5KG, for the compositions $Ni_{50}Fe_{30}B_{20}$ and $Ni_{60}Fe_{20}B_{20}$ the required fields are 1.3KG and 1.6KG respectively. The saturation specific magnetization (σ_s) for different sample are calculated as shown in Table-6.5.

Table-6.5

$Ni_{80-x}Fe_xB_{20}$	x = 20	x = 30	x =40	x =50
σ_s in Am^2/Kg at room temp.	82.66	93.74	121.36	127.14
$\sigma_s(0)$ in Am^2/Kg at 0K	84	95	123	131
T_c	258^0C	336^0C	410^0C	443^0C

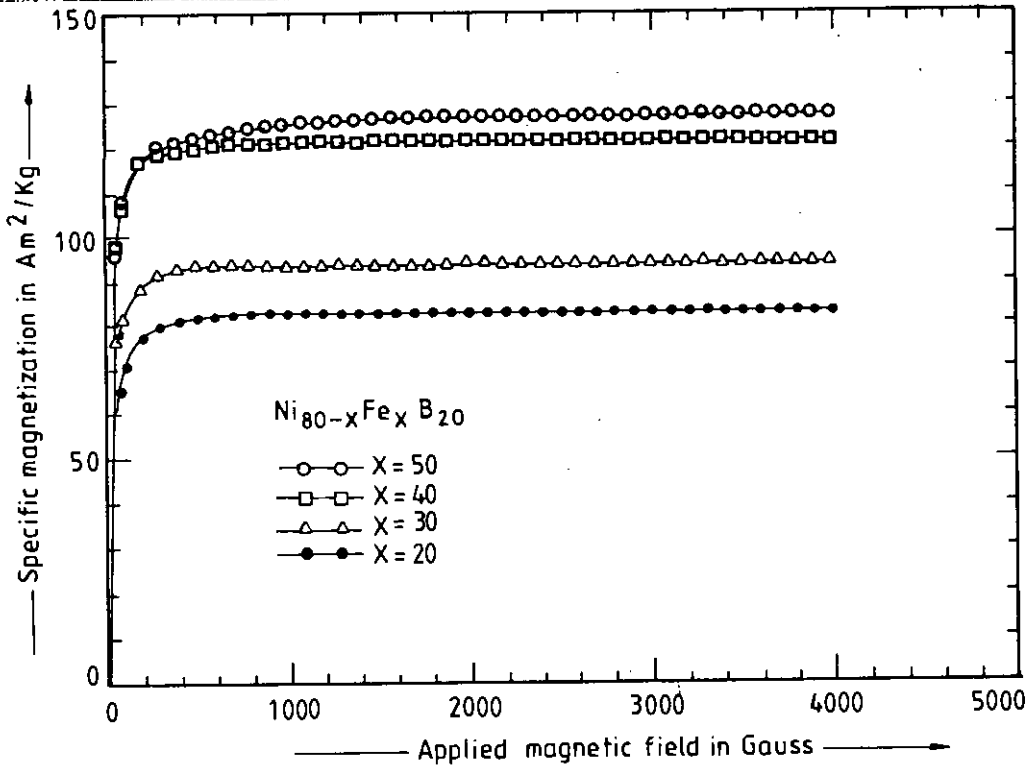

Fig.-6.17 Specific magnetization versus magnetic field of amorphous ribbons with composition $Ni_{80-x}Fe_xB_{20}$

The σ_s decreases with increasing replacement of Fe by Ni as shown in fig-6.18. For Ni-Fe-B amorphous alloys with fixed metalloid B, there is a reduction in moment in the Fe-Ni series with increasing Ni-content in place of Fe. A simple approach is to replace a randomly varying local field at the moment site of Fe by Ni. The data agree qualitatively with the rigid band model using the sample moments $0.6\mu_B$ for Ni and $2.1\mu_B$ for Fe. The results indicating that the average moment of the transition metal alloy decreases with the replacement of Fe with Ni. However, the rigid band model is not strictly followed.

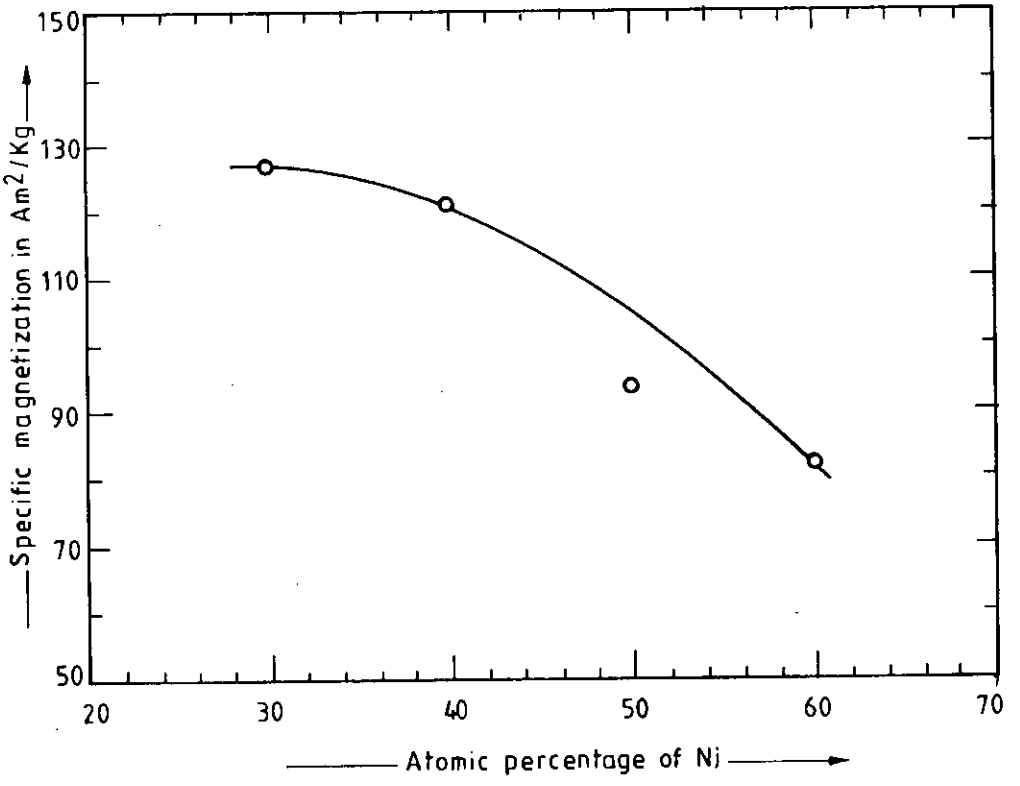

Fig.-6.18 Variation of specific magnetization due to change in the Ni-content in $Ni_{80-x}Fe_xB_{20}$ amorphous ribbons.

6.5.1 Temperature Dependence of Specific Magnetization of Ni-based Amorphous Ribbons.

The temperature dependence of specific magnetization of amorphous ribbons with composition $Ni_{80-x}Fe_xB_{20}$ is shown in fig.-6.19. The T_c is determined from the point of vanishing of magnetization with temperature. Ni-Fe-B alloys with T_c, above the beginning of thermal excitation due to structural relaxations and stress relief have to be considered carefully. The relaxation of local atomic configurations will perturb both

the magnetic and chemical environment, and therefore, the moment distribution will change. Consequently, as temperature is raised towards T_c, substantial irreversible changes in moment distribution and reordering of paramagnetic inclusions is present. The values obtained for T_c decreases with increasing Ni-content which have the same nature that of fig.-6.5. This results is discussed in section-6.2 indicating that in Ni-based alloys, the weak itinerant ferromagnetism leads to an unusual temperature dependence of σ_s.

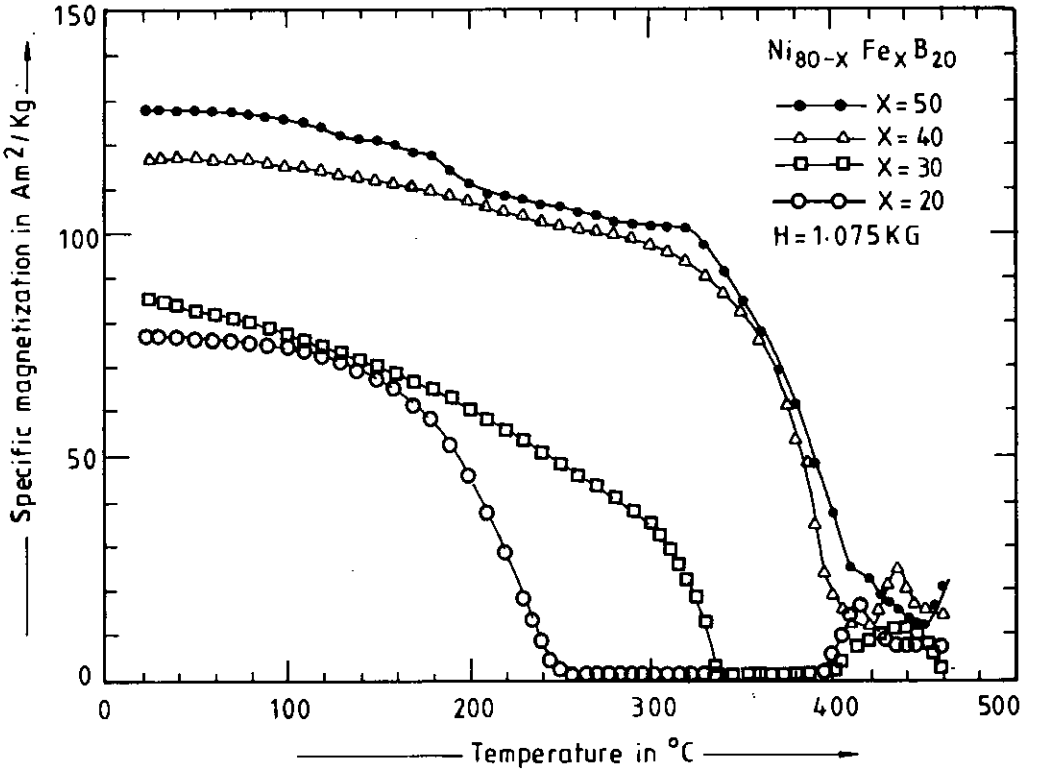

Fig.-6.19 Specific saturation magnetization as a function of temperature for $Ni_{80-x}Fe_xB_{20}$ amorphous ribbons.

A typical temperature dependent saturation specific magnetization measured with H = 4KG. The T = 0K saturation specific magnetization, $\sigma_s(0)$ are obtained by extrapolating to 0K the $\sigma_s(T)$ values measured at various temperature. The extrapolated values of $\sigma_s(0)$ for different ribbons are shown in Table-6.5.

A comparison of experimental data of reduced magnetization $m = \frac{\sigma_s(T)}{\sigma_s(0)}$ versus reduced temperature, $\frac{T}{T_c}$ using mean field theory is shown in fig.-6.20.

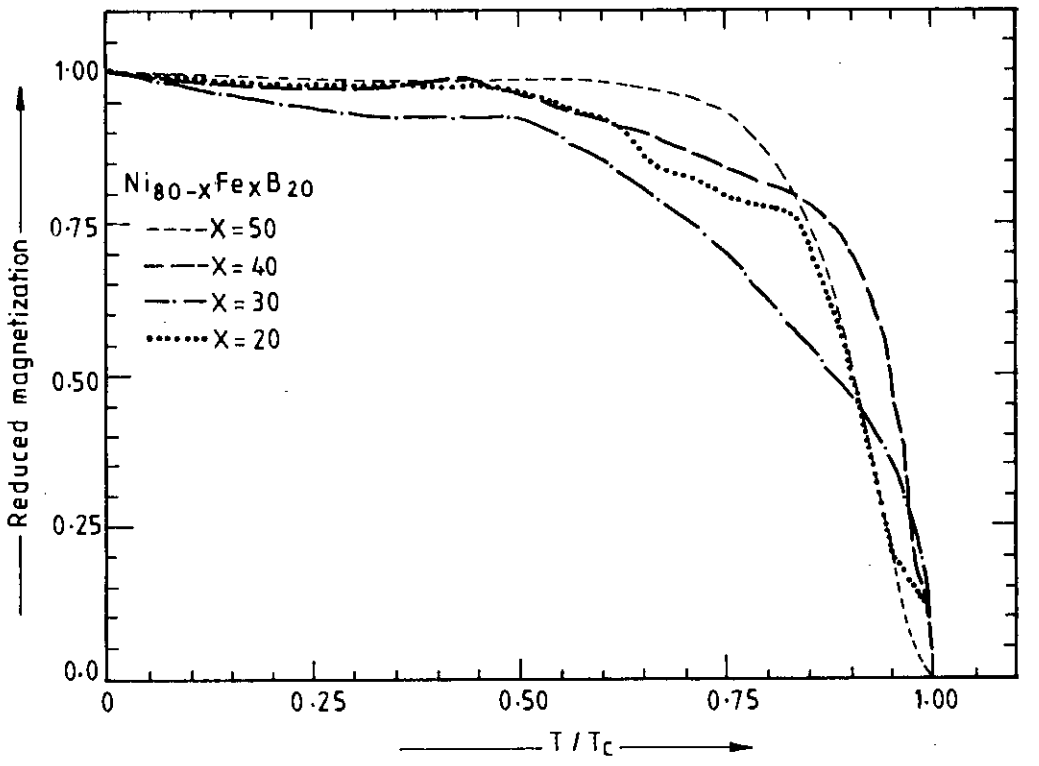

Fig.-6.20 Reduced magnetization $m = \frac{\sigma_s(T)}{\sigma_s(0)}$ versus $\frac{T}{T_c}$ for amorphous ribbons $Ni_{80-x}Fe_xB_{20}$

The graphs represent meanfield calculations for different Ni-Fe-B ribbons, the exchange fluctuation parameter in the exchange interaction lead to the structural disorder. The temperature effect of $\sigma_s(T)$ arises from thermally excited fluctuations in both topological randomness and chemical bonds disorder. It should be natural to consider an exchange interaction disorder. However, no complete theoretical understanding of this behaviour exists at present. Reduced magnetization versus $\frac{T}{T_c}$ curves for amorphous ribbons with composition $Ni_{80-x}Fe_xB_{20}$ lie substantially below that for crystalline nickel.

6.6 Stress Induced Anisotropy Measurements of Ni-based Amorphous Ribbons

The field dependence of the torque versus the angle between the magnetic field and the direction of the preparation axis of Ni-Fe-B ribbons with composition $Ni_{80-x}Fe_xB_{20}$ [x = 20, 30, 40 & 50]. The representative curve for torque versus of the ribbon with arbitrary angle of the amorphous ribbon with composition $Ni_{30}Fe_{50}B_{20}$ for different fields are shown in fig.-6.21. There is a small increase in the torque with increased field. This is origin explained as due to the competing contribution from Fe-Ni pair ordering mechanism for involved. However, a small contribution to K_u, present in alloys which contain only iron as the magnetic species, must be attributed in the orientation of some other structural mohf or defect. It is also possible that larger scale defects or inhomogeneities, such as voids or regions of composition somewhat different from the average, may acquire a characteristic shape and orientation during the preparation of ribbons and there by contribute to stress induced anisotropy (K_u).

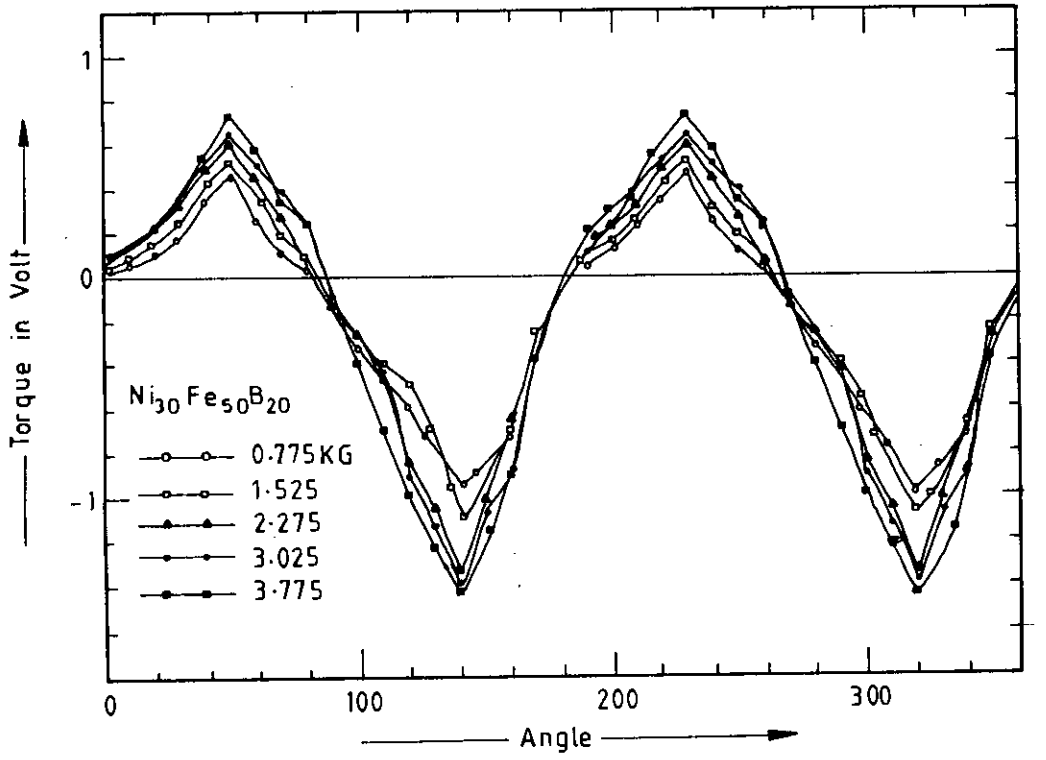

Fig.-6.21 Field dependence of torque versus angle for the amorphous ribbon with composition $Ni_{30}Fe_{50}B_{20}$

For an as-quenched Ni-Fe amorphous ribbons with positive magnetostriction due to the presence of Fe-atoms there is positive magnetostriction in the bulk state. Torque of the metallic ribbon also respond to field. Such effects are best observed in samples that have been totally stress relived in order to eliminate magnetostrictive effects.

The K_u is calculated from the torque versus angle curves by Fourier analysis for each set of temperature and field. The sensitivity of the torque magnetometer is calibrated to be 1 volt $= 4.755 \times 10^{-7}$ J of different scales of sensitivity are used depending on the specimen. Fourier coefficient as determined by computer program and from the torque versus angle data for different values of the angle between the applied field and the axis of the amorphous ribbon for each sample of composition $Ni_{80-x}Fe_xB_{20}$, and by extrapolation of the field up to $H \to \infty$ are shown in fig.-6.22 and fig.-6.23.

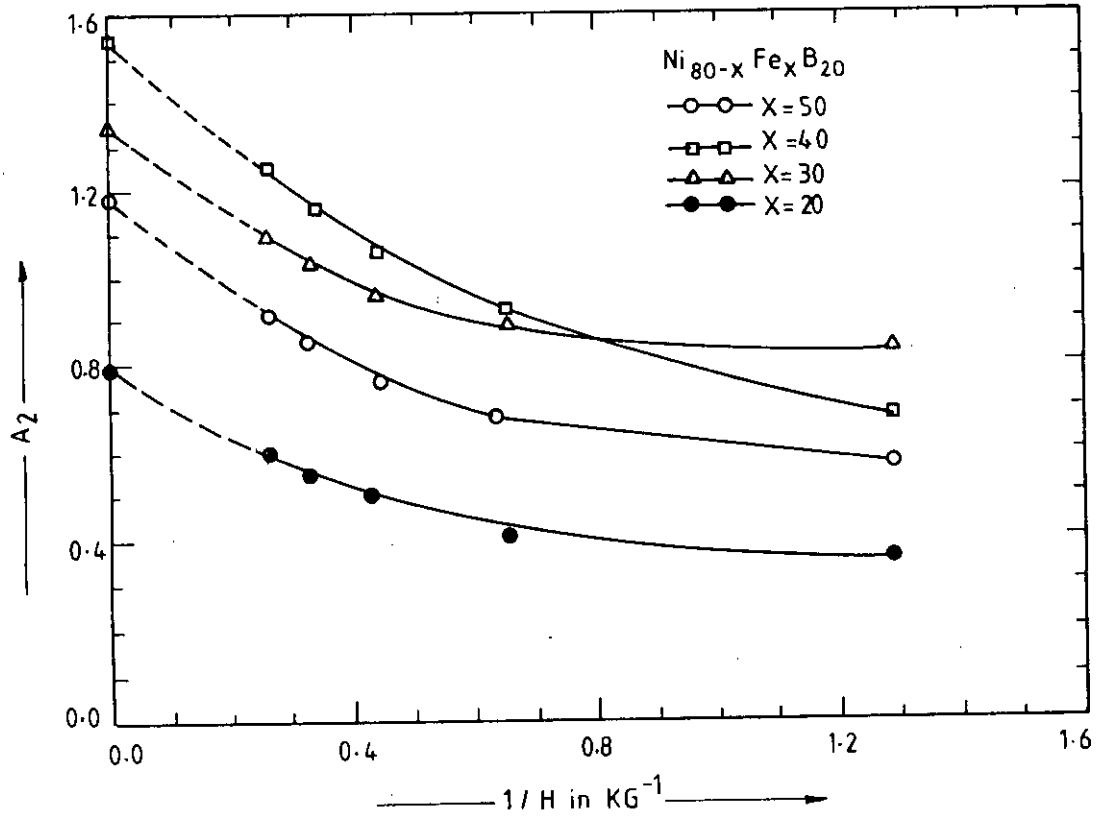

Fig.-6.22 Fourier coefficient for infinite field by extrapolation from A_2 versus 1 / H curve for different compositions of the system $Ni_{80-x}Fe_xB_{20}$

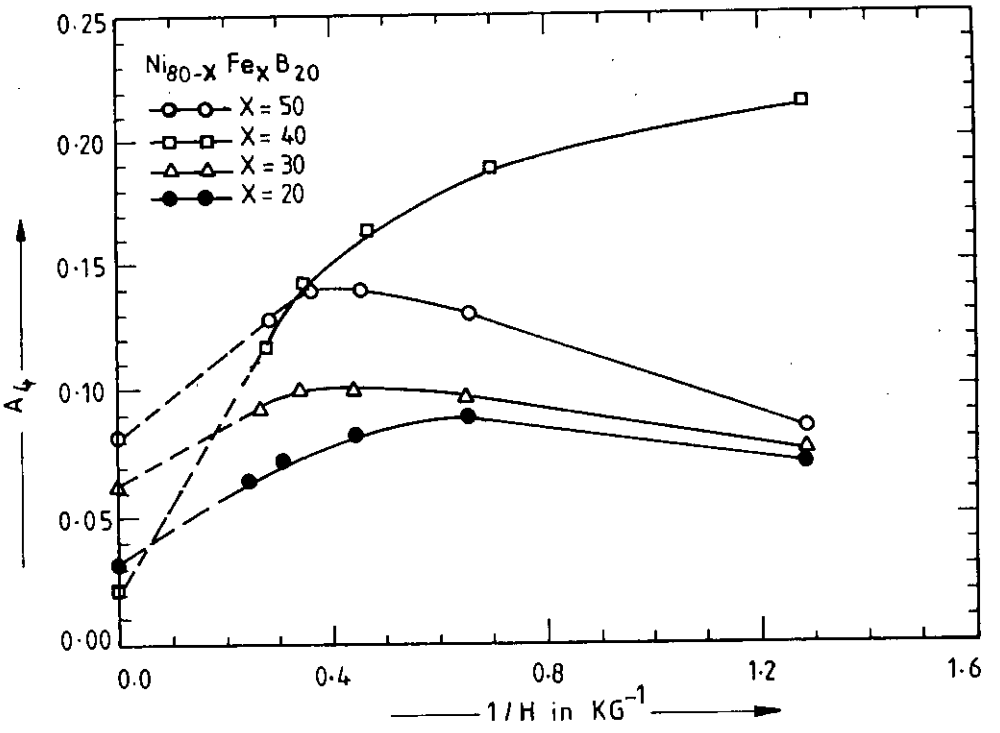

Fig.-6.23 Fourier coefficient for infinite field by extrapolation from A_4 versus 1/H curve for different compositions of $Ni_{80-x}Fe_xB_{20}$ system

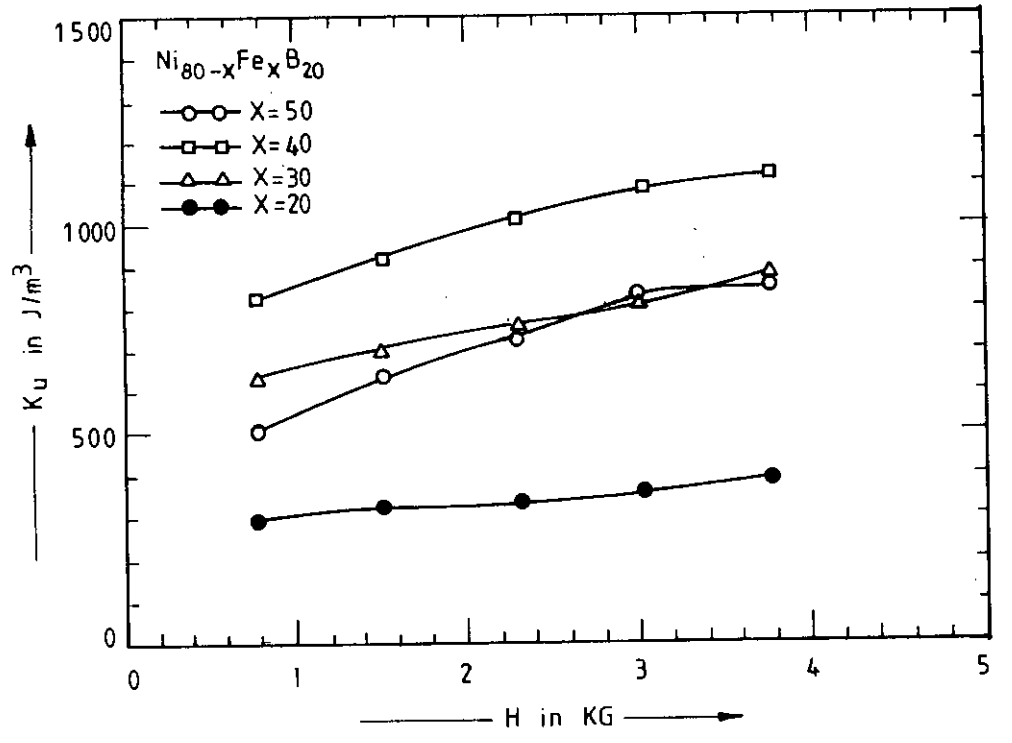

6.24. Field dependence of experimental values of K_u for different compositions of $Ni_{80-x}Fe_xB_{20}$ system

Experimental values of field dependence of K_u for different ribbons with composition $Ni_{80-x}Fe_xB_{20}$ as shown in fig.-6.24. The K_u against 1/H as obtained by extrapolation to saturation anisotropy values are shown in fig.-6.25. The results are shown in Table-6.6

Table-6.6

$Ni_{80-x}Fe_xB_{20}$	x = 20	x = 30	x =40	x =50
K_u in J / m^3 at room temp.	492.43	939.46	1163.43	902.06
K_u in J / m^3 at 0K	740	1350	1480	1320
T_c	260^0C	340^0C	420^0C	445^0C

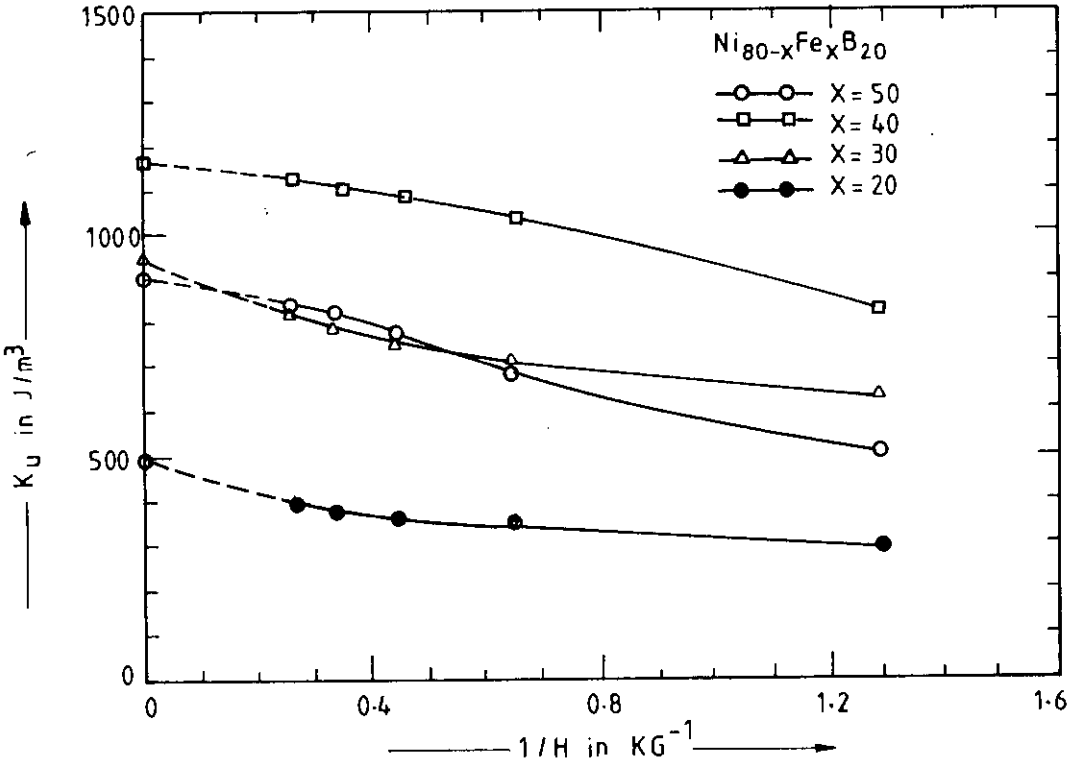

Fig.-6.25 Extrapolated value of K_u for infinite field for different compositions of $Ni_{80-x}Fe_xB_{20}$ system

The experimental results of normalized K_u for amorphous Ni-Fe-B alloys, have almost compositional dependence as predicted by the ordered pair model and hence it is qualitatively established that in both crystalline materials and glasses the field induced anisotropy arises from ordered pairs. However, to obtain this agreement it is necessary to subtract from the measured anisotropy the small but non zero anisotropy obtained in the amorphous ribbons with Ni present. At present, these discrepancies and whatever doubts this cast on the pair ordering model have not been resolved. However, it is clear that, large values of K_u require the presence Fe.

The compositional dependence of K_u in ribbons with Fe contents as shown in fig.-6.26, gives minimum value of K_u at 20 atomic percent of Fe. This dependence of coercive force on composition has the same nature as that of fig.-6.7 and an opposite contribution to μ_i is found in fig.-6.11. K_u is found to be controlled by H_c and μ_i in $Ni_{80-x}Fe_xB_{20}$ amorphous ribbons.

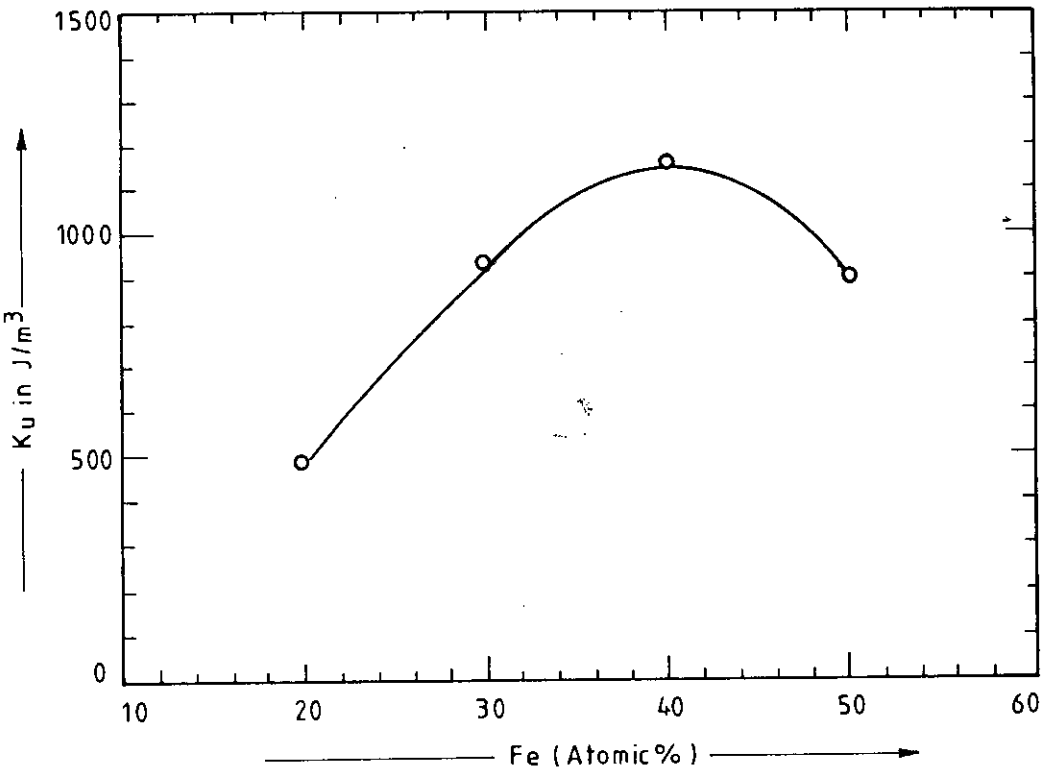

Fig.-6.26 Compositional dependence K_u of amorphous ribbons with composition $Ni_{80-x}Fe_xB_{20}$

6.6.1. Temperature Dependence of K_u

The temperature dependence of stress induced anisotropy of amorphous ribbons with composition $Ni_{80-x}Fe_xB_{20}$ is shown in fig.-6.27. The origin of K_u in this case is most likely the internal stress. In this case, it should be possible to substantially reduce K_u by the stress relieving due to the increase of temperature, and this is indeed observed. The value K_u decreases with increasing temperature, above T_c, K_u is observed to be nearly zero. The extrapolation of K_u to the vanishing value corresponds to the calculated value ferromagnetic transition temperature T_c as shown in Table-6.6. These results are almost nearly the same as the value of T_c measured for the temperature dependence σ_s and μ_i. The K_u is calculated in J/m^3 for different temperatures as shown in Table-6.7.

Table-6.7.

$Ni_{80-x}Fe_xB_{20}$	x =20 K_u in J/m^3	x = 30 K_u in J/m^3	x = 40 K_u in J/m^3	x =50 K_u in J/m^3
25^0C	493	940	1164	902
50^0C	442	874	1159	758
75^0C	436	800	1152	700
100^0C	431	651	1101	640
125^0C	338	623	946	635
150^0C	322	534	923	629
175^0C	290	443	871	597
200^0C	212	363	765	570
225^0C	97	358	608	544
250^0C	43	303	491	511
275^0C	5	197	390	423
300^0C		123	322	375

The T= 0K stress induced anisotropy $K_u(0)$ are obtained by extrapolating $K_u(T)$ to 0K. The $K_u(0)$ for different values of ribbons with composition $Ni_{80-x}Fe_xB_{20}$ are shown in Table-6.6.

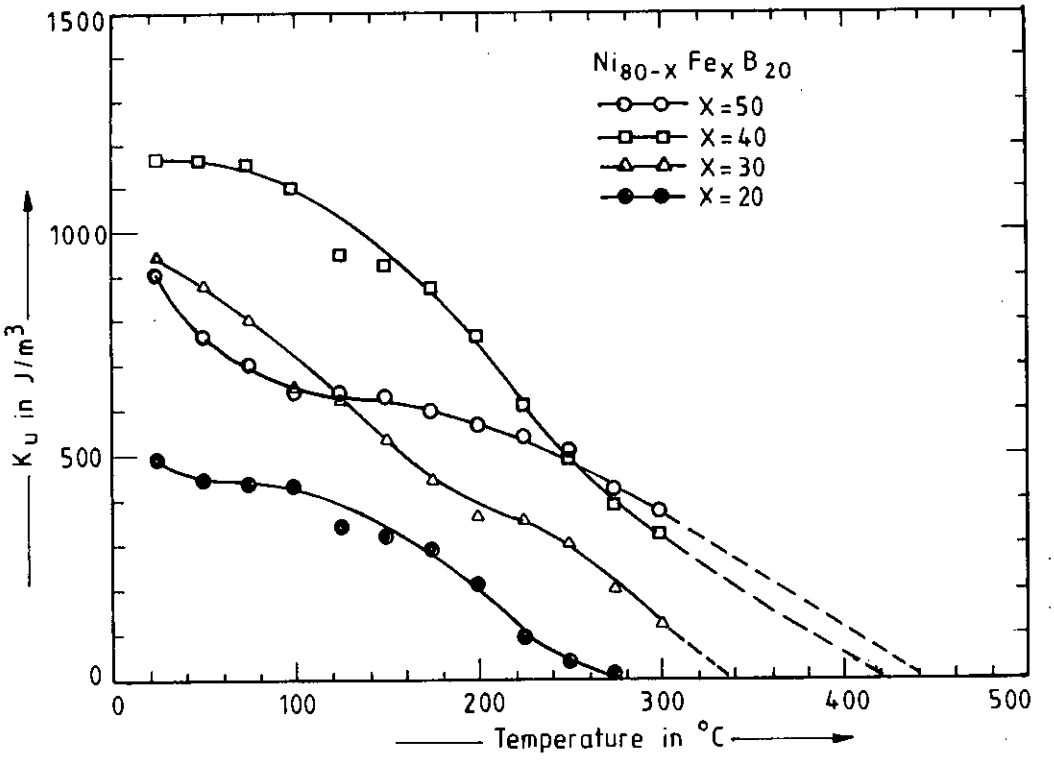

Fig.-6.27. Temperature dependence of K_u of amorphous ribbons with composition $Ni_{80-x}Fe_xB_{20}$

The corresponding curves $\ln\left[\frac{K_u(0)}{K_u(T)}\right]$ versus $\ln\left[\frac{\sigma_s(0)}{\sigma_s(T)}\right]$ in amorphous ribbons with composition $Ni_{80-x}Fe_xB_{20}$ follow the straight line as shown in fig.-6.28. The K_u arising from a disorder caused by randomly oriented easy axis follows a power law: $\frac{K_u(T)}{K_u(0)} = \left[\frac{\sigma_s(T)}{\sigma_s(0)}\right]^n$ with in $2 < n < 6$. The values of n are shown in Table-6.8.

Table-6.8

$Ni_{80-x}Fe_xB_{20}$	x = 20	x = 30	x = 40	x = 50
n	2.01	2.12	6.06	2.77

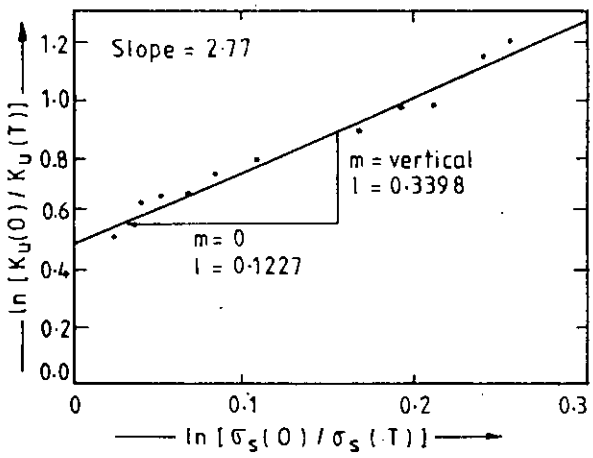

(a) Composition: $Ni_{30}Fe_{50}B_{20}$

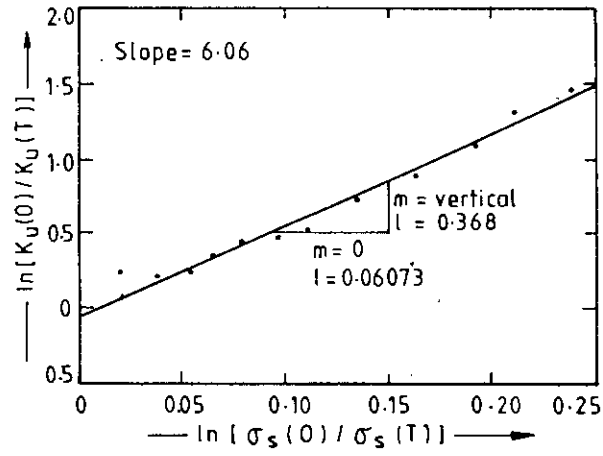

(b) Composition : $Ni_{40}Fe_{40}B_{20}$

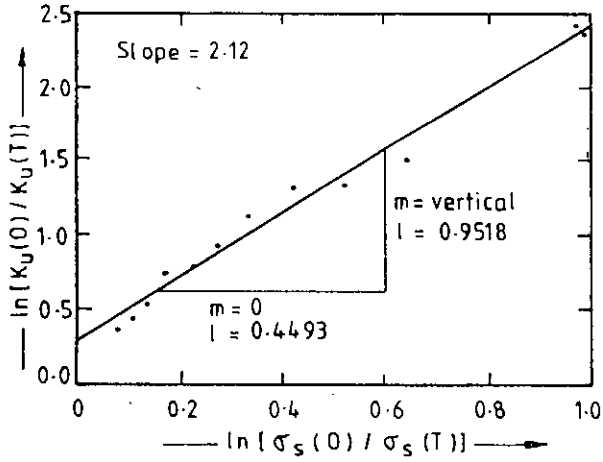

(c) Composition : $Ni_{50}Fe_{30}B_{20}$

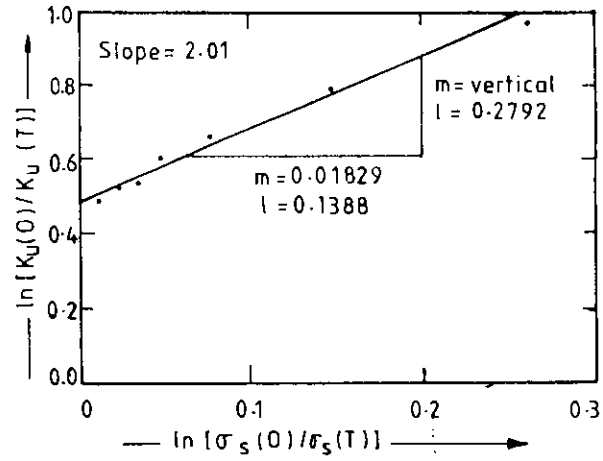

(d) Composition: $Ni_{60}Fe_{20}B_{20}$

Fig.-6.28(a) to(d) $\ln\left[\frac{K_u(0)}{K_u(T)}\right]$ versus $\ln\left[\frac{\sigma_s(0)}{\sigma_s(T)}\right]$ curves of amorphous ribbons with composition $Ni_{80-x}Fe_xB_{20}$ [x = 20, 30, 40 & 50]

6.7. Results and Analysis of Mössbauer parameters for Ni-based Amorphous Ribbons

Mössbauer spectroscopy is a very useful technique for studying the hyperfine field distribution as affected by the nature and number of nearest magnetic atoms in an amorphous alloys. This has been used for identification of magnetic field distribution of magnetic atoms in amorphous ribbons with composition $Ni_{80-x}Fe_xB_{20}$ [x =20, 30, 40 & 50] by the evaluation of the collected spectra. The spectrum has been recorded in constant acceleration mode and the data have been collected in multiscalling mode. The data are collected into two groups. Each group is of 256 channels and the second group gives a mirror image spectrum of the first group. The representative spectrum of the amorphous ribbon with composition $Ni_{40}Fe_{40}B_{20}$ is shown in fig.-6.29. The Mössbauer spectroscopy technique in constant acceleration mode has been used to study hyperfine field and Isomer shifts of Ni-Fe-B system in amorphous state. Pure ^{57}Fe thin foil has been used as the reference material for standarization of the results. The number of counts against velocity of the source is plotted in fig.-4.16.

Room temperature Mössbauer spectra typical of as-quenched amorphous ribbons are obtained and the changes in the spectra corresponding to different compositions of the system $Ni_{80-x}Fe_xB_{20}$ are shown in fig.-6.30. A comparison of the spectrum of pure iron with those of the amorphous ribbons of different compositions shows the shift in the spectral lines and their broadening. This is caused by change in the number of nearest neighbours iron atoms and also their interatomic distances. The numerical values of IS, E_Q, H_{hf}, FWHM and absorption percentage are shown in Table-6.9.

Table-6.9

Sample	IS, mm/s ±0.005	E_Q, mm/s ±0.005	H_{hf}, Tesla ±0.1T	FWHM mm/s, ±0.01	Absorption %
Pure ^{57}Fe foil		0.058	33	0.18	11.38
$Ni_{30}Fe_{50}B_{20}$	0.338	0.087	26.07	1.04	4.59
$Ni_{40}Fe_{40}B_{20}$	0.360	0.175	24.43	0.96	5.06
$Ni_{50}Fe_{30}B_{20}$	0.367	0.204	23.34	0.90	3.07
$Ni_{60}Fe_{20}B_{20}$	0.231	0.117	20.60	0.85	2.20

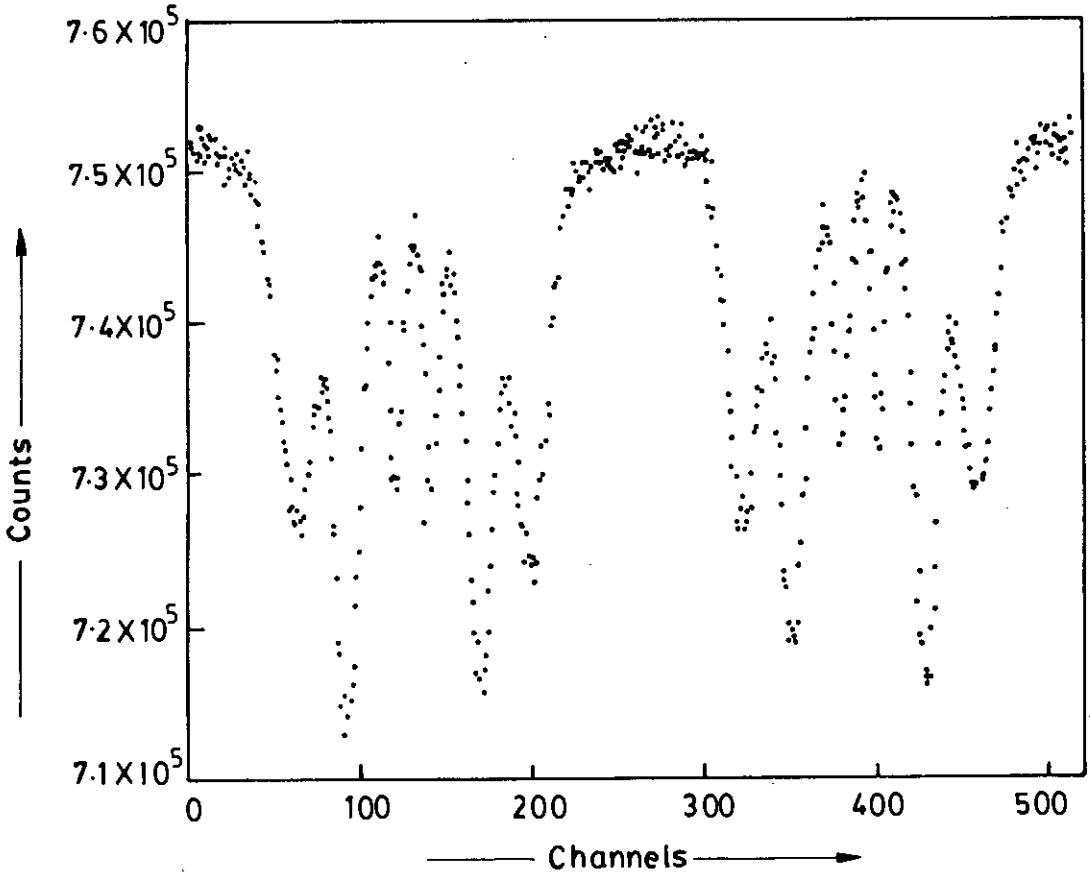

Fig.-6.29 Room temperature Mössbauer transition spectrum for relative counts versus channels of the as-quenched amorphous ribbon with composition $Ni_{40}Fe_{40}B_{20}$

The coulombic interaction alter the energy separation between the ground state and the excited state of the nuclei, thereby causing a slight shift in the position of the observed centroid of the spectrum, which is different in various amorphous ribbons with different compositions giving rise to isomer shifts. The velocity scale was calibrated by a room temperature measurement on a thin natural iron foil sample. The IS's are given relative to the centroid of this spectrum as shown in Table-6.9. IS of all the amorphous ribbons are calculated relative to the centroid of these spectrum from the centroids of the velocity scale of a thin ^{57}Fe sample. As shown in Table-6.9, the IS of the Ni-Fe-B system increases with increasing Ni, till the amount of Ni becomes 50 At.%, and then with further increase of Ni content IS decreases. The iron atoms are in the trivalent state in amorphous ribbons as reflected in the IS value which varies from 0.231 to o.367mm/s.

Quadrupole splitting is the electric quadrupole interaction between the quadrupole moments of the nuclei and the electric field gradient at the nucleus due to the asymmetric distribution of charges on the ions. This provide information on the nature of the chemical bond. Just like IS the E_Q also increase with increasing Ni until the amount of Ni becomes 50 At.% and then decreases with further increase of Ni.

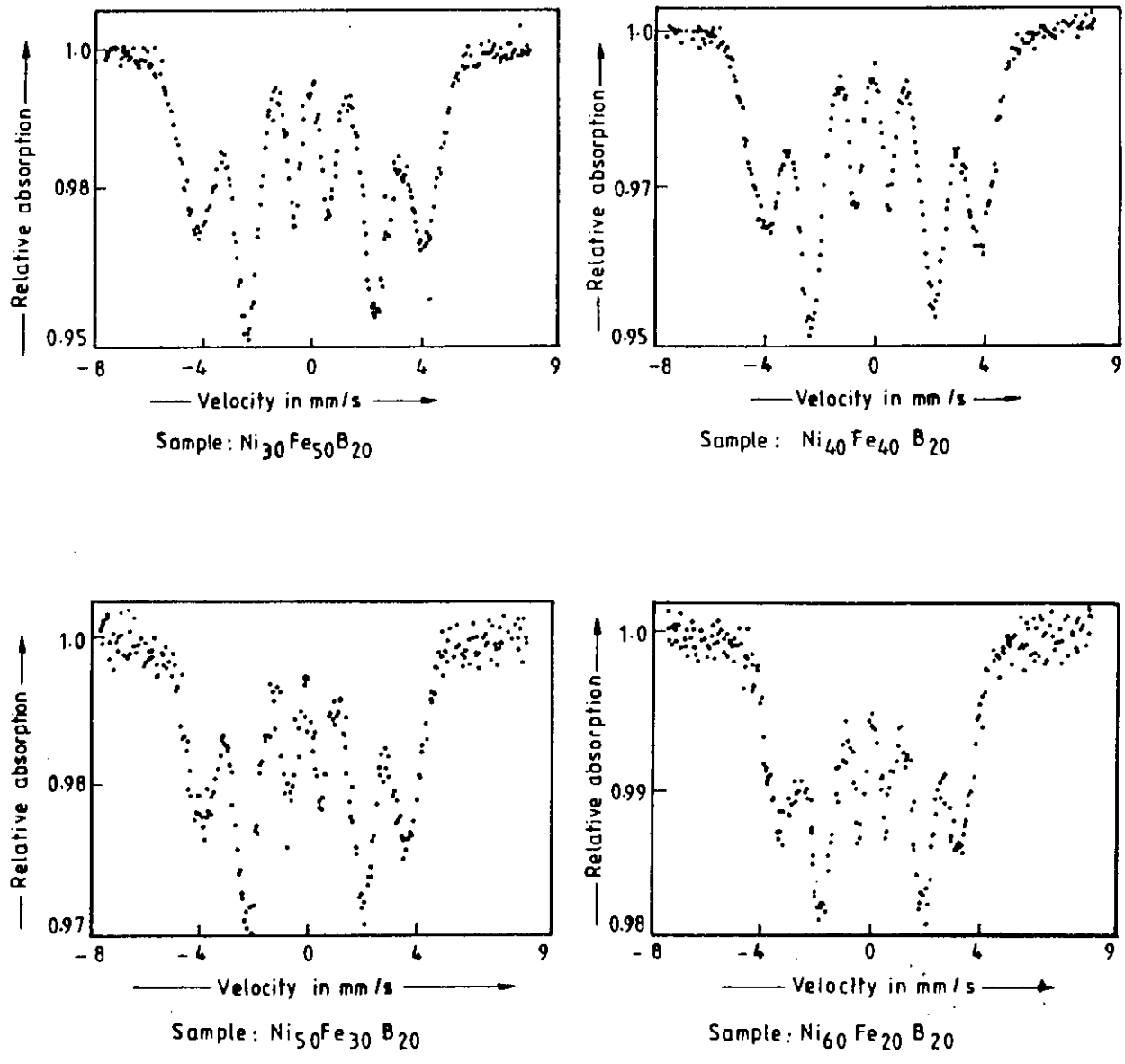

Fig.-6.30 Room temperature spectra of as-quenched amorphous ribbons with composition $Ni_{80-x}Fe_xB_{20}$

Absorption percentage as compered with pure iron decreases in Ni-Fe-B ribbons. These absorption percentage decreases with increasing amount of Ni except for $Ni_{40}Fe_{40}B_{20}$. This is explained as due to the inver effect which occurs due to contributions of magnetostriction of opposite signs from Ni and Fe atoms. These results are shown in Table-6.9.

The effect of change in the composition of Ni-Fe-B amorphous system on the transition line width as measured by FWHM is also shown in Table-6.9. While experimental FWHM of pure iron foil is 0.18mm/s, FWHM of the amorphous ribbons broadening 5 to 6 times. The average magnetic hyperfine field (H_{hf}) of the iron foils is 33T which corresponds to iron magnetic moment of $2.21\mu_B$. Using these standard results, the experimental spectra for the as-prepared samples of Ni-Fe-B ribbons of different composition have been obtained by the best fit with the distribution of the hyperfine field. This is carried out by FORTRAN IV language which does a least χ^2 spectra curve fitting for over lapping Lorentzian lines. The H_{hf} decreases with increasing Ni content as shown in fig.-6.31. The H_{hf} values for different composition of the ribbons agree consistently with corresponding σ_s values, σ_s being larger for samples with higher iron content as expected.

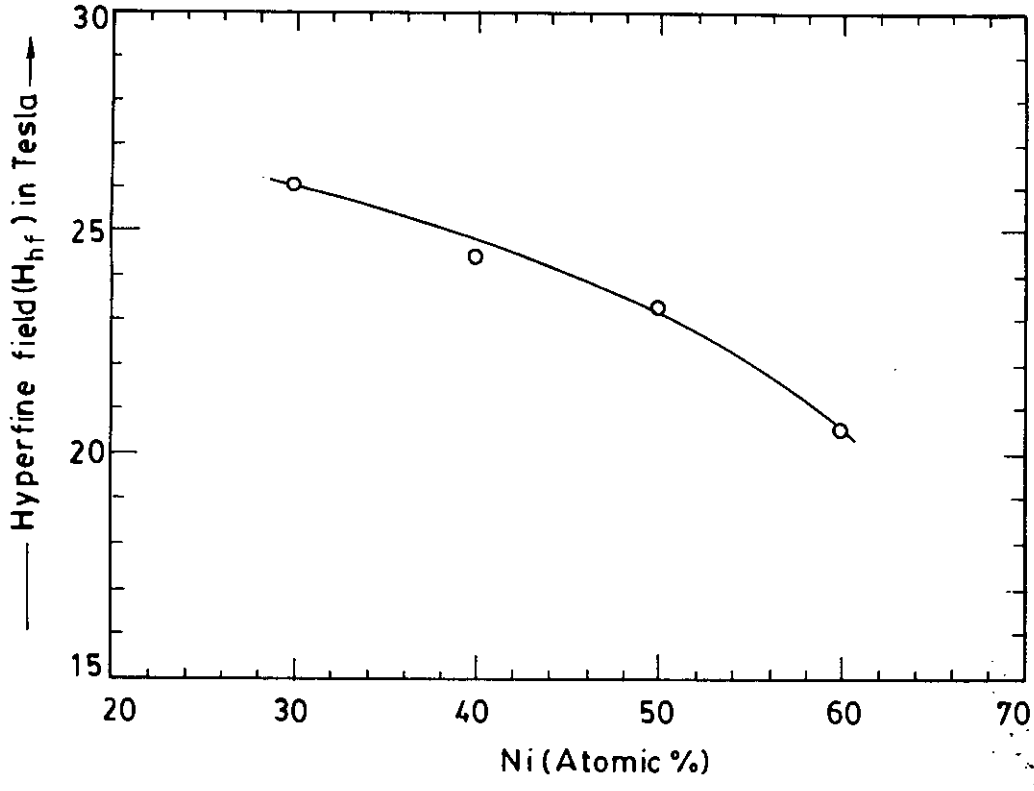

Fig.-6.31. Variation of internal hyperfine field due to change in the Ni-content in $Ni_{80-x}Fe_xB_{20}$ amorphous ribbons.

CHAPTER-7 RESULTS AND DISCUSSION OF Co-BASED AMORPHOUS RIBBONS

7.1. DTA Results of amorphous Cobalt-Iron-Boron-Silicon ribbons as affected by Iron substitution

7.2. Curie temperature measurements of amorphous Cobalt-Iron-Boron-Silicon ribbons

7.3. Determination of Maximum permeability, Maximum induction, Coercive force and Remanence of Co-based Amorphous Ribbons

7.4. Dynamic Magnetic Properties of Co-based Amorphous Ribbons

7.5. Specific Magnetization Measurements of Co-based Amorphous Ribbons

7.5.1. Temperature Dependence of Magnetization of Co-based Amorphous Ribbons

7.6. Stress Induced Anisotropy of Co-based Amorphous Ribbons

7.6.1. Temperature Dependence of K_u

7.7. Experimental Results and Analysis of Mössbauer Parameters for Co-based Amorphous Ribbons

7.0. Results and Discussion of Co-based Amorphous Ribbons

7.1. DTA Results of amorphous Cobalt-Iron-Boron-Silicon ribbons as affected by Iron substitution

Cobalt-Iron-Boron-Silicon amorphous ribbons with composition $Co_{80-x}Fe_xB_{10}Si_{10}$ [x = 0, 2, 4, 6 and 8] are of special interest because, these magnetic systems with high Co content and small amount of Fe content, can help us to understand why the magnetostriction of amorphous 3d metals differ so markedly from that of their crystalline counterparts. An interesting way has been the investigation of the crystallization of Fe-Co-metalloid alloys and the strong correlation between positive and negative magnetostriction and the local symmetry.

The compositional dependence of the glass transition temperature T_g and crystallization temperature T_x of amorphous Co-Fe-B-Si alloys are also studied. It has been observed that the crystallization temperature of these alloys, with constant Si and B changes with Fe content as measured by DTA when the heating rate is maintained at 10^0C / min. In fig-7.1 T_g and T_x correspond to observed exothermic picks of the ribbon with composition $Co_{78}Fe_2B_{10}Si_{10}$. The two anomalies observed in the temperature versus time curve were at $430^0 C$ and $570^0 C$ respectively. Both the anomalies showed peaks, which corresponds to the release of heat at these temperatures due to change in the ordering of the atoms. We identify the first peak as T_g, when the ribbon was transforming from amorphous state to crystalline state. The second peak is considered to be due to the formation of crystalline phase T_x.

In fig-7.2, the results are presented in a summerized form for all the different samples with compositions $Co_{80-x}Fe_xB_{10}Si_{10}$. For all the samples the eutectic points remain unchanged. This shows that all the compositions are equally favourable for producing amorphous ribbons. Fig.-7.3 shows dependences of T_g and T_x on the Fe content in the amorphous alloys. The glass transition temperature T_g of amorphous $Co_{80-x}Fe_xB_{10}Si_{10}$ alloys depends on the Fe content. The glass transition temperatures of these alloys increase sharply with the increase of Fe-content. The crystallization temperatures T_x of $Co_{80-x}Fe_xB_{10}Si_{10}$ alloys are higher than T_g and has almost nearly the same value for all the compositions. The numerical values of T_g and T_x for all samples are shown in Table-7.1.

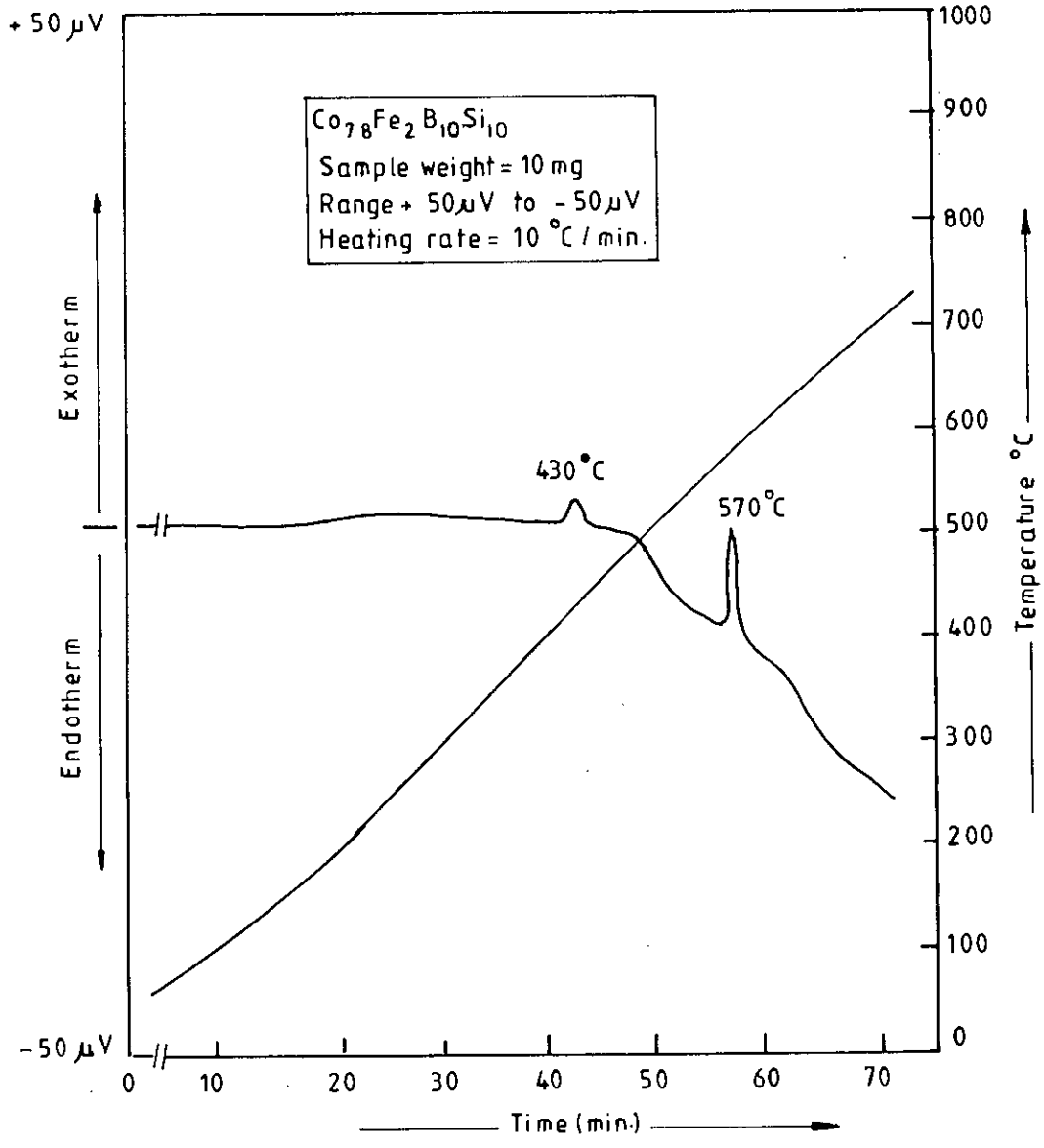

Fig.-7.1 DTA graph of the amorphous ribbon with composition $Co_{78}Fe_2B_{10}Si_{10}$

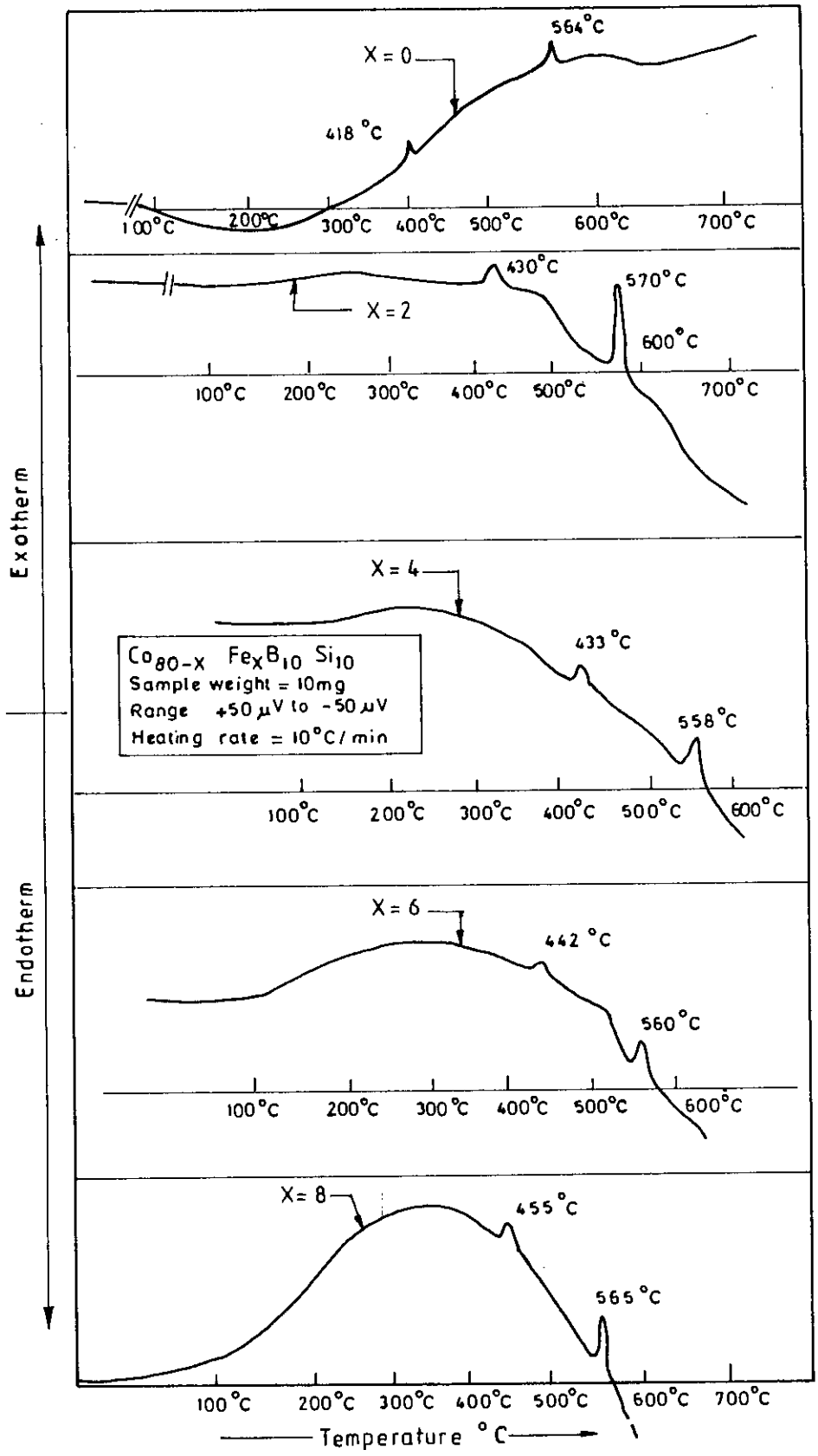

Fig.-7.2 Determination of T_g and T_x from DTA graph of amorphous ribbons with composition $Co_{80-x}Fe_xB_{10}Si_{10}$ [x = 0, 2, 4, 6 & 8].

Table-7.1

$Co_{80-x}Fe_xB_{10}Si_{10}$	T_g	T_x
x = 0	418^0C	564^0C
x = 2	430^0C	570^0C
x = 4	433^0C	558^0C
x = 6	442^0C	560^0C
x = 8	455^0C	565^0C

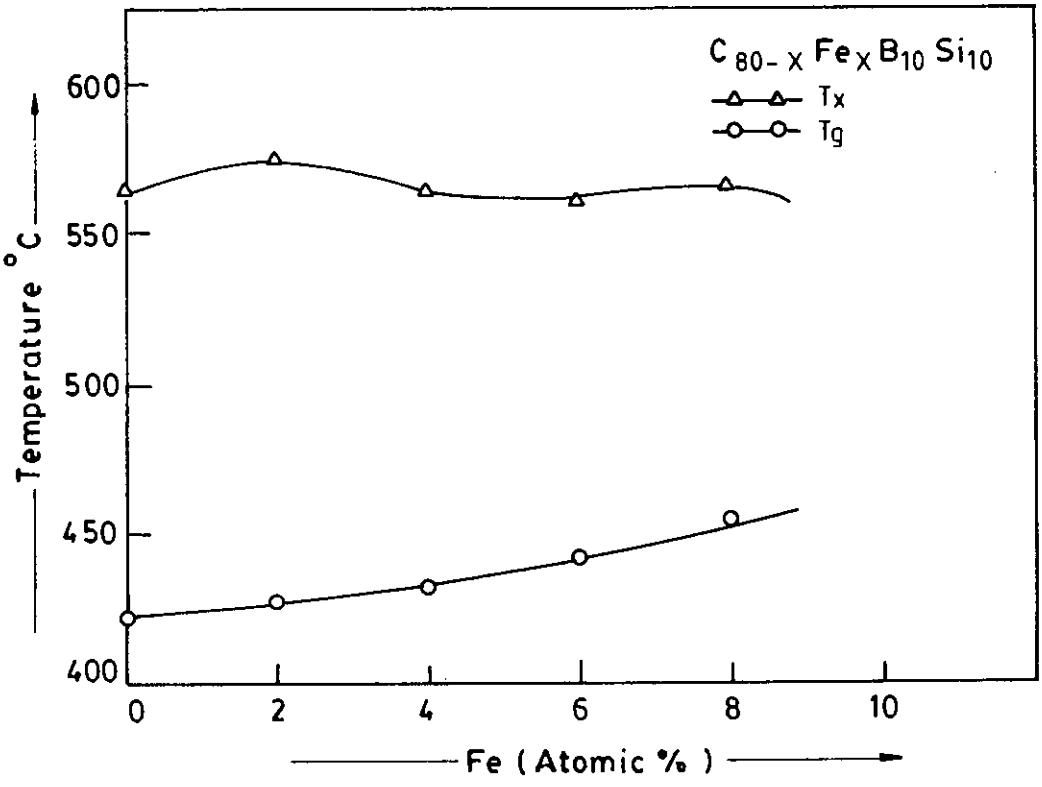

Fig.-7.3 Variation of T_g and T_x due to change in the Fe-content in $Co_{80-x}Fe_xB_{10}Si_{10}$ amorphous ribbons.

7.2 Curie temperature measurements of amorphous Cobalt-Iron-Boron-Silicon ribbons.

Curie temperature has been estimated from the μ VS T curve for amorphous Cobalt-Iron-Boron-Silicon ribbons with composition $Co_{80-x}Fe_xB_{10}Si_{10}$ [x = 0, 2, 4, 6 and 8]. Temperature dependence of permeability of the samples subjected to heating rate of 12^0C / min. are shown in fig-7.4. The numerical values of T_c for all the sample are shown in Table-7.2.

Table-7.2

$Co_{80-x}Fe_xB_{10}Si_{10}$	x = 0	x = 2	x = 4	x = 6	x = 8
T_c	407^0C	421^0C	429^0C	438^0C	443^0C

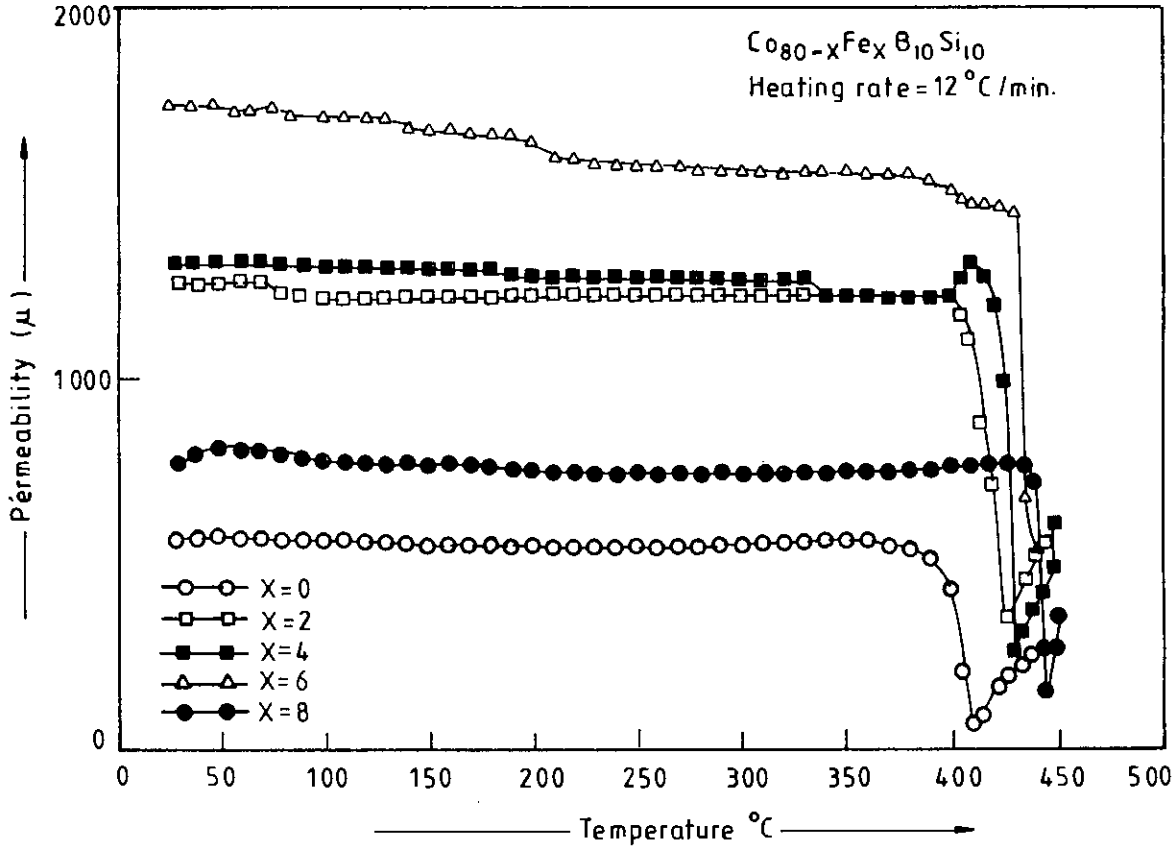

Fig.-7.4 T_c determination from temperature dependence of permeability of amorphous ribbons with composition $Co_{80-x}Fe_xB_{10}Si_{10}$

Fig-7.5 shows the dependence of T_c on the iron content. T_c of Co-based amorphous ribbons increases with the increase of Fe-content. The spread of T_c indicates that there is an enhancement of the Co-Fe interaction. When the disorder is small, so that the above trends continuos, the correlation also continuous to grow leading to the normal phase transition, and permeability falls sharply as observed in the μ VS T curve. Thus amorphous ribbons with increase of iron content are more convenient when these materials are used at an elevated temperature.

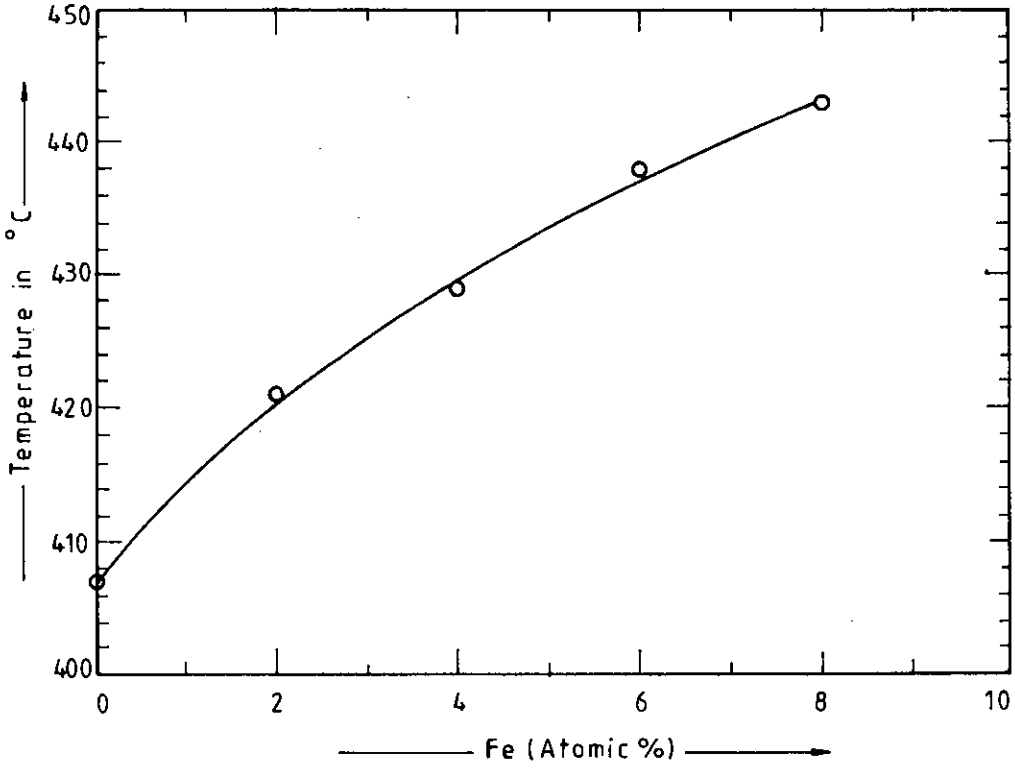

Fig.-7.5 Variation of T_c due to change in the Fe-content in $Co_{80-x}Fe_xB_{10}Si_{10}$ amorphous ribbons.

7.3. Determination of Maximum Permeability, Maximum induction, Coercive force and Remanence of Co-based Amorphous Ribbons

Magnetization processes of as-quenched Cobalt-Iron-Boron-Silicon system with composition $Co_{80-x}Fe_xB_{10}Si_{10}$ [x = 0, 2, 4, 6 and 8] have been measured in static field. Maximum permeability (μ_m) ,saturation magnetic induction (B_s), remanence (B_r), the ratio (B_r/B_s) and Coercive force (H_c) have been calculated for different specimens from the experimental hysteresis curves. The ribbons were wound into the toroidal ring cores having 13 to 15mm outer diameter and 10mm inner diameter. From the hysteresis curves of amorphous ribbons of Cobalt-Iron alloys with 10% boron and 10% silicon as glass forming materials, static magnetic characteristics have been measured using a low static field up to 32A/m for all the compositions except the iron free sample with composition $Co_{80}B_{10}Si_{10}$. A high static field up to 190A/m was used in the case of $Co_{80}B_{10}Si_{10}$ ribbon for its high Coercivity.

Since Cobalt and Iron have opposite values of magnetostriction it is convenient to tailor this alloy systems by continuously altering the relative proportions of the two metals. Besides finding the optimum magnetic characteristics of these amorphous alloy as controlled by composition, the system provides an interesting medium for understanding the mechanism of technical magnetization process and the dependence of magnetic parameters characterising soft magnetic materials. The results are shown in summery from the Table-7.3

Table-7.3

$Co_{80-x}Fe_xB_{10}Si_{10}$	x = 0	x = 2	x = 4	x = 6	x = 8
H_c (A / m)	15.0	5.2	4.8	2.8	6.0
B_r (mT)	374.66	505.78	578.06	650.74	653.97
B_s (mT)	407.17	559.58	625.08	695.11	701.36
B_r/B_s	0.92	0.91	0.93	0.94	0.93
μ_m	3,296	36,606	35,866	74,956	36,406

Fig-7.6 shows the hysteresis curve for four samples with composition $Co_{80-x}Fe_xB_{10}Si_{10}$ [x= 2, 4, 6 and 8] and fig-7.7 shows the hysteresis curve for $Co_{80}B_{10}Si_{10}$. Low H_c values from the hysteresis curves show that materials are magnetically very soft, and very low fields are needed for obtaining saturation magnetization in all the samples except in $Co_{80}B_{10}Si_{10}$.

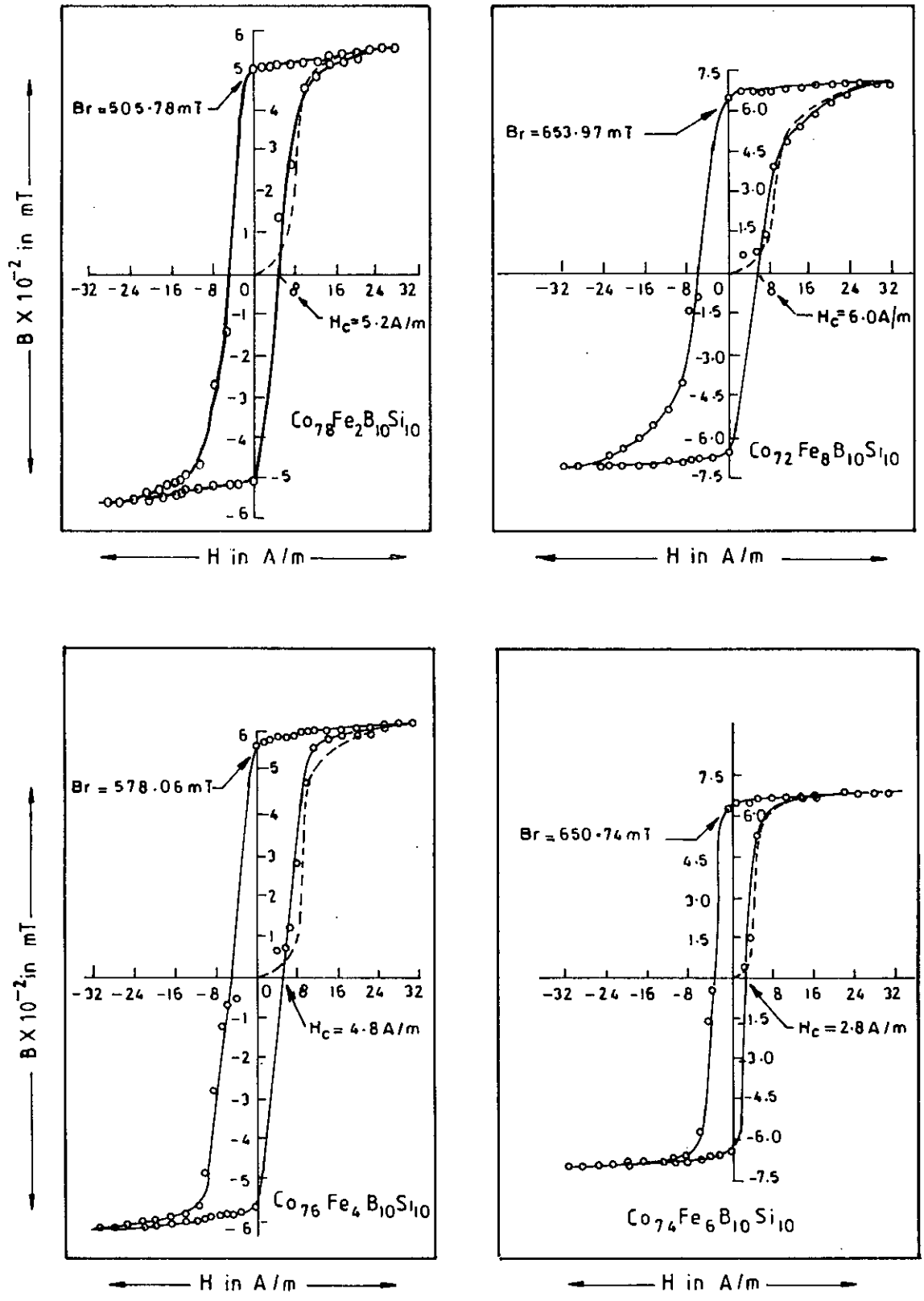

Fig.-7.6 Hysteresis curve of amorphous ribbons with composition $Co_{80-x}Fe_xB_{10}Si_{10}$

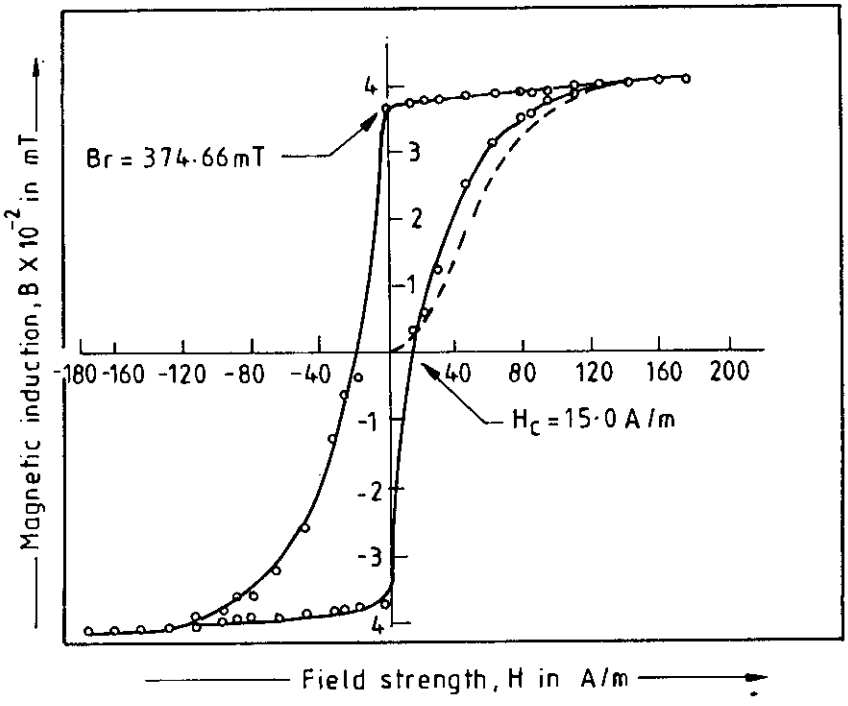

Fig.-7.7 Hysteresis curve of the amorphous ribbon with composition $Co_{80}B_{10}Si_{10}$

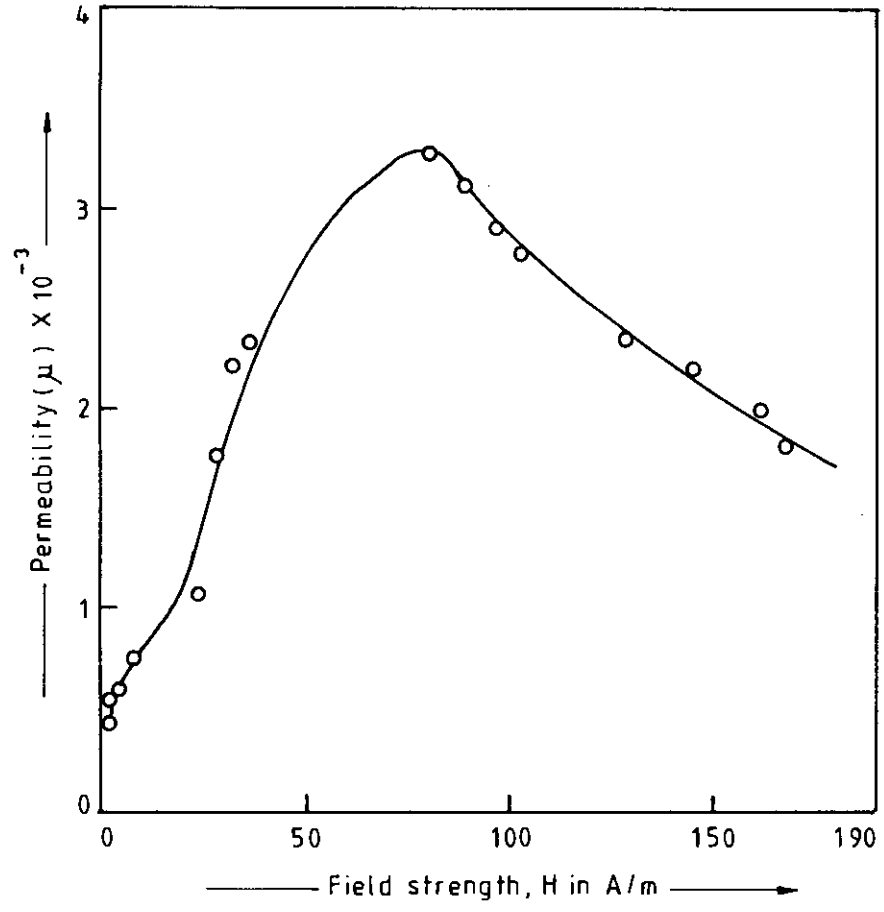

Fig.-7.8 Permeability versus static magnetic field of the amorphous ribbon with composition $Co_{80}B_{10}Si_{10}$

Fig-7.9 shows the variation of B_r, B_s and H_c of the $Co_{80-x}Fe_xB_{10}Si_{10}$ alloy system where x varies from 0 to 8 atomic percent. It is observed that both B_r and B_s increases appreciably with increasing percentage of Iron. This is quite expected because Iron atoms have higher magnetic moment. However, the increase of B_r and B_S are not linear which indicates that the electron transfer mechanism in the 3d band is not very simple.

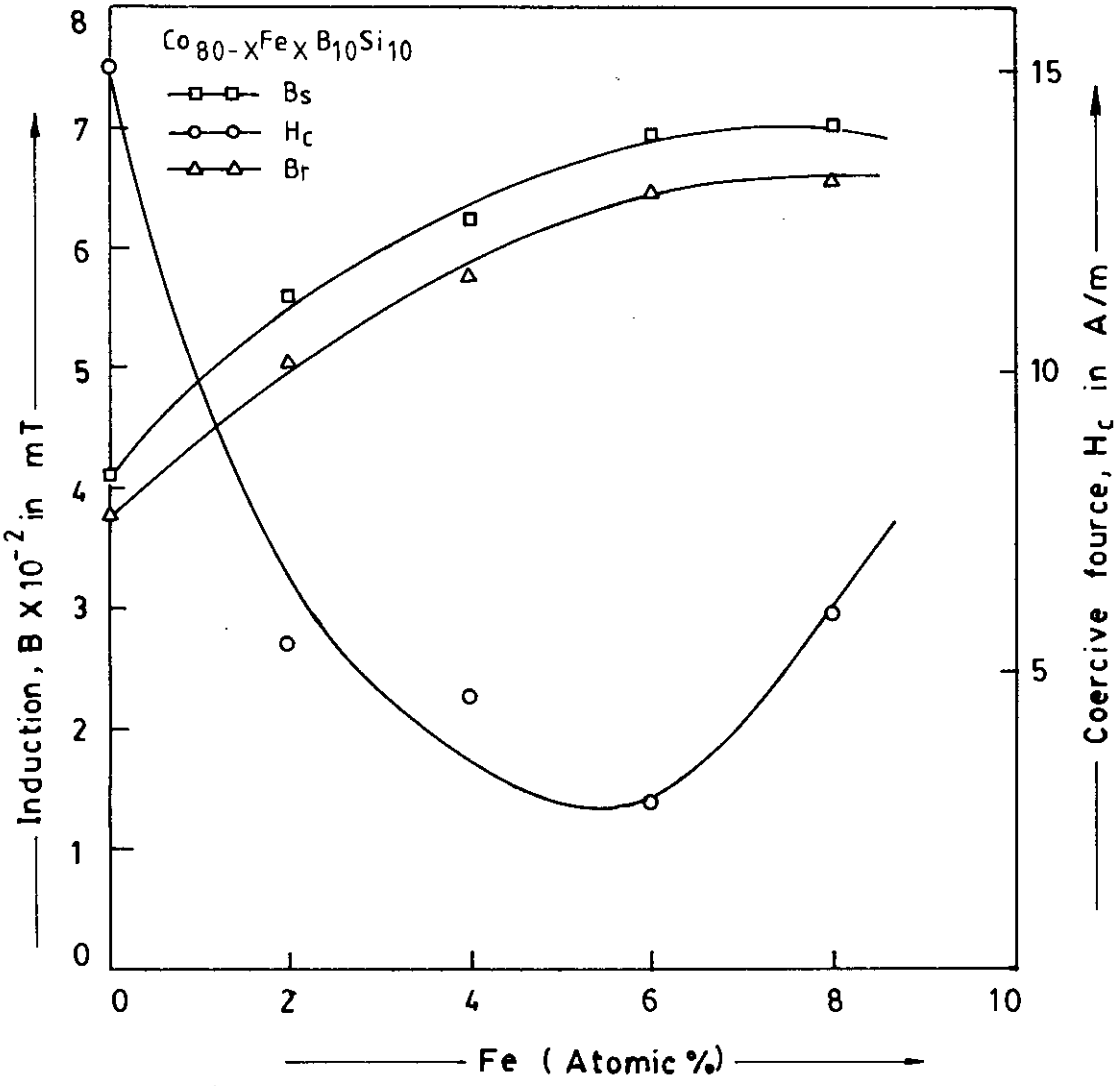

Fig.-7.9 Magnetic induction and coercive force variation with atomic percent of Fe-content of amorphous ribbons with composition $Co_{80-x}Fe_xB_{10}Si_{10}$

The Coercivity of the alloy system initially decreases with increasing Iron up to 6 atomic percent and then increases with the increase of the Fe-content. This is explained in terms of the compositional dependence of magnetostriction which becomes almost zero at 6 atomic percentage of iron in the system. The permeability which is

measured from the initial magnetization curve becomes by far the largest for this particular composition and have a value of 74,956. Thus there is a 24 fold increase of permeability of the $Co_{74}Fe_6B_{10}Si_{10}$ sample as compered with the iron free sample.

Permeability due to static external field from o.5A/m to 32A/m for the ribbons with composition $Co_{80-x}Fe_xB_{10}Si_{10}$ [x= 2, 4, 6 and 8] are shown in fig-7.10. The maximum permeability occurs at different fields 80.95, 10.30, 11.17, 6.28 and 11.60A/m for compositions $Co_{80}B_{10}Si_{10}$, $Co_{78}Fe_2B_{10}Si_{10}$, $Co_{76}Fe_4B_{10}Si_{10}$, $Co_{74}Fe_6B_{10}Si_{10}$ and $Co_{72}Fe_8B_{10}Si_{10}$ respectively and hence corresponding value of μ_m are shown in Table-7.3. The field corresponding to the peaks of the permeability curves are different for different picks. Fig-7.8 shows the permeability due to static external field from o.5A/m to 190A/m for ribbon with composition $Co_{80}B_{10}Si_{10}$.

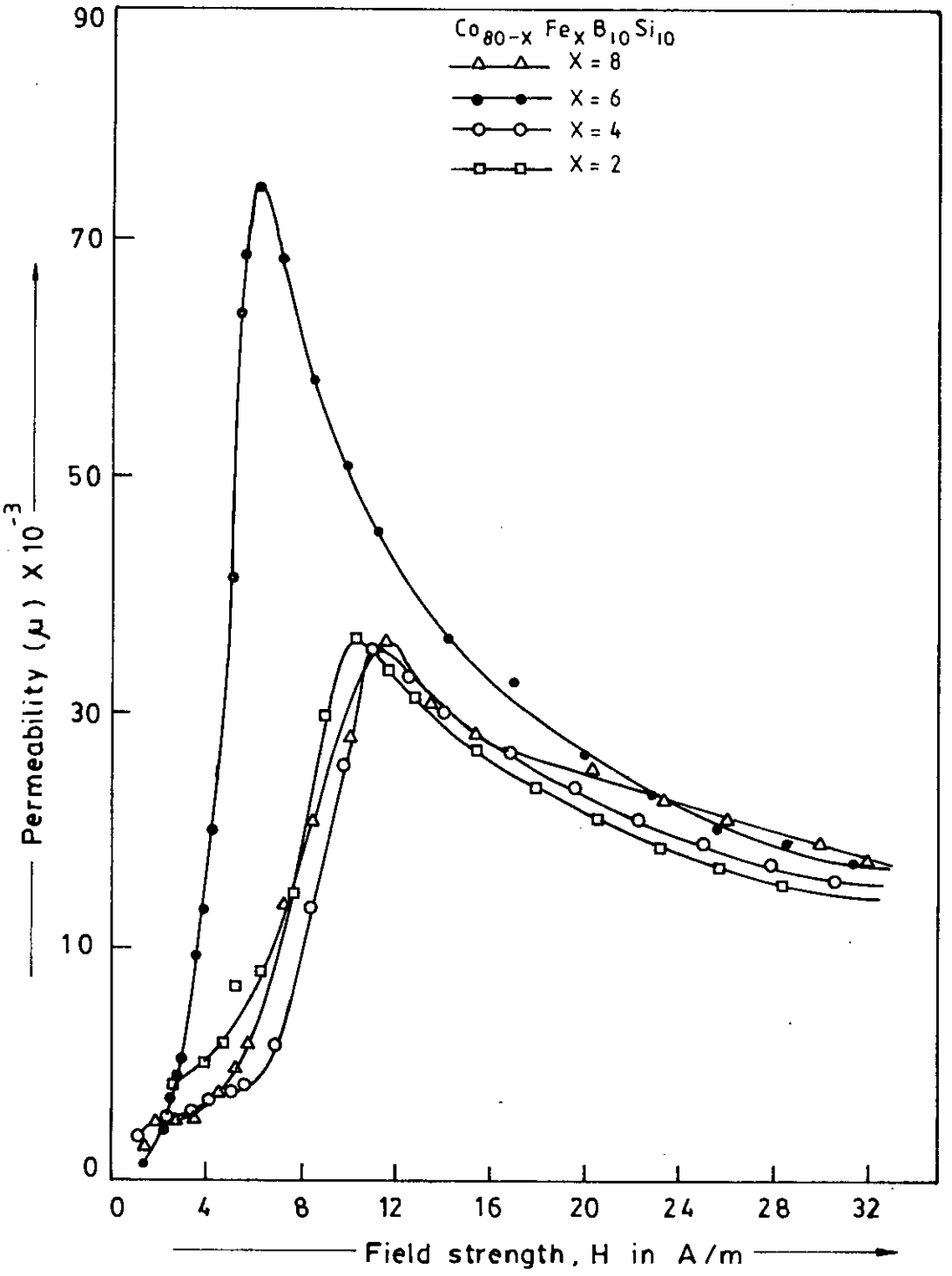

Fig.-7.10 Permeability versus static magnetic field of amorphous ribbons with composition $Co_{80-x}Fe_xB_{10}Si_{10}$ [x = 2, 4, 6 & 8].

7.4. Dynamic Magnetic Properties of Co-based Amorphous Ribbons

Dynamic magnetic properties of as-quenched Co-Fe-B-Si system with composition $Co_{80-x}Fe_xB_{10}Si_{10}$ [x = 0, 2, 4, 6 & 8] have been determined using an impedance analyzer. The compositional dependence of initial permeability (μ_i) is determined for different values of x and their frequency dependence of complex magnetic characteristics, like real and imaginary parts of initial permeability, loss factor and relative quality factor are analyzed. Frequency measurements were performed with an impedance analyzer in the frequency range 0.5KHz to 13MHz at room temperature and with various applied field. The μ_i of the ribbons with composition $Co_{80-x}Fe_xB_{10}Si_{10}$ is calculated from the low A.C. magnetic field dependence of permeability in the limit of frequency 0.5KHz and vanishing magnetic field as shown in fig.-7.11. The results are shown in Table-7.4.

Table-7.4

$Co_{80-x}Fe_xB_{10}Si_{10}$	x = 0	x = 2	x = 4	x = 6	x = 8
μ_i	488	1533	1753	1956	1069

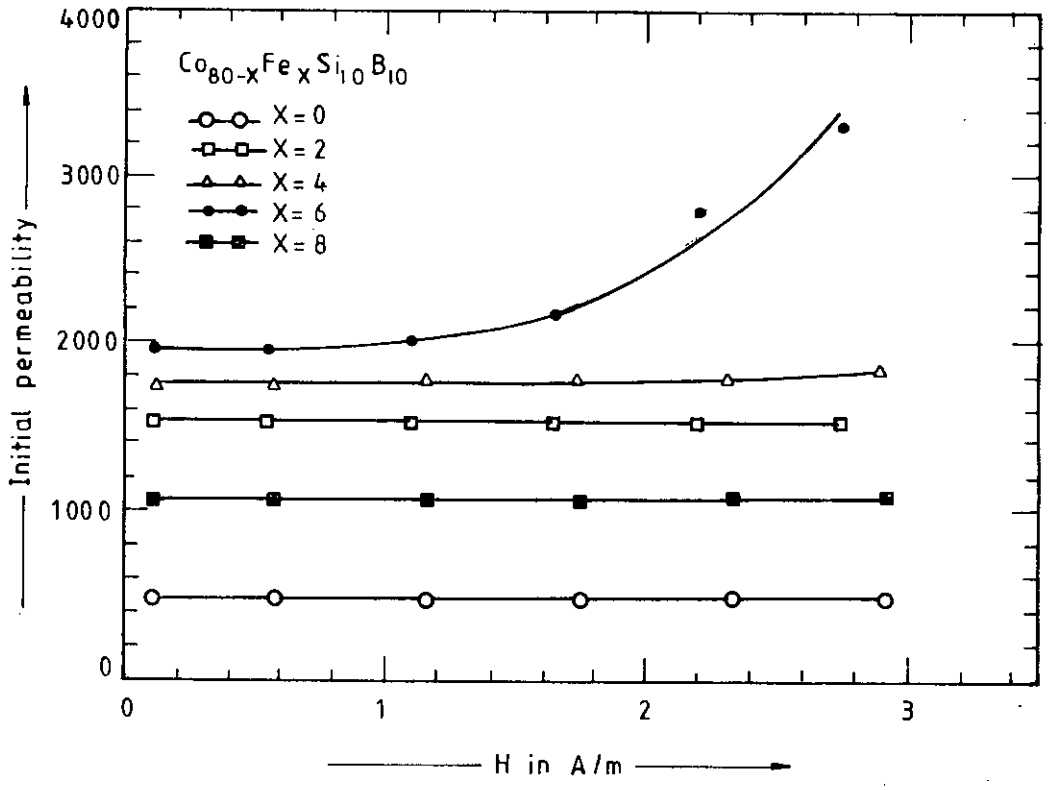

Fig.-7.11 Permeability versus A.C. magnetic field of amorphous ribbons with composition $Co_{80-x}Fe_xB_{10}Si_{10}$

As shown in fig.-7.12, μ_i in the vanishing field region for all the ribbons except for $Co_{74}Fe_6B_{10}Si_{10}$ remains almost constant with the slight variation of the field. Another accurate way to determine the μ_i value is to plot the imaginary part of the complex permeability (μ'') against the real part of the complex permeability (μ'). The μ_i value is determined from the semicircle's diameter i.e. from the intersection of the semicircle with the μ' axis. In the representative fig.-7.12, the results of the as-quenched sample with composition $Co_{74}Fe_6B_{10}Si_{10}$ is given. The calculated parameters of all the samples are shown in Table-7.4.

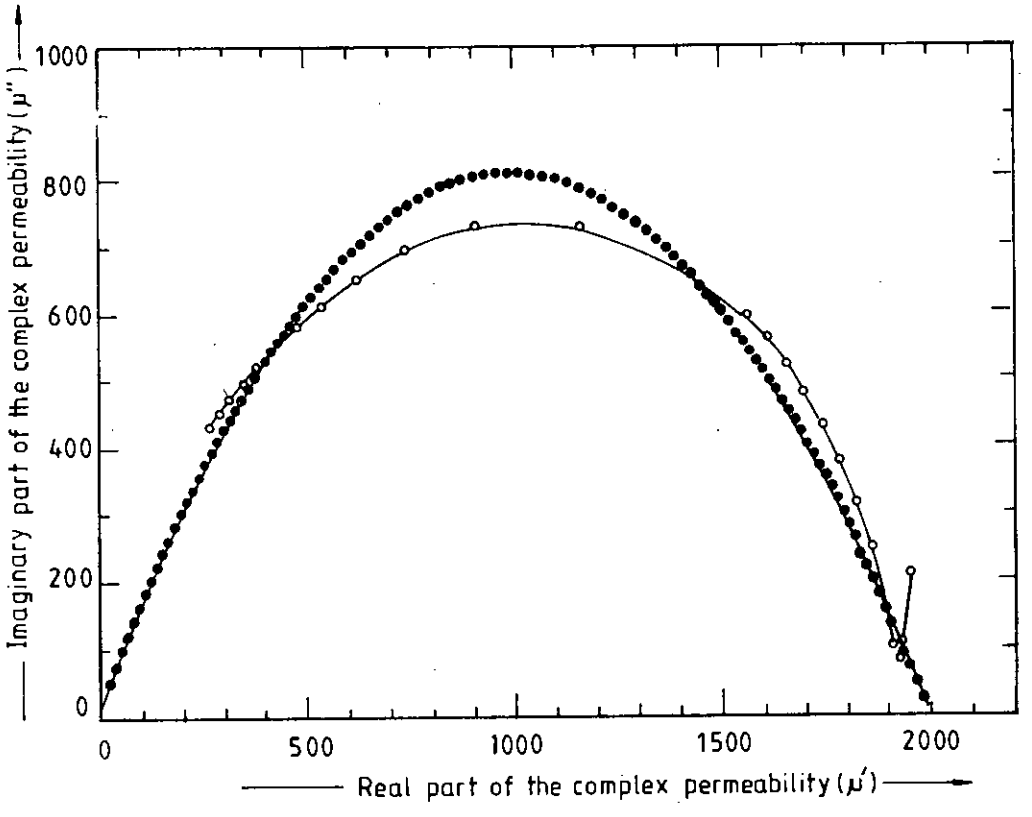

Fig.-7.12 Complex permeability μ'' Vs. μ' plot for the as-quenched ribbon with composition $Co_{74}Fe_6B_{10}Si_{10}$

Fig.-7.13 shows that μ_i of Co-Fe-B-Si amorphous system increases almost monotonously with the replacement of Fe up to 6 At.% for Co, at which a maximum value of 1956 is observed for the relative permeability. This increase of μ_i with increased Fe-content is explained as due to the decrease of the net magnetostriction arising from the cancellation of the negative contribution of Co by the positive contribution of Fe. The maximum value of μ_i of ribbons having 6 At.% Fe is attributed to the minimum magnetostriction and low coercivity at this composition. When the proportion of Fe is increased further to 8 At.%, μ_i decreases which is attributed to the

increase of magnetostriction, as the negative magnetostriction of Co is more than compensated by the positive contribution of magnetostriction of Fe atoms at this composition.

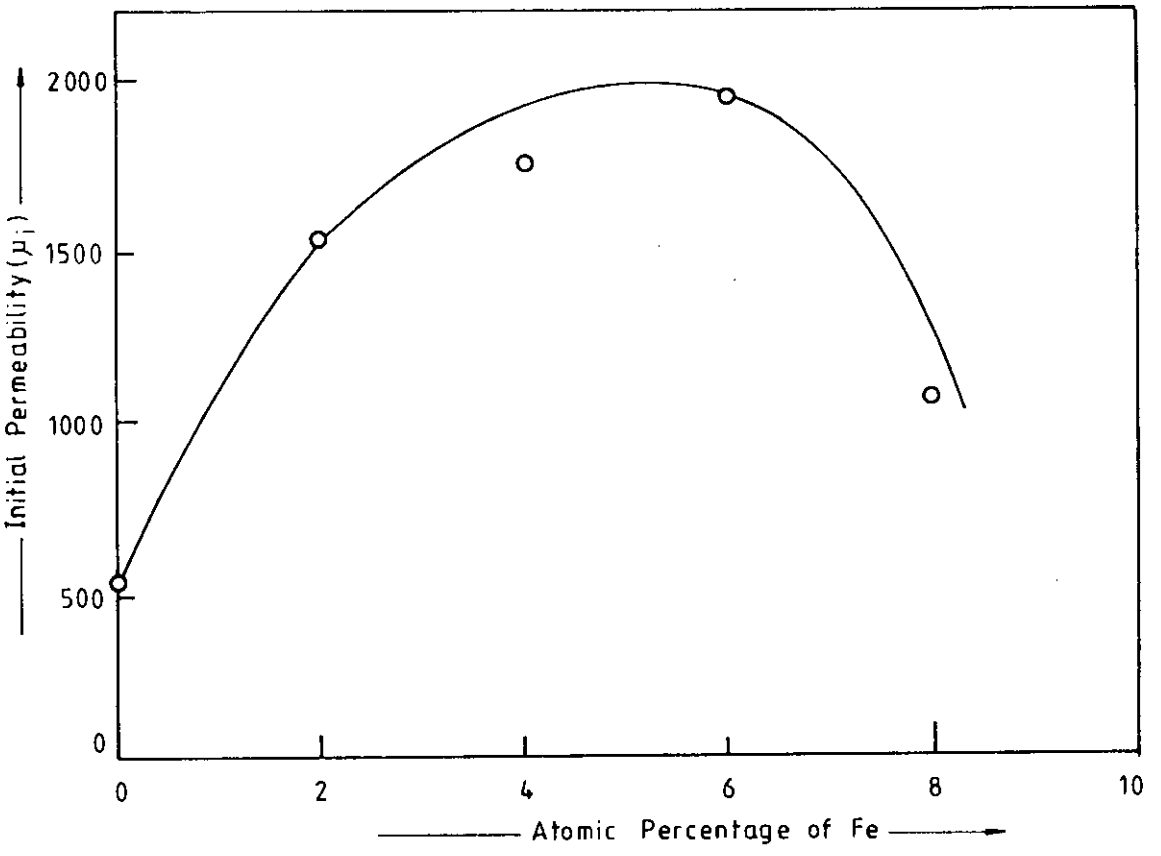

Fig.-7.13 Variation of initial permeability due to change in the Fe-content in $Co_{80-x}Fe_xB_{10}Si_{10}$ amorphous ribbons.

The frequency dependence of the real part of complex permeability is shown in fig.-7.14. The flat region up to the frequency of 1MHz indicate that all the samples with different compositions are suitable as core materials at low fields. While the Fe free sample shows a relative permeability of 488 and maintains almost a constant value even beyond 1MHz, the introduction of Fe, to partly replace Co, increases the permeability enormously. However, the maximum frequency range for which the permeability is maintained constant reduces slightly.

The imaginary part of the complex permeability and loss factor for different compositions over the frequency range 0.5KHz to 13MHz are shown in fig.-7.15 and fig.-7.16 respectively. The frequency dependence of relative quality factor is shown in

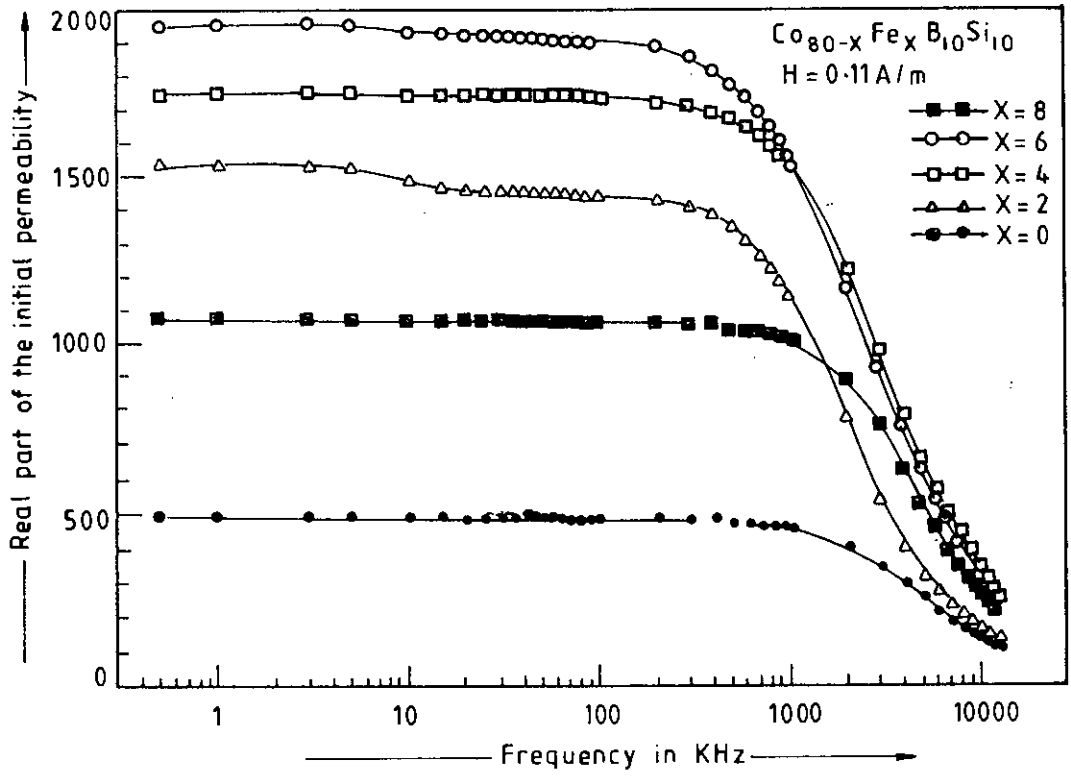

Fig.-7.14 Frequency dependence of the real part of initial permeability of amorphous ribbons with composition $Co_{80-x}Fe_xB_{10}Si_{10}$

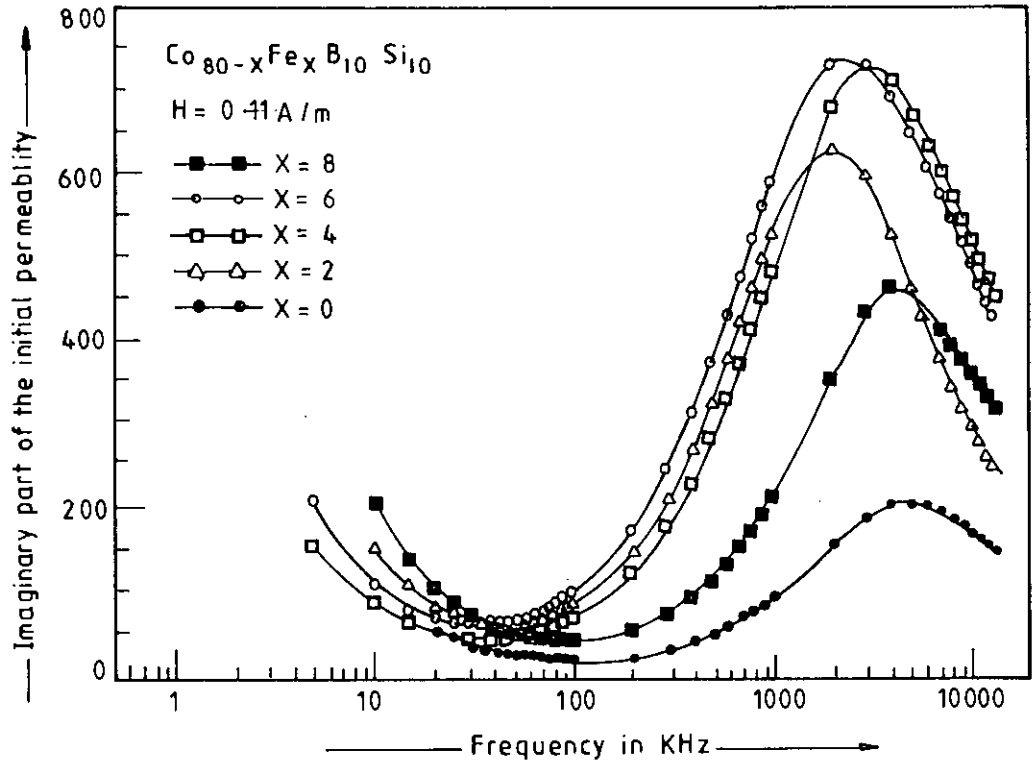

Fig.-7.15 Frequency dependence of the imaginary part of the initial permeability of amorphous ribbons with composition $Co_{80-x}Fe_xB_{10}Si_{10}$

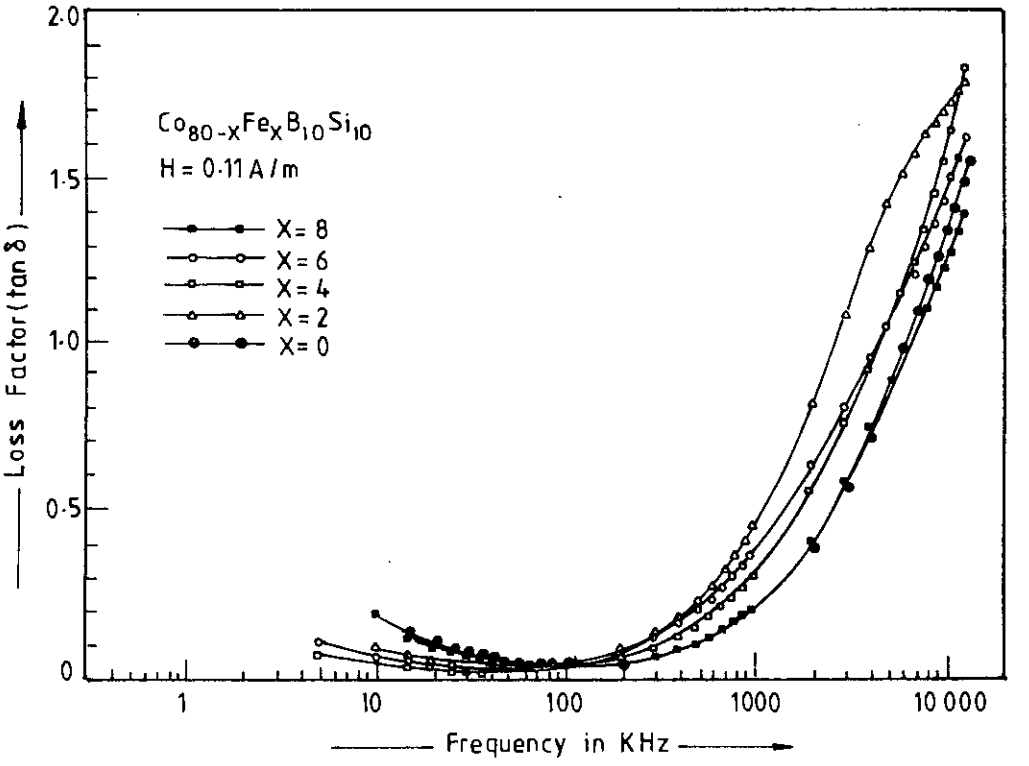

Fig.-7.16 Frequency dependence of loss factors of amorphous ribbons with composition $Co_{80-x}Fe_xB_{10}Si_{10}$

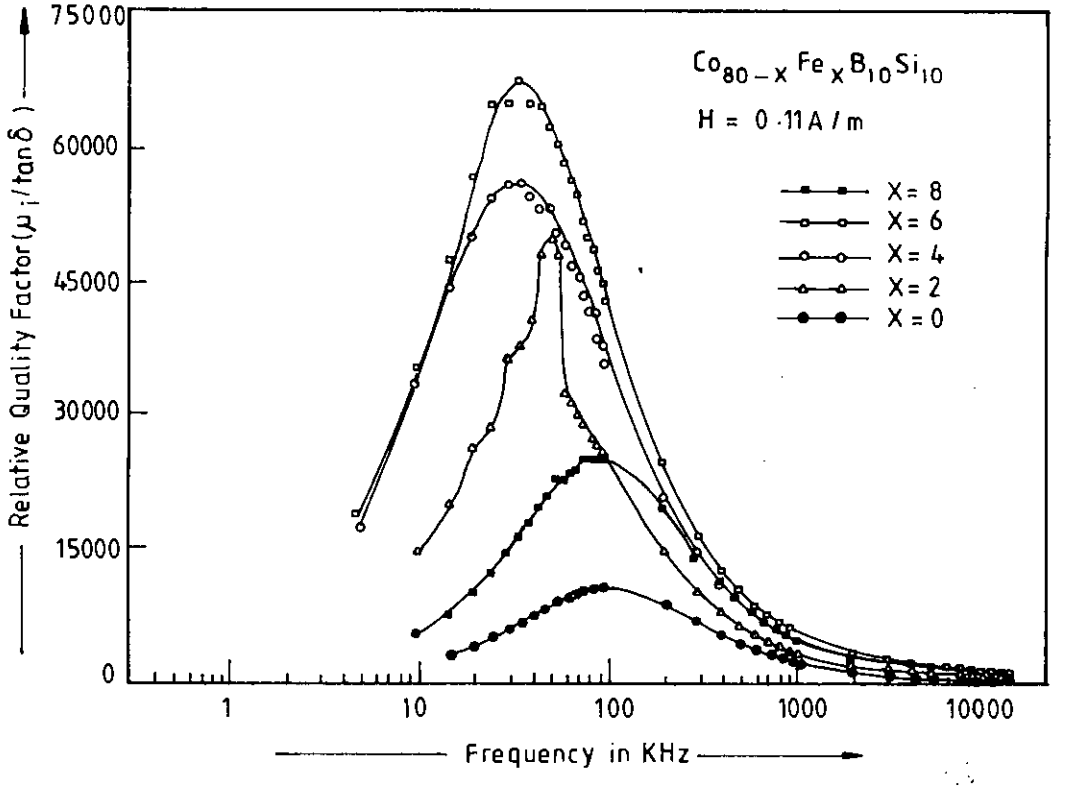

Fig.-7.17 Frequency dependence of relative quality factor of amorphous ribbons with composition $Co_{80-x}Fe_xB_{10}Si_{10}$

fig.-7.17. The relative quality factors are controlled by the real part of the complex permeability and have quite high values in the range 10KHz to 500KHz for the three ribbons having compositions $Co_{78}Fe_2B_{10}Si_{10}$, $Co_{76}Fe_4B_{10}Si_{10}$ and $Co_{74}Fe_6B_{10}Si_{10}$,and quite naturally these samples have low loss factors. The other two samples having compositions $Co_{80}B_{10}Si_{10}$ and $Co_{72}Fe_8B_{10}Si_{10}$ have high loss factors and relative low quality factors.

Fig.-7.18 shows the effect of annealing on the initial permeability (μ_i) of amorphous ribbons with composition $Co_{80-x}Fe_xB_{10}Si_{10}$. The μ_i of all the sample as affected by annealing at different temperatures with annealing time of one hour in each case, is measured at low frequency (1KHz) and in very low field (H = 0.1A/m). The initial permeability decreases monotonously with increasing annealing temperature.

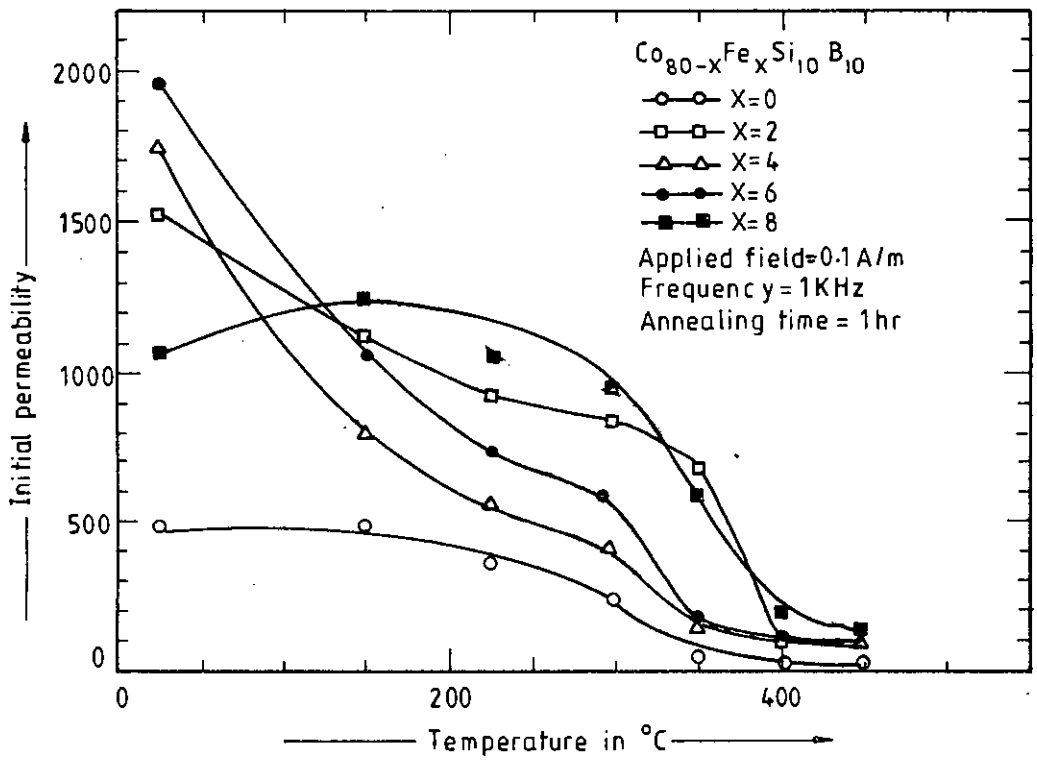

Fig.-7.18 Initial permeability versus annealing temperature of amorphous ribbons with composition $Co_{80-x}Fe_xB_{10}Si_{10}$

The effect of annealing on μ_i is very complex because two factors of apparently opposite effect on μ_i take place. One is the removal of local defects inhomogeneity and stresses that hinder the movement of domains by pinning effect and the other is the growth of the nucleation centres of crystallites that also hinders the movement of domain walls. Since effect of annealing is to remove the pinning centres of the first kind and to enhance the growth of the pinning centres of the second kind, the result of annealing depends on the composition of the amorphous ribbons and the conditions of preparation of the asquenched samples. Our results of annealing on cobalt based samples, which show a decrease of μ_i with annealing time, are explained as due to the growth of the nucleation centres of the crystallites formed during the preparation.

7.5. Specific Magnetization Measurements of Co-based Amorphous Ribbons

The specific magnetization of these Co-Fe-B-Si ribbons with composition $Co_{80-x}Fe_xB_{10}Si_{10}$ [x = 0, 2 ,4 6 & 8] in the as-quenched condition is measured using a V.S.M. The specific magnetization process as a function of field are shown in fig.-7.19. In the case of saturation magnetization it is observed that while ribbon with composition $Co_{80}B_{10}Si_{10}$ reaches its saturation value around 3KG field, $Co_{78}Fe_2B_{10}Si_{10}$ requires 2.8KG, $Co_{76}Fe_4B_{10}Si_{10}$ requires 2.7KG, $Co_{74}Fe_6B_{10}Si_{10}$ requires 2.9KG and $Co_{72}Fe_8B_{10}Si_{10}$ requires 2.7KG. The saturation magnetization (σ_s) for different sample are calculated as shown in Table-7.5.

Table-7.5

$Co_{80-x}Fe_xB_{10}Si_{10}$	x = 0	x = 2	x = 4	x = 6	x = 8
σ_s in Am^2/Kg at room temp.	91.22	103.64	107.35	110.01	113.63
T_c	408^0C	420^0C	429^0C	438^0C	443^0C

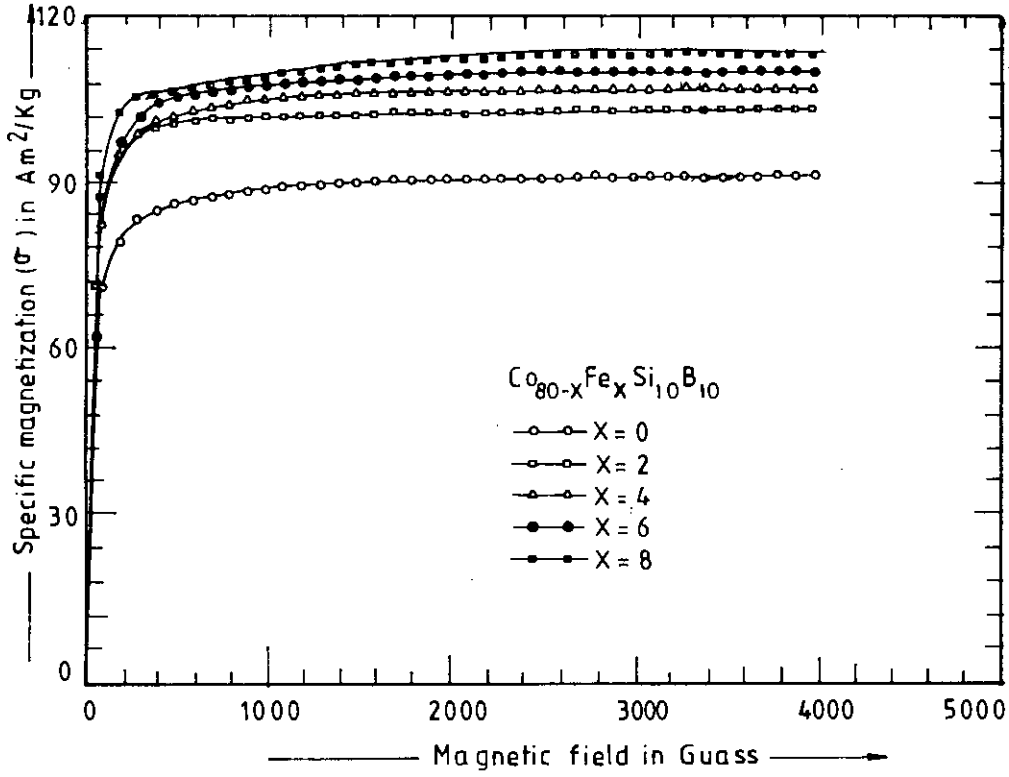

Fig.-7.19 Specific magnetization versus magnetic field of amorphous ribbons with composition $Co_{80-x}Fe_xB_{10}Si_{10}$

Fig.-7.20 shows that the saturation specific magnetization (σ_s) increases with increasing values of Fe-content in the amorphous alloy with composition $Co_{80-x}Fe_xB_{10}Si_{10}$. While it is quite consistent with the results of crystalline Co-Fe alloys and is explained as due to higher magnetic moment of Fe atoms.

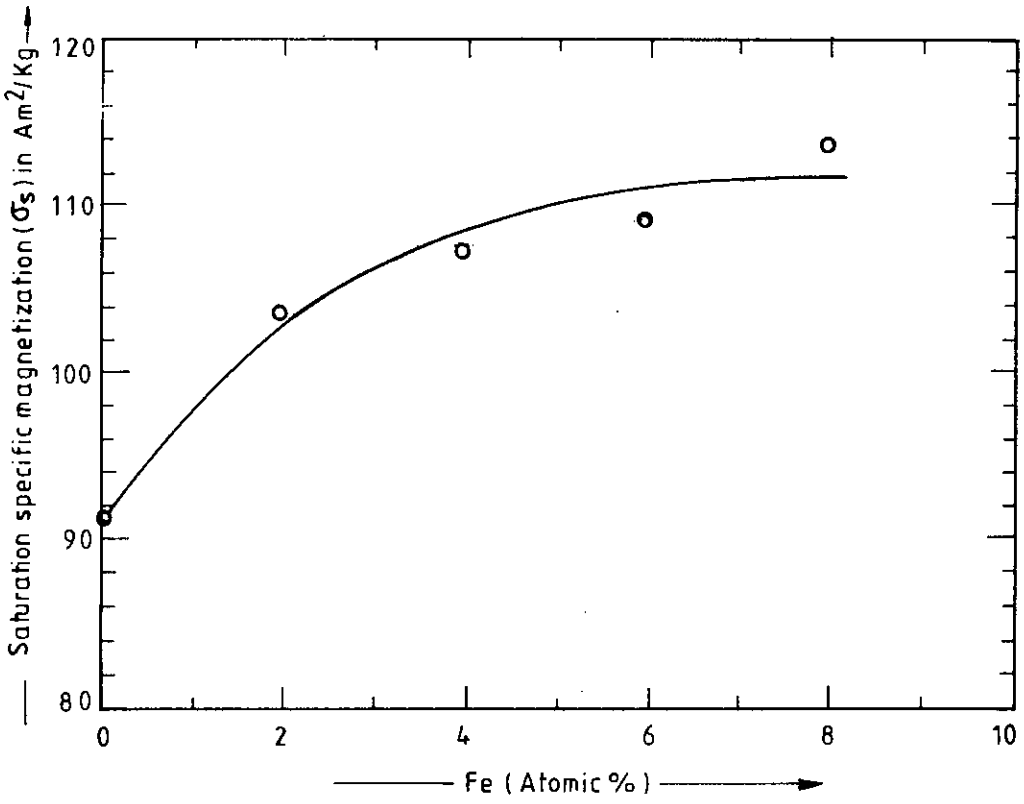

Fig.-7.20 Variation of saturation specific magnetization due to change in the Fe-content in $Co_{80-x}Fe_xB_{10}Si_{10}$ amorphous ribbons.

7.5.1 Temperature Dependence of Magnetization of Co-based amorphous ribbons.

Temperature dependence of magnetization of the samples measured by using a V.S.M. from room temperature to $800^0 C$ is shown in fig.-7.21. With increasing values of Fe in the amorphous alloy the magnetization increases. For accurate determination of the curie temperature, dM/dt curves have been plotted as shown in fig.-7.22 which are derived from fig.-7.21. Sharp peaks of dM/dt for the different compositions indicate that the T_c values are well defined and the measurements are quite accurate. The numerical values of T_c for all the samples are shown in Table-7.5.

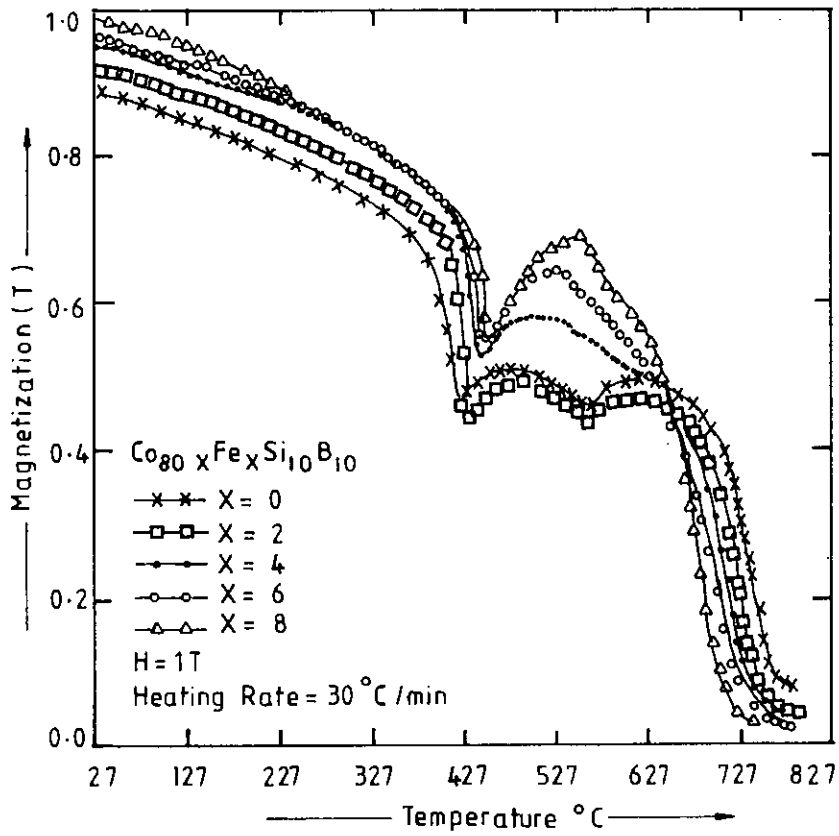

Fig.-7.21 Temperature dependence of magnetization of amorphous ribbons with composition $Co_{80-x}Fe_xB_{10}Si_{10}$

The T_c for the amorphous system, however, increases with increasing amounts of Fe substitution as observed by A.C. initial permeability measurements and also from the temperature dependence of magnetization obtained by V.S.M. Both the measurements gave the same value for the T_c's of each composition. Although the T_c of Co (1057^0C) is higher than that of Fe (770^0C) in the amorphous state, exchange interaction between the magnetic ions is increased by the replacement of Co by Fe, quite contrary to the crystalline state. This is in keeping with the results presented in (7.1-7.2) , where Cargill and Ishikawa have found an enhancement of T_c with Fe substitution up to 10At.%. Since the exchange interactions in the amorphous magnetic system is of the RKKY type which occurs via the conduction electrons, the distance between magnetic atoms is very important. It is thus likely that the addition of Fe helps the conduction electron to enhance the exchange interaction and, hence, the Curie temperature up to certain range.

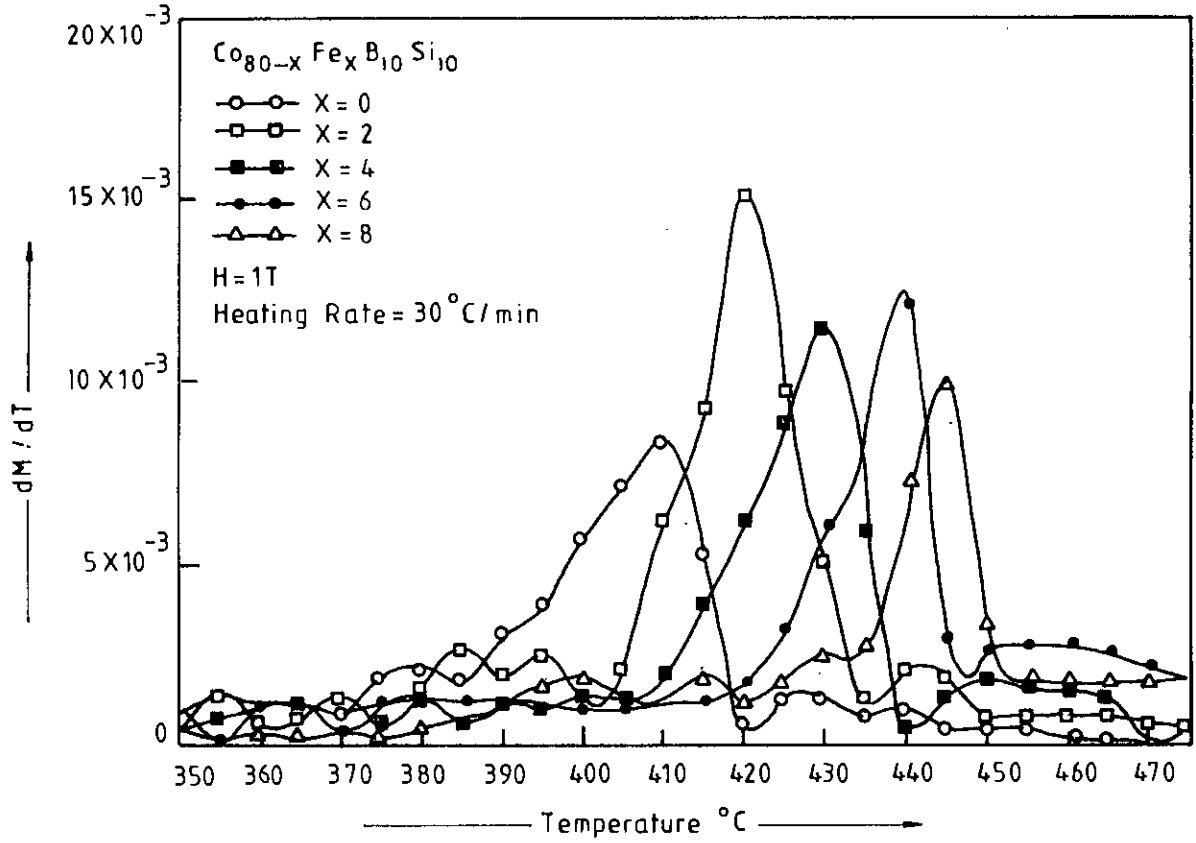

Fig.-7.22 dM/dt versus temperature curve of amorphous ribbons with composition $Co_{80-x}Fe_xB_{10}Si_{10}$

Plots of experimental data with meanfield results of reduced magnetization $m = \frac{M_s(T)}{M_s(0)}$ against reduced temperature $= \frac{T}{T_c}$ for replacement of Co by Fe by different amounts are shown in fig.-7.23. Fig.-7.23 shows the reflection of the strength of the exchange coupling, where the structural disorder in these amorphous alloys induces an exchange fluctuation that causes a pronounced flattening of the temperature dependence of $M_s(T)$ curves as shown in fig.-7.21.

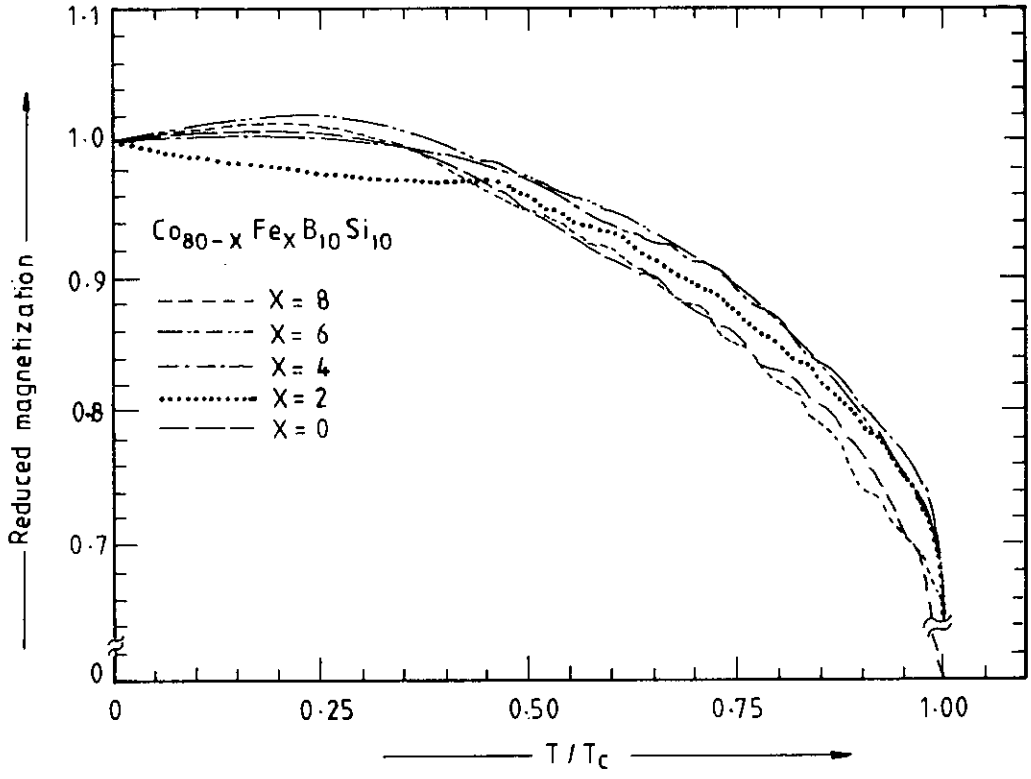

Fig.-7.23 Reduced magnetization versus reduced temperature for amorphous ribbons with composition $Co_{80-x}Fe_xB_{10}Si_{10}$

7.6. Stress Induced Anisotropy of Co-based Amorphous Ribbons

The field dependence of the torque versus angle of Co-Fe-B-Si ribbons with composition $Co_{80-x}Fe_xB_{10}Si_{10}$ [x = 0, 2, 4, 6 & 8]. The representative torque curves of the field dependence of anisotropy of amorphous ribbons with composition $Co_{72}Fe_8B_{10}Si_{10}$ increases with increasing field, while that of the ribbons with composition $Co_{80}B_{10}Si_{10}$ decreases with increasing field as shown in fig.-7.24 and fig.-7.25. This is explained as due to the competing contribution from Fe and Co atoms to anisotropy energy. We assume that the origin of magnetic anisotropy in these ribbons, formed by melt-spinning technique, is due to magnetostrictive strain. This concept is supported by the fact that the anisotropy in these ribbons is unidirectional. Amorphous ribbons have no crystalline structure and therefore have no magnetocrystalline anisotropy. Again samples are prepared as circular discs to avoid any shape anisotropy and associated demagnetizating effect.

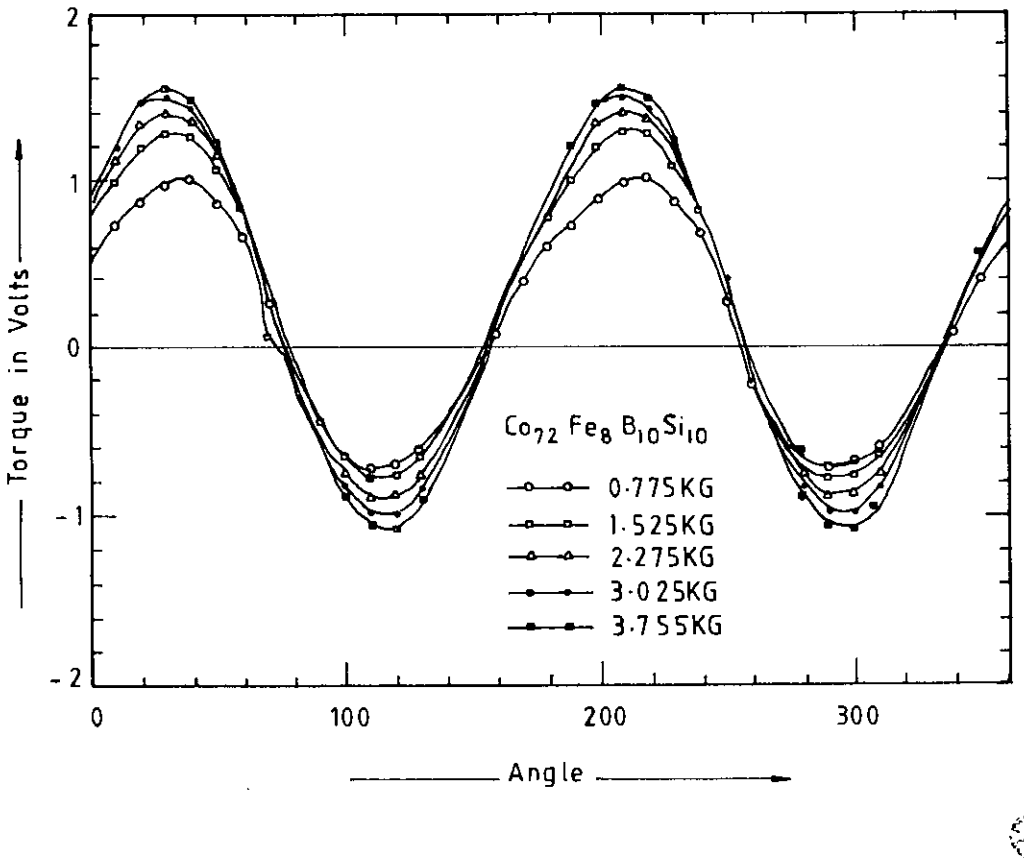

Fig.-7.24 Field dependence of torque versus angle for the amorphous ribbon with composition $Co_{72}Fe_8B_{10}Si_{10}$

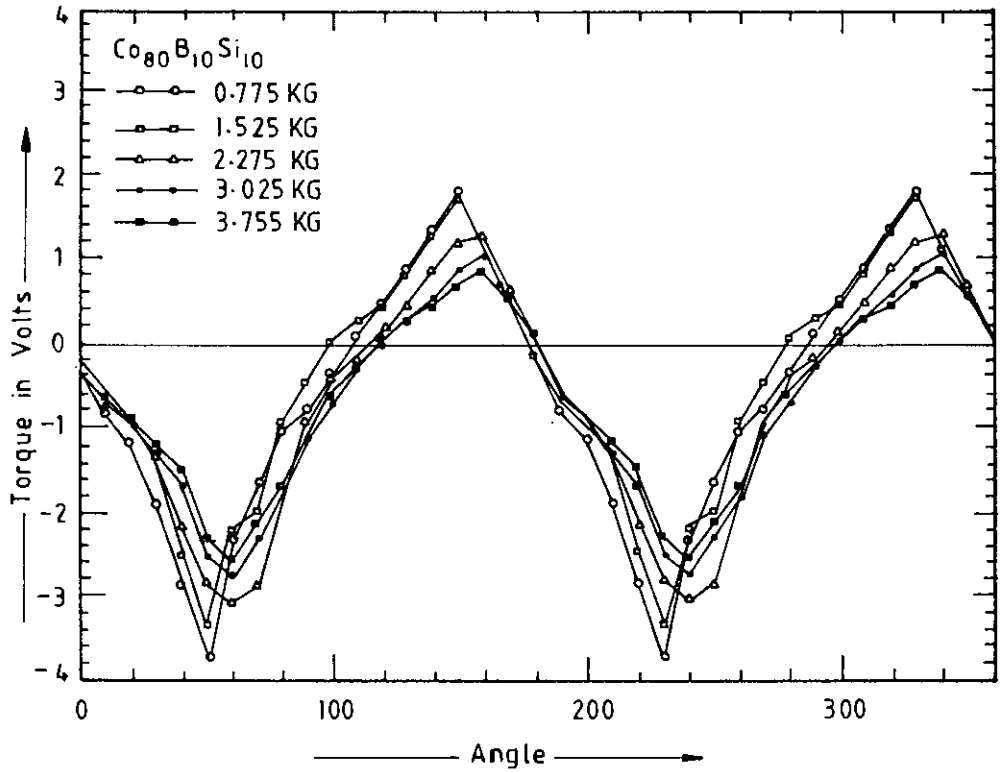

Fig.-7.25 Field dependence of torque versus angle for the amorphous ribbon with composition $Co_{80}B_{10}Si_{10}$

On the other hand the Co-Fe system has positive magnetostriction due to the presence of Fe atoms which has positive magnetostriction in the bulk state. When a material with positive magnetostriction is strained, it develops an easy direction of magnetization along the strain axis. In our prepared specimens the strain is induced along the length due to the tension on the ribbon produced by the centrifugal force. The sign of the magnetostriction constant determine the easy axis of magnetization. Since Fe and Co have opposite signs of magnetostriction which is positive for Fe and negative for Co, it is expected that for high percentage of Fe the magnetostrictive effect of Fe and the corresponding anisotropy will dominate. The reverse effect is expected when the percentage of Fe becomes low. It is, however, not possible to find any quantitative relation between anisotropy and the composition in the case of amorphous materials because, the contributions of different magnetic atoms through their random configurations in the amorphous state is too complicated. Our results are thus explained only in a qualitative way, considering the origin of anisotropy as due to magnetostrictive strain induced technically during the preparation process.

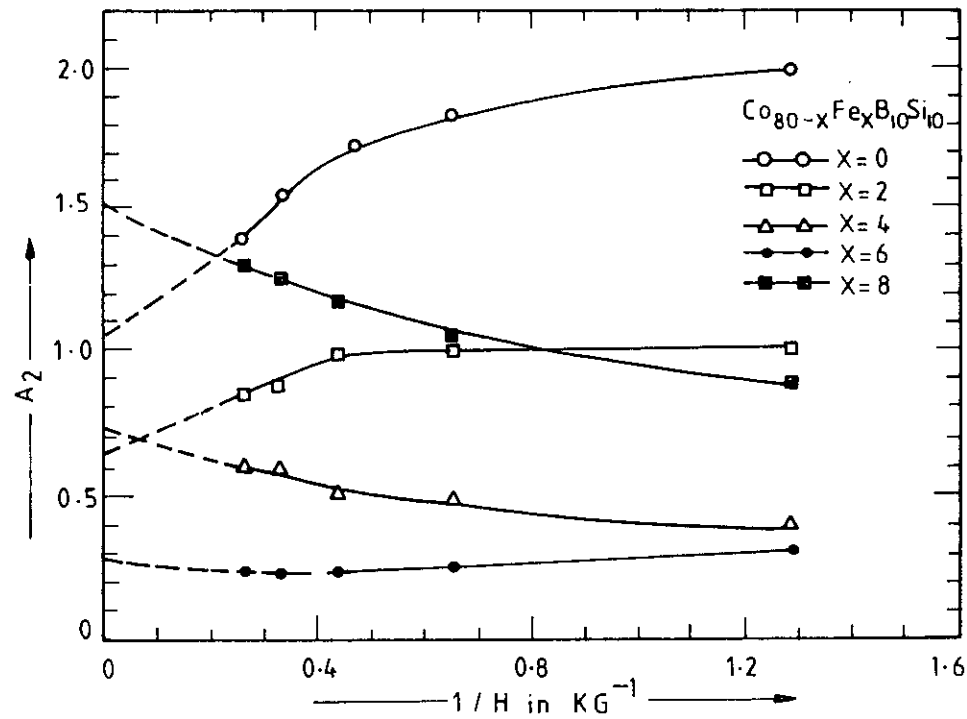

Fig.-7.26 Fourier coefficient for infinite field by extrapolation from A_2 versus 1/H curve for different compositions of $Co_{80-x}Fe_xB_{10}Si_{10}$ system.

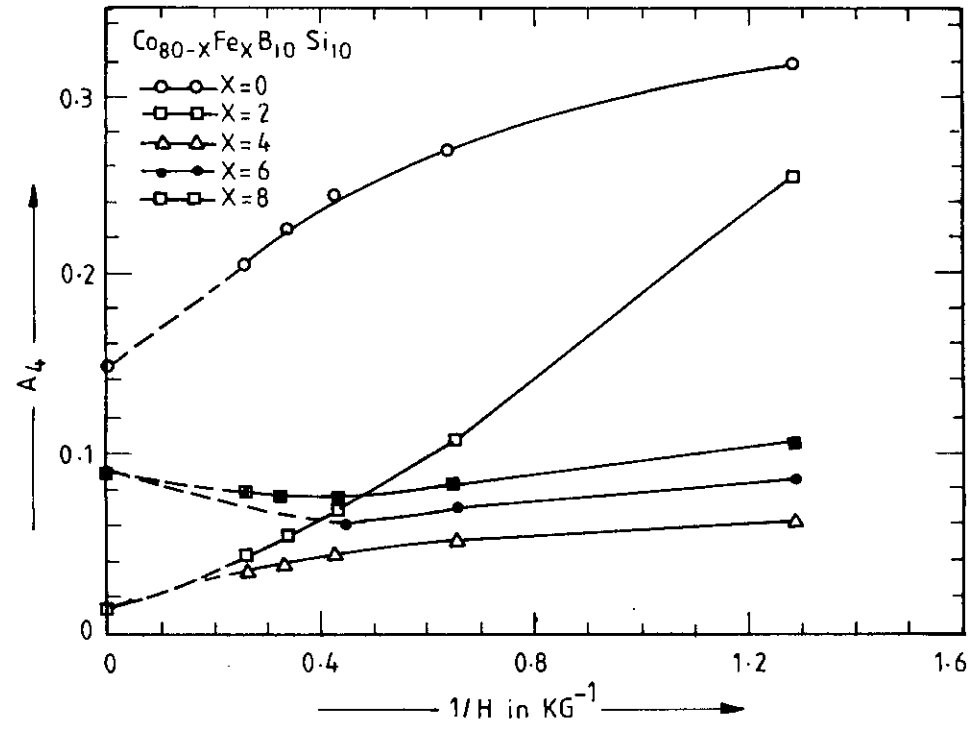

Fig.-7.27 Fourier coefficient for infinite field by extrapolation from A_4 versus 1/H curve for different compositions of $Co_{80-x}Fe_xB_{10}Si_{10}$ system.

Fourier co-efficient are determined from the angle versus torque curves for different values of the applied field and by extrapolation of the field up to $H \rightarrow \infty$ as shown in fig.-7.26 and fig.-7.27. Experimental values of the anisotropy constant K_u for different composition of $Co_{80-x}Fe_xB_{10}Si_{10}$ ribbons for different field are shown in fig.-7.28. The anisotropy constants against 1/H for the different samples as obtained by extrapolation are shown in fig.-7.29. The results are shown in Table-7.6.

Table-7.6

$Co_{80-x}Fe_xB_{10}Si_{10}$	x = 0	x = 2	x = 4	x = 6	x = 8
K_u in J/m^3 at room temp.	1578.64	586.76	374.37	222.36	899.59
K_u in J/m^3 at 0K	2550	1100	520	330	1280
T_c	$410^0 C$	$420^0 C$	$430^0 C$	$440^0 C$	$445^0 C$

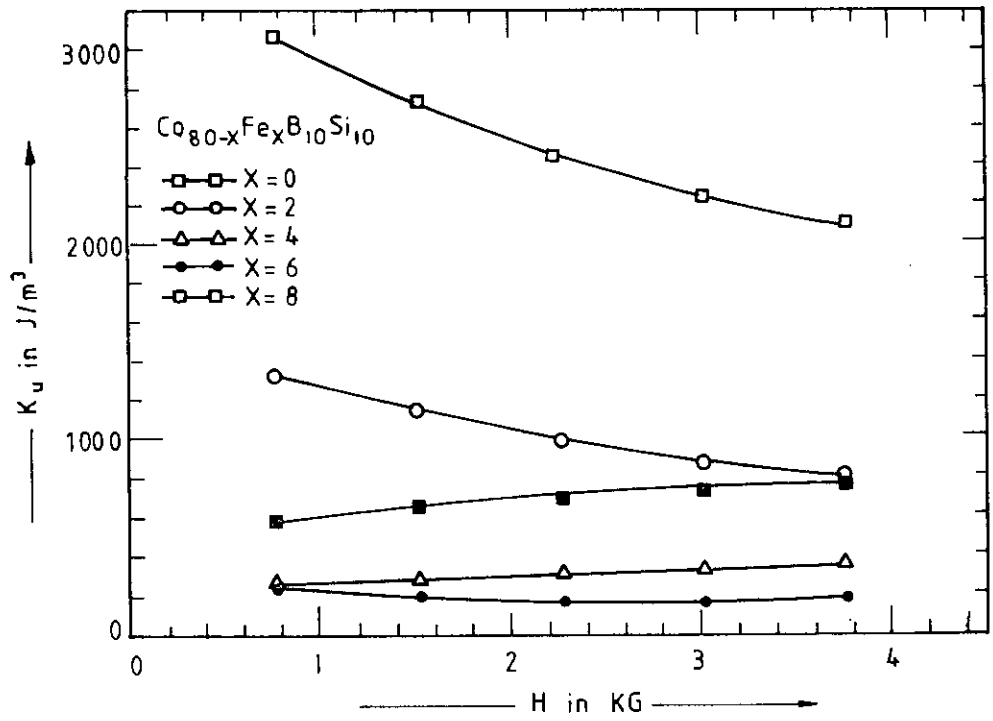

Fig.-7.28 Field dependence of experimental values of K_u for different compositions of $Co_{80-x}Fe_xB_{10}Si_{10}$ system.

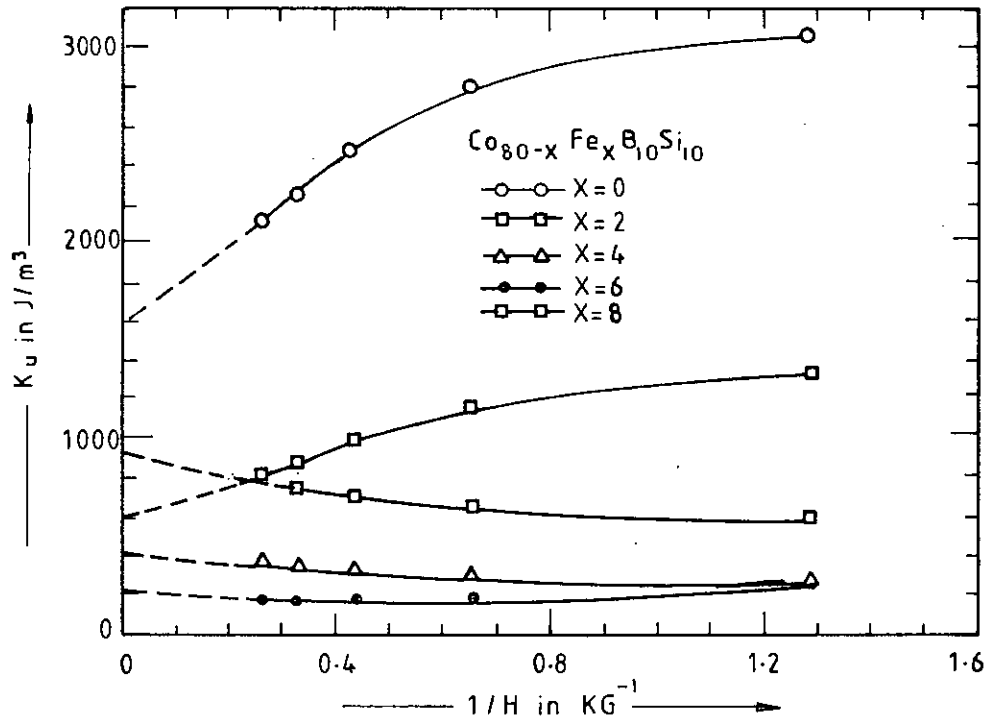

Fig.-7.29 Extrapolated values of K_u for infinite field for different compositions of $Co_{80-x}Fe_xB_{10}Si_{10}$ system.

The compositional dependence of K_u's with increasing Fe-contents is shown in fig.-7.30, which shows the minimum value of anisotropy at 6 At.% of Fe and goes on increasing with increasing value of Fe up to 8 At.%. This increase of anisotropy is explained as due to increasing value of magnetostriction which is positive for Fe and negative for Co. The minimum value of anisotropy at 6 At.% of Fe is explained as due to opposite magnetostrictive contributions from Fe and Co which tends to cancel each others effects.

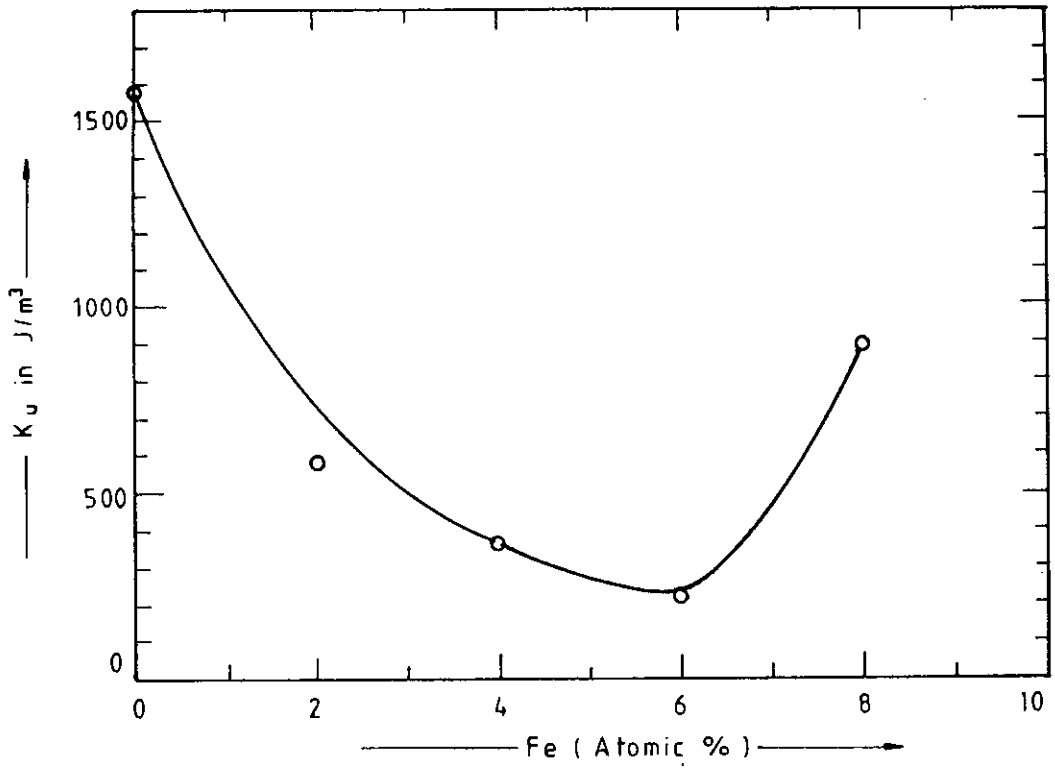

Fig.-7.30 Compositional dependence K_u of amorphous ribbons with composition $Co_{80-x}Fe_xB_{10}Si_{10}$

7.6.1. Temperature Dependence of K_u

The temperature dependence of anisotropy constant (K_u) of amorphous ribbons with Fe substitution of compositions $Co_{80-x}Fe_xB_{10}Si_{10}$ is shown in fig.-7.31. There is almost monotonous decrease of anisotropy with increase of temperature. Much of the experimental effort in the study of field induced anisotropy has been concentrated in the Co-Fe glassy alloys. For the $\lambda=0$ alloy, internal stresses should not contribute to K_u in as-quenched samples. This is indicated by our results shown in fig.-7.30. The composition that corresponds to $\lambda=0$ is expected to be between of 4At.% and 6At.% of Fe. It has been well established that directional ordering of atom pairs leads to the observed anisotropy. Directional order theory predicts a decrease in K_u with increasing temperature and vanishes at T_c. We have extrapolated K_u to zero value at T_c as shown in Table-7.6. The anisotropy constant K_u is calculated in J/m^3 for different temperature as shown in Table-7.7.

The stress induced anisotropy, $K_u(0)$ at T=0 is obtained by extrapolating the temperature dependence curve of $K_u(T)$ to 0K. The extrapolated value of $K_u(0)$ for different ribbons of compositions $Co_{80-x}Fe_xB_{10}Si_{10}$ are shown in Table-7.6.

Table-7.7

$Co_{80-x}Fe_xB_{10}Si_{10}$	x = 0 K_u in J / m^3	x = 2 K_u in J / m^3	x = 4 K_u in J / m^3	x = 6 K_u in J / m^3	x = 8 K_u in J / m^3
25°C	1579	587	374	222	900
50°C	1214	539	349	204	856
75°C	1046	454	340	194	815
100°C	851	385	329	183	741
125°C	835	382	283	147	680
150°C	735	319	251	142	637
175°C	684	286	231	135	601
200°C	528	252	226	129	585
225°C	465	249	199	123	495
250°C	398	229	181	118	464
275°C	320	197	175	110	463
300°C	239	162	147	98	432

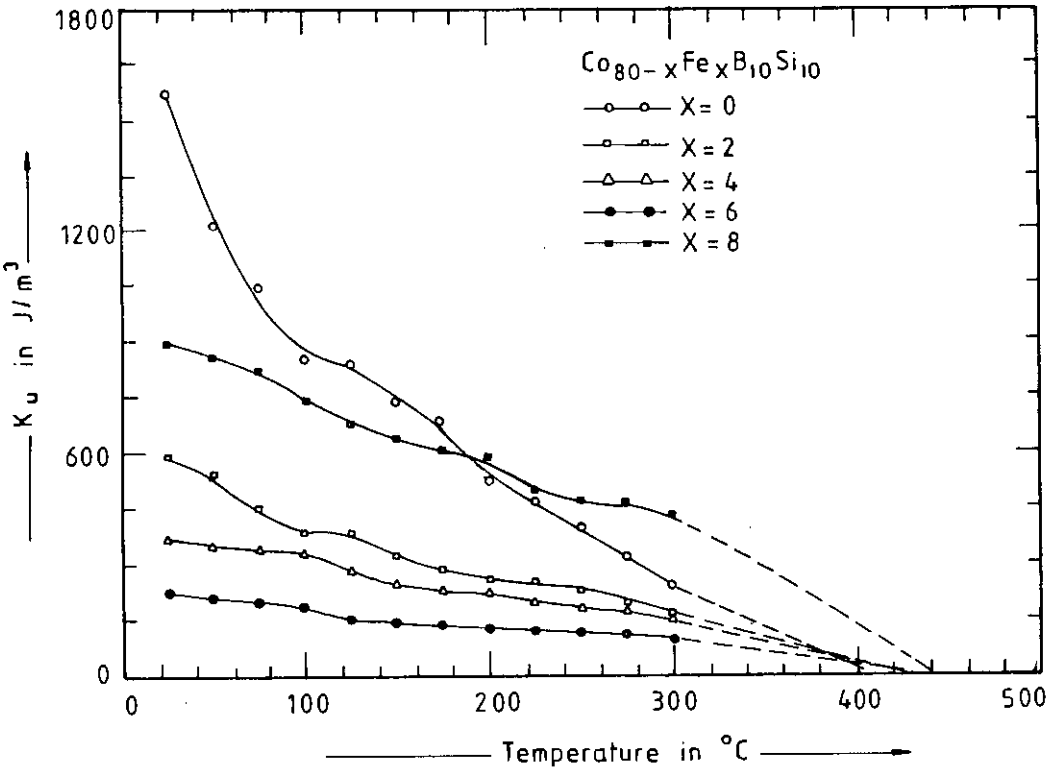

Fig.-7.31 Temperature dependence of K_u of amorphous ribbons with composition $Co_{80-x}Fe_xB_{10}Si_{10}$

The corresponding curves $\ln\left[\frac{K_u(0)}{K_u(T)}\right]$ versus $\ln\left[\frac{M_s(0)}{M_s(T)}\right]$ for the amorphous ribbons with compositions $Co_{80-x}Fe_xB_{10}Si_{10}$ follow straight lines as shown in fig.-7.32(a) to fig.-7.32(e). The K_u arising from the disorder caused by randomly oriented easy axis follows a power law: $\frac{K_u(0)}{K_u(T)} = \left[\frac{M_s(0)}{M_s(T)}\right]^n$ where $4 < n < 10$. The values of n are shown in Table-7.8

Table-7.8

$Co_{80-x}Fe_xB_{10}Si_{10}$	x = 0	x = 2	x = 4	x = 6	x = 8
n	9.56	7.85	6.77	5.75	4.64

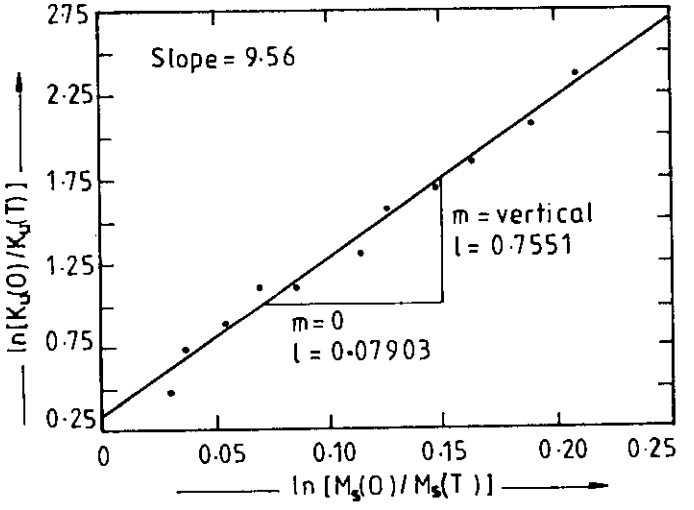

Fig.-7.32(a) $\ln\left[\frac{K_u(0)}{K_u(T)}\right]$ versus $\ln\left[\frac{M_s(0)}{M_s(T)}\right]$ curve of the amorphous ribbon with composition $Co_{80}B_{10}Si_{10}$

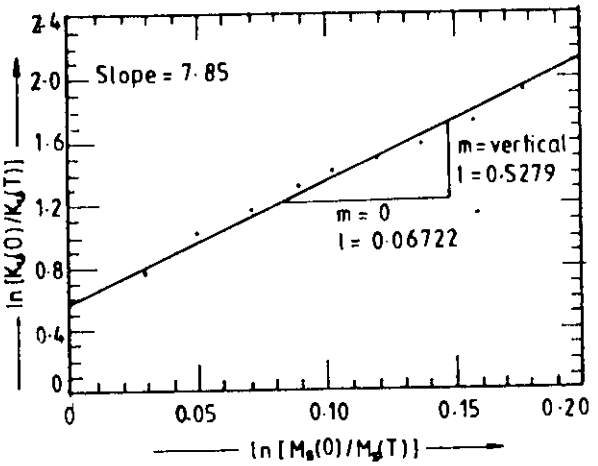

(b) Composition $Co_{78}Fe_2B_{10}Si_{10}$

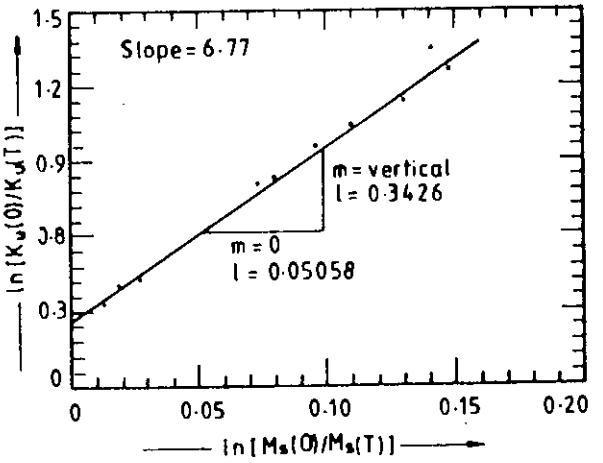

(c) Composition $Co_{76}Fe_4B_{10}Si_{10}$

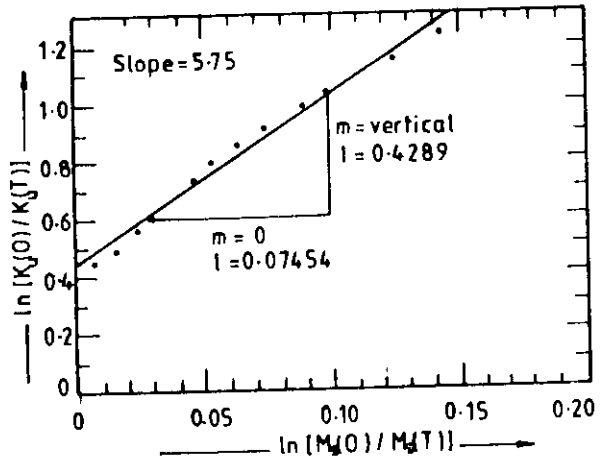

(d) Composition $Co_{74}Fe_6B_{10}Si_{10}$

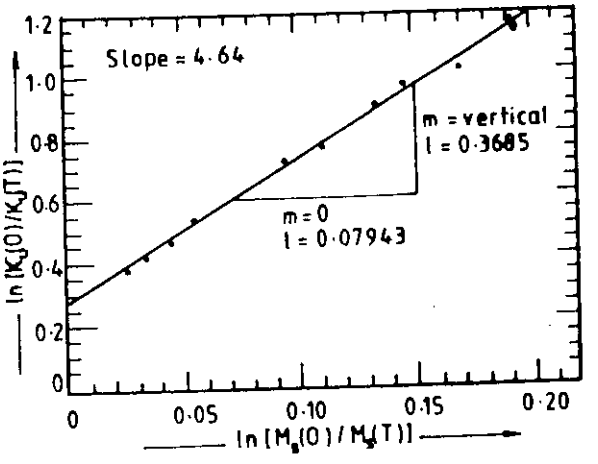

(e) Composition $Co_{72}Fe_8B_{10}Si_{10}$

Fig.-7.32(b) to (e) $\ln\left[\frac{K_u(0)}{K_u(T)}\right]$ versus $\ln\left[\frac{M_s(0)}{M_s(T)}\right]$ curves of amorphous ribbons with composition $Co_{80-x}Fe_xB_{10}Si_{10}$ [x = 2, 4, 6 & 8]

7.7. Experimental Results and Analysis of Mössbauer Parameters for Co-based Amorphous Ribbons

Room temperature Mössbauer spectra typical of as-quenched amorphous ribbons are determined and the change in the spectra corresponding to different composition of the system $Co_{80-x}Fe_xB_{10}Si_{10}$ [x = 2, 4, 6 & 8] are shown in fig.-7.33. A comparison of the spectrum of ^{57}Fe with those of the amorphous ribbons of different compositions shows shifts in the spectral lines and their broadening. The numerical values of IS, E_Q, FWHM, H_{hf} and absorption percentage are shown in Table-7.9.

Table-7.9

Sample	IS, mm/s ±0.005	E_Q, mm/s ±0.005	H_{hf}, Tesla ±0.1T	FWHM mm/s, ±0.01	Absorption %
Pure ^{57}Fe foil		0.058	33	0.18	11.38
$Co_{78}Fe_2B_{10}Si_{10}$	0.147	0.175	25.34	1.05	0.80
$Co_{76}Fe_4B_{10}Si_{10}$	0.264	0.233	25.71	1.05	0.91
$Co_{74}Fe_6B_{10}Si_{10}$	0.176	0.175	26.62	0.99	1.08
$Co_{72}Fe_8B_{10}Si_{10}$	0.206	0.349	26.98	0.99	1.10

Isomer shifts of all the amorphous ribbons are calculated relative to the centroid of these spectrum from the centroids of the velocity scale of thin ^{57}Fe sample. The IS's are given relative to the centroid of this spectrum as shown in Table-7.9. The Fe atoms are in the trivalent state in amorphous ribbons as reflected in the IS value which varies from 0.147 to 0.264mm/s. The E_Q of the Fe and Co atoms in the amorphous ribbons with composition $Co_{80-x}Fe_xB_{10}Si_{10}$ is observed in the range 0.175 to 0.349mm/s as shown in Table-7.9.

The absorption percentage slightly decreases with decreasing Fe-content. These results are shown in Table-7.9. The effect of change in the composition of Co-Fe-B-Si amorphous system on the transition line width as measured by FWHM is also shown in Table-7.9. The experimental FWHM of pure ^{57}Fe foil is 0.18mm/s, FWHM of the amorphous ribbons broadening is 5 to 6 times.

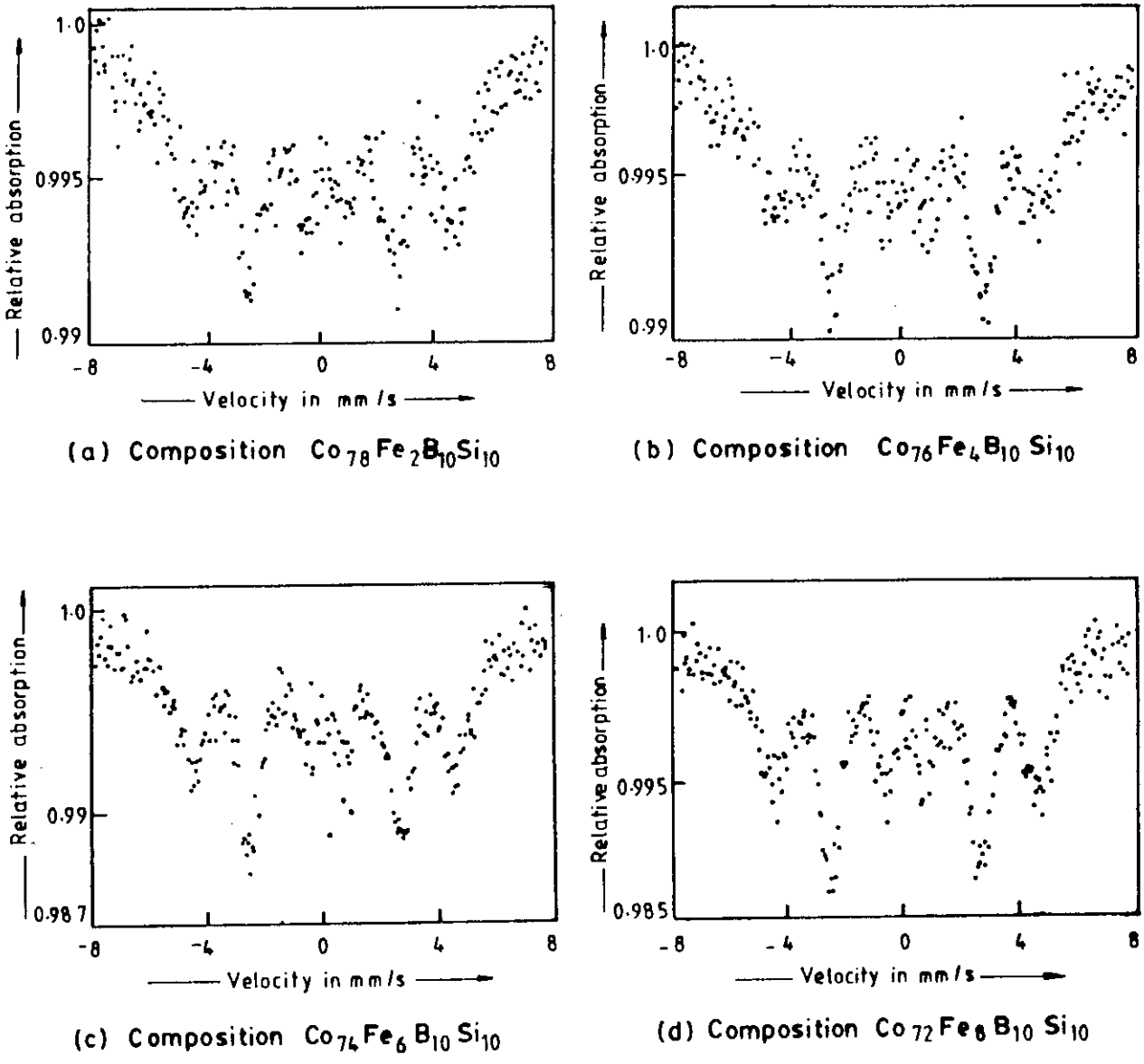

Fig.-7.33 Room temperature Mössbauer spectra of as-quenched amorphous ribbons with composition $Co_{80-x}Fe_xB_{10}Si_{10}$ [x = 2, 4, 6 & 8]

The results of average magnetic hyperfine field (H_{hf}) of the as-quenched amorphous ribbons with composition $Co_{80-x}Fe_xB_{10}Si_{10}$ are shown in Table-7.9. The H_{hf} increases with increasing Fe-content as shown in fig.-7.34. The bulk magnetization value (σ_s), are consistent with magnetic moment distributions of the different samples as reflected in the hyperfine fields.

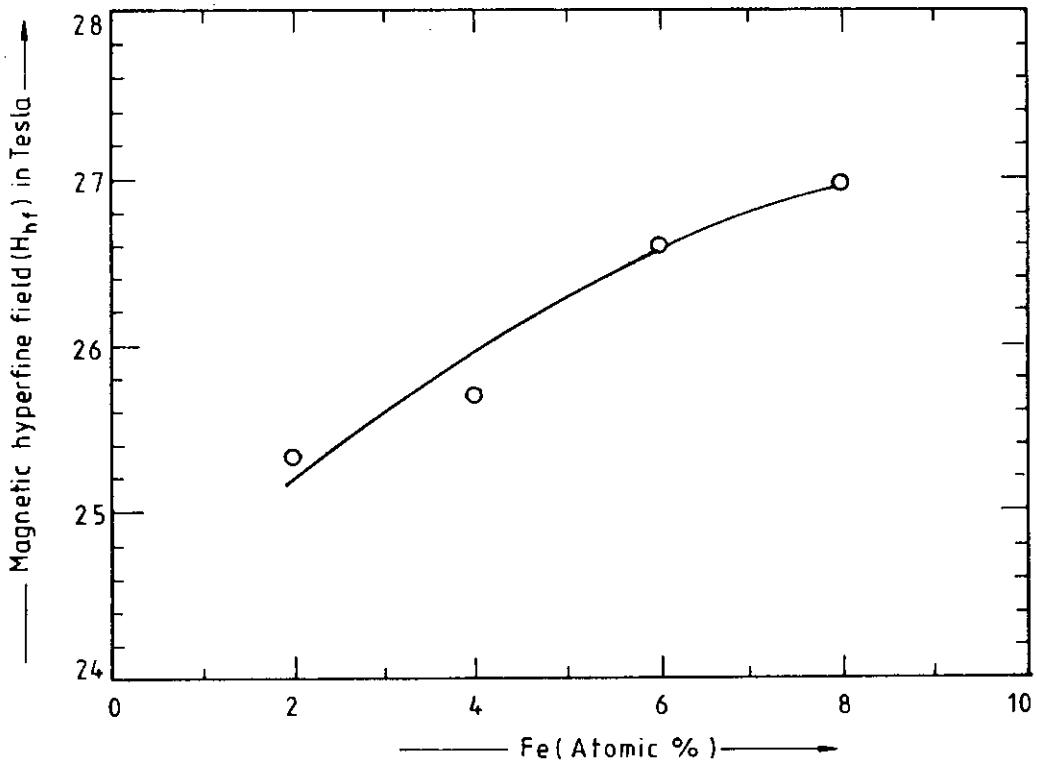

Fig.-7.34 Variation of internal hyperfine field due to change in the Fe-content in $Co_{80-x}Fe_xB_{10}Si_{10}$ amorphous ribbons.

CHAPTER-8 CONCLUSION

8.0. Conclusion

Amorphous ribbons as a potential new magnetic material and a new medium for understanding magnetic ordering characterized by parameters like saturation magnetization, exchange force, anisotropy, permeability, loss factor and hyperfine field has been studied. Three sets of amorphous alloys were chosen with compositions $Fe_{90-x}Si_xB_{10}$, $Ni_{80-x}Fe_xB_{20}$ and $Co_{80-x}Fe_xB_{10}Si_{10}$. The melt spinning technique has been confirmed as a very useful method of preparing ribbons.

From the study of kinetics and the thermodynamic stability as a function of Si content, the best composition for the Fe-based system is obtained as $Fe_{76}Si_{14}B_{10}$ in respect the highest values of T_g and T_x which are 550^0C and 570^0C respectively.

For Ni-Fe-B system, T_g and T_x are found to decrease with increasing replacement of Fe by Ni. The maximum values of T_g and T_x in these cases are found to be 450^0C and 480^0C respectively for the composition $Ni_{30}Fe_{50}B_{20}$. It is interesting to note that the difference between T_g and T_x remains nearly the same with change of composition. The temperature for secondary reaction for both Fe and Ni-based alloys remains practically unchanged with change of composition.

For Co-based amorphous ribbons T_g increases sharply with increasing replacement of Co by Fe. The highest value of T_g which is 455^0C corresponds to the alloy composition $Co_{72}Fe_8B_{10}Si_{10}$. The T_x remains almost unchanged in respect of composition.

For technological uses of amorphous materials at elevated temperature and for magnetic stability it is important to look for compositions that give higher values of T_c. For Fe-based ribbons it is observed that replacement of Fe by 14At.% of Si, keeping B fixed at 10At.%, T_c rises to 448^0C. This composition is most suitable as Fe-Si-B system for both structural and magnetic ordering.

For Ni-based amorphous ribbons T_c decreases monotonically with increasing Ni-content. The highest value of T_c corresponds to the composition $Ni_{30}Fe_{50}B_{20}$.

The Co-Fe alloy system which is very convenient for producing stable amorphous ribbons over a range of compositions behave quite differently from corresponding crystalline state in respect of T_c and saturation magnetization. Although

the T_c of Co is higher than that of Fe, in the amorphous state the exchange interaction between the magnetic ions is increased by the replacement Co by Fe, quite quantrary to crystalline state. The highest value of T_c for Co-Fe-B-Si system corresponds to composition $Co_{72}Fe_8B_{10}Si_{10}$. Since the exchange interaction in the amorphous magnetic system is the RKKY type, it is concluded that the addition of Fe helps the conduction electrons to enhance the exchange interaction and hence the Cure temperature.

3d transition metal metalloid amorphous ribbons as soft magnetic material are characterized by remanence (B_r), saturation magnetic induction (B_s), coercive force (H_c), initial permeability (μ_i), relative quality factor $\left(\mu_i/\tan\delta\right)$ and complex permeability for their high frequency uses. These are experimentally studied for Fe, Ni and Co-based systems to obtain the optimum composition for each system.

For Fe-based ribbons with the general composition $Fe_{90-x}Si_xB_{10}$, B_r and B_s decrease slowly with increasing percentage of Si, while H_c initially decreases with increasing Si-content up to 8At.% and then increases with further increase of Si-content. The initial permeability for this system increases with the increase of Si-content up to 8At.%. The composition which is most suitable as soft magnetic material is $Fe_{82}Si_8B_{10}$ but $Fe_{80}Si_{10}B_{10}$, $Fe_{76}Si_{14}B_{10}$ and $Fe_{84}Si_6B_{10}$ are also nearly equally good as soft magnetic material. All these materials can be used up to 3MHz.

In Ni-based ribbons B_r, B_s and H_c increase with increasing substitution of Fe for Ni except for the sample with composition $Ni_{30}Fe_{50}B_{20}$ in which coercivity decreases in spite of high percentage of Fe. The variation of H_c with composition is explained as originating from the complex combination of magnetostriction arising from Fe and Ni atoms and the anisotropy arising from magnetostrictive strain. The initial permeability of Ni-Fe-B system decreases with increasing Fe content up to 40At.% and then increases with further increase of Fe. The samples with compositions $Ni_{50}Fe_{30}B_{20}$ $Ni_{40}Fe_{40}B_{20}$ and $Ni_{30}Fe_{50}B_{20}$ are all suitable for high frequency uses.

H_c of the Co-based alloy with the general composition $Co_{80-x}Fe_xB_{10}Si_{10}$ initially decreases with increasing replacement Co by Fe up to 6At.% and then increases with further replacement of Co by Fe. Permeability becomes by far the largest for the composition $Co_{74}Fe_6B_{10}Si_{10}$ and have a value of 74,956 with a 24 fold increase of permeability compared to the Fe free sample. This result is explained as due to the reduction of magnetostriction arising from the opposite contributions from Fe and Co atoms. The consequence of this is the maximum initial permeability for the sample with composition $Co_{74}Fe_6B_{10}Si_{10}$.

The effect of annealing on initial permeability is quite different for Co-based system as compared to Fe and Ni-based ribbons. In the first case there is a decrease in initial permeability with increase of the annealing temperature. This is explained as due to the nucleation of crystallites or their growth with annealing. In case of Ni and Fe-based alloys there is an increase in initial permeability with increasing annealing temperature and then it decreases with further increase of annealing temperature. There is an increase of initial permeability with increasing annealing temperature due to the removal of defects and inhomogeneity, but with further increase of annealing temperature the initial permeability decreases due to nucleation of crystallites and their growth.

For all the alloy systems saturation specific magnetization depends on the atomic magnetic moments of the constituent 3d transition elements. The effect of the glass forming material is explained as due to transfer of P-electrons to the 3d band. However, a quantitative agreement is not found on the basis of rigid band model. This shows that amorphous systems can not be treated in the same way as crystalline materials in respect of band structure. This is also evident for the temperature dependence of magnetization which for our amorphous systems decreases faster as compered to crystalline materials with increasing temperature. The structural disorder accompanied by the fluctuation of the exchange integral is responsible for such behaviour of the amorphous system.

The uniaxial anisotropy is observed in all the amorphous systems are explained as mostly due to magnetostrictive strains induced during the preparation process. The compositional dependence of K_u can in general be explained in terms of compositional dependence of magnetostriction. The results of μ_i, H_c and K_u are mutually consistent for all the samples. The temperature dependence of K_u do not follow the power law as suggested by Zener and Carr for crystalline material. However, a consistent power law for K_u, which is different for each of the systems, arising from disorder caused by randomly oriented easy axes, exists with the exponent n lying between 2 and 4 for Fe-based samples; 2 and 6 for Ni-based samples; 4 and 10 for Co-based samples.

The Mössbauer spectra for all the samples clearly show Lorentzian shaped lines in sextet with broad distribution of magnetic hyperfine fields as compared to pure ^{57}Fe foils. These broadening of spectral line width changes with composition. The isomer shifts of Fe-atoms in all the Fe, Ni and Co-based samples behave as trivalent ions. The experimental spectra for the best fit obtained, provide probability distribution of the

hyperfine field which is observed as a single peak corresponding to the amorphous state of the ascast samples. The H_{hf} values for different compositions agree with the corresponding σ_s values, being larger for samples with higher Fe-content.

Further work with finer variation of composition can be useful in detailing out the effect of glass forming material on magnetic characteristics. Low temperature measurements of magnetization is needed to avoid extrapolation that has been used in the present work. Another important study that can be taken up is the measurement of magnetostriction as a function of composition and temperature to confirm the suggestions regarding the origin of induced magnetic anisotropy.

CHAPTER-9 REFERENCES

9.0. References

Chapter-1.

1.1. Duwez, P., R. H. Willens and W. Klement, Jr., 1960, J. Appl. Phys. 31, 1136.

1.2. Simpson, A. W. and D. R. Brambley, 1971, Phys. Stat. Sol. (b) 43, 291.

1.3. Luborsky, F. E., J. J. Becker and R. O. McCary, 1975, IEEE Trans. Magnetics MAG-11, 1644.

1.4. Egami, T., P. J. Flanders and C. D. Graham, Jr., 1975a, AIP Conf. Proc. 24, 697.

1.5. T. Miyazaki, K. Yamauchi, S. Arakawa, Y. Yoshizawa and S. Nakajima, Bulletin Japan Inst. Metals. 26(1987), 299.

1.6. O. Komoto, H. Hujishima, S. Sumiya, H. Itomasa and T. Ojima, Bulletin Japan Inst. Metals. 27(1988), 293.

1.7. H. Fujimori, M. Kikuchi Y. obi and T. Masumoto, Sci. Rep.RITO, A-26(1976), 36.

1.8. H. Warliment and R. Bolli, J. Magn. Magn. Mat. 26(1982), 97.

1.9. Chatelier, H. Le., Bull. SOC.Franc. mineral 1887, 10, 204.

1.10. Nakamura, H. H. and Altas, L. M., Proc. fourth Carbon Conf. Pergamon Press. London 1960, 625.

1.11. Naka, M., S. Tomizawa, T. Watanabe and T. Masumoto, 1976, in Rapidly quenched metals, Section1 (eds. N. J. Grant and B. C. Giessen) (MIT Press, Cambridge, Mass.) P.273.

1.12. Luborsky, F. E., 1977a, Materials Sci. Eng. 28, 139.

1.13. Cohen, M. H. and D. Turnbull, 1961, Nature, 189, 131.

1.14. F. Zhu, N. Wang, R. Busch and P. Haasen, Scr. Metall. Mater. 25(1991).

1.15. J. Bigot, N. Lecaude, J. C. Pearon, C. Milan, C. Ramiarijaona and J. F. Rialland, J. Magn. Magn. Mater. 133(1994) 299-302.

1.16. S. S. Sikder, M. A. Asgar, M. A. Hakim and M. A. Mazid, Journal of Bangladesh Academy of Science, Vol. 20, N0.2, 237-245, 1996.

1.17. J. W. Cable, J. Appl. Phys. Vol.49, No.3, 1527(1978).

1.18. E. Figueroa, L. Lundgren, O. Beckman and S. M. Bhagat, Solid State Commun, Vol.20, 961(1976).

1.19. R. Malmhall, G. Backstrom, S. M. Bhagat and K. V. Rao, J. Phys. F. Met. Phys., Vol.9, No.2, 317(1979).

1.20. R. Valenzuela and J. T. S. Irvine, J. Appl. Phys. 72(4), 15 August 1992.

1.21. K. Shiiki, S. Otomo and M. Kudo, J. Appl. Phys. 52, 2483(1981).

1.22. T. Sasaki, T. Hosokawa and S. Takada, Phys. Ser. 39, 655(1989).
1.23. H. Fujimori, H. Yoshimoto and T. Masumoto, J. Appl. Phys. 52, 1893(1981).
1.24. K. Doi, T. Ayano and K. Kawamura, J. Non-crystalline Solids 34(1979) 405.
1.25. H. S. Chen, R. C. Shorwood and E. M. Gyorgy, Inter. Mag. L. A.(1977).
1.26. C. L. Chen and R. S. Hasegawa, ibid, 49, 1721, (1978)
1.27. R. N. G. Dalpadodo and K. Shirac, J. Appl. Phys., 52(1981) 1917.
1.28. G. Buttino, A Cecchetti, M. Poppi and G. Zini, J. Magn. Magn. Mat. 41(1984) 205-208.
1.29. F. E. Luborsky, J. J. Becker, P. G. rschman and L. A. Johnson, J. Appl. Phys. 49, 1769, 1978.
1.30 J. J. Rhyne, J. H. Schelleng and N/ S. Koon, Phys. Rev. B10, 4674, 1974.
1.31. Luborsky, F. E., R. O. McCary and J. J. Becker, 1976a, in Rapidly quenched metals, Section 1 (eds. N. J. Grant and B. C. Gressen) (MIT Press, Cambridge, Mass.) P.467.
1.32. E. Amano, R. Velenzuela, J. T. S. Irvine and A. R. West, J. Appl. Phys. 67, 5589(1990).
1.33. J. T. S. Irvine, E. Amano and R. Valenzuela, Mater. Sci. Eng. A133, 140 (1991).
1.34. K. M. Polivanov, Izv. Akad. Nauk. SSSR (Ser. Fiz.) 16(1952) 449.
1.35. R.H. Pry and C. P. Bean, J. Appl. Phys. 29(1958) 532.
1.36. J. E. L. Bishop, Brit. J. Appl. Phys. 17(1966) 451.
1.37. G. Ban, L. Szentmiklosi, P. Arato and M. Juhasz, J. Magn. Magn. Mater. 41(1984) 382-384.
1.38. G. Ban, P. Arato and L. Szentmiklosi, J. Magn. Magn. Mat., 37(1983) 309.
1.39. G. Buttino, Aeecchetti, M. Poppi and G. Zini, IEEE Trans. Magn. MAG-18 (1982) 1400.
1.40. S. D. Washko, M. L. Oshorn and W. G. Veeraraghaven. J. Appl. Phys., 52 (1981) 1899.
1.41. G. Lehmann, G. Dietzmann and M. Schaefer, Hermsderfer Techn. Mitt. 80 (1991) 2563.
1.42. M. Schaefer and G. Dietzmann, J. Magn. Magn. Mater. 133 (1994) 303-305.
1.43. Zhang Yan Zhong, J. Magn. Magn. Mat. 68 (1987) 145-150.
1.44. Y. Z. Zhang, Acta Metallurgica Simica, 21 (1985) B189 (in Chinese).
1.45. Y. Z. Zhang, Scientia Sinica, Series A30 (1987) 317 (in English).
1.46. K. Ohta and T. Matsuyama, J. Magn. Magn. Mat. 19 (1980) 165.
1.47. Mizoguch, T. et. al.: Proc. 4th Int. Conf. on Rapidly Quenched Metals, Sendai (1981), P.1195.
1.48. Jagielinski, T., Walecki, T.: Phys. Stat. Sol.(a) 60 (1980) K31.

1.49. Alben R. J. I. Bundnick and G. S. Cargill III 1977, in metallic glasses (eds. H. S. Leamy and J. J. Gilman) (American Society for metals. Metals. Park. Ohio ch.12.
1.50. Felsch. W., 1970, Z. Angew. Phys. 29,218.
1.51. Shimada, Y. and H. Kojima, 1976, J. Appl. Phys. 47, 4156.
1.52. Wright, J. G., 1976, IEEE Trans. Magnetics MAG-12, 95.
1.53. Becker, J. J., F. E. Luborsky and J. L. Walter, 1977, IEEE Trans. Magnetics MAG-13, 988.
1.54. Kouvel, J. S., 1969, in Magnetism and Metallurgy (eds. A. E. Berkowitz and E. Kneller)(Academic Press, New York) P.523-575.
1.55. J. Horvat, E. Babic and Z. Morohnic, J. Magn. Magn. Mater. 86 (1990) L1-L6.
1.56. J. Horvat, Z. Morohnic and E. Babic, J. Magn. Magn. Mat. 82 (1989) 5.
1.57. J. W. Lynn and J. J. Rhyne, in: Spin waves and Magnetic Excitations, eds. A. S. Borovik-Romanov and S. K. Sinha (North-Holland, Amsterrdam, 1988) Part II, cap. 4. P.177.
1.58. S. C. Yu, J. W. Lynn and J. J. Rhyne J. Magn. Magn. Mat. 97(1991) 286-290.

1.59. Lu Bang, Q. Y. Shen, N. Matsumoto, F. Ono, O. Kohmoto, H. Maeta and K. Haruna, J. Magn. Magn. Mat. 104-107(1992) 147-148.
1.60. Y. Yoshizawa, S. Oguma and K. Yamauchi, J. Appl. Phys. 64(1988) 6044.
1.61. Le minh, Bach Tanch Cong, Tran Quoc An and Neguyen Chau, Proceeding of the 2nd International Workshop on Materials Science (IWOMS-95) Hanoi, Oct 1991.
1.62. Kay-Yuan Ho, P. J. Flanders and C. D. Graham, Jr. J. Appl. Phys. 53(1982) 2279.
1.63. J. D. Livingston, W. G. Morris and T. Jagielinski, IEEE, Trans. Magn. 19(1983) 1916.
1.64. H. J. de wit, C. H. M. Witmer and A. Dirne, IEEE Trans. Magn. 23(1987) 2123.
1.65. G. Herzer and H. R. Hilzinger, Physica Scripta, T24 (1988) 22.
1.66. Allia, P., Vinai, F.: Proc. 14th Metalltagung in der DDR, Dresden 1981, P.397.
1.67. Allia, P. etal. Sol. St. Com. 24 (1977) 517.
1.68. Miyazaki, T., Takahashi, M.: Jap. J. A. P. 17 (1978) 1755.
1.69. Ohta, K. et. al. :J. M. M. M. 19 (1980) 165.
1.70. H. Koronmuller, H. Q. Guo, W. Femengel, A. Hofinan and N. Moser, Crystal Lattice Defects Amorphous Mater. 11(1985) 135.
1.71. M. Bourrous and H. Koronmuller, Phy. Stattes. Soladi(a) 113 (1989) 169.
1.72. H. Kronmuller, Phys. Status Solidi(b), 118 (1983) 661.

1.73. A. M. Severino, A. D. Santos and F. P. Missell, Materials Science and Engineering A133 (1991) 132-135.
1.74. Chi, M. C. and R. Alben, 1976, AIP Conf. Proc. 34, 316.
1.75. Fujimori, H., H. Morita, Y. Obi and S. Ohta. 1977, in Amorphous magnetism II (eds. R. A. Levy and R. Hasegawa) (Plenum Press, New York) P.393.
1.76. Sherwood, R. C., E. M. Gyorgy, H. J. Leamy and H. S. Chen, 1976, AIP Conf. Proc.34, 325.
1.77. Sφren Linderoth, J. Magn. Magn. Mater. 104-107, (1992) 128-130.
1.78. L. Dobrzynski, K. Szymanski, J. Wallszewski, A. Malinowski, J. Magn. Magn. Mat. 88 (1990) 23-26.
1.79. K. I. Arai, N. Tsuya, M. Yamada and T. Masomoto, IEEE Trans. Magn. MAG-12 (1976) 939.
1.80. T. E. sharon and C. C. Tsuei, Phys. Rev. B5, 1047, 1972, J. M. D. Coey J. de Physique, C6, 58, 1974.
1.81. K. Raj., J. Durand, J. J. Budnick, S. Skalski, J. Appl. Phys. 49, 1671, 1978.
1.82. Chien, L. L. and R. Hasegawa, 1977, in Amorphous Magetism II (eds. R. A. Levy and R. Hasegawa) (Plenum Press New York) P.289.
1.83. Tsuei, C. C. and H. Llienthal, 1976, Phys. Rev. B13, 4899.
1.84. Chien, C. L. and R. Hasegawa, 1976a, AIP Conf. Proc. 29, 214.
1.85. Rodmarcq, B. M. Piecuch, Chr. Janot. G. Marchal and Ph. Mangin. 1980, Phys. Rev. B21, 1911.
1.86. Chappert, J., J. M. D. Coey, A. Lienard and J. P. Rebouillat. 1981, J. Phys. F11, 2727.
1.87. Chien, C. L., and K. M. Unruh, 1982, Nucl. Instrum Methods 199, 193.
1.88. Gubbens, P. C. M., J. H. F. Appeldorn, A. M. Vander Kraan and K. H. J. Buschow, 1974, J. Phys. F4,921.

Chapter-2

2.1. W.Klement Jr., R. H. Willens and P. Duwez, Nature, 187, 809, 1960.
2.2. Gubanov, A. I. 1960, FIZ. Tver. Tel. 2, 502.
2.3. Pond. R. Jr. and R. Maddin, 1969, Trans. Met. SOC. ALME 245, 2475.
2.4. Mader, S. and A. S. Nowick, 1965, Appl. Phys. Lett. 7, 57.
2.5. Tsuei, C. C. and P. Duwez, 1966, J. Appl. Phys. 37, 435.
2.6. T. Mizoguchi, IBM Research Report RC 6054, 1976.
2.7. R. Alben, J. I. Budnick, G. S. Gargill, III, Metallic glasses (American SOC. for Metals. 1978) p-304.

2.8. E. M. Gyorgy, ibid P-275.
2.9. G. S. Cargill III, Solid State Physics, Vol-30 Ed. Ehrenreich et. al., Academic Press, New York (1975) P-257.
2.10. T. Masumoto, S. Ohnuma, K. Shirakawa, M. Nose and K. Kobayshi, Int. Conf. on Liquid and Amorphous Metals, Grenoble France, 1980.
2.11. Cargill III, G. S., 1975a, Solid State Physics 30, 227.
2.12. Cargill III, G. S., 1976, in Rapidly quenched metals, Section I (eds. N. J., Grant and B. C. Giessen) (MIT Press., Cambridge, Mass) P.293.
2.13. M. A. Asgar, Vol (1984) Mechanical Engineering Research Bulletin (BUET) P.1.
2.14. Alben R., J. I. Budnick and G. S. Cargill III, 1977. in Metallic glasses (eds. H. S. Leamy and J. J. Gilman) (American Society for Metals, Metals Park, Ohio) ch.12.
2.15. Turnbull, D., 1969, Contemp. Phys. 10, 473.
2.16. Duwez, P., R. H. Willens and W. Klement, Jr., 1960, J. Appl. Phys. 31, 1136.
2.17. H. S. Chen, Rep. Prog. Phys. 43, 23 (1980).

Chapter-3

3.1. Turnbull, D., 1974, J. de physique 35, C4-1.
3.2. Takayama, S., 1976, J. Materials Sci. 11, 164.
3.3. Cohen, M. H. and D. Turnbull, 1961, Nature 189, 131.
3.4. Felsch, W., 1969, Z. Phys. 219, 280.
3.5. Luborsky, F. E., 1978, J. Magn. & Magn. Mater. 7, 143.
3.6. K. Yamaguchi and T. Mizaguchi, J. Phys. SOC. Japan, 39, 541, 1975.
3.7. Harris, R., M. Phischke and M. J. Zuckerman, 1973, Phys. Rev. Lett. 31, 160.
3.8. Handrich, K., 1972, Phys. Stat. Sol.(b) 53, K17.
3.9. P. Weiss, J. Phys. Radium, 4(1907) 661.
3.10. J.S. Smart, Effective Field Theories of Magnetism, W. G. Saunders Co., Philadelphia and London, 1966.
3.11. Handrich, K., 1969, Phys. Status Solidi 32, K55.
3.12. Jäger, E., 1977, Phys. Status Solidi 1380, K81.
3.13. Kaul, S. N., 1981b, Phys. Rev. B24, 6550.
3.14. Pan, D., and D. Turnbull, 1974, J. Appl. Phys. 45, 1406.
3.15. Kaneyoshi, T., and I. Tamura, 1984, Phys. Status Solidi B123, 525.
3.16. Keffer, F., 1966, in Ferromagnetism, ed. H.P.J. Wijn (Springer, Berlin) Vol.XVIII. 2, P.1.

3.17. Harris, R., M. Plischke and M. J. Zuckerman, 1973, Phys. Rev. Lett. 31, 160.
3.18. Handrich, K., 1969, Phys. Stat. Sol. 32, K55.
3.19. Hasegawa, R., 1976, AIP Conf. Proc. 29, 216.
3.20. Fujimori, H., Y. obi, T. Masumoto and H. Saito, 1976c, Materials Sci., Eng. 23, 281.
3.21. J. T. S. Irvine, E. Amano, A. Huanosta, R. Valenzuela and A. R. West, Solid State Ionics 40/41, 220, (1990).
3.22. E. Amano, R. Valenzuela, J. T. S. Irivne and A. R. West, J. Appl. Phys. 67, 5589 (1990).
3.23. J. T. S. Ivine, E. Amano and R. Valenzuela, Matewer. Sci. Eng. A133, 140 (1991).
3.24. R. M. Jones, IEEE Trans. Mag. MAG-18, 1559 (1982).
3.25. M. R. J. Gibbs, Proc. Conf. Metallic Glasses Science and Technology, Budapest 1980, Vol.2C. hargitai, J. Bakonyi and T. Kemeny (Kultura, Budapest) P.37.
3.26. J. L. Snoek, Physica, 14, 207 (1948).
3.27. M. H. L. Pryce. Phys. Rev. 80, 1107 (1950)
3.28. R. M. Bozorth, J. F. Dillinger and G. A. Kelsau, Phys. Rev. 45, 742 (1934).
3.29. C. D. graham Jr. and T. Egami, Journal of magnetism and magnetic materials 15-18, 1325 (1980).
3.30. S. Chikazumi, J. Phys. SOC. Japan 5, 327 (1950).
3.31. S. Kaya, Rev. Mod. Phys. 25, 49 (1953).
3.32. L. Neel, Comp. Rend. 225, 109 (1947).
3.33. C. Kittel, E. A. Nesbitt and W. Shockley, Phys. Rev. 77, 739 (1950).
3.34. R. J. gimbino, J. Ziegler and J. J. Cuomo, Appl. Phys. Letters 24, 99 (1974).
3.35. N. Heiman, A. Onton, D. F. Kyser, K. Lee and C. R. Cxuarnievi, AIP Conf. Proc. 24, 573 (1974).
3.36. Sataro Esno and Shozo Fujiware, J. Appl. Phys. 331 (1974).
3.37. M. A. Asgsar and S. S. Sikder, Indian J. Phys. 71A(6), 689-696 (1997).
3.38. Akulov, N., Z. Phys. 100, 197 (1936).
3.39. Carr Jr., W. J., Phys. Rev. 109, 197 (1958).
3.40. Zener, C., Phys. Rev. 96, 1335 (1954).
3.41. Van Vleck, J. H., J. Phys. Radium, 20, 124 (1956).
3.42. Carr Jr., W. J., Phys. Rev. 108, 1158 (1957).
3.43. Keffer, F., Phys. Rev. 100, 1692 (1955).
3.44. J. C. Slonczewski, Phys. Rev. 11, 1341 (1958).
3.45. K. Yosida and M. Tachiki, Prog. Theor. Phys.17, 331 (1957).
3.46. Egami T., P. J. Flanders and C. D. Graham Jr., 1975, AIP Conf. Proc. 24, 697.
3.47. Miyazaki T. and M. Takahashi, 1978, J. Appl. Phys. 17, 1755.

3.48. Suzuki, Y., and N. Ohta, 1988, J. Appl. Phys. 63, 3633.
3.49. Fähnle, M., and J. Furthmüller, 1989, Phys. Status Solid. A116, 819.
3.50. Berry, B. S. and W. C. Pritchet, 1976, AIP Conf. Proc. 34, 292.
3.51. Sherwood, R. C. , E. W. gyorgy, H. J. Leamy and H. S. Chen, 1976, AIP Conf. Proc. 34, 325.
3.52. F. J. Litterest, J. Physique Letts., 36, L197, 1975.
3.53. P. G. d. Gennes, J. Apys. Radium, 23, 620 (1962).
3.54. S. K. Ghatak (unpublished).
3.55. R. Alben, J. Becker and M. Chi, J. Appl. Phys. 49, 1653 (1978).
3.56. J. Durand, in: Glassy Metala II (Springer, Berlin 1983).
3.57. L. W. Eagg and S. S. Hanna, Rev. Mod. Phys., 31, 711 (1959).
3.58. S. S. Hanna, J. Herberle, C. Littlejohn, G. J. Perlow, R. W. Perston and D. H. Vincent, Phys. Rev. Letters, 4, 177 (1960).
3.59. Chien, C. L. and R. Hasegawa, 1977, in Amorphous magnetism II (eds. R. A. Levy and R. Hasegawa) (Plenum Press, New York), p.289.
3.60. Mössbauer effect: Principle and Applications Gunther K. Wertheim Academic Press, New York, 1964.
3.61. U. Gonser, Ed. , Topics in Applied Physics, Springerverlag, Berlin heidelberg, New York (1973).
3.62. O. C. Kistner and A. W. Sunyar, Phys. Rev. Letters 4, 229 (1960).
3.63. V. I. Goldanskii and R. H. Herber, Eds., Chemical Applications Academic Press, New York (1964).
3.64. H. Kopferman, Kernmoments Akad, Verlagsges; M. Frankfurt (1956).
3.65. C. J. Ballhausen, Introduction in to the theory of Liggnnd Fields, Mc Graw-Hill, New delhi (1962).
3.66. M. H. Cohen and F. Reif, Solid State Phys., 5, 321 (1957).
3.67. S. L. Ruby and P. D. Flinn, Rev. Mod. Phys., 36, 351 (1964).
3.68. R. L. Collins, J. Chem. Phys., 42, 1072 (1965).
3.69. R. L. Collins and J. C. Travis, Mössbauer effect methodology ed., I. J. Gruvermun, Plenum Press, New York (1967).
3.70. R. M. Sternheimer, Phys. Rev., 80, 102 (1950).
3.71. R. M. Sternheimer and H. M. Foley, Phys. Rev., 102, 731 (1956).
3.72. R. M. Sternheimer, Phys. Rev., 84, 244(1951).
3.73. E. Fermi, Z. Physik, 60, 320 (1930).
3.74. R. A. Ferrel, Am. J. Phys., 28, 484 (1960).
3.75. G. T. Rado, Am. J. Phys., 30, 716 (1962).
3.76. K. E. Watson and A. J. Freeman, Phys. Rev. 123, 2027 (1961).

Chapter-4

4.1. Chatelier, H. Le., Bull SOC. franc. mineral, 1887, 10, 204.

4.2. M. A. Mazid and M. A. Chowdhury, "Design and Construction of a Forner type vibrating sample magnetometer.", AECD/MMD/1, June, 1986 (Bangladesh).

4.3. S. Forner, Rev. Sci. Instr. 27, 548 (1956).

4.4. Westerstrandh, A., Gafvert, U., Lundgren, L. Physica Scripta, 14, 5-10 (1976).

4.5. Akulov, N., Z. Phys. 100, 197 (1936).

4.6. An Introduction to Mössbauer spectroscopy, Leopold May, Plenum Press, New York, 1971.

4.7. Mössbauer spectroscopy, N. N. Greewood and T. C. Gibb Chapman and Hall Ltd., London, 1971.

4.8. Mössbauer study of Electric field gradients in Natural Mica and Synthetic spnel systems, Anjali Krishnamoorthy, Ph. D. Thesis, University of Rajasthan, Jaipur, 1980.

4.9. Ericsson, Private communication (1985).

4.10. Rajkamal, Private communication (1986).

Chapter-5

5.1. Wright, J. G., 1976, IEEE Trans. Magnetics MAG-12, 95.

5.2. F. E. Luborsky, J. J. Becker and R. O. McCary, IEEE Trans. Mag. Mag. 11, 1644, (1975).

5.3. M. Kersten:, Z. Angew, Phys. 7, 313 (1956), 8, 382, 496 (1956).

5.4. Durand, J. and M. Yung, 1977, in Amorphous magnetism II (eds. R.A. Levy and R. Hasegawa) (Plenum Press, New York) P.275.

5.5. Overshott, K. J. IEEE Trans. Magn. MAG-17, 2698 (1981).

5.6. Nathusingh, D. and Smith, C. H. J. Proc. Conf. on power Conversion 7, paper B2 San Diego (1980).

5.7. M. A. Mazid and M. A. Chowdhury, "Design and Construction of a Forner type vibrating sample magnetometer.", AECD/MMD/1, June, 1986 (Bangladesh).

5.8. M. A. Asgar and S. S. Sikder, Indian J. Phys. 71A(6), 689-696 (1997).

Chapter-6

6.1. H. J. Kronmuller, J. Appl. Phys., 52, 1859 (1981).

6.2. H. J. Kronmuller, J. Magnetism Magn. Mate. 24, 159 (1981).

6.3. F. E. Luborsky, J. J. Becker, and R. O. McCary, IEE Trans. Magn. MAG-11, 1644 (1975).

6.4. D. Nathusingh and C. H. Smith, C. H. J. Proc. Conf. on Power Conversion 7, paper B2 San Diego (1980).

Chapter-7

7.1. G. S. Cargill III; Aip Cnf., Proc. 24 (1975) 138.

7.2. Y. Ishikawa, " Physics and applications of Invar Alloys, Honda Memorial series No.3" (Maruzen Company, LTD, 1978) P.165.

PUBLICATIONS

Publications of the author on Ph.D. research works and relevant field

1. S. S. Sikder, M. A. Asgar, **"The kinetics of atomic and magnetic ordering of Co-based amorphous ribbons as affected by iron substitution"**, Thermochimica Acta 326 (1999) 119-126.

2. M. A. Asgar and S. S. Sikder, **"Influence of glass forming material on atomic and magnetic ordering of Fe-based metallic glass"**, Indian J. Phys. 73A (4), 493-502 (1999).

3. S. S. Sikder, M. A. Asgar and F. A. Khan, **"Study of the temperature dependence of magnetic anisotropy of amorphous ribbons with composition $Co_{80-x}Fe_xB_{20}$ [x = 2.5, 5.0, 7.5 & 10]"**, Journal of Bangladesh Academy of Science, Vol.23, No.1, 43-51, 1999.

4. S.S.Sikder , M. A. Asgar, M. A. Hakim and M. A. Mazid, **"The effect annealing on the magnetization process of Iron-Boron ribbon"**, Journal of Bangladesh Academy of Science . Vol.20, No.2, 237-245, 1996

5. M. A. Asgar and S. S. Sikder ; **"The effect of annealing on magnetostriction of amorphous Iron-Boron ribbon"**, Indian J. Physics 71A(6), 689-696 (1997).

6. S. S. Sikder, M. A. Asgar and M. A. Hakim, **"Temperature dependence of a.c. initial permeability of amorphous ribbons with composition $Co_{80-x}Fe_xB_{10}Si_{10}$ [x = 0, 2, 4, 6 & 8]"**, Indian J. Phys. 73A(5), 639-646 (1999)

7. S. S. Sikder, M. A. Asgar and M. A. Hakim, **"Study of glass transition, crystallization and ferromagnetic transition temperatures of amorphous Nickel-Iron-Boron ribbons as affected by composition"**, The Bangladesh J. Sci. Res. 16, 121 (1998).

8. S. S. Sikder, M. A. Asgar and M. A. Hakim, **"Static and dynamic magnetic properties of Nickel-Iron-Boron metallic glass"**, (accepted for publication in Journal of Bangladesh Academy of Science).

9. S. S. Sikder, M. A. Asgar, M. A. Hakim, M. R. Bari, M. A. Chowdhary, N. Chau and N. H. Nghi, **"Effect of iron substitution on the static and magnetic characteristics of cobalt based amorphous ribbons"**, (submitted for publication in Nuclear Science and Applications).

10. S. S. Sikder, M. A. Asgar, B. K. Srivastava and A. Krishnamurthy, **"The study of hyperfine fields of amorphous ribbons with composition $Ni_{80-x}Fe_xB_{20}$ by Mössbauer technique"**, (submitted for publication in Journal of Bangladesh Academy of Science).

11. S. S. Sikder, M. A. Asgar, B. K. Srivastava and A. Krishnamurthy, **"Mössbauer spectroscopy studies of amorphous Iron-Silicon-Boron system with compositions $Fe_{90-x}Si_xB_{10}$ [x = 6, 8, 10,12 & 14]"**, (submitted for 20th Bangladesh Science Conference Proceeding, 1998).

12. S. S. Sikder and M. A. Asgar; **"Temperature dependence of specific magnetization of amorphous ribbons with composition $Ni_{80-x}Fe_xB_{20}$ [x = 20, 30, 40 & 50]"**, (submitted for International Symposium on Recent Advances in Physics Conference Proceeding, 1999).

13. S. S. Sikder, M. A. Asgar and F. A. Khan; **"Evaluation of stress induced anisotropy in magnetic amorphous ribbons with composition $Fe_{90-x}Si_xB_{10}$ [x = 6, 8, 10, 12 & 14]"** (submitted for International Symposium on Recent Advances in Physics Conference Proceeding, 1999).